Field Induced Phase Transitions in Ferroelectric Materials

Feldinduzierte Phasenübergänge in ferroelektrischen Werkstoffen
Zur Erlangung des akademischen Grades Doktor-Ingenieur (Dr.-Ing.)
genehmigte Dissertation von Dipl.-Phys. Daniel Jason Franzbach aus Kassel
Januar 2014 — Darmstadt — D 17

TECHNISCHE
UNIVERSITÄT
DARMSTADT

Fachbereich Material- und Geowissenschaften
Institut Nichtmetallisch Anorganische Werkstoffe
Graduate School of Computational Engineering

Field Induced Phase Transitions in Ferroelectric Materials
Feldinduzierte Phasenübergänge in ferroelektrischen Werkstoffen

Genehmigte Dissertation von Dipl.-Phys. Daniel Jason Franzbach aus Kassel

1. Gutachten: Jürgen Rödel
2. Gutachten: Ralf Müller

Tag der Einreichung: 30. Juli 2013
Tag der Prüfung: 02. September 2013

Darmstadt — D 17

Erklärung zur Dissertation

Hiermit versichere ich, die vorliegende Dissertation ohne Hilfe Dritter nur mit den angegebenen Quellen und Hilfsmitteln angefertigt zu haben. Alle Stellen, die aus Quellen entnommen wurden, sind als solche kenntlich gemacht. Diese Arbeit hat in gleicher oder ähnlicher Form noch keiner Prüfungsbehörde vorgelegen.

Darmstadt, den 28. Juli 2013

(D. J. Franzbach)

Für Tabea

Contents

List of Figures

List of Tables

Symbols and Abbreviations

Symbol	Units	Meaning
α_p		Polarizability
α_i	Vm/As	Second order (quadratic) landau coefficient (vector)
β_{ij}	$\mathrm{Vm}^5/(\mathrm{As})^3$	Fourth order Landau coefficient (second-rank tensor)
C	K	Curie constant
$\mathbb{C}_{ijkl}$	N/m^2	Linear stiffness (fourth-rank tensor)
$\mathbb{C}^D_{ijkl}$	N/m^2	Linear stiffness for constant D_i (fourth-rank tensor)
$\mathbb{C}^E_{ijkl}$	N/m^2	Linear stiffness for constant E_i(fourth-rank tensor)
χ_{ij}	As/Vm	Dielectric susceptibility (second-rank tensor)
D_i	C/m^2	Electric displacement field (vector)
d	m	Thickness, distance
$\mathbb{d}_{ijk}$	m/V	Piezoelectric constant (third-rank tensor)
d^*_{33}	pm/V	Effective piezoelectric constant (in field direction)
δ_{ijkl}	$\mathrm{Vm}^{1}3/(\mathrm{As})^7$	Eighth order Landau coefficient (fourth-rank tensor)
δ_{ij}		Kronecker symbol
δ_R		Rhombohedral lattice distortion
δ_T		Tetragonal lattice distortion
E	N/m^2	Young's modulus
E_i	V/m	Electric field (vector)
$E_{i,j}$	N/m^2	Green's strain tensor (second-rank tensor)
E_C	V/m	Coercive field
E_D	V/m	Depolarizing field
$\mathbb{e}_{ijk}$	N/Vm	Piezoelectric constant (third-rank tensor)
ϵ_{ij}	As/Vm	Absolute permittivity (second-rank tensor)
ϵ_0	As/Vm	Vacuum permittivity ($\sim 8.8541 \cdot 10^{-12}$)
ϵ_r		Relative permittivity (isotopic)
ϵ^T_r		Relative permittivity (stress-free, isotopic)
ϵ^S_r		Relative permittivity (clamped, isotopic)
F^{es}_i	N	Electrostatic force (vector)
F^{me}_i	N	Mechanical force (vector)

G	J/m^3	Gibbs free energy
G_{LD}	J/m^3	Landau energy
G_0	J/m^3	Energy threshold for 180 °C
G_1	J/m^3	Energy threshold for 90 °C
$\mathbb{g}_{ijk}$	Vm/N	Piezoelectric constant (third-rank tensor)
γ_{ijk}	$\mathrm{Vm}^9/(\mathrm{As})^5$	Sixth order Landau coefficient (fourth-rank tensor)
$\mathscr{H}^{el}$	J/m^3	Dielectric Enthalpy
$\mathscr{H}^{ela}$	J/m^3	Elastic energy
$\mathscr{H}^{diel}$	J/m^3	Dielectric energy
$\mathscr{H}^{coup}$	J/m^3	Electromechanical coupling energy
$\mathbb{h}_{ijk}$	V/m	Piezoelectric constant (third-rank tensor)
k_{ij}		Electromechanical coupling factor (second-rank tensor)
M	A/Vm	Mobility parameter
$\mathbb{M}_{ijkl}$	$\mathrm{m}^2/\mathrm{V}^2$	Electrostrictive tensor (fourth-rank tensor)
N	$1/\mathrm{m}^3$	Atom/molecule density
$\mathbf{n}_s$		Surface normal vector
p_i	Asm	Electric dipole moment (vector)
P_i	As/m^2	Dielectric polarization (vector)
P_r	As/m^2	Remanent polarization
$\mathbf{P}_s$	As/m^2	Spontaneous polarization (vector)
P_0	As/m^2	Equilibrium polarization
$\mathbb{p}_i^{pyro}$	$\mathrm{As}/\mathrm{m}^2\mathrm{K}$	Pyroelectric constant (vector)
ϕ	V	Electrostatic potential
Q, q	As	Charge
$\mathbb{Q}_{ijkl}$	$\mathrm{m}^4/(\mathrm{As})^2$	Electrostrictive tensor (fourth-rank tensor)
R_A, R_B	m	Cation radius
R_X	m	Anion radius
r_i, $\mathbf{r}$	m	Position vector
ρ	C/m^3	Charge density
S_{ij}	m/m	Strain (second-rank tensor)
S_{ij}^0	m/m	Spontaneous strain (second-rank tensor)
S_0	m/m	Spontaneous strain (in field direction)
S_r	m/m	Remanent strain (in field direction)

S_s	$\mathrm{m/m}$	Switching strain (in field direction)
S^0	$\mathrm{m/m}$	Equilibrium strain of a unit cell
S_{33}^*	$\mathrm{m/m}$	Usable strain (in field direction)
σ_s	$\mathrm{As/m^2}$	Surface charge density
σ_b	$\mathrm{As/m^2}$	Bound surface charge density
t	s	Time
T	K	Temperature
T_{ij}	$\mathrm{N/m^2}$	Stress (second-rank tensor)
T_C	$\mathrm{N/m^2}$	Coercive stress
t_G		Goldschmidt’s tolerance factor
T_0	K	Phase transition temperature (Curie Point)
Θ	K	Curie temperature
U	V	Voltage
u_i	m	Mechanical displacement (vector)
V	$\mathrm{m^3}$	Volume
ν		Poisson’s ratio
W	Nm	Work

Vector quantities are printed in bold ($\vec{P} \equiv \mathbf{P}$). Furthermore, the Einstein notation is used to keep coordinate formulas clearly arranged. According to this convention, when an index variable appears twice in a single term summation over all of its possible values is implied (mostly over the three spatial coordinates):

$$P_i = \chi_{ij} E_i \quad \Leftrightarrow \quad P_i = \sum_{j=1}^{3} \chi_{ij} E_j \tag{0.1}$$

where P_i and C_{ij} are also equivalent representations of vectors and tensors. Characteristic values like the remanent polarization or strain are actually vectors and matrices.

1 Introduction

1.1 Motivation

Today's modern life is unimaginable without applications based on ferroelectric materials. Due to their large dielectric constant in the range between 100 and 100 000 [1, 2] they find their application in high performance and thin film capacitors. Additionally, the nonlinear constitutive behavior of ferroelectric materials allows the realization of tunable electric components even at high frequencies (10 GHz) [3, 4]. This is, for example, used in modern multi-band cellar phone antennas [5]. The existence of a spontaneous dipole moment, which can be switched between several stable remanent states, makes these materials also suitable for electric data storage in a novel non-volatile version of random access memory (FeRAM - ferroelectric RAM) [6]. In addition to purely electrical applications, ferroelectric materials belong to a larger class of electroactive materials, called piezoelectrics. In contrast to most of the other piezoelectric materials, ferroelectrics are not required to be mono-crystalline to show piezoelectric behavior. This characteristic allows a cheaper and more flexible production of polycrystalline piezoelectric components. Piezoelectric actuators based on polycrystalline ferroelectric ceramics are today dominating the application field of ultrasound sources/detectors, loudspeakers for active sound damping, pressure sensors, common rail fuel-injection systems and as positioners in scanning tunneling or atomic force microscopes [7]. In 2009 the global market for piezoelectric actuators was about 6.587 billion US-\$, as illustrated in Figure 1.1 a). The average annual growth rate is estimated at 13 % and the market is expected to grow up to 12.290 billion US-\$ in 2014.

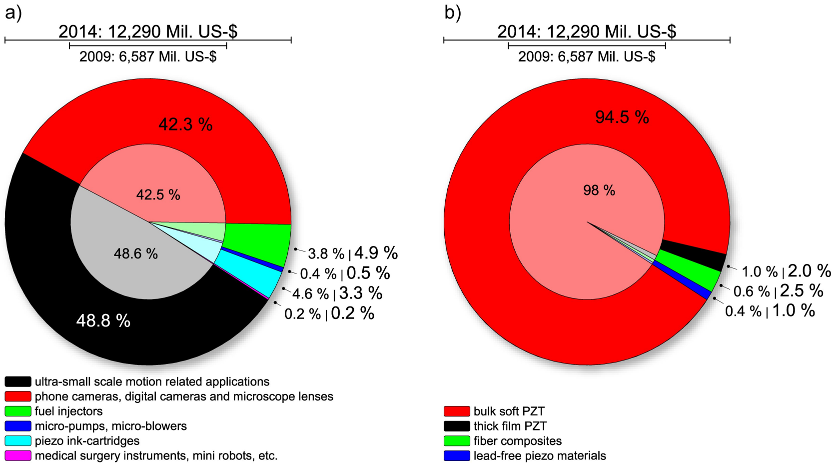

Figure 1.1: Global market shares of piezoelectric actuators with respect to (a) applications and (b) materials [8, 9]. The scale bars on top of each plot denotes the market size. Reproduction of the data is under the kind permission by Innovative Research and Products, Inc

The ferroelectric effect has been known since 1921, when it was first discovered in the highly nonlinear and hysteretic dielectric behavior of Rochelle (Seignette) salt crystal by J. Valasek. He originally named the effect after the material in "Rochelle (Seignette) electricity" [10, 11]. This name was later changed in ferroelectricity to highlight the analogy in the behavior to the phenomena of ferromagnetism. Unfortunately, Rochelle salt was too fragile and the measured ferroelectric effect was very small. No meaningful applications were found until the discovery of polycrystalline barium titanate ($BaTiO_3$) in

1940 [12] and lead titanate ($PbTiO_3$) in 1951 [13]. It turned out that besides their distinct non-linear and hysteretic dielectric behavior, these ferroelectric ceramics were polycrystalline solids that show a strong electromechanical coupling, the so-called piezoelectric effect that can be used for a variety of applications.

Most of the material properties of a ferroelectric material improve drastically in the vicinity of a phase transition between two different ferroelectric phases or between the paraelectric and a ferroelectric phase. Unfortunately, these effects only apply in a small temperature range. An important step in the development of the today's high performance materials was the discovery of a temperature-stable morphotropic phase boundaries in solid solutions of materials with different phases like lead zirconate titanate $Pb(Zr_{1-x}Ti_x)O_3$ [14], which made property enhancement due to the phase transition useful for applications.

Since the discovery of the ferroelectric effect, various material models were developed in order to understand the fundamental processes and to improve the performance and reliability of ferroelectric materials and applications. The interactions in the system of electric dipoles are similar to those between magnetic dipoles in ferromagnetic systems. But the fact that the polarization system is strongly coupled to the system mechanics prohibits a simple carry-over from ferromagnetic theories. Instead it is necessary to include the mechanics in the theoretical model. Ab initio and molecular dynamics (MD) calculations [15–19] can determine the behavior of single atoms or molecules in the solid by numerically solving the electric state of many-body systems. The main advantage is that no phenomenological parameters from experiments are required. Results may be used to determine macroscopic thermodynamic properties of the system that can be used by other material models [17–19]. However, these models are limited to a very small structure size of a few elementary cells. In contrast, micro-mechanical models are able to simulate the macroscopic behavior of polycrystalline ferroelectrics [20]. Typically, switching energy criteria for the spontaneous polarization are proposed and the particular switching region is assumed to be an entire grain or domain. Therefore, microscopic effects such as domain walls and intergranular stresses can only be included indirectly. Thus influences of defects and different sorts of grain boundaries can not be studied. Phase field models based on Landau theory work on a mesoscopic scale and are able to close the gap between the other two models [21, 22]. They are based on the thermodynamic mean field approximation that all the essential physical degrees of freedom can be described by continuous fields; the physical processes on the atomic scale are treated as a single averaged effect. The system dynamic on the atomic length scale therefore remains unobtainable. Both models require many phenomenological parameter that can be either determined from experiments or from ab initio calculations. Because of the complexity of the coupled partial differential equations and the fact that the resolution of the FEM mesh has to be in the vicinity of domain wall size, phase field models are limited to structures in the order of magnitude of a single grain. However, predicted switching criteria can be used to adjust the parameters of micro-mechanical models.

Traditionally, lead-based perovskite ceramics, such as $Pb(Zr,Ti)O_3$, have been dominantly used for electro-mechanical applications; as shown in Figure 1.1 b) in 2009 99 % of the produced piezoelectric actuators was based on PZT [9]. In the last years, attempts were undertaken to avoid environmental pollution from the production of lead based piezoceramics. Promising new candidates are giant strain materials like BNT-6BT-2KNN [8]. Without the application of an external field these materials show no ferroelectric order. Instead, it is assumed that randomly oriented non-interacting nano-domains are formed. By applying an external field it is possible to induce a phase transition to a polar phase, which corresponds to the generation of a large strain. Because this polar state is not stable when the field is removed, low remanence and large usable strains are found in these materials. Unfortunately, these fields are too large for real applications. The solution is the combination with a chemically compatible polar material to serve as seeds for the phase transition and to lower the required fields. New material models are necessary to identify the optimal material combination, composition, and microstructure.

1.2 Outline

The focus of this work lies in the theoretical description of electrical field- and mechanical stress-induced phase transitions and their influence on the material behavior of ferroelectric single crystals, polycrystals and composite materials. Phase transitions are interesting phenomena that lead to improved properties of the ferroelectric material.

Chapter 2 gives a short introduction on the basic formalism of electrostatics and continuum mechanics, which are the foundations of material models of ferroelectrics. In addition, some fundamentals of crystallography will be discussed to understand the atomistic reason of the ferroelectric effect. In the first part of Chapter 3, a two dimensional Landau type model is presented, which is used to study electrical field-induced tetragonal → orthorhombic phase transitions in arbitrary ferroelectric single crystal materials. The Landau energy landscape was varied to examine the influence of the switching energies and the polarization rotation path on the predicted phase transition field. In the second part, the model is expanded to three dimensions. Landau parameters from literature were used to predict the tetragonal → orthorhombic phase transition behavior of $BaTiO_3$. Large signal measurements on single crystalline $BaTiO_3$ were performed to verify the model and to compare the predictive capabilities of the various Landau potentials.

In Chapter 4, the Landau model is further expanded to describe polycrystalline ferroelectrics like $Pb(Zr,Ti)O_3$ under uniaxial compressive strain and electric field. In contrast to micro-mechanical models, the Landau energy model intrinsically considers tetragonal ⟷ rhombohedral phase transitions. These induced transitions provide a good explanation for the exceptional switching strain of rhombohedral $Pb(Zr,Ti)O_3$ compositions close to the MPB.

Chapter 5 and 6 elucidate a different type of field-induced phase transition. Novel lead free materials BNT-6BT-2KNN show exceptional unipolar usable strain values that are larger than $Pb(Zr,Ti)O_3$. Without any applied field these materials show nearly no remanent polarization and strain. Internal mechanisms prohibit the development of long range interactions between the unit cells, so that the system decays in a disordered nano-domain state. Unfortunately, the fields that are required to induce a phase transition to a polar phase are too high for most applications. A composite structure with a chemical compatible ferroelectric material is used to decrease the required electric field. Two models are proposed to predict the dielectric behavior of a composite from the behavior of both components. In Chapter 5 the composite is replaced by a series configuration of two nonlinear hysteretic capacitors. The model is verified by comparing the results to experimental data from composite samples, and used to identify optimal material parameter combination for future materials. In the second model that is presented in Chapter 6, a two dimensional phase field implementation is expanded by a material model for the high strain material. In contrast to the previous case, this model allows one to study the influence of the microstructure on the composite effect. The model is then applied to test cases to demonstrate its capabilities.

2 Theoretical Background

2.1 Ferroelectric Materials

Unlike common dielectrics, ferroelectric materials have a crystal structure that exhibits a spontaneous electric dipole moment that is coupled to the mechanical unit-cell distortion. This leads to a strong nonlinear dielectric behavior and a hysteresis for applied electric fields that are large enough to cause switching of the spontaneous polarization. In addition, the applied electric fields influence the value and the direction of the unit-cell distortion of the ferroelectric material, which is called the inverse piezoelectric effect. These exceptional properties and physical interactions result in a complex nonlinear constitutive behavior. This chapter will first give a short introduction on the basic formalism of electrostatics and continuum mechanics, which are the foundation for the ferroelectric materials models that are introduced and used in the following chapters. It will also give an overview of the fundamental physical mechanisms that lead to the remarkable physical properties of ferroelectric materials. In addition, some fundamentals of crystallography will be discussed to understand the atomistic reason of the ferroelectric effect. More detailed descriptions can be found elsewhere [14, 23–25] as well as in the works cited.

2.1.1 Electrostatics Fundamentals

Two point charges interact with each other via the electrostatic force ($\mathbf{F}^{es}$). The magnitude and the direction of this force acting on an individual point charge depends on the distance, the absolute value and the sign of the two point charges. The electrostatic force acting on q_1 in Figure 2.1 a) is given by:

$$\mathbf{F}_1^{es} = \frac{q_1 q_2}{4\pi\epsilon_0} \cdot \frac{\mathbf{r}_1 - \mathbf{r}_2}{||\mathbf{r}_1 - \mathbf{r}_2||^3} \tag{2.1}$$

where q_1 and q_2 denote the electric charge of the particular point charge, $\mathbf{r}_{1,2}$ is the distance vector between both point charges q_1 and q_2, and ϵ_0 ($\approx 8.854 \cdot 10^{-12}\,\mathrm{C/Vm}$) is the vacuum permittivity. Electric charges are quantified in integer multiples of the elementary charge e ($\approx 1.602 \cdot 10^{-19}\,\mathrm{C}$), which is the absolute charge of a single electron. Equation 2.1 is known as *Coulomb's Law* . If there are multiple (N) point charges at different positions $\mathbf{r}_i$ the absolute electrostatic force a test point charge q_0 at position $\mathbf{r}_0$ will experience is given by the sum of all two-particle forces (see Figure 2.1 b):

$$\mathbf{F}_0^{es}(\mathbf{r}_0) = q_0 \sum_{i=1}^{N} \frac{q_i}{4\pi\epsilon_0} \frac{\mathbf{r}_0 - \mathbf{r}_i}{||\mathbf{r}_0 - \mathbf{r}_i||^3} \tag{2.2}$$

Equation 2.2 can be generalized to the case of a volume with a continuous volume charge distribution $\rho(\mathbf{r})$ instead of multiple point charges:

$$\mathbf{F}_0^{es}(\mathbf{r}) = q_0 \int\limits_V \frac{\rho(\tilde{\mathbf{r}})}{4\pi\epsilon_0} \frac{\mathbf{r} - \tilde{\mathbf{r}}}{||\mathbf{r} - \tilde{\mathbf{r}}||^3} d^3\tilde{r} \tag{2.3}$$

where the integral is evaluated over the total volume V of the charge distribution. This is schematically illustrated in Figure: 2.1 c).

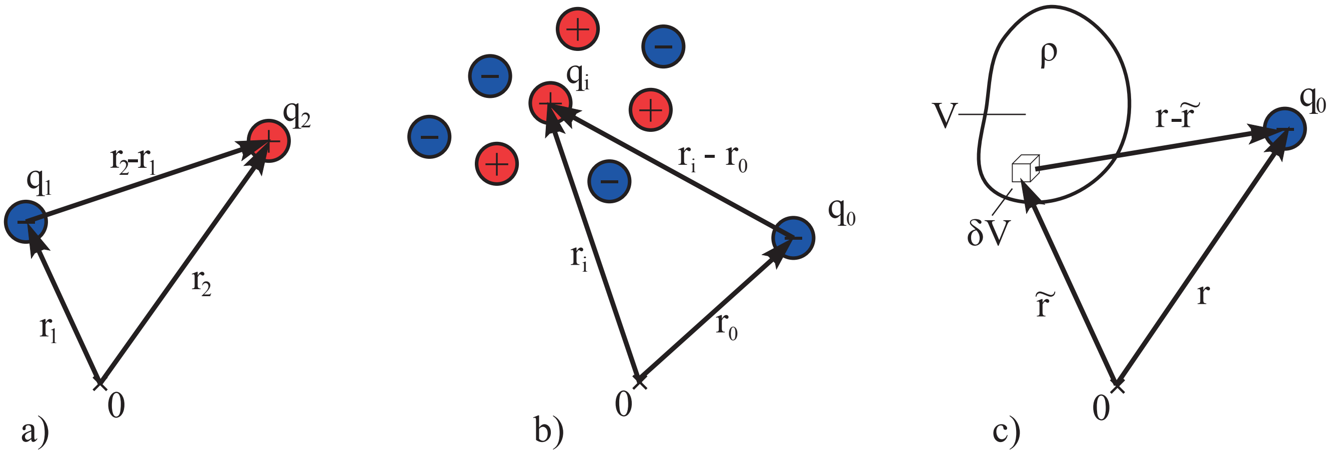

Figure 2.1: Coulomb interaction between a) two point charges q_1, q_2; b) a test charge q_0 and a system of point charges q_i; c) a test charge q_0 and a continuous charge distribution ρ within the volume V

The electrostatic force a test charge experiences is proportional to its own charge, M. Faraday introduced a more general formulation of the electrostatic force that is independent of the used test charge. The electric field $\mathbf{E}(\mathbf{r})$ is the vector field that describes the electrostatic force $\mathbf{F}_0^{es}(\mathbf{r})$ acting on an electric point charge at the position $\mathbf{r}$ normalized with its charge q. The electric field of a charge distribution $\rho(\mathbf{r})$ is given by:

$$\mathbf{E}(\mathbf{r}) \equiv \frac{\mathbf{F}_0^{es}(\mathbf{r})}{q_0} = \int_V \frac{\rho(\tilde{\mathbf{r}})}{4\pi\epsilon_0} \frac{\mathbf{r}-\tilde{\mathbf{r}}}{\|\mathbf{r}-\tilde{\mathbf{r}}\|^3} d^3\tilde{r} \tag{2.4}$$

The field of a charge distribution can also be formulated in the differential instead of the integral form.

$$\nabla \cdot \mathbf{E}(\mathbf{r}) = \frac{1}{\epsilon_0}\rho(\mathbf{r}) \tag{2.5}$$

where ∇ denotes the vector differential (Nabla-) operator. Equation 2.5 is known as *Gauss' Law* and is valid in this form only for charge distributions in vacuum.

If a test charge is moved along an arbitrary path Γ from the position r_A to the position r_B through an electrical field $\mathbf{E}$ a certain amount of work must be done. This work $W_{A,B}$ is given by the path integral $d\mathbf{s}$ along the path Γ over the electrostatic force $\mathbf{F}^{\mathbf{es}}$:

$$W_{A,B} = \int_\Gamma \mathbf{F}^{\mathbf{es}} d\mathbf{s} = -q_0 \int_\Gamma \mathbf{E} d\mathbf{s} \tag{2.6}$$

It can be shown that the electric field is a conservative vector field in the stationary (time independent) case, i.e., that the integrals in Equation 2.6 are path independent [26]. As a direct consequence the electric field can be described as a gradient of a scalar potential:

$$\mathbf{E}(\mathbf{r}) = -\nabla\phi(\mathbf{r}) \quad \Leftrightarrow \quad W_{A,B} = q_0(\phi(\mathbf{r}_B) - \phi(\mathbf{r}_A)) \tag{2.7}$$

where $\phi(\mathbf{r})$ is the scalar electrostatic potential at position $\mathbf{r}$. The electrostatic potential of point charge q at position $\mathbf{r}_0$ or a continuous volume charge distribution $\rho(\mathbf{r})$ can be directly derived from Equation 2.4:

$$\phi(\mathbf{r}) = \frac{q}{\|\mathbf{r}_0 - \mathbf{r}\|}, \quad \phi(\mathbf{r}) = \int \frac{\rho(\tilde{\mathbf{r}})}{\|\tilde{\mathbf{r}} - \mathbf{r}\|} d^3\tilde{r} \tag{2.8}$$

Combining the Equations 2.5 and 2.7 leads to the electrostatic potential in differential form:

$$-\frac{\rho(\mathbf{r})}{\epsilon_0} = \nabla \cdot \mathbf{E} = \nabla \cdot (\nabla \phi(\mathbf{r})) \equiv \Delta \phi(\mathbf{r}) \tag{2.9}$$

This second order partial differential equation is known as the electrostatic *Poisson's Equation* with the Laplace operator $\Delta \equiv \nabla^2 = (\partial^2/\partial r_1^2 + \partial^2/\partial r_2^2 + \partial^2/\partial r_3^2)$.

Electrostatics in Matter

Until now all relations have assumed a vacuum condition and a fixed charge distribution.[*] Condensed matter consists of positively charged atom cores and bound negatively charged electrons that can be influenced by external electrical fields. Assuming an ideal insulating dielectric material, the binding energy of the electrons is of a sufficient height to stop their removal from their associated localized atomic orbits. Instead, the electric field causes a shift of the charged particles from their equilibrium positions, creating local distributions of bound charges ρ_b. These local distributions lead to internal electrical fields, so that the total electric field at a certain position inside the dielectric material is given by a superposition of the external and local electric field and can vary drastically with ρ_b. To reformulate the *Gauss Equation* (Eq. 2.5), considering the effects from the dielectric material, it is necessary to set up a mathematical description of the complex microscopic bound charge distribution. Unfortunately, a typical material consists of $\sim 10^{23}$ particles per cm^3 and every finite temperature leads to random fluctuations of the charged particles inside the dielectric material. Hence, an exact microscopic description of the dielectric material behavior is presently unobtainable.

Fortunately, most of the macroscopic behavior can be described with sufficient accuracy by using a simplified expression for ρ_b. In most cases the fast fluctuations of the charged particles (e.g., due to temperature) are neglected because they are much faster than the effects of interest; the charge distribution is represented by the time average. To further simplify the distribution of bound charges ρ_b, the so called multipole expansion, is used. Although, instead of using the exact relation (Eq. 2.8), a Taylor-like expansion of $\frac{\rho_b(\tilde{r})}{\|\tilde{r} - r\|}$ is used to determine the dependency between ρ_b and the associated dielectric potential resulting from a dielectric region with volume δV:

$$\phi(\boldsymbol{r}) = \frac{Q}{\|\mathbf{r}\|} + \frac{\boldsymbol{r}\boldsymbol{p}}{\|\mathbf{r}\|^3} + \frac{1}{2} Q_{kl} \frac{r_k r_l}{\|\mathbf{r}\|^5} + \text{higher order terms,} \tag{2.10}$$

where $Q = \int_{\delta V} \rho(\boldsymbol{r}) d^3r$ is the total charge inside δV, $\boldsymbol{p} = \int_{\delta V} \rho(\boldsymbol{r})\boldsymbol{r}\, d^3r$ is the electric dipole moment of δV, and $Q_{kl} = \int_{\delta V} \rho(\boldsymbol{r})(3r_k r_l - \delta_{kl}\|\boldsymbol{r}\|^2) d^3r$ is the electric quadrupole moment of δV. The origin of the coordinate system lies in this case in the center of δV. Thus the properties of ρ_b are separated in terms of the total charge Q, the dipole moment P, and higher orders terms (quadrupole moment Q_{jk}, ...). In charge neutral dielectric systems the zeroth order of the multi-pole expansion vanishes. In most cases, contributions from terms with a higher order than one are small enough to be neglected, which means that the dielectric properties of the effective bound charge distribution in a dielectric material can often be approximated by their electric dipole moment.

---

[*] Moving charges are part of electrodynamic theory, which lies beyond the scope of this discussion.

An electric dipole consists of two charges $(q, -q)$ with an opposite sign separated by a distance* $\|\mathbf{d}\| > 0$. The dipole moment $\mathbf{p}$ is defined as

$$\mathbf{p} \equiv q\mathbf{d}, \tag{2.11}$$

where the dipole vector is pointing parallel to the distance vector from the negative to the positive charge (see Figure 2.2). Electrical dipole moments can also be attributed to more complex charge distributions, i.e., multiple point charges or volume charge densities $\rho(\mathbf{r})$ with separated centers of positive and negative charges†.

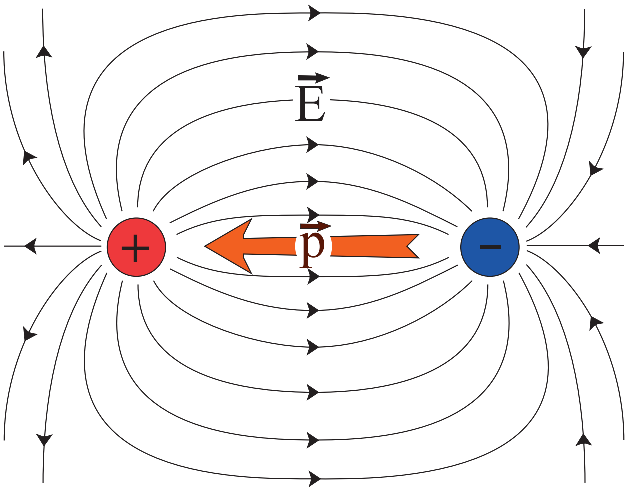

Figure 2.2: Dipole moment **p** and electrical field **E** of two charges

$$\mathbf{p} = \sum_i q_i \mathbf{r}_i, \quad \mathbf{p} = \int_V \rho(\mathbf{r})\mathbf{r}\, dV \tag{2.12}$$

where all point charges q_i at positions $\mathbf{r}_i$ are summed and the integral evaluated over the total volume V of the charge distribution. This dipole moment is the first order term of the multi pole expansion mentioned above. The electric field (compare Figure 2.2) caused by an electric dipole can be deduced by a linear superposition of two fields caused two point-charges with a charge of q and -q in a distance $\mathbf{d} = \mathbf{p}/q$ and is given by

$$\mathbf{E}_{dipole}(\mathbf{r}, \mathbf{p}) = \frac{1}{4\pi\epsilon_0}\left(\frac{3(\mathbf{p}\cdot\mathbf{r})\mathbf{r}}{r^5} - \frac{\mathbf{p}}{r^3}\right), \tag{2.13}$$

for greater distances the field of a dipole decreases with r^{-3} in three dimensions. Polarization density is used to describe the local dipole moment of a macroscopic body. This vector field, often referred to as polarization $\mathbf{P}$ is defined as the dipole moment per volume unit:

$$\mathbf{P} = \lim_{V\to 0}\frac{\Delta\mathbf{p}}{\Delta V} = \frac{d\mathbf{p}}{dV} \tag{2.14}$$

---

[*] According to convention, **d** is pointing from the negative towards the positive electric charge.

[†] Center of positive/negative charges $\mathbf{R}_{+/-}$:
For discrete point charges $\mathbf{R}_{+/-} = 1/Q\sum_i \mathbf{r}_i q_i^{+/-}$.
For continuous charge densities: $\mathbf{R}_{+/-} = 1/Q\int_V \rho^{+/-}\mathbf{r}dr^3$.
$q_i^{+/-}$: positive/negative point charges charges, $\rho^{+/-}$: density of the positive/negative charges

Along the boundaries, respectively the surfaces of a homogeneous polarized material, a bound surface charge density σ_b can be observed that is proportional to the polarization $\mathbf{P}$.

$$\sigma_b = \mathbf{P} \cdot \mathbf{n}_S \tag{2.15}$$

with the unit vector $\mathbf{n}_S$ perpendicular to the materials surface. These surface charges are often compensated by free charge carriers from the sample environment, so that they can only be measured directly after the poling process. With this concept of polarization one can introduce the electric displacement field $\mathbf{D}$

$$\mathbf{D} \equiv \epsilon_0 \mathbf{E} + \mathbf{P}\,. \tag{2.16}$$

Equation 2.16 is called the electrostatic constitutive equation, and can be used to formulate Equation 2.5 in a more general manner:

$$\nabla \mathbf{D}(\mathbf{r}) = \rho(\mathbf{r}) \tag{2.17}$$

Equation 2.17 is also known as the *first Maxwell Equation*. The exact dependency of the dielectric polarization on the external electric field is in general complex and cannot be directly deduced due to its mathematical complexity and a lack of knowledge of the microscopic details of the material. Fortunately, the assumption of a linear dependency fits the behavior of most common dielectric materials in the region of moderate electric field intensities, such that

$$\mathbf{P} = \epsilon_0 \chi \mathbf{E} \tag{2.18}$$

where χ is the dielectric susceptibility. Instead of being a fixed material constant, χ is usually a function of the temperature of the dielectric material as well as the frequency of the external electric field. In anisotropic materials χ depends also on the field direction and is in fact a tensor of the second order. A directional dependency in susceptibility is, for example, the reason for birefringent properties of some crystals like calcite. With the exception of a few materials like single crystals, ferroelectrics, or rarely polymers that can exhibit a distinct direction dependency of their dielectric properties, most common materials behave isotropic and can be sufficiently described by a scalar electric susceptibility. Combining Equations 2.18 and 2.16 yields an expression for the electric displacement in terms of the dielectric susceptibility χ:

$$\mathbf{D} = \epsilon_0 \underbrace{(1+\chi)}_{\equiv \epsilon_r} \mathbf{E} = \epsilon_0 \epsilon_r \mathbf{E} \tag{2.19}$$

where $\epsilon_r \equiv (1 + \chi_\epsilon)$ is the dimensionless relative permittivity. Similar to χ, ϵ_r is a measure of the polarizability of the material. In concrete terms it describes the ratio of electric charges that can be stored in a parallel plate test capacitor with and without the dielectric material between the plates. Typical values for ϵ_r are < 5 for organic and < 20 for inorganic solids. It is obvious that for anisotropic materials ϵ_r is a second order tensor. For the case of a single atom or molecule the polarizability α_p is used instead of the susceptibility χ. Analogue to χ, the polarizability α_p is defined for the linear relation:

$$\mathbf{p} = \alpha_p \mathbf{E} \tag{2.20}$$

where α_p is a scalar value for systems with a spherical symmetry. To describe molecules with an anisotropic polarization behavior α has to be a second order tensor. The Clausius Mossotti Equation

(Eq. 2.21) links the susceptibility or relative permittivity of an atom/molecule-ensemble with their number density N and a single atom/molecule polarizability α.

$$\epsilon_r = 1 + \frac{3N\alpha_p}{3\epsilon_0 - N\alpha_p} \tag{2.21}$$

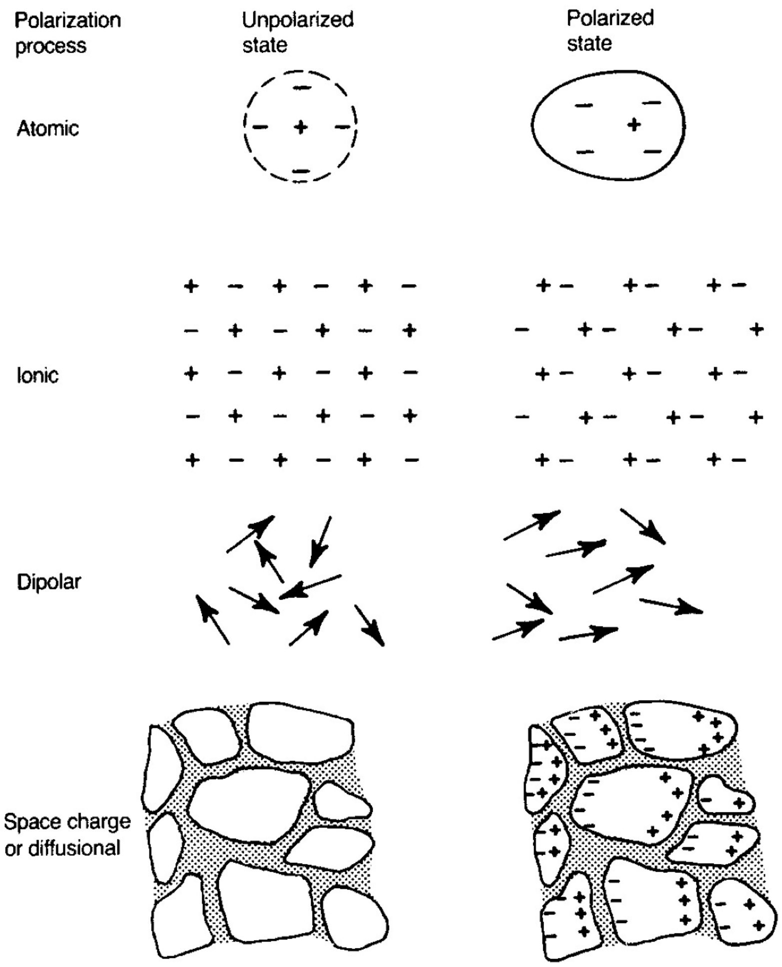

Figure 2.3: Schemes of the four polarization mechanisms in dielectric materials [24]

In different material systems one can find four major polarization mechanisms, which are schematically shown in Figure 2.3:

1. **Electron Polarization:** The negatively charged electrons of the atomic shell are shifted against the positively charged atomic core by an external electrical field. This phenomenon can be found in all types of materials, although it is negligible in comparison to the other three mechanisms, if they are also present in the specific material.

2. **Ion Polarization:** The positive cations and the negative anions are shifted away from one another due to the external field. This mechanism requires an ionic crystal such as Na^+Cl^-.

3. **Orientation Polarization:** Only possible in so-called polar materials that contain permanent orientable dipoles. Examples are water (H_2O-dipoles) and all ferroelectrics. The permanent dipoles

are aligned by an external electric field. This mechanism is highly influenced by the ambient temperature.

4. **Space/Surface Charge Polarization:** The separation of mobile charged carriers in conductive materials by the external electrical field. In multiphase and polycrystalline materials there is also the possibility that charges are generated at the phase/grain boundaries.

The first three polarizing processes are commonly grouped under the term of displacement polarization. With impedance spectroscopy it is possible to measure the contributions of the different mechanisms due to their unequal frequency dependency [27].

2.1.2 Continuum Mechanics

The formation and reorientation of the microscopic spontaneous polarization in piezoelectric materials changes the crystallographic structure. This leads to macroscopic deformations and the formation of internal stresses within the crystallographic structure. To describe internal stresses and macroscopic deformations caused by the spontaneous polarization as well as applied external mechanical loads, it is important to first define a nomenclature for mechanics of continuous media.

The Strain Tensor

In continuum mechanics, the location of every point in a solid body can be described by a position vector x_i. In the stress-free equilibrium state all related position vectors $\{x_i, ...\}$ define the reference configuration. During deformation the point x_i moves to a new position x_i^*. This new position can be written in terms of the former position vector x_i by introducing a displacement vector u_i, which generally depends on time t and the point coordinate x_i:

$$u_i = x_i^* - x_i \tag{2.22}$$

As shown in Figure 2.4, the deformation of an infinitesimal vector dx_i at the position x_i to the vector dx_i^* at the position x_i^* can be described by the following equation:

$$dx_i^* = dx_i + du_i = dx_i + u_{i,j} dx_j, \quad u_{i,j} = \frac{du_i}{dx_j} \tag{2.23}$$

where $u_{i,j}$ is the displacement gradient tensor. Considering the change in the quadratic length ds of dx_i ($ds^2 = dx_i \cdot dx_i$), one can find the following relation:

$$ds^{*^2} - ds^2 = (u_{i,j} + u_{j,i} + u_{k,i} u_{k,j}) dx_j dx_i \tag{2.24}$$

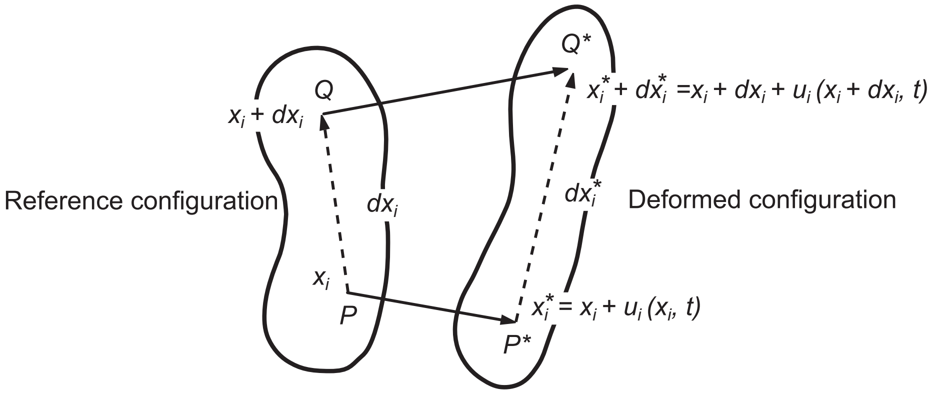

Figure 2.4: Displacement of neighboring material points P and Q [28]

which can be used to define the *Green's Strain Tensor* E_{ij} as follows

$$E_{ij} \equiv \frac{1}{2}(u_{i,j} + u_{j,i} + u_{k,i}u_{k,j}) \tag{2.25}$$

and rewrite Equation 2.24:

$$ds^{*^2} - ds^2 = 2dx_i E_{ij} dx_j \tag{2.26}$$

In other words, the strain tensor describes the local change in length of an infinitesimal vector at the position x_i during a deformation process. Due to its definition the strain tensor is symmetric, which means $E_{ij} = E_{ji}$.

In case of small displacement gradients, i.e., $|u_{i,j}| \ll 1$ one can neglect the quadratic term in the strain tensor, resulting in the following definition of the small strain tensor $\mathbb{S}_{ij}$

$$\mathbb{S} = S_{ij} \equiv \frac{1}{2}(u_{i,j} + u_{j,i}) \tag{2.27}$$

where S_{ij} is a symmetric tensor of the 2^{nd} order like the *Green's Strain Tensor* E_{ij}

The Stress Tensor

A deformation, i.e., strain, in a deformable body has its origin in a mechanical load from internal or external sources. The distribution of this load at every point in the body can be described by a symmetric 2^{nd} order tensor, called the stress tensor. Two different kinds of forces are possible: surface forces, which are contact forces that act on the surface of a free body, and body forces, which act on a volume or mass of the body [29].

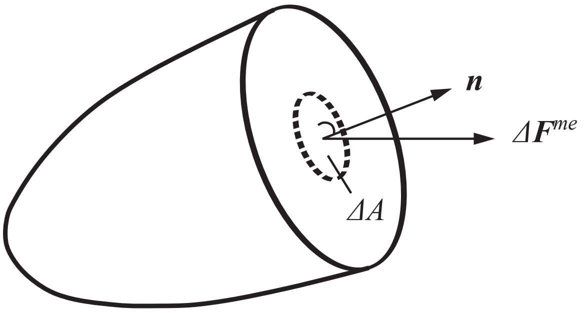

Figure 2.5: Force $\Delta\mathbf{F}^{me}$ on area ΔA with outer unit normal vector $\mathbf{n}$ ([28])

We can say that every point of the body lies on a surface, either on a real external bounding surface or an arbitrarily defined internal surface obtained at a cross-section of the body. As shown in Figure 2.5 the incremental force vector $\Delta\mathbf{F}^{me}$ acts on the incremental surface area ΔA. Going to the infinitesimal limit we can define the stress vector on the surface plane A as

$$T_i^A \equiv \lim_{\Delta A \to 0} \frac{\Delta F_i^{me}}{\Delta A} = \frac{dF_i^{me}}{dA} \tag{2.28}$$

Given that there are three linear independent possibilities to choose the surface plane, three different stress vectors can be found. Those three vectors give the form of the stress tensor relative to the coordinate system spanned by the normal vectors of the three surfaces:

$$T_{ij} = \left[\frac{\partial F_i^{me}}{\partial A_1}, \frac{\partial F_i^{me}}{\partial A_2}, \frac{\partial F_i^{me}}{\partial A_3} \right] = \begin{bmatrix} T_{11} & T_{12} & T_{13} \\ T_{21} & T_{22} & T_{23} \\ T_{31} & T_{32} & T_{33} \end{bmatrix} \tag{2.29}$$

To visualize the stress tensor we can assume a cubic body (see Figure 2.6). The diagonal components

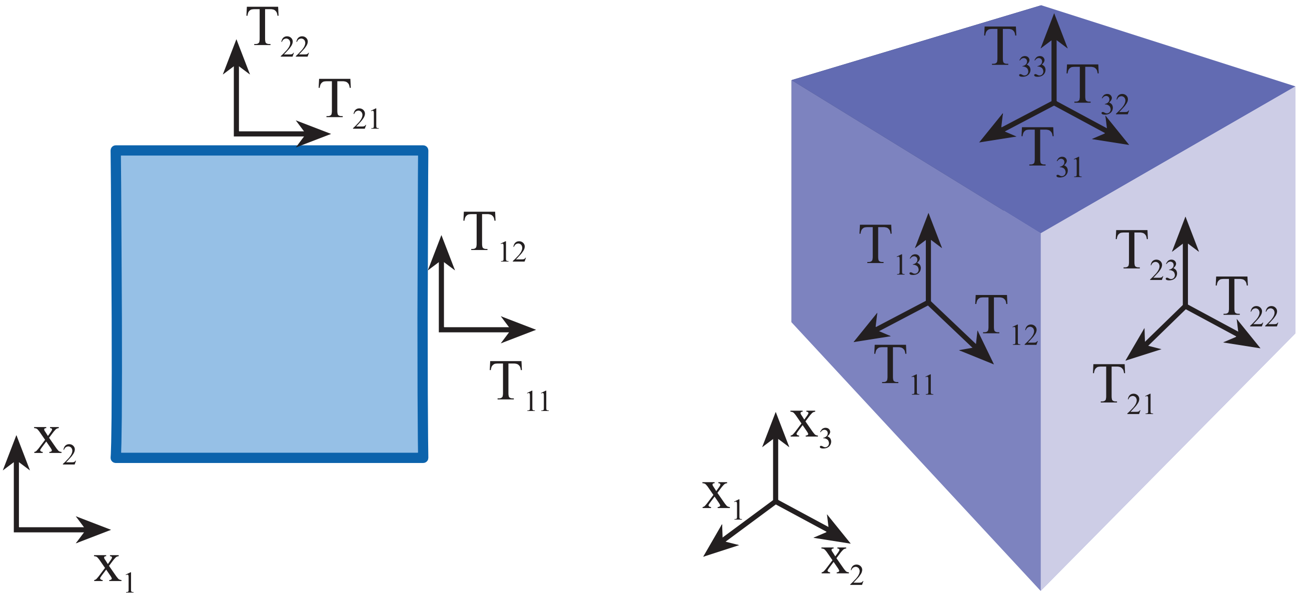

Figure 2.6: Components of the stress tensor in two and three dimensions

T_{ii} describe normal stresses in the x_1-, x_2- and x_3-directions, whereas the non-diagonal components T_{ij}, $(j \neq i)$ describe the shear stresses. It can be shown that T_{ij} must equal T_{ji} to ensure an equilibrium of the linear momentum. As a result T_{ji} contains only six independent components.

In a linear-elastic* body the stress and strain relationship can be described by the constitutive equation:

$$T_{ij} = \mathbb{C}_{ijkl} S_{kl} \tag{2.30}$$

where $\mathbb{C}_{ijkl}$ is the linear stiffness tensor. Equation 2.30 is also known as the general form of *Hooke's Law*. The stiffness tensor C_{ijkl} is a tensor of the fourth rank, i.e., it consists of 81 components, but due to the symmetry of T_{ij} and S_{kl} and the existence of a strain energy a maximum 21 coefficients can be independently chosen in case of a total anisotropic material. In case of materials with a higher symmetry, the number of independent coefficients is reduced. This symmetry can be used to simplify Equation 2.30 to:

$$T_i = \mathbb{C}_{ij} S_j \tag{2.31}$$

---

* The linear elasticity behavior is valid for sufficiently small strain values in nearly every solid body.

by introducing a matrix notation known as *Voigt notation* [25]:

$$T_{ij} \Rightarrow \qquad T_i = \begin{bmatrix} T_{11}, & T_{22}, & T_{33}, & T_{23}, & T_{31}, & T_{12} \end{bmatrix}^T \tag{2.32}$$

$$S_{kl} \Rightarrow \qquad S_j = \begin{bmatrix} S_{11}, & S_{22}, & S_{33}, & 2S_{23}, & 2S_{31}, & 2S_{12} \end{bmatrix}^T \tag{2.33}$$

$$\mathbb{C}_{ijkl} \Rightarrow \qquad \mathbb{C}_{ij} = \begin{bmatrix} \mathbb{C}_{1111} & \mathbb{C}_{1122} & \mathbb{C}_{1133} & \mathbb{C}_{1123} & \mathbb{C}_{1131} & \mathbb{C}_{1112} \\ \mathbb{C}_{2211} & \mathbb{C}_{2222} & \mathbb{C}_{2233} & \mathbb{C}_{2223} & \mathbb{C}_{2231} & \mathbb{C}_{2212} \\ \mathbb{C}_{3311} & \mathbb{C}_{3322} & \mathbb{C}_{3333} & \mathbb{C}_{3323} & \mathbb{C}_{3331} & \mathbb{C}_{3312} \\ \mathbb{C}_{2311} & \mathbb{C}_{2322} & \mathbb{C}_{2333} & \mathbb{C}_{2323} & \mathbb{C}_{2331} & \mathbb{C}_{2312} \\ \mathbb{C}_{3111} & \mathbb{C}_{3122} & \mathbb{C}_{3133} & \mathbb{C}_{3123} & \mathbb{C}_{3131} & \mathbb{C}_{3112} \\ \mathbb{C}_{1211} & \mathbb{C}_{1222} & \mathbb{C}_{1233} & \mathbb{C}_{1223} & \mathbb{C}_{1231} & \mathbb{C}_{1212} \end{bmatrix} \tag{2.34}$$

In isotropic materials the stiffness tensor $\mathbb{C}_{ij}$ can be written in terms of the *Young's modulus* E and the *Poisson's ratio* ν of the solid body:

$$\mathbb{C}_{ij} = \frac{E}{(1+\nu)(1-2\nu)} \begin{bmatrix} 1-\nu & \nu & \nu & 0 & 0 & 0 \\ \nu & 1-\nu & \nu & 0 & 0 & 0 \\ \nu & \nu & 1-\nu & 0 & 0 & 0 \\ 0 & 0 & 0 & \frac{1-2\nu}{2} & 0 & 0 \\ 0 & 0 & 0 & 0 & \frac{1-2\nu}{2} & 0 \\ 0 & 0 & 0 & 0 & 0 & \frac{1-2\nu}{2} \end{bmatrix} \tag{2.35}$$

2.1.3 Piezoelectric Materials

Piezoelectricity describes the linear first order coupling mechanism between dielectric and elastic phenomena. It was first discovered in 1880 by brothers Pierre and Jacques Curie. They found the ability of some crystalline materials, such as Quartz or Rochelle salt, to generate an electric field in response to an applied mechanical loading. The direct piezoelectric effect was defined as *”electric polarization produced by mechanical strain in crystals belonging to certain classes, the polarization being proportional to the strain and changing sign with it”* [23]. Later, the existence of the inverse piezoelectric effect was experimentally proven by the Curie brothers after being theoretically predicted by Gabriel Lippmann. The inverse effect denotes a strain of the piezoelectric crystal in response to an applied electric field. Both effects result from the same fundamental property of the crystal; they are opposite counterparts.

Required Crystal Symmetry

The electro-mechanical coupling effect has its origin in the crystal structure of the piezoelectric material. A crystal structure can be classified by the symmetry elements it possesses. It was shown that in a three dimensional Euclidean space thirty-two different crystal classes, or point groups, exist. The symmetry of the underlying crystal class is important, as it significantly impacts many of the physical properties of the crystal. A necessary prerequisite for piezoelectricity is a lack of centrosymmetry of the atomic crystal structure. Since there are eleven different centrosymmetric crystal classes, twenty-one remain as possible piezoelectric materials. Out of these 21 crystal classes only 20 (compared to Table 2.1) show piezoelectric behavior. The missing non-centrosymmetric cubic class 432 has a combination of other symmetry elements, which prohibit piezoelectricity.

Table 2.1: Piezoelectric crystal classes

Crystal system	Crystal class
triclinic	1
monoclinic	2, m
orthorhombic	222, mm2
tetragonal	4, $\bar{4}$, 422, 4mm, $\bar{4}$2m
trigonal	3, 32, 3m
hexagonal	6, $\bar{6}$, 622, 6mm, $\bar{6}$2m
cubic	23, $\bar{4}$3m

Piezoelectric Constitutive Equations

The term piezoelectricity includes all linear electro-mechanical coupling mechanisms. For a mathematical description of these effects, it is necessary to extend the mechanic constitutive equation (Equation 2.30) and the electric constitutive equation (Equation 2.16) by respective coupling terms. Assuming a stress free anisotropic, homogeneous piezoelectric solid under isothermal conditions, the mechanical strain S_{ij} and dielectric displacement D_i of a steady state is given by the following piezoelectric constitutive equations:

$$\begin{aligned} S_{ij} &= (\mathbb{C}_{ijkl})^{-1} T_{kl} + (\mathbb{d}_{kij}) E_k \\ D_i &= \mathbb{d}_{ijk} T_{jk} + (\epsilon_r^T)_{ij} E_j \end{aligned} \tag{2.36}$$

where $\mathbb{d}_{kij}$ is the piezoelectric coupling tensor, $(\epsilon_r^T)_{ij}$ is the "free" dielectric constant of the stress free material and $(\mathbb{C}_{ijkl}^E)^{-1}$ the inverse mechanical stiffness (also called the mechanical compliance), for a constant electric field condition ("short circuit condition"). Similar constitutive equations for mechanically clamped and fixed dielectric displacement conditions ("open circuit condition"), as well as for the possible combination between both, can be introduced by using thermodynamical arguments. By doing so three additional but equivalent pairs of constitutive equations that describe the dependencies between the different material parameters can be found [30]:

$$\begin{aligned} T_{ij} &= \mathbb{C}_{ijkl}^E S_{kl} - (\mathbb{e}_{kij}) E_k \\ D_i &= \mathbb{e}_{ijk} S_{jk} + (\epsilon_r^S)_{ij} E_j \end{aligned} \tag{2.37}$$

$$\begin{aligned} T_{ij} &= \mathbb{C}_{ijkl}^D S_{kl} - \mathbb{h}_{ijk} D_k \\ E_i &= -\mathbb{h}_{ijk} S_{jk} + (\epsilon_r^T)_{ij}^{-1} D_j \end{aligned} \tag{2.38}$$

$$\begin{aligned} S_{ij} &= (\mathbb{C}_{ijkl}^D)^{-1} T_{kl} + (\mathbb{g}_{ijk})^T D_k \\ E_i &= -\mathbb{g}_{ijk} T_{jk} + (\epsilon_r^S)_{ij}^{-1} D_j \end{aligned} \tag{2.39}$$

where $\mathbb{e}_{ijk}$, $\mathbb{g}_{ijk}$ and $\mathbb{h}_{ijk}$ denote the other piezoelectric tensors for clamped closed circuit-, the clamped open circuit-, and the stress-free open circuit conditions. In each case, the electrical and mechanical boundary conditions decide, which pair of constitutive equations 2.36, 2.37, 2.38, and 2.39 and therefore, which piezoelectric coefficient has to be used. It is possible to deduce the relationships between the four coefficients $\mathbb{d}_{ijk}$, $\mathbb{e}_{ijk}$, $\mathbb{g}_{ijk}$ and $\mathbb{h}_{ijk}$ by using the equations 2.36, 2.37, 2.38, and 2.39:

$$\begin{aligned} \mathbb{d}_{ijk} &= \mathbb{e}_{ilm}(\mathbb{C}_{lmjk}^E)^{-1} = \mathbb{g}_{ljk}(\epsilon_r^T)_{il} \\ \mathbb{e}_{ijk} &= \mathbb{d}_{ilm}\mathbb{C}_{lmjk}^E = \mathbb{h}_{ljk}(\epsilon_r^T)_{il} \\ \mathbb{g}_{ijk} &= \mathbb{d}_{ljk}(\epsilon_r^T)_{li}^{-1} = \mathbb{h}_{ilm}(\mathbb{C}_{lmjk}^D)^{-1} \\ \mathbb{h}_{ijk} &= \mathbb{e}_{ljk}(\epsilon_r^T)_{il}^{-1} = \mathbb{g}_{ilm}(\mathbb{C}_{lmjk}^D) \end{aligned} \tag{2.40}$$

All piezoelectric constants are in general tensors of the third order with a total of 27 entries. However, due to the crystal symmetry of piezoelectric materials, most tensor components have to be zero or identical. In Eq. 2.41 an example for piezoelectric tensor of the 6mm crystal class is shown in Voigt notation, with only three independent components d_{33}, d_{31}, and d_{15}

$$d_{ij} = \begin{bmatrix} 0 & 0 & 0 & 0 & d_{15} & 0 \\ 0 & 0 & 0 & d_{15} & 0 & 0 \\ d_{31} & d_{31} & d_{33} & 0 & 0 & 0 \end{bmatrix} \tag{2.41}$$

Unlike for non-piezoelectric materials, the value for the relative permittivity ϵ_r and the mechanical stiffness $\mathbb{C}_{ijkl}^E$ in piezoelectric materials depend on the electric conditions of the piezoelectric material during measurement. The superscript of $\mathbb{C}_{ijkl}^E$ and $\mathbb{C}_{ijkl}^D$ denotes whether the value for the mechanical stiffness was measured at constant electrical field E or at constant dielectric displacement D. In addition, one must differentiate between two different measurement conditions for the dielectric permittivity: The "free" dielectric constant is measured at constant (zero) stress condition ϵ_r^T, and the "clamped" dielectric constant is measured at constant (zero) strain condition ϵ_r^S. In piezoelectric materials it is possible that both dielectric constants differ significantly from each other.

The Electromechanical Coupling Factor

From a more general point of view the direct and the reverse piezoelectric effect are a conversion process from mechanical to electrical energy and vice versa. The dielectric enthalpy $\mathcal{H}^{el}$, a measure for the total internal energy of a linear piezoelectric, is given by

$$\mathcal{H}^{el} = \frac{1}{2}\left(S_{ij}T_{ij} + D_i E_i\right) \tag{2.42}$$

Inserting the expressions for S_{ij} and D_i from Eq. 2.36 leads to:

$$\mathcal{H}^{el} = \underbrace{\frac{1}{2}T_{ij}(\mathbb{C}^E_{ijkl})^{-1}T_{kl}}_{\mathcal{H}^{ela}} + \underbrace{\frac{1}{2}E_i(\epsilon_r^T)_{ij}E_j}_{\mathcal{H}^{diel}} + \underbrace{\frac{1}{2}T_{ij}\mathbb{d}_{ijk}E_k + \frac{1}{2}E_i d_{ijk}T_{jk}}_{2\mathcal{H}^{coup}} \tag{2.43}$$

where $\mathcal{H}^{ela}$ is the elastic contribution, $\mathcal{H}^{diel}$ the dielectric contribution and $\mathcal{H}^{coup}$ is the contribution of the electro-mechanical coupling to the system enthalpy. According to [31] it is now possible to define the piezoelectric coupling factor (”*the ratio of the mutual elastic and dielectric self-energy*”) as the following quotient:

$$k \equiv \frac{\mathcal{H}^{coup}}{\sqrt{\mathcal{H}^{ela} \cdot \mathcal{H}^{diel}}} \tag{2.44}$$

In the general case of an one-dimensional polycrystalline piezoelectric bar* under an external field parallel (k_{33}) or perpendicular (k_{31}) to the length of the bar the coupling factor can be expressed:

$$k_{33} = \frac{\mathbb{d}_{33}}{(\epsilon_r^T)_{33}(\mathbb{C}^E_{33})^{-1}} \qquad k_{31} = \frac{\mathbb{d}_{31}}{(\epsilon_r^T)_{33}(\mathbb{C}^E_{11})^{-1}} \tag{2.45}$$

For other configurations of stress, electric field or different piezoelectric point-groups corresponding coupling factors can be obtained in a similar way. It is important to note that not all configurations will result in the stress components in the numerator and the denominator canceling, meaning that the coupling coefficient in these cases is also dependent on external variables and do not describe the intrinsic properties of the material.

The square of the coupling factor k^2 is a measure of the efficiency of the conversion process. Given by the second law of thermodynamics, unavoidable loss mechanisms lead to a maximum conversion efficiency below one. Coupling factors for known piezoelectric materials range between 0.1 for quartz and 0.9 for Seignette’s salt at its Curie point ($24°C$). Furthermore, it is possible to use the electromechanical coupling factor to find an expression for the relation between the free ϵ_r^T and the clamped dielectric permittivity ϵ_r^S:

$$\epsilon_r^S = \epsilon_r^T(1-k^2) \tag{2.46}$$

and the elastic compliance for constant electrical field $(\mathbb{C}^E)^{-1}$ and a constant dielectric displacement $(\mathbb{C}^D)^{-1}$:

$$(\mathbb{C}^D)^{-1} = (\mathbb{C}^E)^{-1}(1-k^2) \tag{2.47}$$

---

* point group ∞m

2.1.4 Ferroelectric Materials

Out of the twenty piezoelectric crystal classes with one or more polar axes, ten exhibit a unique polar axis, with a spontaneous polarization of their unit cells in the absence of an external electrical field. These ten crystal classes are called polar and form the group pyroelectrics.

Pyroelectric Effect

Pyroelectricity is the ability of polar crystals to generate a temporary voltage when the crystal temperature is changed. This is a direct consequence of the the spontaneous polarization resulting from the polar axis. Under general circumstances a non-zero total polarization* in a polar material is screened by a surface charge distribution σ_s. This charge distribution has its origin in the charges from the surrounding medium, or internal mobile charges like slow moving ions. Because of the isolating nature of pyroelectric materials σ_s can only slowly react to changes of the total polarization. Given that the absolute value of the spontaneous polarization depends on the temperature (see Chapter 2.2 for more details) a variation in temperature will result in an amount of uncompensated surface charges. For small temperature change ΔT one can find a linear dependency ([32]):

$$\Delta P_i = \mathbb{p}_i^{\text{pyro}} \Delta T \tag{2.48}$$

where ΔP_i is the change in polarization and $\mathbb{p}_i^{\text{pyro}}$ is the pyroelectric coefficient. Pyroelectricity is a necessary but not a sufficient condition for ferroelectric behavior.

Ferroelectric Hysteresis

In addition to the existence of a unique polar axis in the crystal, the reversibility of its spontaneous polarization by an external electric field above a certain value anti-parallel to the polarization direction is an additional criteria for ferroelectricity. Unlike in ferromagnetic systems, where the existence of a spontaneous magnetization implies directly its reversibility, the presence of a spontaneous polarization does not automatically imply the ability to reverse its direction. This reversibility leads to a hysteretic shape of the field dependent polarization (P-E) loop. In Figure 2.7 (a) a schematic P-E loop of an ideal ferroelectric material is depicted. As shown, the polarization curve at (1) has a linear dielectric response superposed with a constant negative offset from the spontaneous polarization.

If an external electric field, oriented anti-parallel to the polarization, exceeds a certain threshold value the constant offset instantly changes its sign (2). This critical field is referred to as the coercive field E_c. The process of the polarization offset is called ferroelectric switching. In the ideal model ferroelectric switching is a symmetric process, so if the field in situation (1') is reduced below E_c, the offset changes its sign again (2'). In real materials defects and impurities can lead to a non-symmetric hysteresis curve [33]. At zero field only the constant polarization offset remains, which corresponds to the spontaneous polarization P_s due to the polar nature of the material. This idealistic uniaxial polarization hysteresis curve is the main characteristic feature of a ferroelectric. The experimentally measured P-E loops of a ferroelectric $BaTiO_3$ single crystal are shown in Figure 2.7 (b). The curve is very similar to the idealistic model. The main difference is that the switching is not completely instantaneous, especially the beginning and end of the switching process has a rounded shape. The reason for this behavior is that single crystals are not completely homogeneous and contain defects that can locally influence E_c. The result

---

* $P_{\text{total}} = \int_V \mathbf{P}(\mathbf{r}) d^3 r$, where $\mathbf{P}(\mathbf{r})$ is the polarization and V is the volume of the crystal

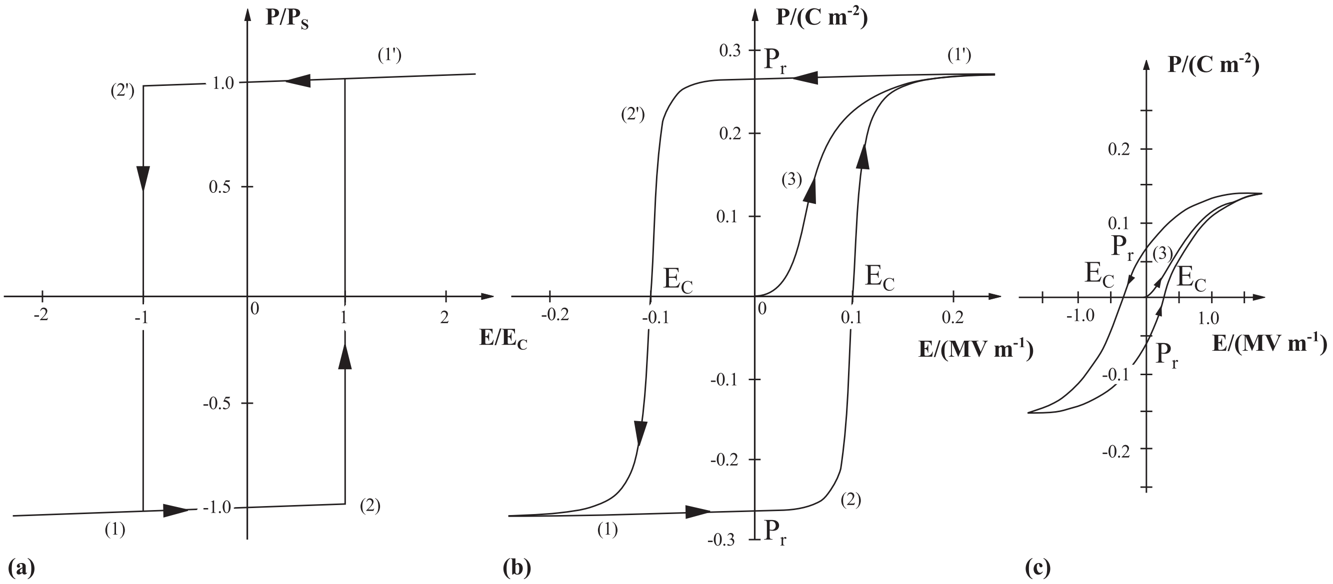

Figure 2.7: Hysteresis loops for (a) an ideal ferroelectric material (b) a single-domain single crystal of $BaTiO_3$ and (c) a $BaTiO_3$ ceramic. [24]. (1) indicates the reversible regime, where the ferroelectric system shows linear dielectric behavior, whereas (2) indicates the irreversible regime where ferroelectric switching takes place. (3) indicates the poling curve of the ferroelectric material.

is that different areas inside the ferroelectric single crystal* switch at different values of the external field leading to domain nucleation and domain wall movement. Most ferroelectric single crystals show a net polarization of zero after processing due to the formation of a domain structure. The value of P_i at zero field is called the remanent polarization P_r and may differ from the value of the spontaneous polarization in real materials. To deduce the value for the spontaneous polarization from experimental data the linear region in the hysteresis curve above the coercive field has to be extrapolated to the y-axis (external electric field equals to zero). Most ferroelectric materials that are used for applications are polycrystals. In these ceramic materials the different orientation of the crystallites and the influences of the grain boundaries lead to a much lower P_r and E_c and to a more rounded P-E hysteresis loop, where it is more difficult to distinguish between the linear dielectric and the switching contribution. The main characteristics, however, are still clearly visible in the experimental measurements (Figure 2.7 (c)). Line (3) in the single- and polycrystalline P-E loop describes the poling behavior, which is further explained in Section: Poling/Switching of Ferroelectric Single- and Polycrystals.

Ferroelectric Domains

When a polar single crystal in its paraelectric phase is cooled below the material specific Curie temperature T_C, it will undergo a phase transition to a ferroelectric phase. Initially the dipole moments of every unit cell (elementary dipoles) will randomly relax to one of the possible stable polarization directions given by the crystal structure. This random initial state is not stable because of the large system energy resulting from the electrical and mechanical coupling of the elementary dipoles. As a result, the system starts a relaxation process to a stable configuration, i.e., minimizing of the system energy. Experimental measurements have shown that stable configurations are complex structures of different regions with

---

* Also called ferroelectric domains. Further information can be found in the Chapter Ferroelectric Domains.

homogeneous polarization [34, 35]. These regions are called ferroelectric domains, analogue to the ferromagnetic case. The boundary between two neighboring domains is called a domain wall. Domain walls can be classified by the angle between the polarization directions in the adjacent domains. The thickness of a domain wall depends on the ferroelectric material system, e.g., around 0.5 nm in $PbTiO_3$ [15], $20-80$ nm in $KTiOPO_4$ and about 150 nm in $LiNbO_3$ [36], as well as on the domain wall type.

The experimentally observable complex domain structures are caused by the different interaction mechanisms that determine the total system energy. A nonzero net polarization leads to a depolarizing field*, or respectively surface charge densities, that increase the system energy (Figure 2.8). Therefore, an inhomogeneous polarization distribution consisting of domains is energetically favored. However, the formation of a polarization gradient, i.e., a domain wall, also increases the system energy, so that the resulting domain structure has to be a compromise of both effects. The lower the domain wall energy, the more domains are formed during the relaxation process. Also, the favored class of the domain walls depends on the strength of the different interaction mechanisms. For example, in tetragonal systems only 90°- and 180°-domain walls are allowed by the crystal structure. On one hand, the formation of a 180°-domain wall possesses a larger polarization gradient than a 90°-domain wall. However, the crystal structure of ferroelectric materials is elongated along the direction of the spontaneous polarization and shortened in the orthogonal direction. This deviation is called the spontaneous strain and leads to a lattice mismatch in case of 90°-domain walls. The internal strain increases the energy, which is needed to form a 90°-domain wall. Thus, it depends on the material parameters for the spontaneous strain, the material stiffness, and the polarization gradient energy parameters, which of these two domain wall possibilities is favored in the specific tetragonal material. It has to be kept in mind that these considerations are made for an ideal ferroelectric system. Deviations from this ideal model in real systems, such as charged lattice defects, multiple phases, pores and polycrystalline microstructures strongly influence the domain structure in a real ferroelectric crystal. In addition to the defects inside the bulk, the nature of the surface of the ferroelectric materials and additionally the surface of each crystallites in polycrystal ferroelectrics influences the shape, size and orientation of the domain structure [35, 37]. For small structures like quantum dots or single grains the following empirical relation between the domain size and the diameter of the ferroelectric structure can be found:

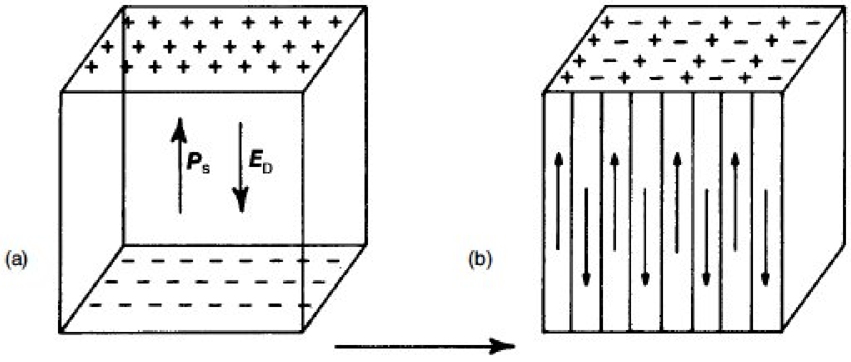

Figure 2.8: (a) Surface charge associated with spontaneous polarization; (b) formation of 180° domains to minimize electrostatic energy [24].

$$\text{Domain size} = (\text{Structure diameter})^m \tag{2.49}$$

---

* Electric field generated by the resulting electric dipole moment

where the exponent m is nearly 1/2 for structures between 1 and $10\mu m$, slightly smaller for structures above $10\mu m$ and bigger for structures below $1\mu m$ [38].

Poling/Switching of Ferroelectric Single- and Polycrystals

Currently, polycrystalline ferroelectric ceramics are typically used in piezoelectric actuator and transducer applications. Ceramic piezoelectric materials require less complex production processes compared to those of single crystal piezoelectrics, which leads to lower costs. Polycrystalline materials consist of many randomly oriented single crystals (”crystallites”) with a random size distribution that are separated by grain boundaries. Consequently one would expect no remarkable piezoelectricity in these materials due to the macroscopic isotropy in all physical properties following from the the random distribution of the single crystal grains. This is in fact the case for an unpoled polycrystalline materials after processing, where each grain possesses a random domain configuration resulting in a vanishing total polarization. However, the single crystal grains are ferroelectric. Therefore, with the application of a static electric field, under appropriate conditions of temperature, mechanical load and time it is possible to align the polarization of the crystallites in the direction of the external field. This aligning process of the domains inside an untreated ”virgin” sample is called poling. The greater the number of different polarization states allowed by the crystal structure, the more closely the polarization of a randomly oriented crystallite can be oriented in the direction of the poling field. Thus, rhombohedral (3m) structures, which allow eight directions, permit a better alignment than tetragonal (4mm) structures with only six possible polarization directions. In some materials both structures are present at a compositional phase boundary. In theses cases, the external field is sometimes able to transform the unit cell from one structure to the other. The number of alternative crystallographic directions is increased to 14, which increases the polarizability of the material. After poling, the polycrystal keeps a remanent polarization in the direction of the former poling field and does no longer behave isotropic. Due to the break of the former ”statistical symmetry” the material is now capable of piezoelectric, pyroelectric and electro-optic behavior. Like polycrystalline ferroelectrics, most ferroelectric single crystals do not show a net polarization after processing or after cooling down from the Curie temperature due to the formation of an energetically favored balanced domain distribution. In pure single crystals, external electrical fields of a sufficient value parallel to one of the polar axis of the crystal, are able to change the initial domain distribution into a stable single domain state, which is the corresponding poling process in single crystals. Virgin samples can be identified by the typical poling curve that occurs in dielectric measurements when the samples are measured for the first time (Figure 2.7 (b) (3) and (c) (3)).

Poling and switching, which denotes the rearrangement of the polarization system in a poled sample, are similar processes. The realignment of the polarization system in a single- or polycrystal is based mainly on two elementary mechanisms: the domain nucleation and the domain wall movement. In the first case the external electrical driving force increases the number of domains oriented in energetically favored directions during the poling/switching process by the nucleation of new domains. This nucleation of new domains can be directly observed in measurements [39]. The second important mechanism is the volume growth of domains that are energetically favored at the expense of neighboring domains with an energetically unfavored polarization orientation by a shifting of the intermediate domain wall. This movement can be restrained by different types of defects in the structure [40] or at the sample surface [41]. However, the existence of internal stresses and grain boundaries leads to a certain amount of pinned domains, which cannot be aligned by external electric fields with a field strength below the breakdown field [42]. These pinned domains lower the value of the maximum achievable remanent polarization in the polycrystal ferroelectric material. The amount of pinned domains can be reduced by heating up the ferroelectric material to temperatures close to the Curie temperature before the application of the poling field [43]. This ”hot poling” improves the performance of ferroelectric ceramics significantly.

The mineralogist G. Rose was the first who examined crystalline calcium titanate ($CaTiO_3$) in 1839. He later named the crystal after the Russian mineralogist L. A. Perovski. This name, ”Perovskite”, is today used to label the whole class of $A\,B\,X_3$-compounds, with two cations A and B that can have a variety of charges and an anion X that binds both, which crystallize in the same atomic structure like calcium titanate. Some of the most commonly used ferroelectrics belong to the group of perovskites. For example, lead zirconate titanate $Pb(Zr_{1-x}\,Ti_x)O_3$ is a ceramic material often used for piezoelectric actuators and ultrasound transducers as well as Barium titanate $BaTiO_3$, which can be found in thermistors and high frequency electronics.

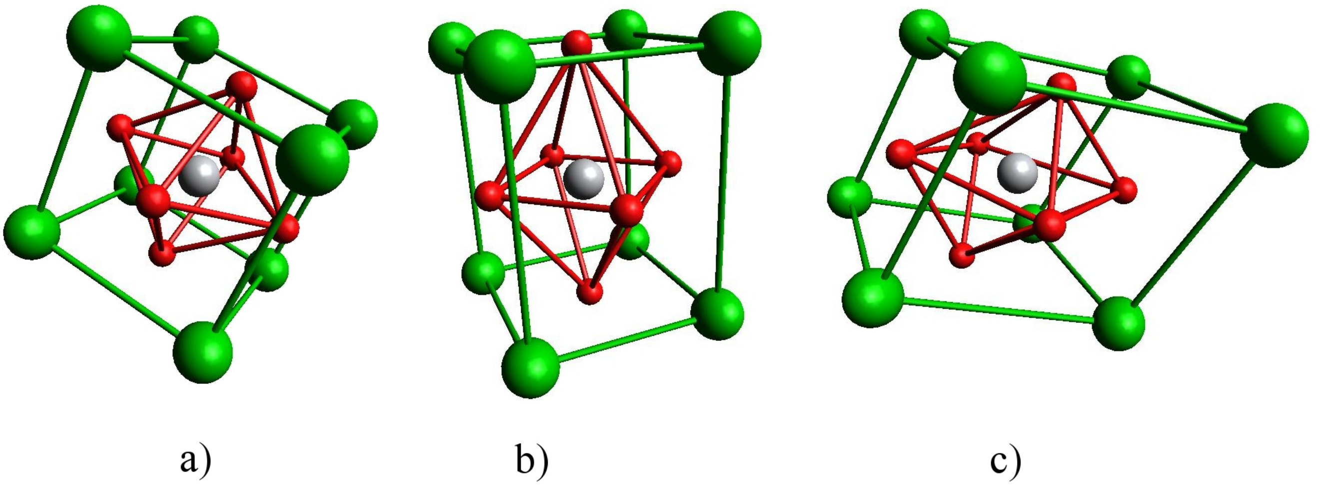

Figure 2.9: Typical variants of the Perovskite unit cell of $Pb(Zr_{1-x}\,Ti_x)O_3$ (green spheres: A cation, Pb^{2+}; white spheres: B cation, Zr^{4+} and Ti^{4+}; red spheres: X O^{2-}): a) cubic, b) tetragonal distorted and c) rhombohedral distorted

The idealized structure of $Pb(Zr_{1-x}\,Ti_x)O_3$ can be described (compare Figure 2.9), as a simple cubic unit cell with the large A-cation Pb^{2+} on the corners and the smaller B-cation Zr^{4+} and Ti^{4+} at the body centered position. The X-anions O^{2-} are situated in the center of the side faces, so that they form an octahedra around small cation in the center of the elementary cell. To form such an ideal cubic perovskite structure the ionic radii of the involved elements have to fulfill the following relation:

$$t_G = \frac{R_A + R_X}{\sqrt{2}(R_B + R_X)} = 1, \tag{2.50}$$

where t_G is the Goldschmidt tolerance factor and R_A, R_B and R_X indicate the radius of the large and small cation and the anion, respectively. In practice the tolerance factor of stable systems can vary between 0.84 and 1.09, which results in a slightly distorted perovskite structure [44].

In the simple cubic form the B^{4+}-cation has only one energetic stable position exactly at the center of the unit cell. Due to symmetry this simple cubic perovskite structure is nonpolar. If the unit cell structure is distorted to a tetragonal, orthorhombic or rhombohedral structure the stable position for the B^{4+}-cation is shifted away from the center of the unit cell; the perovskite structure becomes polar. Moreover, additional stable positions for the B^{4+}-cation appear in the structure. An external field can move the cation from one of these stable positions to another; the perovskite structure is also ferroelectric. A ferroelectric phase transition from a paraelectric to a ferroelectric phase in a perovskite is therefore accompanied by a structural phase transition from a simple cubic to a tetragonal (rombohedral, orthorhombic) unit cell shape.

Antiferroelectricity

In most cases, the interaction between the electric dipole moments of neighboring elementary cells energetically favors a parallel orientation. There are, however, a few notable exceptions , e.g.,$PbZrO_3$ and $NaNbO_3$ possess a polar phase, where an anti-parallel dipole orientation exists. This effect, the dielectric counterpart of anti-magnetism, was predicted by Kittel in 1951 and is called antiferroelectricity [45]. The temperature dependency of the antiferroelectric coupling mechanism remains constant, the dielectric permittivity exhibits a Curie-Weiss-like behavior with a singularity at T_C. Above the Curie temperature first or second order phase transitions to ferroelectric or paraelectric phases can be found. Possible arrangements of the electric dipole system are schematically depicted in Figure 2.10 (C) and 2.10 (D).

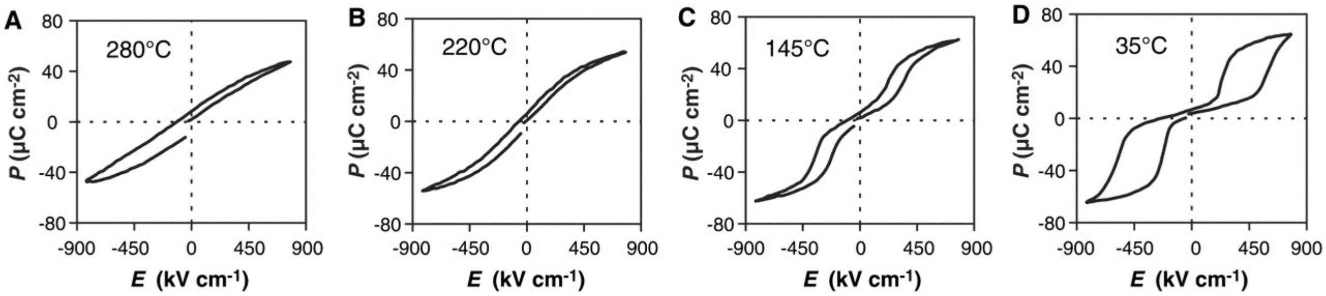

Figure 2.10: Electrical measurements of $Pb(Zr_{0.95}Ti_{0.05})O_3$ films on cooling. (A to D) Uncompensated polarization P versus applied electric field E at 10 kHz. (A) Lossy paraelectric behavior at 280 °C. (B) The qualitative form of this hysteresis loop taken at 220 °C is unchanged through the ferroelectric to paraelectric transition at $T_0 = 220$ °C. (C and D) Evidence for antiferroelectricity is seen below 190 °C. [46]

As result of the anti-parallel polarization formation, antiferroelectric materials show no remanent polarization at zero field. With the application of a high enough external electric field the polarization system is able to switch in a parallel configuration. From this point, the material behaves like a ferroelectric. If the external electric field or mechanical stress decreases under a certain threshold value the material returns to its antipolar configuration. This leads to the characteristic double hysteresis curve in polarization. But the double hysteresis curve is not a sufficient criteria for antiferroelectricity. Other phenomena are capable of creating polarization-electric field double loop behavior [14]. It should be remarked that due to a center of symmetry antiferroelectric materials are unable to show piezoelectric properties.

Curie-Weiss Law

Due to a structural phase transition in the crystal structure at a transition temperature T_0, often referred to as Curie point [14], ferroelectric materials lose their spontaneous polarization and become paraelectric. Above T_0 the electric susceptibility χ of the ferroelectric material can be described as

$$\chi(T) = \frac{C}{T - \Theta} \tag{2.51}$$

where C is a material specific Curie constant* and Θ is the Curie temperature. For ferroelectrics that undergo a first order phase transition†, where important characteristics like dielectric constant, polarization, lattice constant, etc. change discontinuously with temperature, both temperature constants, T_0 and Θ, can differ by more than 10° C. In the case of a second order phase transition, where the important characteristics change continuously but with a discontinuity in the slope with temperature, there is no measurable difference between them. The temperature characteristic of χ corresponds to the behavior of the magnetic susceptibility in ferromagnetic systems, where it was first revealed by P. Curie and P.E. Weiss. In the magnetic case the Curie-Weiss law can be directly derived from Heisenberg's theory of ferromagnetism [47], and it was adopted for ferroelectrics due to the great similarity between both systems. From Eq. 2.51 it can be seen that the electric susceptibility becomes singular at the phase transition temperature ($T = T_0$). Because of the phase transformation in the atomic lattice taking place at this temperature, the Curie point can be determined by structural measurements, whereas the Curie temperature is a formula constant and can only be determined by extrapolation of measured data.

Electrostriction

Similar to piezoelectricity, electrostriction describes a deformation that occurs due to an applied electric field. The electrostrictive strain is often negligible compared to the piezoelectric strain. However, under certain conditions, especially in ferroelectrics [48] and ferroelectric relaxor materials [49], the electrostrictive effect can be sufficiently large to be of interest. Unlike the piezoelectric strain, the sign of the deformation does not depend on the polarity of the material.

The electrostrictive strain of a crystal can be described by a fourth rank symmetric tensor either concerning the electric field **E** ($\mathbb{M}_{ijkl}$) or the polarization **P** ($\mathbb{Q}_{ijkl}$) inside the structure.

$$S_{ij} = \mathbb{M}_{ijkl} E_k E_l = \mathbb{Q}_{ijkl} P_k P_l \tag{2.52}$$

The strain of a ferroelectric mono-domain single crystal is given by Equation 2.52, where the polarization includes the contributions from the linear dielectricity and the offset due to the spontaneous polarization. The spontaneous strain S^0_{ij}, meaning distortion of the crystal lattice at zero external electrical field, can therefore be determined from the spontaneous polarization $\mathbf{P}_s$, if $\mathbb{Q}_{ijkl}$ is known:

$$S^0_{ij} = \mathbb{Q}_{ijkl} (P_s)_k (P_s)_l \tag{2.53}$$

One could imagine even higher (third-, fourth-, ...) order electro-mechanical coupling effects, but they are likely too small to be of interest.

Ferroelastic Effect

Ferroelectric materials often also exhibit ferroelastic behavior. A crystal is called ferroelastic if the direction of the electric polarization can be switched by an external mechanical stress over a certain threshold, the so-called coercive stress T_C. This behavior is explained by the example of a tetragonal ferroelectric material. The unit cell of the system is elongated in the direction parallel-, and shortened in the directions perpendicular to the spontaneous polarization. If a compressive external stress is applied parallel to the direction of the polarization, while polarization directions perpendicular to the external stress become energetically favored. If the stress reaches the value of T_C the system switches to one of the four

---

[*] Usually in the order of 10^3 -10^5 °C

[†] A more detailed description of the different types of phase transitions can be found in Chapter˜2.2

energetically favored polarization orientations. Ferroelastic switching leads to a nonlinear stress-strain curve, shown in Figure 2.11. Starting from either a virgin state (1) or a domain configuration where all domains are oriented parallel or antiparallel to the external mechanical stress T, the initially linear S-T-curve flattens when the value of the coercive stress T_C is reached (3). In this region the predominantly part of the decrease in mechanical strain originates from the ferroelastic domain switching. After all possible ferroelastic domain switching processes took place the S-T-curve changes back to a linear elastic behavior (4). If the external strain is reduced back to zero the strain decreases approximately linear. The ferroelectric domain switching processes are not reversible, so that the strain at zero stress (5) is significantly lower than at the beginning.

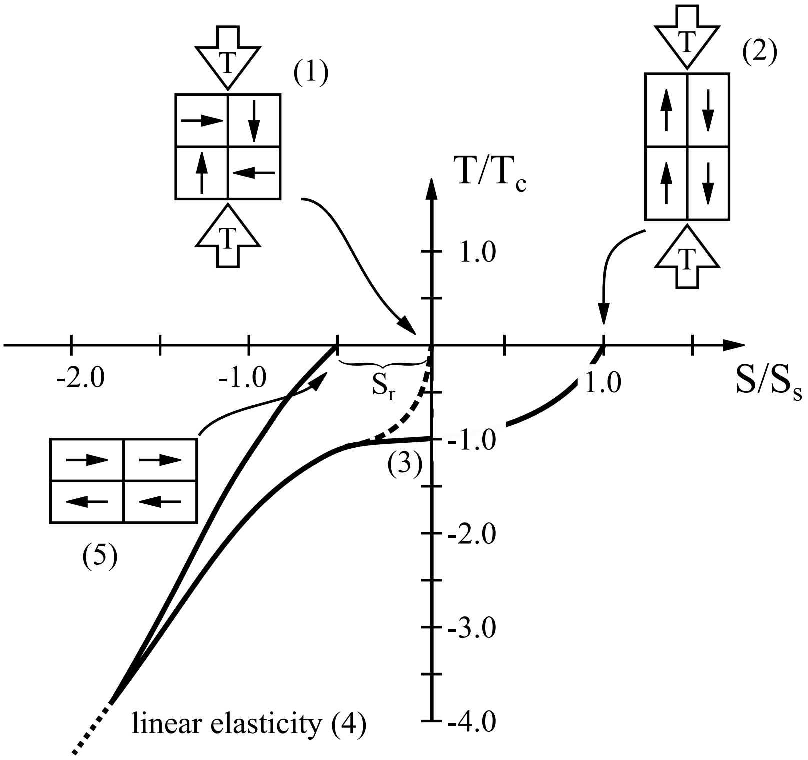

Figure 2.11: Schematic representation of ferroelastic switching in ferroelectric single crystals. The value of mechanical strain S longitudinal to the direction of the external mechanical load T is plotted in multiples of the spontaneous strain S_s. T is normalized by the coercive stress T_C, which is the threshold value. The curvature of S is caused by the same reasons then in the case of ferroelectric switching.

The opposite process, where the application of a tensile stress perpendicular to the polarization direction, lead to a switching process of the polarization back into the parallel orientation, is theoretically possible. However, the mechanical stability of ferroelectric single crystals and ceramics in tension is typically lower than T_c. Importantly for the tetragonal case, stress can only induce 90° switching processes because at least two adjacent polarization directions are energetically equivalent. Therefore no remanent polarization can be generated but it is possible to depolarize an initially poled structure. The ferroelastic effect can be used for pressure assisted poling of ferroelectric ceramics to decrease the necessary poling electric field, especially of high E_C-materials [42]. Further discussions of ferroelastic properties by the example of PLZT can be found in [50].

2.2 Landau Theory for Structural Phase Transitions

A structural phase transition occurs when a solid material spontaneously changes its crystallographic structure, symmetry and constitutive behavior. One of the simplest theories that is used to describe structural phase transitions is Landau's phenomenological model [51]. Devonshire was the first who used the principles of the Landau-Ginsburg theory to formulate a model of the phase transition from paraelectric cubic $BaTiO_3$ to ferroelectric tetragonal $BaTiO_3$. Up to now, this model forms the basis for much of the current understanding of ferroelectric phenomena. It is derived by following the principle postulates from thermodynamics that the behavior of a macroscopic system in a high-symmetry ($BaTiO_3$: paraelectric cubic phase) state can be described by specifying only a few state variables. This is no longer the case in phases with a lower symmetry ($BaTiO_3$: ferroelectric tetragonal/orthorhombic phase) after a phase transition. To describe the system in a phase with a lower symmetry an additional variable is required. This parameter is called the order parameter and is related to the respective phase transition and indicates the level of order in a system and characterizes the state of the system during a phase transition. Following this definition the order parameter is only an abstract value. However, in most cases it can be identified with a specific microscopic process. In ferroelectric⟷paraelectric phase transitions, the order parameter is the spontaneous polarization P_s of the unit cells. This order parameter is typically zero in the phase with higher symmetry, and non-zero in every other phase with lower symmetry. In case of a solid $BaTiO_3$ single crystal, the paraelectric cubic phase is the state with the highest symmetry. The basic idea of Landau theory is to deduce the macroscopic properties of the thermodynamic system on the basis of a polynomial expansion of the Gibbs free energy in terms of the order parameter. Although the model was derived as a "local" theory, i.e., for systems in the direct vicinity of the phase transition, it turned out that in some cases, especially in ferroelectric systems, the model includes a much larger validity range. Landau theory is a thermodynamic "phenomenological" model. It is based on a mean field approach, which means that microscopic interactions are considered as locally averaged field variables with low spacial fluctuations, instead of being treated individually. Even though the theory is able to describe all important macroscopic phenomenas that occur during a phase transition in a closed model, microscopical processes that causes the phase transformation are not directly considered, nor described by the model. The necessary free energy expansion coefficients, often called Landau coefficients, are mostly determined by fitting macroscopic experimental data [52–56], or they can also be deduced from first-principle calculations [57].

Ferroelectric Phase Transitions (1^{st}-, and 2^{nd}-Order)

The description of the one dimensional ferroelectric ⟷ paraelectric phase transition in terms of Landau theory is discussed for the simplified example of a mono-domain single crystal with only one polar axis in its ferroelectric phase in the following section. Moreover, mechanical stress free boundary conditions are assumed. A Taylor expansion is used to get an expression of the polarization dependent part of the Gibbs free energy of the system G_{LD} in terms of the order parameter, the total polarization P:

$$G_{LD} = G_0 + \alpha P^2 + \beta P^4 + \gamma P^6 + \text{higher order terms} \tag{2.54}$$

where G_0, α, β, and γ denote the expansion (Landau) coefficients of the even orders that specify the height and the shape of the free energy landscape. Because of the system symmetry, all odd expansion coefficients have to be zero. In the simplified case of a uniaxial temperature driven ferroelectric ⟷ paraelectric phase transition, terms up to the sixth order are necessary. However, the description of more complex systems and the consideration of external mechanical or electrical loads may require higher order terms up to the twelfth order [58]. A general assumption is that only the first Landau coefficient α is dependent on the temperature T and that this dependency follows the Curie-Weiss law:

$$\alpha(T) = \frac{T - \Theta}{2\epsilon_0 C} \tag{2.55}$$

where Θ denotes the Curie temperature and C the Curie constant. It has to be remarked that Θ is not necessarily identical to the phase transition temperature T_0. This assumption allows one to derive an expression for the temperature dependence of the equilibrium polarization P_s of the unloaded system in its ferroelectric phase, given by the symmetric minima of G_{LD}:

$$P_s(T) = \pm\sqrt{\frac{-\beta + \sqrt{\beta^2 - 3\alpha(T)\gamma}}{3\gamma}} \qquad \left.\frac{dG_{LD}}{dP}\right|_{P_s} = 0 \tag{2.56}$$

If an electric field is applied to the ferroelectric system, additional terms have to be added to the formulation of the free energy G:

$$G = G_{LD} - EP - \frac{1}{2}E\epsilon_0 E \tag{2.57}$$

For slowly fluctuating electric fields, the ferroelectric system will always be in an equilibrium state, where the first derivative of G with respect to P vanishes. In this case, it is possible to derive expressions for the electric field E and the contributions of the spontaneous polarization to the total system permittivity χ_P^{-1} from the formulation of the free energy in Equation 2.57 [59]:

$$E(P,T) = \frac{dG_{LD}}{dP} = 2\alpha(T)P + 4\beta P^3 + 6\gamma P^5 \tag{2.58}$$

$$\epsilon_0\chi_P(T) = \left(\frac{dE(P,T)}{dP}\right)^{-1} = \left(2\alpha(T) + 12\beta P^2 + 30\gamma P^4\right)^{-1} \tag{2.59}$$

In ferroelectrics the contributions of the spontaneous polarization on the systems permittivity are typically the predominant mechanism ($\chi \approx \chi_P$). The behavior of $P_s(T)$ and $\chi(T)$ in the vicinity of the phase transition depends on the order of the phase transition. If β is negative and γ positive one speaks of a first oder phase transition. In this case G exhibits three minima below T_0, at $P = 0$ and $P = \pm P_s$ as depicted on the right side of Figure 2.12 that are even existent for temperatures slightly above T_0. At $T = T_0$ all minima are energetically equivalent, meaning that at this temperature the system will be in one of these stable states. Above T_C the energy of the minima at $P = \pm P_s$ increases compared to the central minimum. The energetically unfavored states become metastable, meaning that the system may be stable in this state, but a small perturbation of the system can result in a relaxation of the system to the globally stable minimum at $P = 0$. Below T_0 the opposite situation can be observed; the minimum at $P = 0$ becomes metastable. Assuming that the system always relaxes to minima with the lowest energy, the order parameter $P_s(T)$ exhibits a discontinuous jump to at $T = T_0$ (Figure 2.12, top right), which is one of the fundamental characteristics of first order phase transitions. Besides the spontaneous polarization, the inverse susceptibility also shows a discontinuous jump at T_0. It is possible to derive an expression for the Curie temperature Θ [59]:

$$\Theta = T_0 - \frac{3}{16}\frac{2\epsilon_0 C(\beta/4)^2}{\gamma}, \tag{2.60}$$

meaning that in the case of a first order phase transition Θ is always smaller than T_0.

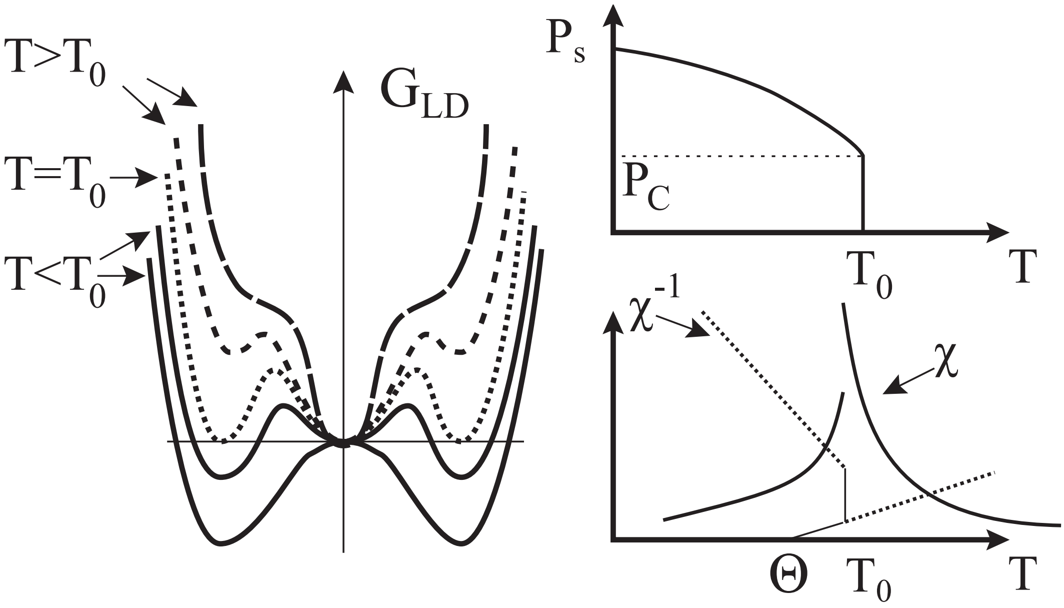

Figure 2.12: Landau energy, polarization and permittivity for phase transitions of the 1^{st}-order [60].

If β is a positive value, the phase transition is of the second order. These types of phase transitions are often found in ferroelectric materials. Below T_0, G has only two symmetric minima at $P = \pm P_s$. When temperature is elevated these minima shift towards towards $P = 0$. At T_0 both minima merge together and form a single minimum; no metastable local minima exist at T_0. This results in a continuous decrease of P_s until it vanishes for temperatures above T_0. The decrease of P_s below T_0 for elevating temperature is given by:

$$P_s(T) = \sqrt{\frac{T_0 - T}{2\epsilon_0 C\beta}} \tag{2.61}$$

At T_0 the minimum of the Landau energy is flat, resulting in a singularity of the susceptibility. Even small electric fields can induce large polarization changes. In real materials, defects and inhomogeneities lead to a broadening of the peak. Above T_0, $\chi(T)$ is described by the Curie-Weiss Law (Equation 2.51), below T_0 the following equation can be derived:

$$\chi(T) = \frac{1}{2}\frac{C}{T_0 - T} \tag{2.62}$$

This means that the inverse permittivity can be described by two linear functions with a contact point at $(T_0, 0)$, whereas the slope below T_0 is negative and twice as large as above. A schematic illustration of the polarization and susceptibility as a function of temperature can be found in Figure 2.13. An important difference to first order phase transitions is that in case of a second order phase transition, the Curie temperature Θ is identical to the phase transition temperature T_0.

Not all phenomena can be sufficiently described by this simplified Curie temperature dependence of G. Examples for a more complex temperature dependency can be found in Chapter 3, where the temperature dependence of the tetragonal→orthorhombic phase transition, induced by electric fields of single crystalline $BaTiO_3$ is discussed in detail.

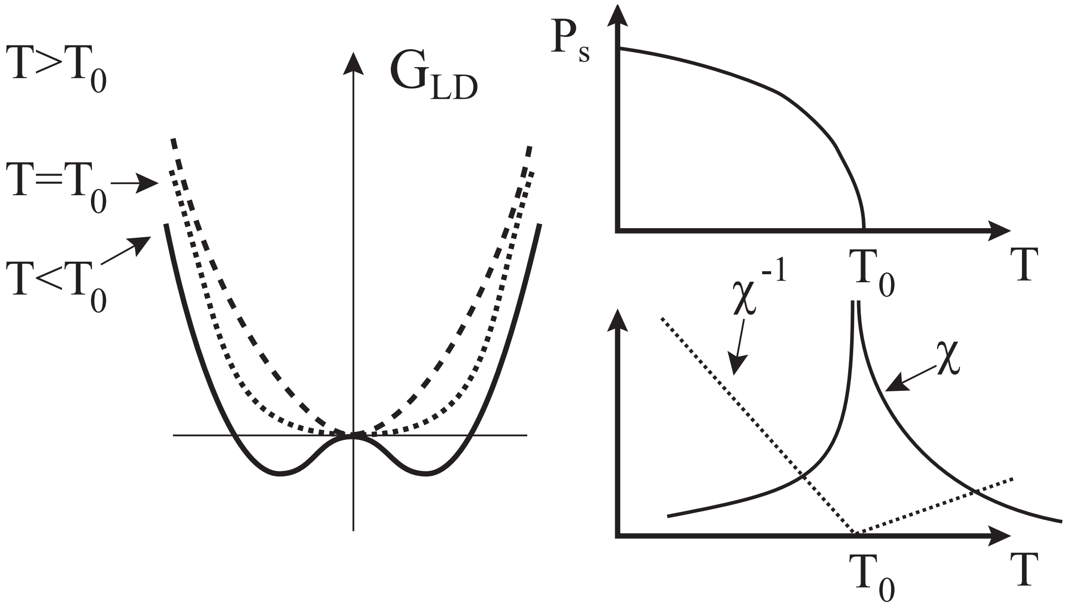

Figure 2.13: Landau energy, polarization and permittivity for phase transitions of the 2^{nd}-order [60].

3 Electric Field-Induced Structural Phase transitions in Ferroelectric Single Crystals

3.1 Introduction

Unlike the classical structural phase transition between a polar and a non-polar phase, or different polar phases that occur if the system temperature of a ferroelectric crystal reaches the corresponding transition temperature, a field-induced phase transition occurs when an external electrical or mechanical load of a certain strength is applied along a specific crystallographic axis that results in a change of the physical properties of the crystal [61, 62]. An alternative interpretation is that the external load influences the Curie temperature, leading to a shift of the phase diagram [63]. A field-induced structural phase transition happens when a phase boundary nucleates and translates through the crystal. The fundamental understanding of this type of transition is very important for the development of improved piezoelectric materials, due to the drastic increase of the piezoelectric properties of ferroelectric materials in the vicinity of a phase transition that can be triggered at constant temperatures. Recent experimental as well as theoretical studies on different ferroelectric systems identify field-induced phase transitions as the fundamental mechanism behind the performance of important piezoelectric materials that are used today [64–73]. An outline of the important findings in this field are discussed in the following section.

Due to their superior electromechanical coupling along certain crystallographic axes, ferroelectric single crystals are widely utilized in sensing and transduction applications [74]. Especially single crystal relaxor ferroelectrics, such as $Pb(Zn_{1/3}Nb_{2/3})O_3$-$PbTiO_3$ and $Pb(In_{1/2}Nb_{1/2})O_3$-$Pb(Mg_{1/3}Nb_{2/3})O_3$-$PbTiO_3$ [75, 76] have been comprehensively investigated due to their excellent piezoelectric properties, electromechanical coupling, and unipolar strain capabilities that far exceed even polycrystalline $Pb(Zr_{1-x},Ti_x)O_3$ [14]. Further investigations revealed that relaxor ferroelectric single crystals display induced phase transitions during the application of large electrical [75, 77] and mechanical [77–79] loading, resulting in a nonlinear jump in polarization and strain. Unlike the jump in polarization and strain during ferroelectric switching, these phase transitions are fully reversible when the external load is removed, providing an explanation for the increase of the usable strain in these materials.

The existence of this effect, however, is not limited to relaxor single crystal ferroelectrics. It is believed that field-induced phase transitions phenomena could be a promising explanation for the superior piezoelectric properties of $Pb(Zr_{1-x}Ti_x)O_3$ for compositions close to the MPB, since structural examinations from B. Noheda et. al. [80] and R. Guo et. al. [81] revealed the existence of a monoclinic distortion in the material at compositions close to the MPB. D. Damjanovic proposed a flattening of the Landau energy function [72]. Further in situ structural measurements using XRD and neutron diffraction at different temperatures and electrical loads identified the same fundamental mechanisms in PMN-PT and gave additional proof for the importance of influence of field-induced phase transitions on the piezoelectric performance of ferroelectric materials[82]. In addition, the existence of field-induced phase transitions has been further supported by in situ XRD measurements on $Pb(Zn_{1/3}Nb_{2/3})O_3$-$PbTiO_3$ that have shown that the macroscopic strain of single crystal samples corresponds directly to the microscopic strains in the crystal lattice [64].

First principle calculations by H. Fu and R.E. Cohen predicted that the field-induced phase transition occurred through a polarization rotation mechanism from a rhombohedral to a tetragonal crystal orientation [83]. They showed that such a transition can generate a giant piezoelectric response also in single crystal $BaTiO_3$ at low temperatures. Experimental measurements of the piezoelectric effect along non-polar directions in $BaTiO_3$ single crystals have supported their findings [84], which makes these phenomena of interest for numerous applications, such as thin films, where in-plane strains have been shown to shift the Curie temperature of perovskites by hundreds of degrees Celsius [85, 86], or electromechanical energy harvesting through an Oleson cycle [87, 88]. Recent research has shown that field-induced phase transitions are the key feature in cutting edge polycrystalline lead-free ferroelectric materials that display an exceptional usable unipolar strain during electric field loading. This phenomenon is understood to be due to a similar temperature-dependent field-induced phase transition. Instead of a polarization rotation process between neighboring ferroelectric phases, the transition occurs between a macroscopic non-polar (ergodic relaxor) and a macroscopic polar (ferroelectric) order [89]. The special features of this type of field-induced phase transition are further discussed in Chapter 5 and 6.

In this chapter a Landau model is presented to simulate the polarization response of a mono-domain ferroelectric single crystal to an applied electrical load along an off-axis direction. According to Bell [90], a field-induced phase transition can be understood as the rotation of the polarization into a metastable orientation that corresponds to a different ferroelectric phase. First examinations were done on an arbitrary two dimensional ferroelectric material, to study the influences of the shape of the Landau energy landscape on the phase transition field. The energy thresholds for 90° and 180° switching as well as the polarization rotation path where used to vary the shape of the Landau energy. The results from this study have been published in Applied Physics Letters [91]. The model is then expanded to three dimensions and used to calculate the induced-phase transition behavior of $BaTiO_3$ for electric loading along the $\langle 110\rangle_c$- and $\langle 110\rangle_c$ crystallographic axis. The simulation results using various Landau energy landscapes that were reported from different researchers were compared to measurements of oriented $BaTiO_3$ single crystals to evaluate their predictive capabilities concerning field-induced tetragonal→orthorhombic phase transitions. These results have been published in Applied Physics Letters [92].

3.2 Landau Model of Field-Induced Phase Transitions

It was shown that piezoelectric anisotropy as well as the enhanced piezoelectric response of a ferroelectric domain along non-polar axis can be described by using an established phenomenological thermodynamic approach [72, 93, 94]. These effects, which can be observed in many perovskite systems, especially for compositions close to the MPB, are caused by the rotation of the polarization towards an off-axis external load and therefore are a direct consequence of the topology of the underlying Landau energy landscape. This energy landscape also influences the rotational behavior of the polarization and the coercive field for non-180 ° switching processes, meaning changes to the landscape through temperature variations or the application of external loads will also influence the polarization rotation behavior. As a mean-field approach, the Gibbs free energy G of a single ferroelectric domain under external electrical load and stress free mechanical boundary conditions, can be generally expressed as an expansion in term of the polarization P_i:

$$G = G_{LD} - E_i P_i - \frac{1}{2} E_i \epsilon_{ij} E_j \tag{3.1}$$

$$G_{LD} = \alpha_{ij} P_i P_j + \beta_{ijkl} P_i P_j P_i P_j + \gamma_{ijklmn} P_i P_j P_k P_l P_m P_n + \delta_{ijklmnop} P_i P_j P_k P_l P_m P_n P_o P_p + \text{h.o.t.} \tag{3.2}$$

where E_i denotes the external electrical field, α_{ij} is the dielectric stiffness tensor, and β_{ijkl}, γ_{ijklmn}, and $\delta_{ijklmnop}$ are the higher order stiffness coefficients, also called Landau parameters. The symmetry of the energy landscape matches the symmetry of the ferroelectric phase. As a direct consequence all odd coefficients have to be zero. Because of the phenomenological character of the model, most coefficients do not directly correspond to specific material properties and are determined by fitting of experimental data. Following the principle of minimum energy, a stable system polarization is indicated by a minimum in the free energy landscape.

A representation of the Landau energy landscape G_{LD} for an exemplary tetragonal ferroelectric material is shown in Figure 3.1. The three dimensional plot on the right shows the minimal Landau energy in each direction. The equivalent tetragonal energy minima are clearly visible along the directions of the axis of the coordinate system. On the left, the full polarization dependence of the Landau energy in the $P_{[100]}$-$P_{[010]}$-plane is shown. The stable polarization directions of the tetragonal phase, which are situated at the minima of the distribution, are indicated by white dots. Without an external electrical load all four minima are energetically equivalent due to the symmetry of the system. In some cases, not all minima are energetically equivalent, for example some of the more complex energy landscapes possess additional minima along other crystallographic directions, or due to a break of the symmetry by the application of an external load. Minima with a higher energy are metastable states, which means that the polarization can relax into lower energy minima for large enough perturbations of the system, for example by thermodynamic fluctuations.

The necessary number of coefficients, or the maximum order of G_{LD} in P_i to represent a given ferroelectric system with a sufficient accuracy depends on the type of the ferroelectric material, the temperature, and the nature of the considered phenomenas. In literature, reports on fourth-order [95, 96], sixth-order [52, 93], eighth-order [53–55], and even twelfth-order [58] free energy potentials can be found. Previous work has shown that Equation 3.1 results in an energy landscape that defines the stable polarization orientation as well as the electromechanical properties and polarization rotation path as a function of thermal, electrical, and mechanical fields [72]. If the energy distribution is dynamically changed by an external electrical field, the polarization of the ferroelectric system does not instantly follow. Instead, the time dependent evolution of the polarization can be determined by solving the evolution equation [97]:

$$\frac{dP_i}{dt} = -M \frac{\delta G(P_i, E_i)}{\delta P_i} \tag{3.3}$$

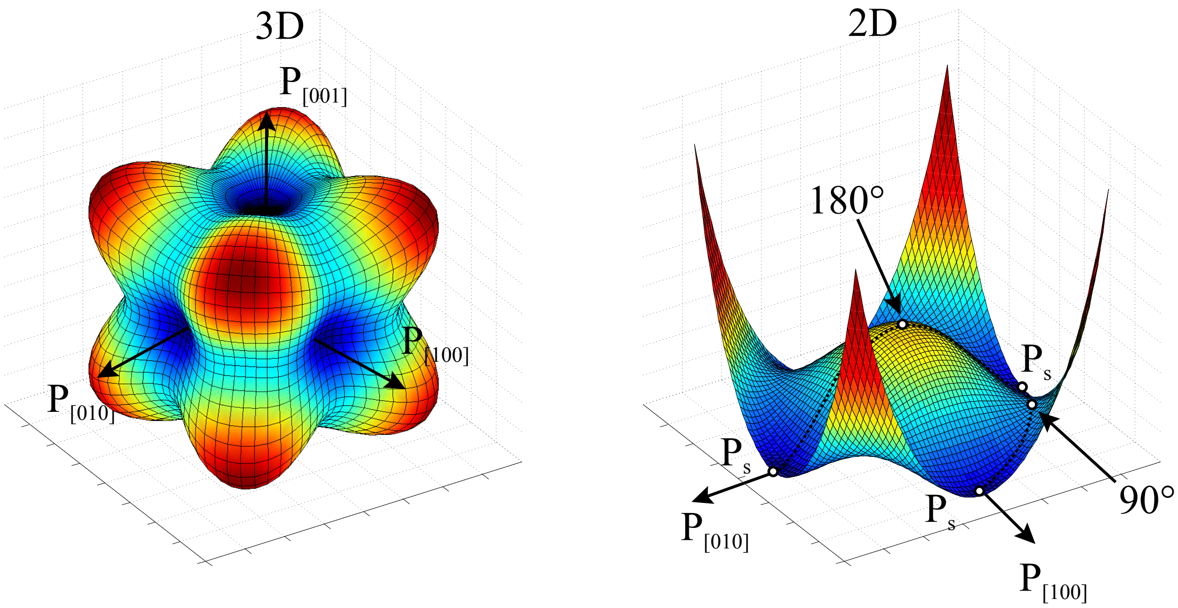

Figure 3.1: Three dimensional (on the left) and two dimensional (on the right) representation of the free (Landau) energy landscape for a tetragonal ferroelectric material. Dark blue indicates regions of polarization orientations with a lower free energy, dark red regions with higher free energy. In the three dimensional representation the minimal Landau energy in each direction is shown. In the two-dimensional case, the energetically equivalent minima of the tetragonal phase are marked with white dots, as well as the intermediate orthorhombic and cubic phases. Dashed lines indicate the corresponding switching paths for 90 ° polarization rotation and 180 ° polarization inversion processes.

where M denotes the mobility parameter and G the Gibbs free energy function from Equation 3.1 of the ferroelectric systems. M is a phenomenological parameter that can be determined by adapting the dynamic polarization behavior to corresponding experimental data [98].

Switching mechanisms in ferroelectric poly-domain single crystals can be classified into two categories: 180 ° polarization inversion and non-180 ° polarization rotation, whereas the possible rotation angles are given by the symmetry of the respective ferroelectric phase. Systems with a tetragonal symmetry, for example, possess 90 ° rotation. The corresponding polarization paths during inversion as well as rotation in tetragonal systems is illustrated in Figure 3.1 on a two dimensional free energy landscape representative of a tetragonal crystal. In the case of polarization inversion, the external electric field that induces the polarization reorientation is aligned antiparallel to the polarization of the crystal. With increasing electric field, the minimum of the free energy migrates towards the center of the coordinate system, which results in a decrease of the absolute polarization. When the external electric field reaches the value of the coercive field, the polarization overcomes energetic barrier, represented by the maximum of the Landau energy at the origin of the coordinate system. At this point the polarization of the system vanishes, i.e., the ferroelectric system approaches an intermediate cubic phase (see Figure 3.2 a). Above this point the polarization switches from the coordinate origin to the favored energy minimum, located 180 ° from the original polarization direction.

The second case typically appears when the external field inducing the switching process is oriented in the direction of a stable polarization variant that is less than 180 ° away from the original polarization direction, e.g., 90 ° for the tetragonal phase, 70.53° and 109.47° in the rhombohedral phase, and 60°, 90 °, and 120° in the orthorhombic phase. In this case, the stable minimum migrates into the direction of the external field along a path, which is given by the direction of the external electric field and the shape of the Landau energy landscape [99]. These polarization rotation paths can also be calculated by using molecular dynamics simulations [100]. During a rotation process the polarization is pointing into non-stable, off-axis directions, either in one direction of another high symmetry phase[*] or an intermediate low symmetry monoclinic phase (see Figure 3.2 b). The absolute value of the polarization and the spontaneous strain can increase or decrease during rotation, depending on the Landau energy shape and the appropriate electrostrictive coefficients. Therefore, polarization rotation can increase the global mechanical strain of the crystal and the formation of large internal stresses along the domain-walls, in contrast to 180° switching processes. Typically, the energy threshold for polarization rotation is lower than for polarization inversion processes [101]. This is the reason why in real materials two 90° polarization rotation steps can be often observed, where a 180° polarization inversion is expected [76, 102]. This two step switching behavior, however, is sensitive to mechanical stress and can be suppressed by an external mechanical load [103].

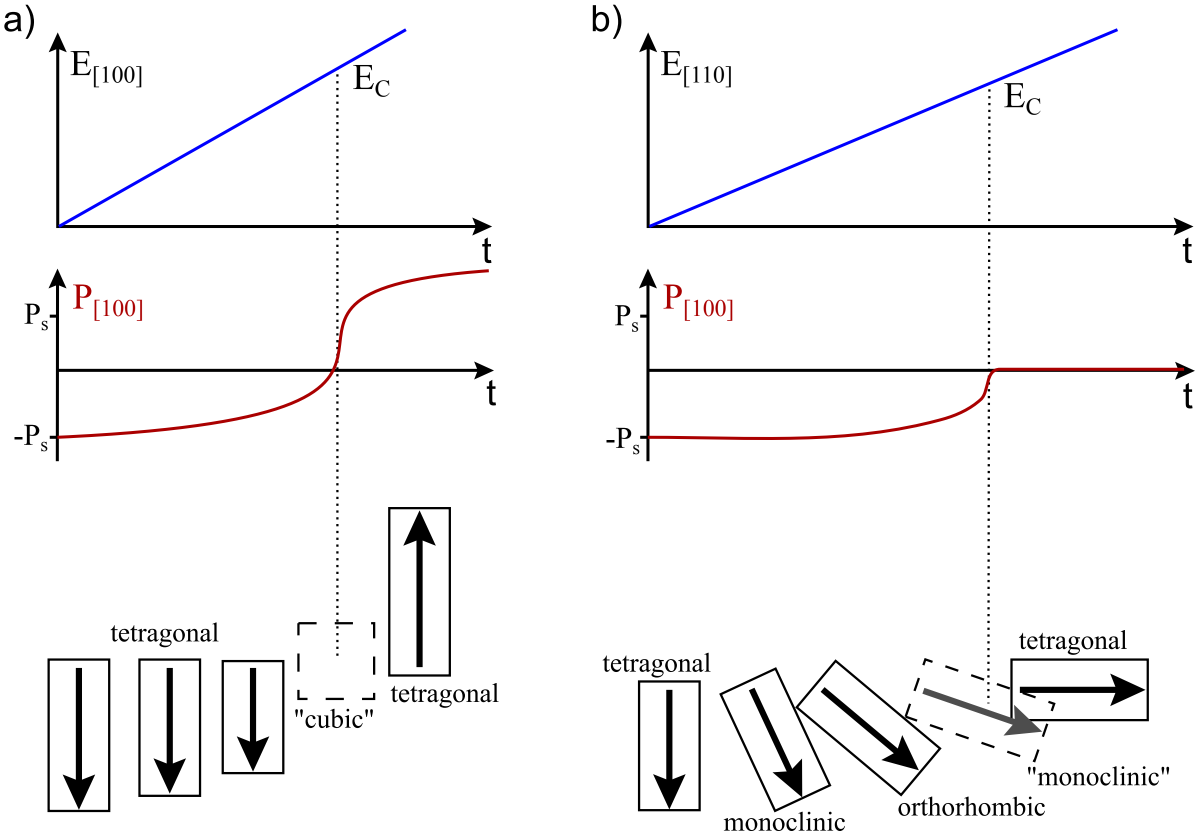

Figure 3.2: Polarization and unit cell distortion during ferroelectric switching in tetragonal materials: a) 180° polarization inversion in the case of an antiparallel external field and b) 90° polarization rotation in case of a perpendicular external field. The dashed unit cell denotes intermediate polarization states that are only temporarily reached during the irreversible part of the switching process. In the case of a polarization inversion, the ferroelectric domain traverses a non-stable cubic phase, whereas in case of a rotation the polarization goes through an intermediate monoclinic, orthorhombic, and again a monoclinic phase. Some of these phases can be stable when the external field is kept at a constant value.

---

[*] tetragonal, rhombohedral, and orthorhombic

3.2.1 Two Dimensional Landau Model

In the following chapter the influence of the Landau energy landscape on the field-induced phase transition behavior and the polarization rotation path is presented. Therefore, the representation of the Landau free energy (Equation 3.2) was limited to two dimensions to reduce the number of necessary parameters and the complexity of the calculations. This dimensional limitation also restrains the ferroelectric phases and polarization rotation processes that can be adequately represented by the model. A rhombohedral system is not feasible in two dimensions, whereas tetragonal and orthorhombic phases can be represented in two dimensions by limiting the allowed polarization directions to one principal plane, as shown in Figure 3.3. Within this plane both 180 ° as well as 90 ° switching processes can be represented in both phases, allowing to study tetragonal (T) to orthorhombic (O) phase transitions during 90 ° switching without being influenced by the two dimensional simplification. The 60° and the 120° switching processes in the orthorhombic phase, however, have no two dimensional equivalent. For these polarization rotations and also thinkable tetragonal (T) to rhombohedral (R) and orthorhombic (O) to rhombohedral (R) transitions, a full three dimensional model is necessary.

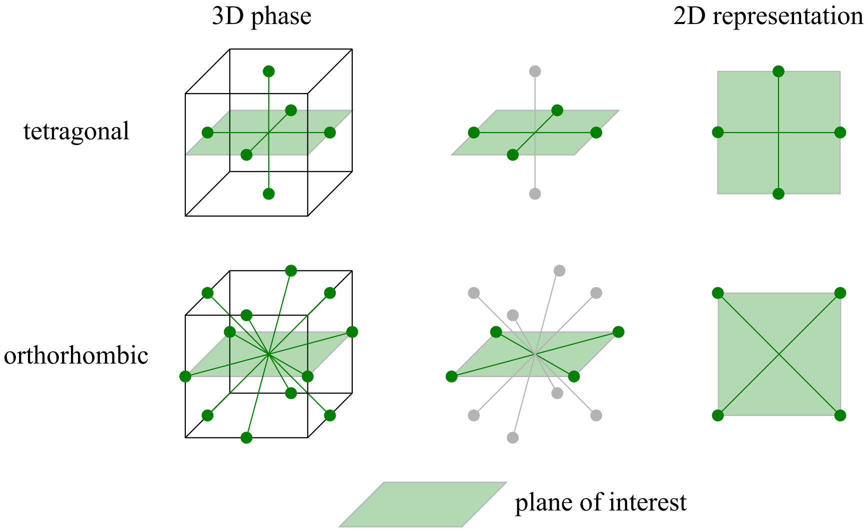

Figure 3.3: Energetically equivalent polarization variants for the tetragonal and orthorhombic crystal structure and their two dimensional representation

For this study, a mono-domain single crystal of an arbitrary tetragonal ferroelectric material was assumed. Given by the tetragonal (4mm) symmetry, the free energy has four symmetric energetically equivalent minima with a polarization equal to P_s, which denotes the spontaneous polarization in the unloaded state (Figure 3.5a). This leads to the following differential criterion for the two dimensional Landau energy function at the position of the minima:

$$\left.\frac{\partial G_{LD}(P_1, P_2)}{\partial P_1}\right|_{P_s,0} = 0 \tag{3.4}$$

The energy of the tetragonal minima of the Landau energy were referenced to zero, resulting in an alternative definition of G_0 as the energy barrier between 180 ° domains, and therefore the energy threshold for ferroelectric switching due to polarization inversion in the mechanical stress-free state:

$$G_{LD}(0,0) = G_0 > 0 \tag{3.5}$$

$$G_{LD}(\pm P_s, 0) = G_{LD}(0, \pm P_s) = 0 \tag{3.6}$$

Two characteristic parameters were introduced, q and G_1, to define the rotation path and the height of energy barriers for 90 ° switching due to polarization rotation, respectively. They are shown graphically in Figure 3.4. During a 90 ° switching process, the polarization will follow the path of the lowest energy between two stable polarization variants. According to the system symmetry, it can be assumed that the 90 ° energy barrier, i.e., the point of the highest energy value the polarization traverses (G_1) during rotation is situated in the orthorhombic $\langle 110\rangle_c$ crystal direction, at a distance of $P_s' = \sqrt{2}qP_s$ to the symmetry center of the energy landscape, as shown in Figure 3.4. These characteristics lead to the last two constraints that the energy landscape defined by the Landau coefficients has to fulfill:

$$G_{LD}(qP_s, qP_s) = G_1 \tag{3.7}$$

$$\left.\frac{\partial G_{LD}(P_1,P_2)}{\partial P_1}\right|_{qP_s,qP_s} = 0 \tag{3.8}$$

The lowest order approach for G_{LD} that still fulfills all required constraints from the Equations 3.4, 3.6, 3.7, and 3.8 is a sixth order (2-4-6) function:

$$G_{LD}(P_1,P_2) = G_0 + \alpha_1(P_1^2+P_2^2) + \beta_{11}(P_1^4+P_2^4) + \beta_{12}P_1^2P_2^2 + \gamma_{111}(P_1^6+P_2^6) \tag{3.9}$$

where G_0 is the energy of the reference state, α_1, β_{11}, β_{12}, and γ_{111} are the dielectric stiffnesses, i.e., Landau coefficients that determine the energy landscape as a function of the orthogonal components of polarization P_i assumed to lie along the pseudo-cubic axes of the unit cell. The remaining non-zero component γ_{112} of the 2-4-6 Landau function is not necessarily required to fulfill the constraints, or to represent a tetragonal or orthorhombic phase and has therefore been set to zero.

Inserting the general formulation of this Landau energy (Equation 3.9) into the constraint Equations 3.4, 3.6, 3.7, and 3.8 leads to a system of linear equations. The solution is an expression of the Landau coefficients α_1, β_{11}, β_{12}, and γ_{111} in terms of the energy barrier for 180 ° switching G_0, the spontaneous polarization P_s, the new parameters for the energy barrier G_1, and the rotation path q for 90 °-rotation processes:

$$\begin{aligned}
\alpha_1 &= \frac{G_0}{P_s^2}\left(\frac{G_1/G_0 + 2q^6 - 1}{q^2(1-q^4)}\right)\\
\beta_{11} &= \frac{G_0}{P_s^4}\left(\frac{2(1-G_1/G_0) - 3q^2 - q^6}{q^2(1-q^4)}\right)\\
\beta_{12} &= -\frac{G_0}{P_s^4}\left(\frac{2q^6 - 6q^4 + 3q^2 - G_1/G_0(3q^2-1) - 1}{q^4(1+q^2)}\right)\\
\gamma_{111} &= \frac{G_0}{P_s^6}\left(\frac{G_1/G_0 - 1 + 2q^2}{q^2(1-q^4)}\right)
\end{aligned} \tag{3.10}$$

Furthermore, there are additional constraints that must be satisfied by G to provide a physically realistic energy landscape. Since these constraints were not taken into account while determining the expressions for α_1, β_{11}, β_{12}, and γ_{111}, they limit the range in which q and G_1 can be chosen. First of all, the coefficient for the term with the highest order in P (γ_{111}) must be greater than zero. This ensures that the system energy goes to infinity for large polarization values. A second necessary constraint is that $G(P_i = 0)$ must be a local maximum at $G(P_i = 0)$ representing the energy threshold for 180 ° polarization inversion processes. The existence of an extremum at $P_i = 0$ is trivially given by the inherent symmetry of G. Therefore the only additional demand emerging from this constraint is that the Landau coefficient of the

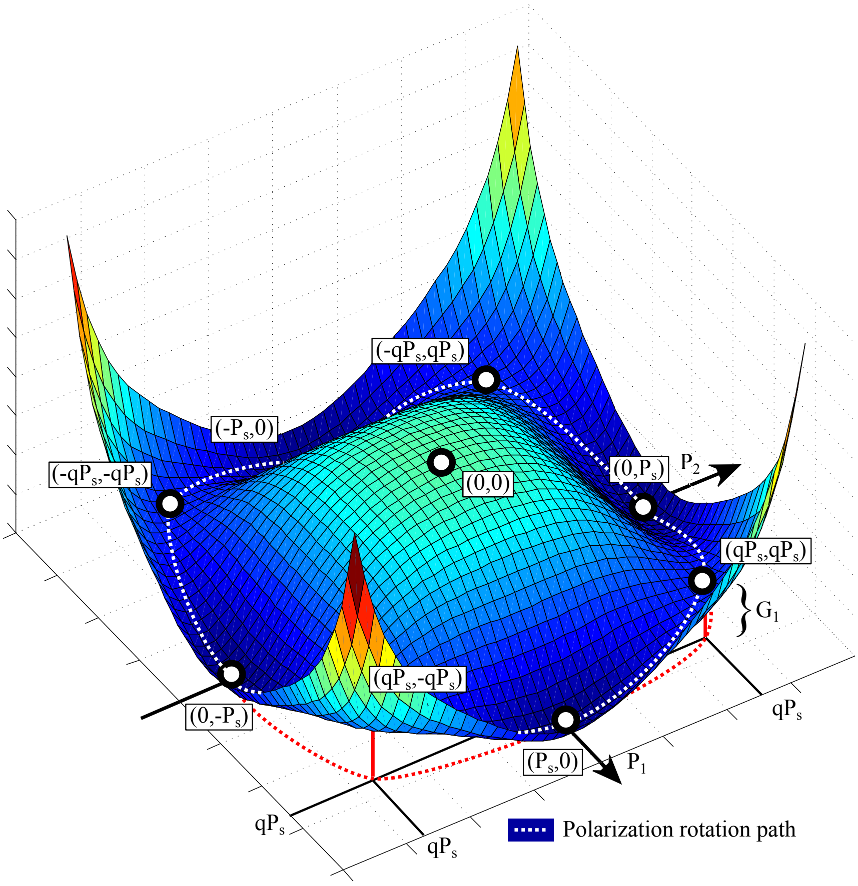

Figure 3.4: Two dimensional Landau energy landscape for $\sqrt{2}q = 0.9$ and $G_1/G_0 = 0.4$. Dark blue indicates regions of polarization orientations with a lower free energy, dark red regions with higher free energy. The polarization rotation path is indicated by the white dashed line along the energy surface and as a projection by the red dashed line in the P_1-P_2-plane. White dots mark the visible positions of the local tetragonal minima at $(\pm P_s, 0)$ and $(0, \pm P_s)$ as well as the saddle points in the orthorhombic directions at $\pm(qP_s, qP_s)$ and $\pm(-qP_s, qP_s)$.

quadratic term α_1 must be less than zero. Furthermore, it is important that the local maximum at $P_i = 0$ and the local minima at $\mathbf{P} = (\pm P_s, 0)$ and $\mathbf{P} = (0, \pm P_s)$ represent the only extrema. It was found that the Landau coefficients no longer fulfill these additional constraints, providing physically impossible energy landscapes, when $G_1/G_0 < 0.2$ or $G_1/G_0 > 0.8$ and $0.7 < \sqrt{2}q < 1.2$. A similar implementation of the Landau coefficients has been previously implemented by [104].

When an external electric field is applied to the system, the energy landscape begins to distort accordingly. This is shown schematically in Figure 3.5, where the electric field is applied to an originally tetragonal single-domain system along the $\langle 110 \rangle_c$ axis. Without an external electric field all four minima have an identical energy state. Upon the application of an electric field in the orthorhombic $\langle 110 \rangle_c$ crystallographic orientation the two minima most favorably aligned ($(P_s, 0)$, and $(0, P_s)$) begin to rotate into a monoclinic phase, whereas the unfavorably aligned minima ($(-P_s, 0)$ and $(0, -P_s)$) become energetically unstable (Figure 3.5b). This effect increases with an increase in the electric field, with the minima becoming more closely aligned to the applied field (Figure 3.5c). Eventually, a single minimum along the $\langle 110 \rangle_c$ direction is formed, as shown in Figure 3.5d. According to Bell [90] this mechanism corresponds to the T→O phase transition and the corresponding electric field is the critical T→O phase transition field E_0. Additional increases in the electric field further stabilize the orthorhombic phase.

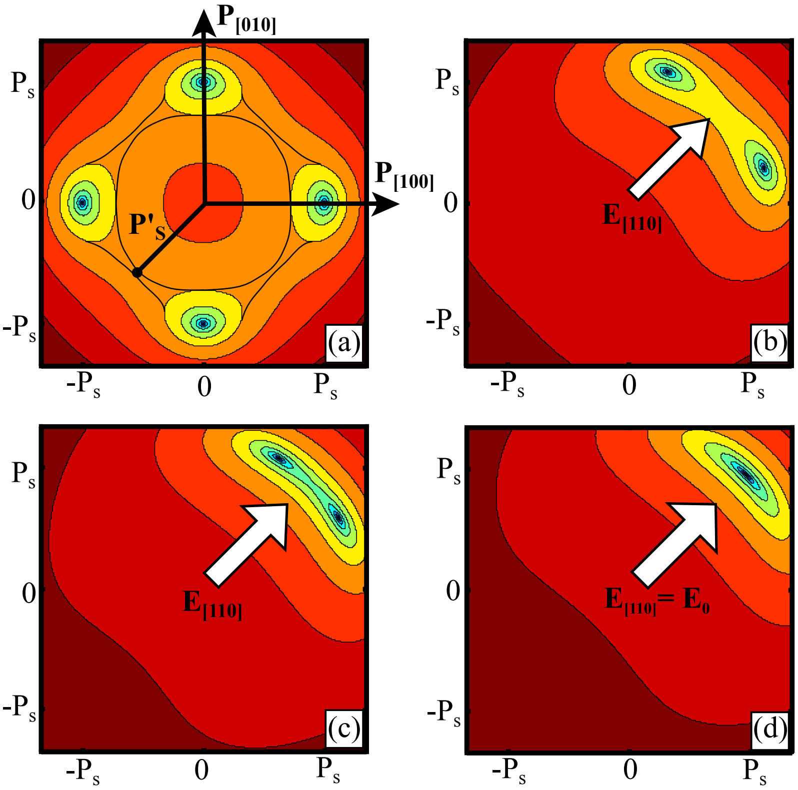

Figure 3.5: Energy landscape for a tetragonal poly-domain single crystal without electric field (a), where dark blue indicates a lower energy state than dark red. G_0 and G_1 are located at $P_i = (0,0)$ and $P_i = \mathbf{P}'_\mathbf{s} = (\mathbf{qP_s}, \mathbf{qP_s})$, respectively. Upon increasing the electric field along the orthorhombic crystallographic direction there is a corresponding polarization rotation, until at a critical electric field the stable polarization direction is found along the $\langle 110 \rangle$ orientation [91].

To calculate the polarization response of a tetragonal mono-domain single crystal to an external electric field in the orthorhombic crystal direction, the Landau potential was included into a finite element implementation of a two dimensional phase field model[*] [105, 106]. As previously mentioned, the dimensional simplification does not affect the primary conclusions of this work; the polarization rotation from the tetragonal to the orthorhombic phase is a strictly two-dimensional process. An implicit time integration scheme and a nonlinear Newton iteration was used to solve the evolution Equation 3.3 and to investigate the T→O phase transitions due to a stepwise increased electric load. The necessary mobility parameter M was chosen to be large enough to ensure a nearly steady state behavior of the system. Influences of the mobility parameter were studied by the variation of the loading rate.

Representative results of the phase field calculations are shown in Figure 3.6. The rate-dependent T→O phase transitions predict hysteretic behavior during unipolar electric field loading that is dependent on the crystallographic orientation. With increasing loading rate, defined by the mobility parameter, there is an increase in hysteresis. This is due to a more stable orthorhombic phase during unloading, whereas the loading path remains relatively insensitive to the loading rate. It is clear from Figure 3.6 that an electric field oriented along the $\langle 110 \rangle$-direction displays quasi-discontinuous polarization rotation, in contrast to the instantaneous phase transition predicted by Bell [90]. However, even a small misorientation of the applied field on the order of a few degrees, the typical tolerance specification for medical ultrasound manufacturers, can lead to a remarkable decrease in hysteresis and linear piezoelectric properties at low fields. In addition, during unloading a slight rounding preceding the O→T is found with increasing

---

[*] A description of all model equations can be found in Chapter˜6 as well as in the references cited.

off-axis loading. This effect was found to increase considerably when the parameter q decreases (see Figure 3.6 b). This suggests that the appearance of a continuous field-induced phase transition that is observed in ferroelectric single crystals can be explained by the shape of the Landau energy landscape instead of an inhomogeneous distribution of critical fields due to inhomogeneities in the material [107].

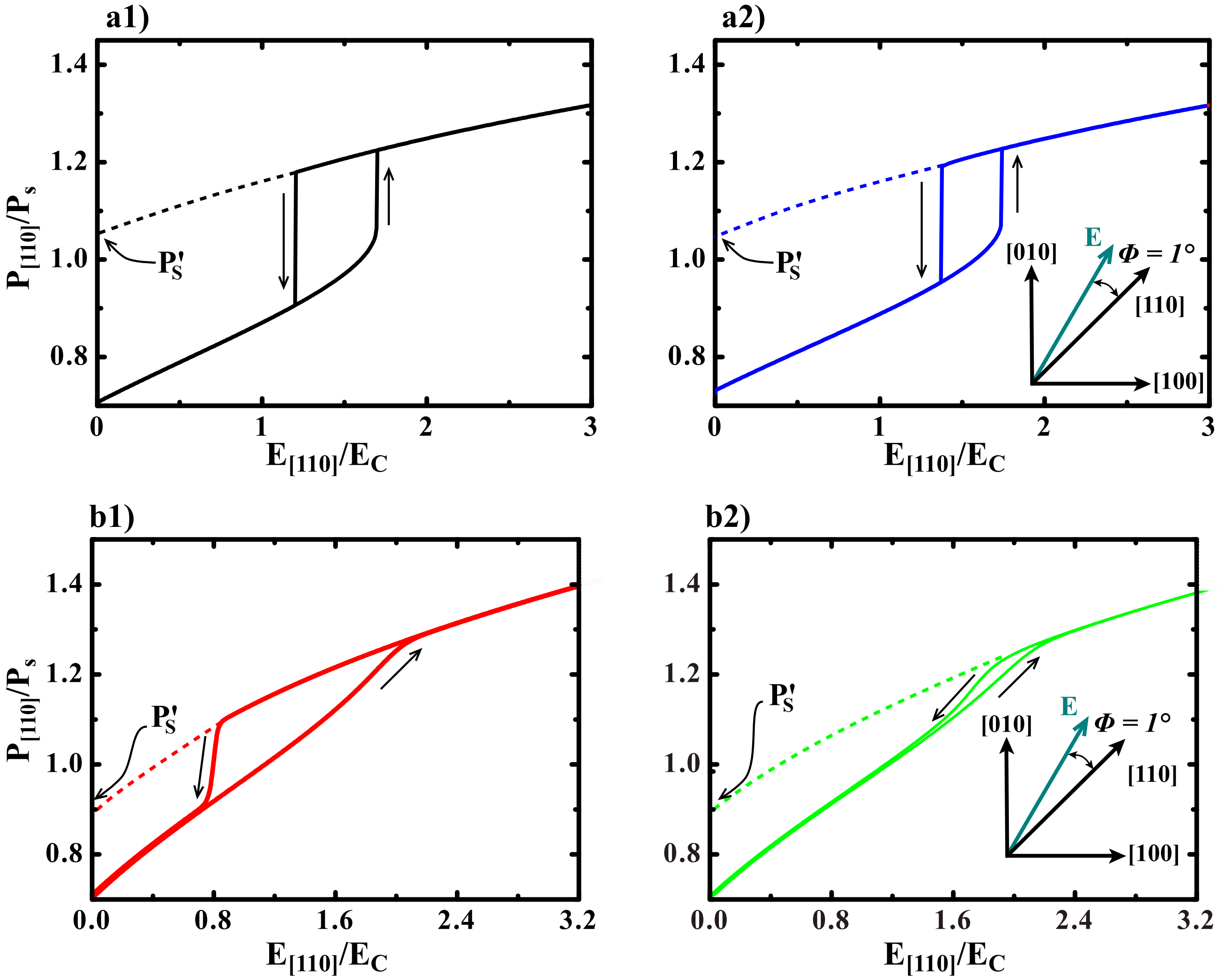

Figure 3.6: Unipolar electric field-induced polarization for parameters of $\sqrt{2}q = 1.05$ (a) and $\sqrt{2}q = 0.9$ (b) along the $\langle 110 \rangle$-direction and with an off-axis angle of 1° to the $\langle 110 \rangle$-crystallographic orientation (a2, b2), as shown schematically in the inset figure. Polarization and electric field are normalized by the spontaneous polarization at zero applied load and the coercive electric field, respectively. The size and the shape of the simulated field-induced phase transition behavior depends significantly on both parameters [91].

In addition to the rotation path during ferroelectric switching between orthogonal tetragonal variants, the fitting parameter q also controls the critical field E_0 required for a phase transition and the magnitude of the discontinuity during phase transition, which are both also dependent on the ratio of 90° to 180° energy barriers (Figure 3.7). Conversely, this means that the value of E_0 as well as the shape of the hysteretic phase transition contain important informations about the shape of the Landau energy landscape of the respective ferroelectric phase and should therefore be considered when determining the Landau coefficients. In the presented model, the calculated ratio of critical-to-coercive field (E_0/E_C)

was predicted to be in the range between 1.2 and 6.7, indicating that domain switching always precedes field-induced phase transitions. For T→O phase transitions of typical relaxor-based ferroelectrics, such as ⟨001⟩-oriented PMN-28 %PT [108] or PZN-4.5 %PT [109], E_0/E_C lies between 2.0 and 3.0, and fits perfectly within the previously calculated range supporting the predictions made by the Landau calculations.

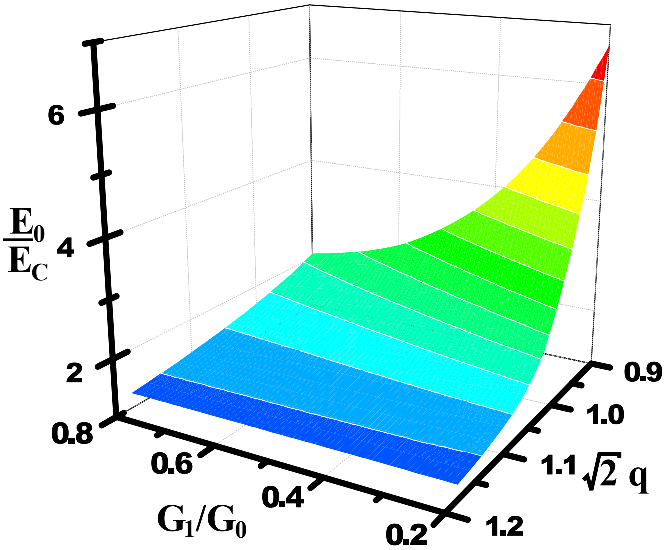

Figure 3.7: The critical phase transition field in relation to the coercive electric field as a function of the fitting parameter q, which defines the path of polarization rotation during a 90° domain switch, and the ratio of energy barriers for 90° and 180° switching (G_1/G_0).

3.2.2 Three Dimensional Landau Model

So far, the simulations were performed for T→O induced phase transitions in an arbitrary two dimensional tetragonal mono-domain single crystal. Extending the study to also cover T→R transitions requires a three dimensional implementation of the thermodynamic Landau model. In this case, the required Landau coefficients were not determined like for the previous two dimensional implementation. Instead, the parameters of an exemplary model system were used, to allow for a comparison of the modeling results to data from experimental measurements. The macroscopic uniaxial polarization in response to the application of an electric load of ferroelectric materials is accessible by large signal measurements using a Sawyer-Tower setup. High-purity mono-domain single crystals are required, to avoid extrinsic effects from the domain structure and interactions with local defects that are both not included in the thermodynamic model. In addition to the availability of the respective single crystals, existing reports on the proper Landau coefficients are desired.

Although single crystalline $Pb(Zn_{1/3}Nb_{2/3})O_3$-$PbTiO_3$ and $Pb(In_{1/2}Nb_{1/2})O_3$-$Pb(Mg_{1/3}Nb_{2/3})O_3$-$PbTiO_3$ are readily available and an interesting candidate for our study, their relaxor nature precludes them from use with classical Landau theory. There have been to date no reports on the Landau parameters of relaxor single crystals, the description of these materials with a phenomenological LGD theory is complicated by the transition from short- and long-range order with increasing $PbTiO_3$-content [110] and compositional heterogeneity [111] as well as random fields [112]. So far, the most promising model material for measurements of field-induced phase transitions is barium titanate, $BaTiO_3$. This perovskite material has been discovered nearly 80 years ago, is one of the best known ferroelectric materials. At room temperature $BaTiO_3$ has a ferroelectric tetragonal (P4mm) symmetry, which importantly, undergoes a phase transition to the ferroelectric orthorhombic phase (Amm2) at about 8 °C. It can be assumed that the necessary fields to induce such a transition at room temperature are low enough. The growth of $BaTiO_3$ single crystals is well documented [113–115] and high quality oriented crystals are commercially available for most common crystal directions, and can be prepared in a mono-domain state. $BaTiO_3$ was extensively studied in the last century, and is often taken as a model system [116]. Numerous investigators have proposed Landau coefficients for $BaTiO_3$ [52–55]. Initially, A. J. Bell and L. E. Cross described the Gibbs free energy of $BaTiO_3$ in their work with a 6th-order expansion in terms of polarization without consideration for the possible temperature- or field-dependence of the higher order dielectric stiffness coefficients [52]. To include temperature effects into this 6th-order representation, all three axial coefficients (α_1, β_{11}, and γ_{111}) are linearly dependent on the temperature, which was found to accurately reproduce many of the structural and ferroelectric properties of bulk single crystal $BaTiO_3$ as well as the phase transition temperatures. However, first principle calculations suggest a more complicated temperature dependence of the different Landau coefficients in a 6th-order than an 8th-order representation [57]. The discovery of the outstanding increase of the cubic to tetragonal transition temperature from 125°C [117, 118] to 600°C [86, 119] in thin film $BaTiO_3$ under large epitaxial compressive strain of about 1.6 %, which can not be predicted with the 6th-order Landau description, necessitated the extension of the free energy function. To capture this observed behavior, the Landau polynomial was expanded to the 8th-order, resulting in temperature-dependence for only the quadratic Landau coefficient α_1 [53].

Table 3.1: Temperature dependent Landau coefficients of $BaTiO_3$

Coefficients	Bell and Cross [52]	Li et al. [53]	Y. Wang et al. [54]	J. Wang et al. [55]	Units
α_1	$3.34 \times (T - 108)$	$4.124 \times (T - 115)$	$3.61 \times (T - 118)$	$5T_s \times \left[\coth\left(\frac{T_s}{T}\right) - \coth\left(\frac{T_s}{115}\right)\right]$	$10^5\ \mathrm{m^2N/C^2}$
β_{11}	$4.69 \times (T - 120)$	-209.7	$0.04 \times (T - 46)$	-1.154	$10^8\ \mathrm{m^6N/C^4}$
β_{12}	3.23	7.974	$0.067 \times (T - 33)$	6.53	$10^8\ \mathrm{m^6N/C^4}$
γ_{111}	$-5.52 \times (T - 170)$	129.4	$-0.032 \times (T - 43)$	-2.106	$10^9\ \mathrm{m^{10}N/C^6}$
γ_{112}	4.47	-1.950	-2.2	4.091	$10^9\ \mathrm{m^{10}N/C^6}$
γ_{123}	4.919	-2.501	5.51	-6.688	$10^9\ \mathrm{m^{10}N/C^6}$
δ_{1111}	0.0	3.863	4.84	7.590	$10^{10}\ \mathrm{m^{14}N/C^8}$
δ_{1112}	0.0	2.529	2.53	-2.193	$10^{10}\ \mathrm{m^{14}N/C^8}$
δ_{1122}	0.0	1.637	2.80	-2.221	$10^{10}\ \mathrm{m^{14}N/C^8}$
δ_{1123}	0.0	1.367	9.35	2.416	$10^{10}\ \mathrm{m^{14}N/C^8}$

More recently, there has been a discussion whether an 8th-order expansion in polarization with a linear temperature dependence of four of the coefficients (α_1, β_{11}, β_{12}, and γ_{111}) is required to fully capture the high temperature paraelectric ferroelectric phase transition behavior in response to an electric field [54]. Later work aimed to improve the representation of the low temperature phase transition, especially under compressive strain, in $BaTiO_3$ thin films by incorporating a stress dependence of various Landau coefficients and a hyperbolic cotangent dependence of α_1 on temperature to consider the influence of quantum effects [55]. The extensive documented Landau parameters and the availability of high quality single crystal samples makes $BaTiO_3$ an ideal model system for our theoretical and experimental study. The various coefficients under mechanical stress-free conditions can be found in Table 3.1.

The resulting three dimensional energy landscapes at room temperature (25 °C) are depicted in Figure 3.8. Each shape represents the angular distribution of the minimal energy along the corresponding direction. The value of the minimal energy is represented by different colors. Dark blue represents low energy values, while red represents areas with a higher energy. This is further supported by the shape, where points further from the origin $P_i = (0,0,0)$ have a higher energy state. It is clear that each Landau energy landscape represents a tetragonal crystal with six energetically equivalent minima along the tetragonal $\langle 100 \rangle_c$ crystallographic axis, eight equivalent maxima along the rhombohedral $\langle 111 \rangle_c$ crystallographic axis, and twelve equivalent minima along the orthorhombic $\langle 110 \rangle_c$ crystallographic axis that have a higher energy state than the tetragonal directions. However, the energetically favored path for 90° polarization rotations between two neighboring tetragonal energy minima in all four curves extends along the orthorhombic orientation.

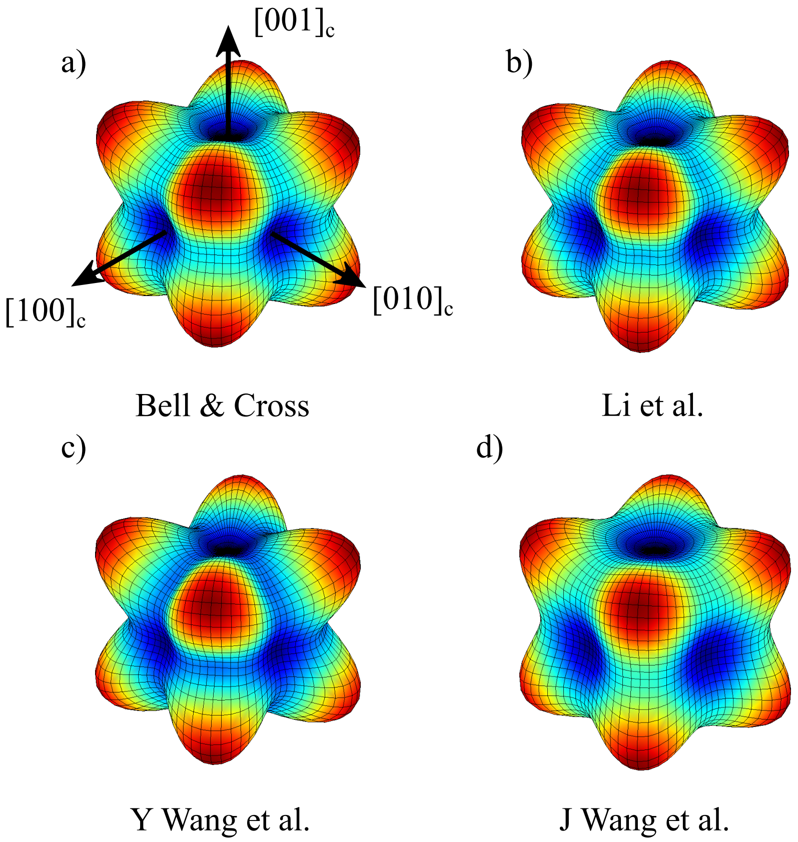

Figure 3.8: Minimal free energy of 4 different three dimensional Landau energy functions at 25°C [52–55] in radial direction. The radius as well as the color indicates the value of the minimal energy in the corresponding direction. Dark blue indicates polarization directions with a low free energy, whereas red indicates directions with a high free energy.

The polarization response of $BaTiO_3$ to electric loading along the polar tetragonal $\langle 100 \rangle_c$ and the nonpolar orthorhombic $\langle 110 \rangle_c$ and the nonpolar rhombohedral $\langle 111 \rangle_c$ direction were calculated for all four different Landau potentials (Table 3.1). Like in the previous case, it was assumed that the crystal is in a mono-domain state, which means that all effects from domain-walls are neglected. The particular evolution Equation 3.3 was solved at increasing electric loading steps in the respective crystallographic direction by an implicit time integration, including Newton iteration. To neglect the influences of the mobility parameter M it was assumed that the system is fully saturated in an equilibrium state at each loading level. Therefore, M was only important for the stability of the numerical solution and has no influence on the final result. The initial condition for the first loading step was set to a tetragonal configuration; such that $\mathbf{P} = P_s \cdot \mathbf{n}_{[001]}$ where $\mathbf{n}_{[001]}$ represents the unit vector along the $[001]_c$ axis; all further loading steps used the solution of the previous loading step as their initial configuration. Although various sets of Landau coefficients have been provided for $BaTiO_3$, the fundamental observations are the same for each. For that reason the following discussion will use the Landau coefficients from J. Wang et al. [55]. The qualitative differences between the potentials became apparent for the temperature dependence of the T→O along the orthorhombic $\langle 110 \rangle_c$ axis and are therefore discussed in Section 3.3.3.

Simulations of $\langle 100 \rangle_c$-Oriented Crystals

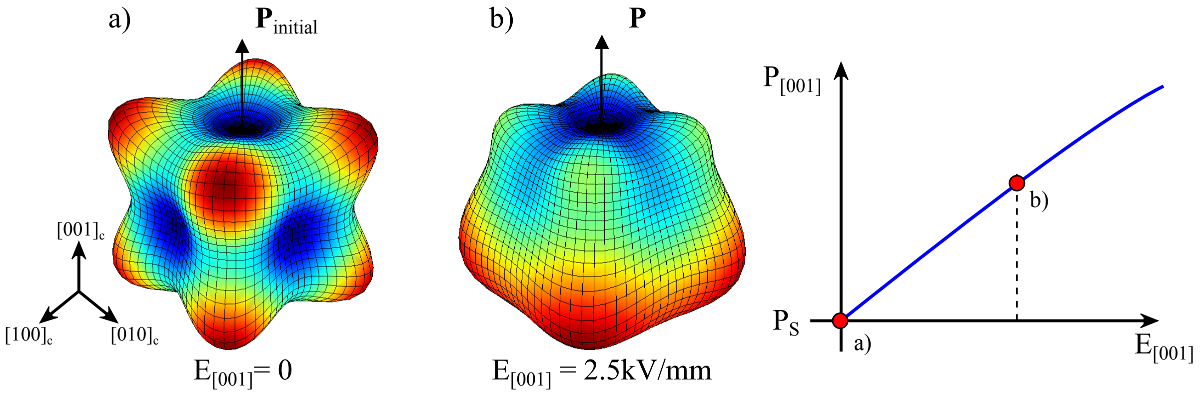

Figure 3.9: Change in the minimal Gibbs free energy [55] at 25°C for an applied electric field along the tetragonal [001]c direction. The radius as well as the color indicates the minimal energy in the corresponding direction. Dark blue indents indicate polarization directions with a low free energy, whereas red bulges indicate directions with a larger free energy. $\mathbf{P}_{initial}$ indicates the initial value of the polarization, respectively the stable polarization direction at zero field, whereas $\mathbf{P}$ represents the polarization direction influenced by the current electric field, which is identical for fields parallel to $\mathbf{P}_{initial}$. On the right hand side, the calculated change in macroscopic polarization along the tetragonal direction is plotted, starting from the value of the spontaneous polarization $\mathbf{P}_S$). Red dots are indicating the corresponding macroscopic response at the respective energy landscapes.

The calculated unipolar P-E-behavior along the tetragonal direction at 25 °C is shown in Figure 3.9, where the calculated P-E curve in field direction and the three dimensional landscapes are shown. At zero-field the energy landscape possesses a $4mm$ symmetry with energetically equivalent global minima along tetragonal directions (Figure 3.9 a). When an electric field is applied parallel to the initial polarization ($\mathbf{P}_{initial} = [0, 0, P_s]$), the orientation of the polarization does not change (Figure 3.9 b). The minimum in the direction of $\mathbf{P}_{initial}$ is energetically stabilized by the external field, whereas all other minima are destabilized. As a result, the macroscopic polarization parallel to the applied field increases nearly linearly. This behavior was expected and corresponds to experimental observations from the unipolar measurements in $BaTiO_3$ that are presented in the next section (Figure 3.14), with the exception of the domain-structure effects that are neglected in the calculations. Because the linear dielectric background of the $BaTiO_3$ is not considered in the model, the slope of the calculated P-E curve is approximately half that measured in experiments.

Simulations of $\langle 110\rangle_c$-Oriented Crystals

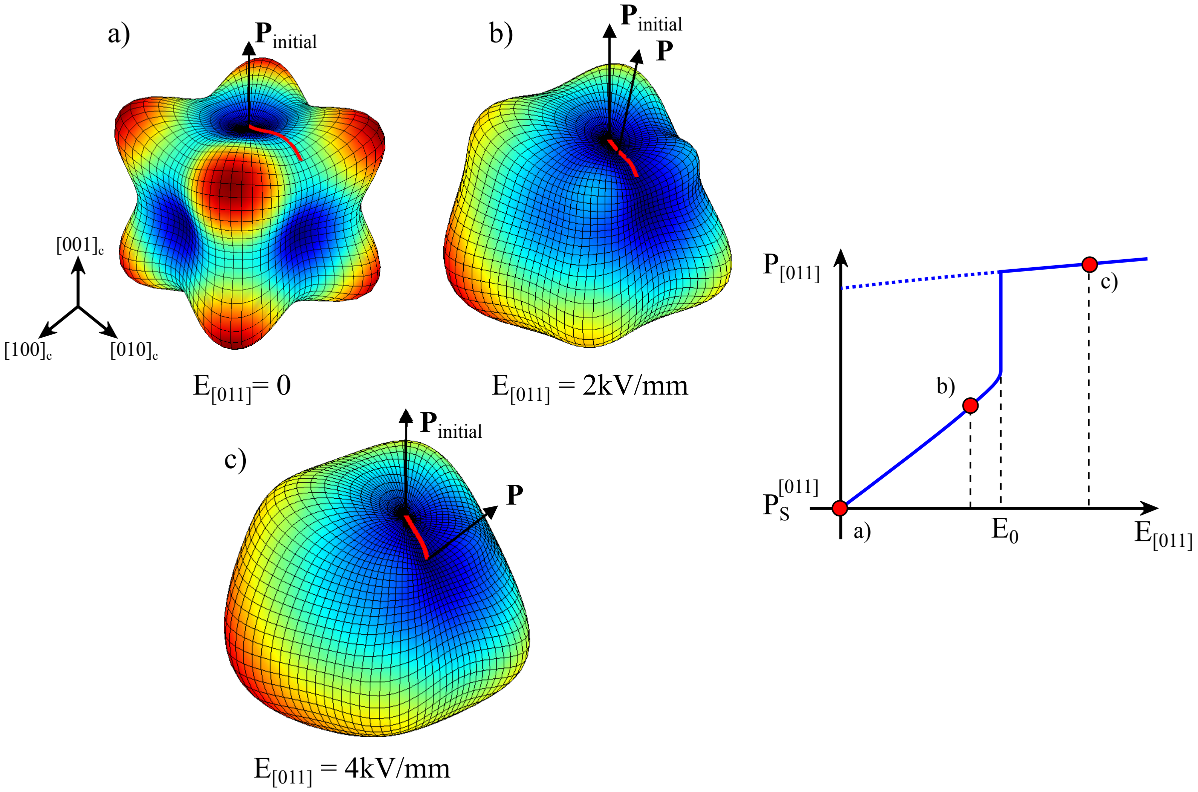

Figure 3.10: Change in the minimal Gibbs free energy [55] at 25°C for an applied electric field along the orthorhombic [011]c direction. On the right hand side, the calculated change in macroscopic polarization is plotted along the orthorhombic direction, starting from the value of the spontaneous polarization $\mathbf{P}_S^{[011]} = \cos(\pi/4\mathbf{P}_S)$. Red dots are indicating the corresponding macroscopic response at the respective energy landscapes.

Figure 3.10 shows the electric field dependent energy landscape for a $\langle 110\rangle_c$ oriented mono-domain crystal at 25 °C together with the correspondingly macroscopic P-E behavior. The initial configuration of the polarization as well as the Gibbs free energy landscape at zero field is the same as in Figure 3.9. Applying an electric field along an orthorhombic direction results in the rotation of the polarization direction away from the tetragonal towards the orthonormal direction parallel to the applied electric field (Figure 3.10 b). For electric fields below the critical value E_0, the polarization increases linearly with the external field. Because of the contributions from the polarization rotation, the slope of the P-E curve below E_0 is more than one order of magnitude larger than for a $\langle 110\rangle_c$-oriented electric field. This makes contributions from the linear dielectric response of the $BaTiO_3$ negligible; the value predicted by the calculation is in a good agreement with the experimental observations. At the same time, the external field lowers the energy of the local minimum along the orthorhombic direction in comparison to the tetragonal minimum of the initial configuration. When the external field reaches the critical value E_0, the Gibbs free energy landscape flattens between the minimum in the tetragonal and in the orthorhombic direction. As a direct consequence, the polarization switches immediately into the orthorhombic direction, which is accompanied by a discontinuous jump in the macroscopic P-E curve. This effect can be interpreted as an electric field-induced T→O phase transition [90]. If the electric load is further increased above E_0, the polarization direction remains constant and the absolute minimum of the Gibbs free energy in the orthorhombic direction is further stabilized. In this field region (Figure 3.10 c), the polarization again increases linearly with the electric field, but with a significantly reduced slope. This is because the polarization increase no longer contains contributions from polarization rotation. Calculations were found to be approximately 32 % lower than measured values, similar to observations in the $\langle 100 \rangle_c$-oriented crystals. Moreover, using the electrostrictive coefficient that was determined from the dielectric measurements along the tetragonal direction to calculate the S-E curve along the orthorhombic direction, leads to a much lower discontinuous change in S.

Unlike in the experimental data, a spontaneous reverse O→T phase transition was not found in the simulations during unloading. This is due to the existence of a local minimum in the orthorhombic direction in the Landau potentials. In the real material defects or thermal fluctuations, which are not included in the model, would lead to a local decay of the orthorhombic phase and initiate the reverse-transition process [120]. This resulted in the prediction of larger hysteresis loops than experimentally observed.

3.2.3 Simulations of $\langle 111 \rangle_c$-Oriented Crystals

The electric field-dependent energy landscapes together with the corresponding macroscopic P-E behavior are shown in Figure 3.11 for $\langle 111 \rangle_c$-oriented $BaTiO_3$. The polarization rotation path during electric loading is indicated by a green line. The additional energetically unfavored local energy minima along the orthorhombic directions and the maxima along the rhombohedral directions are also clearly visible in Figure 3.11 a). If the field is applied along the $\langle 111 \rangle_c$ direction, the polarization orientation is rotated towards the direction of the field (Figure 3.11 b). As long as the electric field lies below E_1 the polarization increases nearly linearly with the field, again with a steep slope by virtue of the contribution from the polarization rotation. When the field gets closer to E_1, a rotation towards one of the neighboring orthorhombic minima is observable. At E_1, the free energy flattens between the tetragonal and the orthorhombic minima, which results in a field-induced T→O phase transition like in the case of an electric load in the orthorhombic direction. The P-E curve indicates this phase transition by a jump. If the field is further increased, the polarization is rotated from the orthorhombic to the rhombohedral minimum. This means that the slope of the polarization still contains contributions from polarization rotation (3.11 c). The difference in slope between the tetragonal and orthorhombic phase in this case is not as large as for electric loads in the orthorhombic direction. Additionally, a further increase in field will begin to induce a local energy minimum along the rhombohedral direction. At E_2 the free energy again flattens, this time between the new rhombohedral and the orthorhombic minimum, accompanied by a second jump in the P-E curve along the $\langle 111 \rangle_c$ direction. This effect can be analogously interpreted as a field-induced O→R phase transition. However, the $\langle 111 \rangle_c$ orientation is unstable, which results in a spontaneous R→O reverse transition at E_2' during unloading. A corresponding reverse O→T transition is not found; the orthorhombic phase remains meta-stable down to the zero-field state.

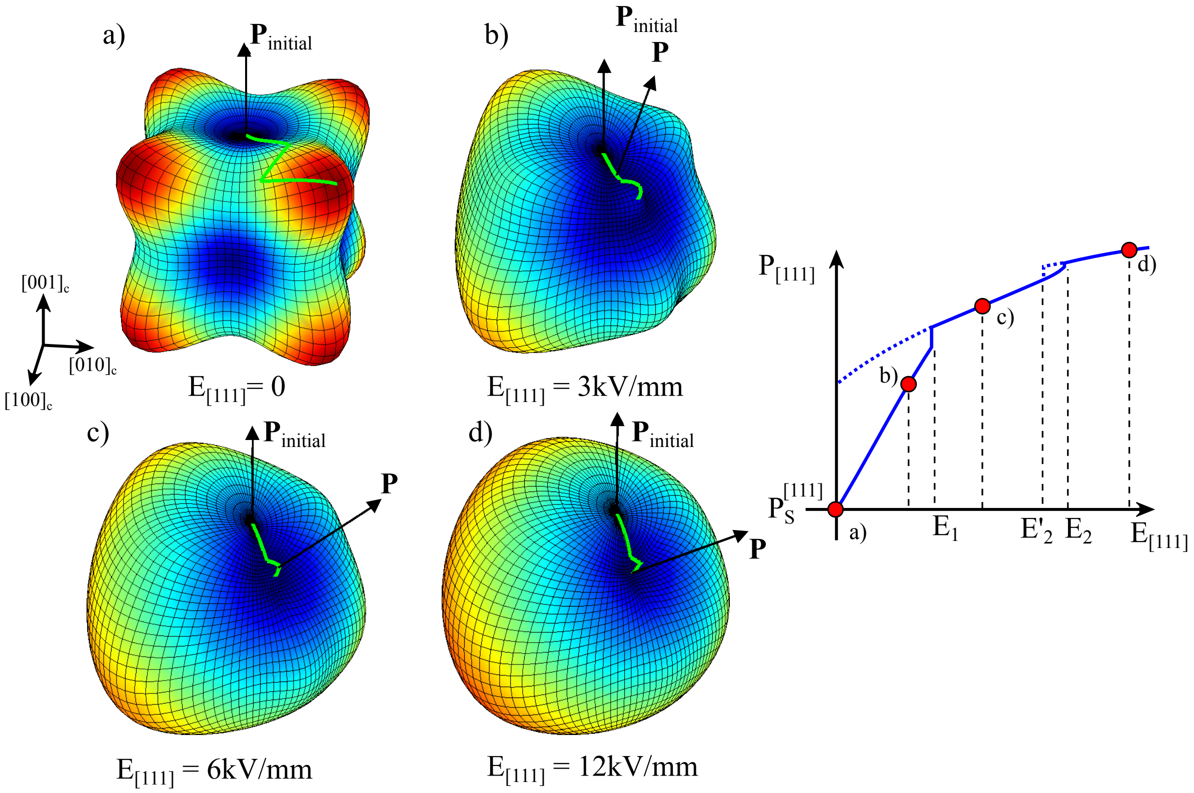

Figure 3.11: Change in the minimal Gibbs free energy [55] at $25\,^{\circ}\mathrm{C}$ for an applied electric field along the rhombohedral [111]c direction. On the right hand side, the calculated change in macroscopic polarization is plotted along the rhombohedral direction, starting from the value of the spontaneous polarization $\mathbf{P}_S^{[111]} = \cos(0.304\pi\mathbf{P}_S)$. Red dots are indicating the corresponding macroscopic responses at the respective energy landscapes.

In the following section the theoretical predictions are compared to macroscopic large electric field behavior of $BaTiO_3$ along the corresponding crystallographic directions. Commercially available single crystals (CrysTec GmbH) with a sample size of 2 mm x 2 mm x 1 mm, oriented so that the 1 mm thickness direction corresponded either to the $[100]_c$, $[110]_c$, or $[111]_c$ crystallographic orientation were obtained. Each 2 mm x 2 mm surface was sputtered with a thin silver electrode. With this configuration it was possible to apply an external electrical field either parallel to the tetragonal polar direction or a non-polar orthorhombic or rhombohedral direction, depending on the respective crystallographic orientation. Although the single crystals were delivered in a single domain state, a poly-domain structure can be generated by the conditions during the sample preparation [121], which may serve as a source of deviation between simulations and measurement. After electroding the single crystal samples, it was no longer possible to verify the particular domain distribution inside the initially mono-domain samples via polarized light microscopy. Additionally, even if the single domain state survived the preparation process, it is unlikely that the crystal relaxes back into a mono-domain state after the first electric loading cycle. However, the comparison of the spontaneous polarization to that along the polar $\langle 110 \rangle_c$ direction revealed that the domain configuration in the remanent state of the $\langle 110 \rangle_c$ oriented samples has a comparable polarization to that of a mono-domain state. Moreover, to ensure that the assumption of a stable mono-domain state does not influence the results, calculations were done using a full phase-field implementation in cooperation with the group from Prof. Chen, described in detail [22]. The simulation results for the macroscopic polarization and strain determined with the phase field model were identical to the simpler LD-based thermodynamic calculations. The polarization and strain were characterized in response to a unipolar and bipolar electric field with a triangular waveform at 1 Hz, which is slow enough to neglect the frequency dependence of the measured curves [122] and therefore justifies the quasi-static assumption that was made for the previous calculation. A Sawyer-Tower arrangement was used to measure the uniaxial polarization in field direction, while the uniaxial strain was measured with a linear variable differential transformer (LVDT) arrangement. Mechanical stresses resulting from the LVDT arrangement were small enough to assume mechanical stress-free boundary conditions for the sample surfaces. The following discussion presents the room temperature experimental results in accordance to the crystallographic orientation of the applied electric field.

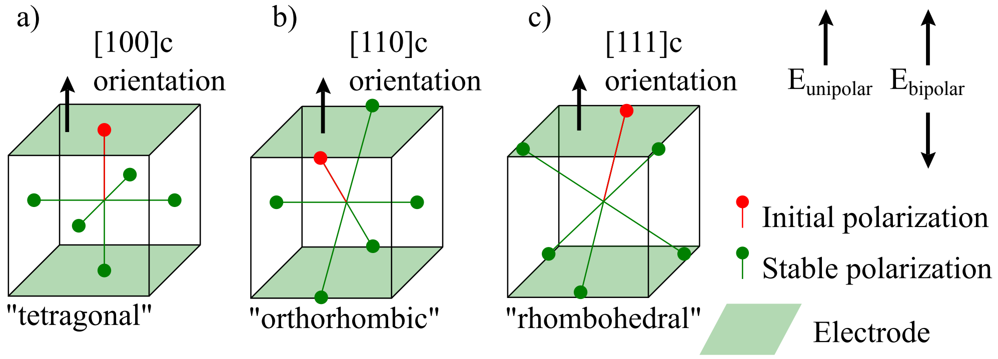

Figure 3.12: [100]c, [110]c, and [111]c oriented $BaTiO_3$ single crystal samples of the different measurement series. Each orientation is characterized by the respective directional vector that is perpendicular to the electrode surface, marked as light green surfaces. Green spheres and lines are indicating the directions of all possible stable polarization directions of the tetragonal phase, whereas the red sphere and line denote the predominant polarization direction before each measurement.

Applying an electric field along the $\langle 100\rangle_c$ oriented crystals resulted in an electric field parallel to a tetragonal polar axis (Figure 3.12 a). Representative room temperature polarization and strain hysteresis loops during bipolar electrical field loading with an amplitude of 3 kV/mm are shown in Figure 3.13. It is apparent that the sample was already poled before measurement; no poling curve could be observed. The *P*-*E* curve corresponds well to the typical single crystal polarization hysteresis curve (compare Figure 2.7 (2), [123]), whereas the *S*-*E* curve slightly deviates from the expected symmetric single crystal butterfly loop [123]. The value of the spontaneous polarization ($P_s = 0.29\,\mathrm{C/m^2}$) and the total switchable strain $S_s = 0.1\,\%$ are nearly identical to experimental findings from literature [123]. The value for the coercive field $E_c = 0.26\,\mathrm{kV/mm}$, however, is significantly ($\sim 30\,\%$) smaller than previously reported [123, 124]. It should be mentioned here that ferroelectric switching in bulk $BaTiO_3$ is a combined process of single domain switching and domain dynamics [125]. Therefore, these deviations can be due to differences in the manufacturing processes, leading to variations in defect types and density inside. Defects can influence the domain structure of single crystals and thereby decrease the coercive field [126].

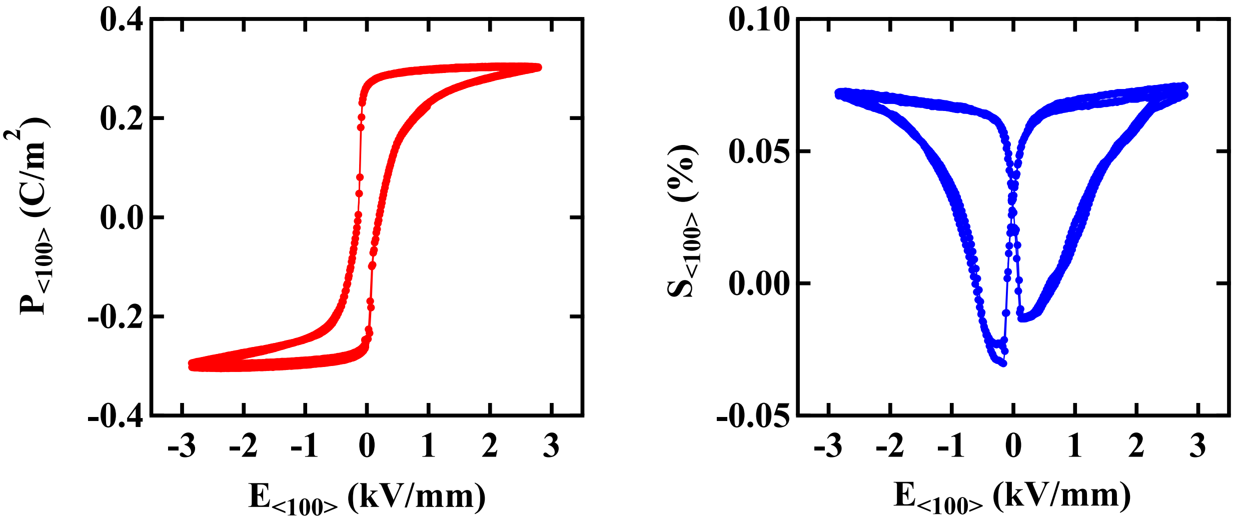

Figure 3.13: Macroscopic bipolar polarization (*P*-*E* curve) and strain (*S*-*E* curve) of a $\langle 100\rangle_c$-oriented $BaTiO_3$ single crystal at room temperature.

The large signal *P*-*E*- and *S*-*E* curves for a unipolar load with an electrical field amplitude of 4.7 kV/mm are shown in Figure 3.14. It is important to note here that it is not possible to determine the absolute polarization from experiments using unipolar loads. Instead, the polarization values represent the change in polarization from the remanent state during electrical loading. Before the measurements were performed, the samples were electrically poled into the direction of the unipolar field. Therefore, no ferroelectric switching and only a linear dielectric behavior of the polarization is expected. However, looking at the *P*-*E* curve in Figure 3.14, one observes an initial steep linear increase of the polarization up to an external load of approximately 0.5 kV/mm. If the field is further increased, the slope of the *P*-*E* curve drastically decreases. At higher fields the slope remains nearly constant and the curve shows the expected linear behavior. The small visible deviations of the *P*-*E* curve from a straight line can be ascribed to the leakage current [127]. This is supported by the *S*-*E* curve, which is not influenced by any leakage current. This curve shows the same trend, but hardly deviates from a linear behavior. The steep initial increase in the polarization as well as in the strain is likely due to the presence of a polydomain configuration in the remanent state, which can be explained by the existence of defects that produce local electrical and mechanical fields large enough to disrupt the mono-domain configuration at low applied field values. This results in a twinned-domain configuration at zero external field [126]. External loads between 0 and 0.5 kV/mm are able to change the domain configuration closer to a single domain configuration. This reorientation results in the steep rise of the polarization compared to the high field slope, where no additional polarization can be produced by a reorientation of the domain structure. This behavior is also visible in the bipolar hysteresis data (Figure 3.13), where the value of the spontaneous polarization P_s that represents the polarization of a single domain state is around 12 % larger than the value of remanent polarization. The maximum unipolar strain for an electric load of 3 kV/mm, a characteristic value for possible actuator applications is relatively small with $S^{max} = 0.07\,\%$.

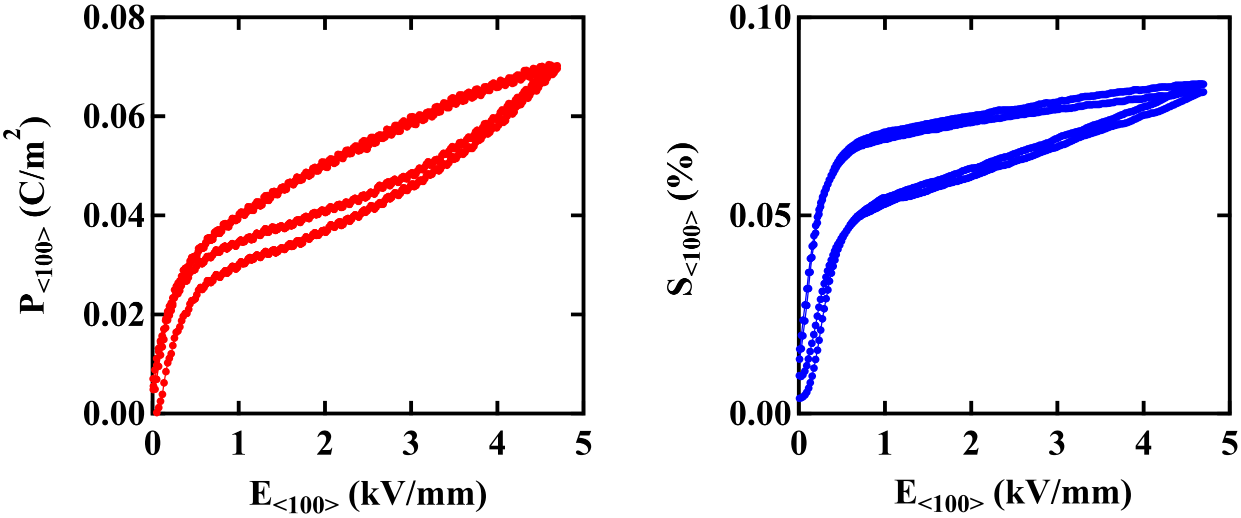

Figure 3.14: Macroscopic unipolar large signal polarization (P-E curve) and strain (S-E curve) of a $\langle 100 \rangle_c$ oriented $BaTiO_3$ single crystal at room temperature.

3.3.2 $\langle 110\rangle_c$ Crystallographic Orientation

When the single crystal is oriented so that the thickness direction corresponds to the $\langle 110\rangle_c$ crystallographic orientation, any voltage applied to the surface electrodes will result in an electric field along a orthorhombic non-polar crystallographic direction (see Figure 3.12 a). Any mechanical stress was avoided during sample preparation and measurement to avoid the formation of a domain structure. A Berlincourt meter was used to determine the direction of the polarization, i.e., the correct polarity for the unipolar electrical load. This experiment represents the situation that was previously described in detail in Section 3.2.1. Using known Landau coefficients (Table 3.1), it was possible to estimate the necessary electric field to be $\sim 2\,{}^{\mathrm{kV}}/_{\mathrm{mm}}$ that is required to induce a tetragonal-to-orthorhombic (T→O) phase transition. Representative unipolar measurements at room temperature can be seen in Figure 3.15. Initially, the sample shows a nearly linear response to an increase in the external electrical load. This was expected as there was no driving force for ferroelectric domain switching in a single domain tetragonal $\langle 110\rangle_c$-oriented single crystal. In contrast to the previous results for $\langle 100\rangle_c$ oriented single crystals, no initial rise of the polarization was observed. This indicates that a domain-structure that might perhaps formed during measurement or sample preparation did not contributed to the observed polarization response.

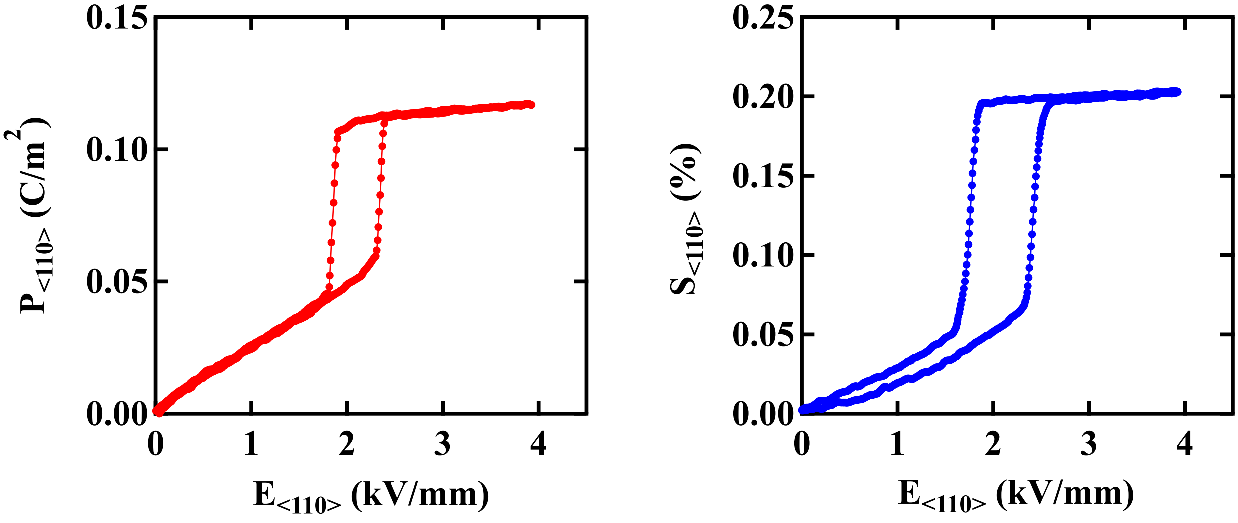

Figure 3.15: Macroscopic unipolar large signal polarization (P-E curve) and strain (S-E curve) of a $\langle 110\rangle_c$ oriented $BaTiO_3$ single crystal at room temperature.

When the field is increased above $2.3\,{}^{\mathrm{kV}}/_{\mathrm{mm}}$, a discontinuous jump in the polarization and strain can be observed. Following this phase jump, the sample again shows an approximately linear response to the increasing field. Here, however, there is a change in the slope; the initial linear response is steeper than after the jump in polarization. When the electrical field is removed, the polarization of the sample linearly decreases until a reverse phase transition back to the original ferroelectric T phase is observed at $1.9\,{}^{\mathrm{kV}}/_{\mathrm{mm}}$, resulting in the development of hysteresis. The shape of the P-E curve closely resembles that from the previous calculations (Figure 3.6), indicating that a phase transition via a polarization rotation mechanism from the initial T to the O direction has taken place during external electric field loading. Moreover, the S-E curve also demonstrates a distinct jump at the same critical field. The change in strain during the phase transition is two times larger than predicted with the tetragonal electrostrictive coefficient $\mathbb{Q}_{33}$ determined from previous measurements, supporting the assumption of a transition into the orthorhombic phase. In addition the maximum unipolar strain that is obtained at $3\,{}^{\mathrm{kV}}/_{\mathrm{mm}}$, $S^{max} = 0.2\,\%$, exceeds the value along the tetragonal orientation by a factor of three and lies in the range of ceramic PZT [14]. It should be noted that each $\langle 110\rangle_c$ oriented crystal could be used for only a maximum number of 10-20 measurement cycles before it disintegrated due to mechanical breakdown. The discontinuous jump in strain was large enough to generate cracking and subsequent sample failure.

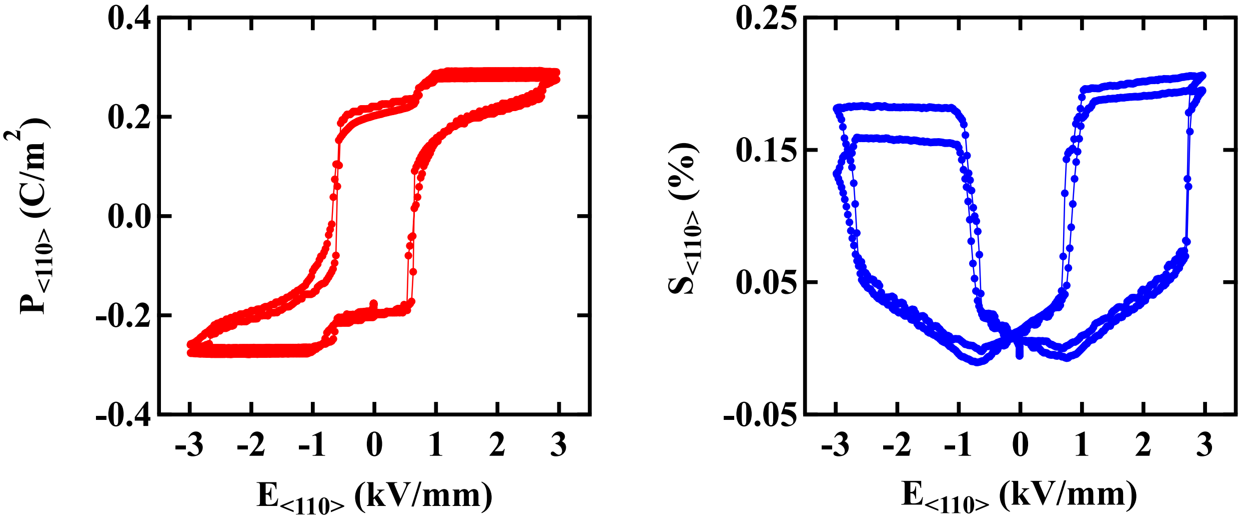

Figure 3.16: Macroscopic bipolar polarization (P-E curve) and strain (S-E curve) of a $\langle 110\rangle_c$-oriented $BaTiO_3$ single crystal at room temperature.

The same field-induced T→O phase transitions are also visible for bipolar loading. Bipolar P-E- and S-E curves at room temperature can be found in Figure 3.16. These graphs are a superposition of a regular bipolar hysteresis loop and two anti-symmetric T→O phase transition hysteresis loops. The coercive field $E_c = 0.63\,\mathrm{kV/mm}$ is in a good agreement with values from literature [123] and therefore significantly larger than along the tetragonal direction. When determining the value for the remanent and the spontaneous polarization, one notices that both values are identical, $P_r = P_s = 0.20\,\mathrm{C/m^2}$, indicating that the remanent state is similar to a mono-domain state. The value of P_s is in excellent agreement with the theoretical prediction based on the crystal orientation and the value along the tetragonal crystallographic direction from previous measurements:

$$P_s^{\langle 110\rangle_c} = \cos(\pi/4)\; P_s^{\langle 100\rangle_c} = \frac{1}{\sqrt{2}}\, 0.29\,\mathrm{C/m^2} \approx 0.205\,\mathrm{C/m^2} \tag{3.11}$$

where $\pi/4$ denotes the angle between the tetragonal and the orthorhombic crystallographic direction. Moreover, it is obvious that the S-E-curve from Figure 3.16 deviates significantly from that along the tetragonal crystallographic direction (Figure 3.13). As expected from the unipolar measurements, the S-E-curve along the orthorhombic direction is dominated by the contributions of the phase transition. This can also be seen in terms of usable strain for both crystal orientations, meaning the difference between the strain at zero and at maximum field ($3\,\mathrm{kV/mm}$). Along the tetragonal direction this value is $S^{\star}_{[100]c} = 0.04\,\%$, which is about five times smaller than along the orthorhombic direction $S^{\star}_{[110]c} = 0.20\,\%$.

In summary, it was possible to experimentally observe the field-induced T→O phase transitions predicted by the thermodynamic-based model (Sec. 3.2.1). The transition is accompanied by a distinct increase in the strain that can not be described by the tetragonal electrostrictive coefficient. Moreover, the critical field at which the phase transition takes place was close to the value predicted by simulations.

Voltage applied to the surface electrodes of samples oriented along the $\langle 111 \rangle_c$ crystal direction generates an electric field that is oriented parallel to a rhombohedral non-polar axis (see Figure 3.12 c). Representative bipolar P-E and S-E hysteresis loops for $\langle 111 \rangle_c$ oriented $BaTiO_3$ crystals at room temperature are shown in Figure 3.17 . Comparing these curves to those along the orthorhombic direction (Figure 3.16), no discontinuous jump or other feature suggesting a field-induced phase transition can be observed. In addition, the P-E and especially the S-E curve are not fully symmetric, as expected from the symmetry of the stable polarization directions (Figure 3.12 c). This lack of symmetry could be due to a significant misalignment of the single crystal samples. This is also supported by the value of the spontaneous polarization $P_s \sim 0.20\,\mathrm{C/m^2}$, which is larger than the theoretical prediction based on the crystal orientation and the value along the tetragonal crystallographic direction from the previous measurement:

$$P_s^{\langle 111 \rangle_c} = \cos(0.304\pi)\ P_s^{\langle 100 \rangle_c} = \frac{1}{\sqrt{3}}\,0.29\,\mathrm{C/m^2} \approx 0.167\,\mathrm{C/m^2} \tag{3.12}$$

where 0.304π denotes the angle between the tetragonal and the rhombohedral crystallographic direction. Unlike for the $\langle 110 \rangle_c$ oriented samples, the remanent polarization $P_r = 0.13\,\mathrm{C/m^2}$ is much smaller compared to the $\langle 111 \rangle_c$ projection of the spontaneous polarization, indicating a poly-domain initial polarization configuration. The coercive field of $E_c = 0.52\,\mathrm{kV/mm}$, however, is comparable to $\langle 110 \rangle_c$ oriented crystals and lies within the boundaries of the values from literature [123, 124].

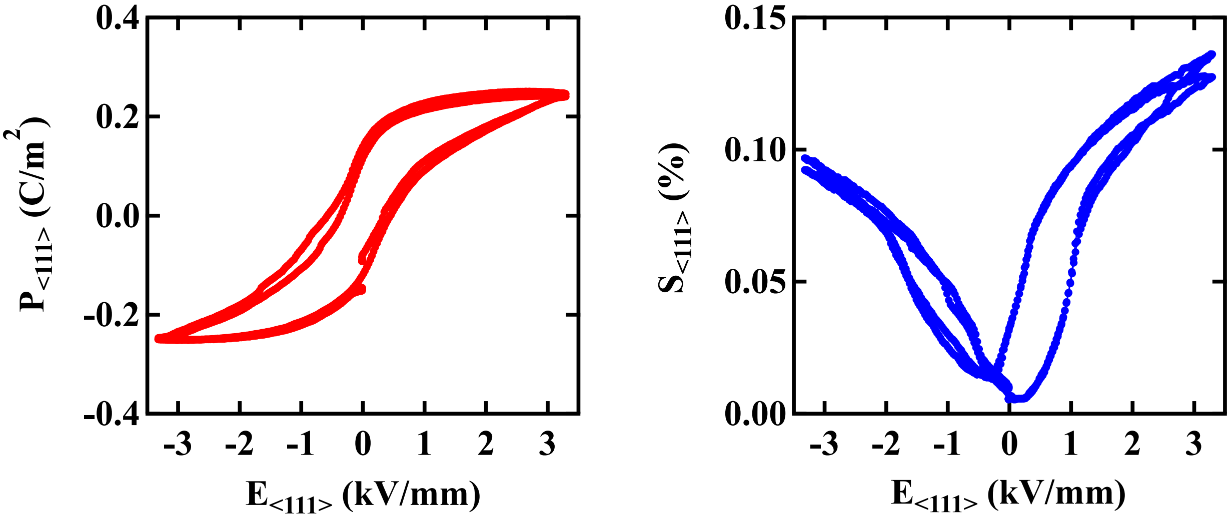

Figure 3.17: Macroscopic bipolar polarization (P-E curve) and strain (S-E curve) of a $\langle 111 \rangle_c$-oriented $BaTiO_3$ single crystal at room temperature.

Unfortunately, the unipolar measurements of $\langle 111 \rangle_c$ oriented $BaTiO_3$ crystal were more difficult than previous crystal cuts. An effect similar to a nonlinear leakage current influenced all polarization measurements and made the obtained data unreliable. The strain measurements, however, were unaffected by these systematic measurement errors. An example of a unipolar S-E curve along the $\langle 111 \rangle_c$ direction is shown in Figure 3.18. It can be seen that the curve, after an initial nearly linear increase, changes its slope around $2.5\,\mathrm{kV/mm}$. Above $2.5\,\mathrm{kV/mm}$ the slope of the curve saturates, resulting in a slope smaller than the initial slope. If the field is decreased, the path of the unloading regime of the S-E curve differs from the initial loading path. This hysteretic behavior is similar to that previously seen in the $\langle 110 \rangle_c$ oriented

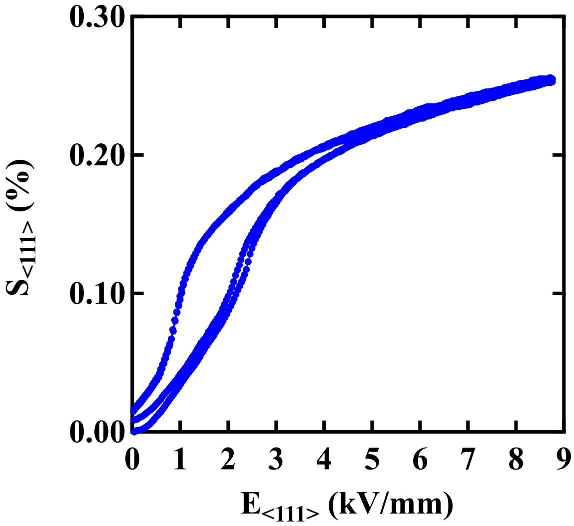

Figure 3.18: Macroscopic unipolar large signal strain (S-E curve) of a $\langle 111\rangle_c$ oriented $BaTiO_3$ single crystal at room temperature.

crystals. The effect seen here, however, has a more diffuse character. Previous dielectric measurements by Wada et al. [84] showed a similar hysteresis around 3.3 kV/mm in the S-E-curve of a $\langle 111\rangle_c$ oriented $BaTiO_3$ single crystal. Estimations from Landau theory predict a T→O field-induced phase transition around 3.5 kV/mm as well as a O→R field-induced phase transition above 9 kV/mm at room temperature. However, the electric breakdown of the samples was found to be below 9 kV/mm, limiting the maximum field amplitude. For electric fields below 9 kV/mm, no feature that could be interpreted as a O→R phase transition was found.

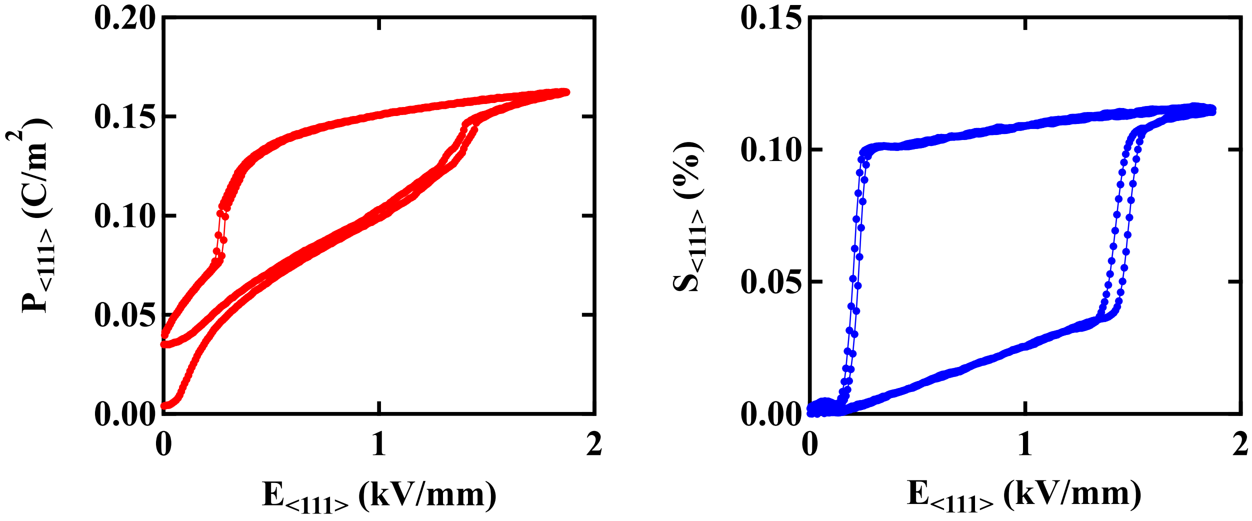

Figure 3.19: Macroscopic unipolar large signal strain (S-E curve) of a $\langle 111\rangle_c$ oriented $BaTiO_3$ single crystal at 15 °C.

One possible solution to reduce the critical transition field is to decrease the temperature of the sample closer to the Curie temperature for the structural T→O phase transition of ∼ 8 °C. For this purpose, the sample and the sample holder were placed in a climate chamber that could be actively cooled. The sample temperature was estimated by measuring the temperature of the dielectric oil in the sample holder with a thermocouple probe before each measurement. Typically, the room temperature in the laboratory was around 25 °C. Using the climate chamber, temperature was reduced to 15 °C without the formation of condensation on the sample or sample holder. Two main differences to the room temperature measurements were immediately apparent: (i) the polarization data was no longer influenced by the nonlinear offset and (ii) the breakdown field of the samples decreased drastically, limiting the maximum load amplitude to 2 kV/mm. The results during unipolar electric load at 15 °C are shown in Figure 3.19. The observed phase transition is very clearly visible in the S-E as well as in the P-E curve. The nearly discontinuous jump in strain at the transition field is likely the cause of the lower breakdown strength. As previously found in $\langle 110\rangle_c$ crystals, large, sudden changes in strain can lead to sample cracking that weaken the structure of the single crystal. Unfortunately these maximum field limitations prohibited the observation of the second phase transition at higher fields.

To investigate the influence of temperature a field-induced phase transition, the macroscopic polarization and strain of $\langle 110\rangle_c$-oriented $BaTiO_3$ single crystals was characterized at various temperatures between 20 °C and 50 °C (Figure 3.20) During measurement the sample was located in a temperature controlled oil bath (± 1°C accuracy). The maximum electric field ($4\,{}^{kV}/_{mm}$) had to be increased at higher temperatures to adequately determine the phase transition field. At temperatures above 50°C, the critical phase transition field exceeded the dielectric strength of the crystals, limiting the experimental temperature range. Electric field-induced T→O phase transitions are observable at each temperature. With increasing sample temperature the critical transition electric fields for both forward and reverse transition processes were found to increase, corresponding to a decrease in the amount of observed hysteresis and a change of the hysteresis shape to a more continuous transition. There is also an apparent decrease in the jump in polarization and strain during the phase transition with increasing temperature, e.g., at 20 °C the polarization increases by $0.6\,{}^{C}/_{m^2}$ during the T→O transition, while at 40 °C this is reduced to $\sim 0.2\,{}^{C}/_{m^2}$. Additionally the initial slope of the polarization, i.e., the dielectric permittivity in the tetragonal phase along the orthorhombic crystallographic direction decreases at higher temperatures. Polarization and strain measurements display similar behavior although at higher temperatures, the strain-electric field loops begin to display an open hysteretic behavior. It is possible that this is partially due to sample degradation during testing at lower temperatures, which was also responsible for the mechanic a breakdown after 10-20 measurement cycles.

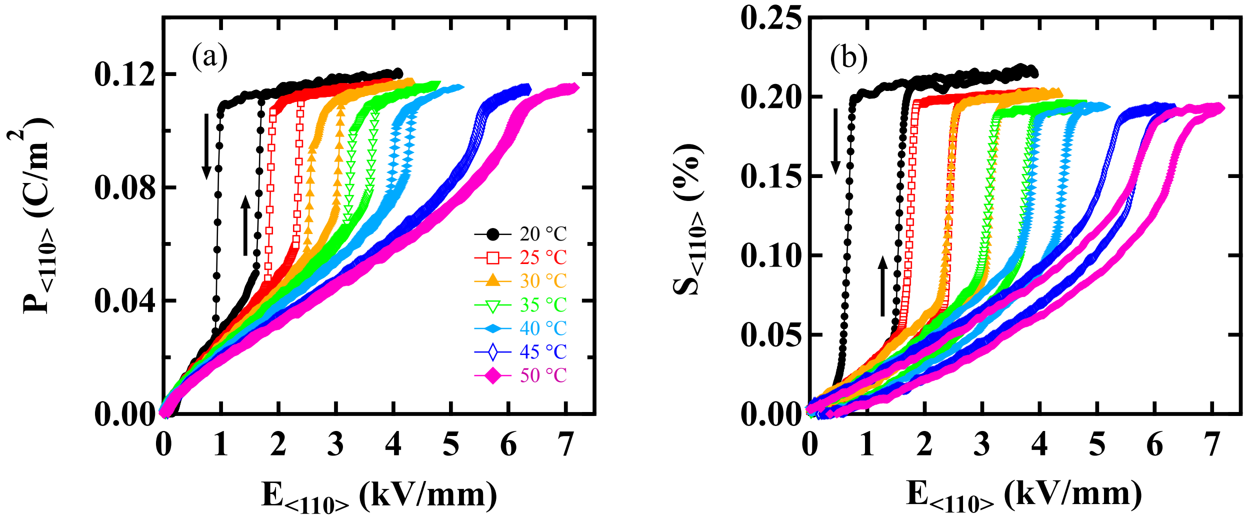

Figure 3.20: Macroscopic polarization (a) and strain (b) of $\langle 110\rangle_c$-oriented $BaTiO_3$ single crystals during electric loading [92].

Experiments showed a distinct, temperature-dependent T→O phase transition along the $\langle 110\rangle_c$ direction at different temperatures and a similar feature along the $\langle 111\rangle_c$ direction at 15 °C, which make these attractive for theoretical investigations. To analyze the temperature-dependent unipolar measurements calculations were performed at the same temperatures. The variation in temperature influences at least one Landau coefficient, and therefore changes the Gibbs free energy landscape. This study allowed us to compare the different potentials in term of their capability to represent the off-axis Gibbs free energy especially regarding field-induced T→O phase transition.

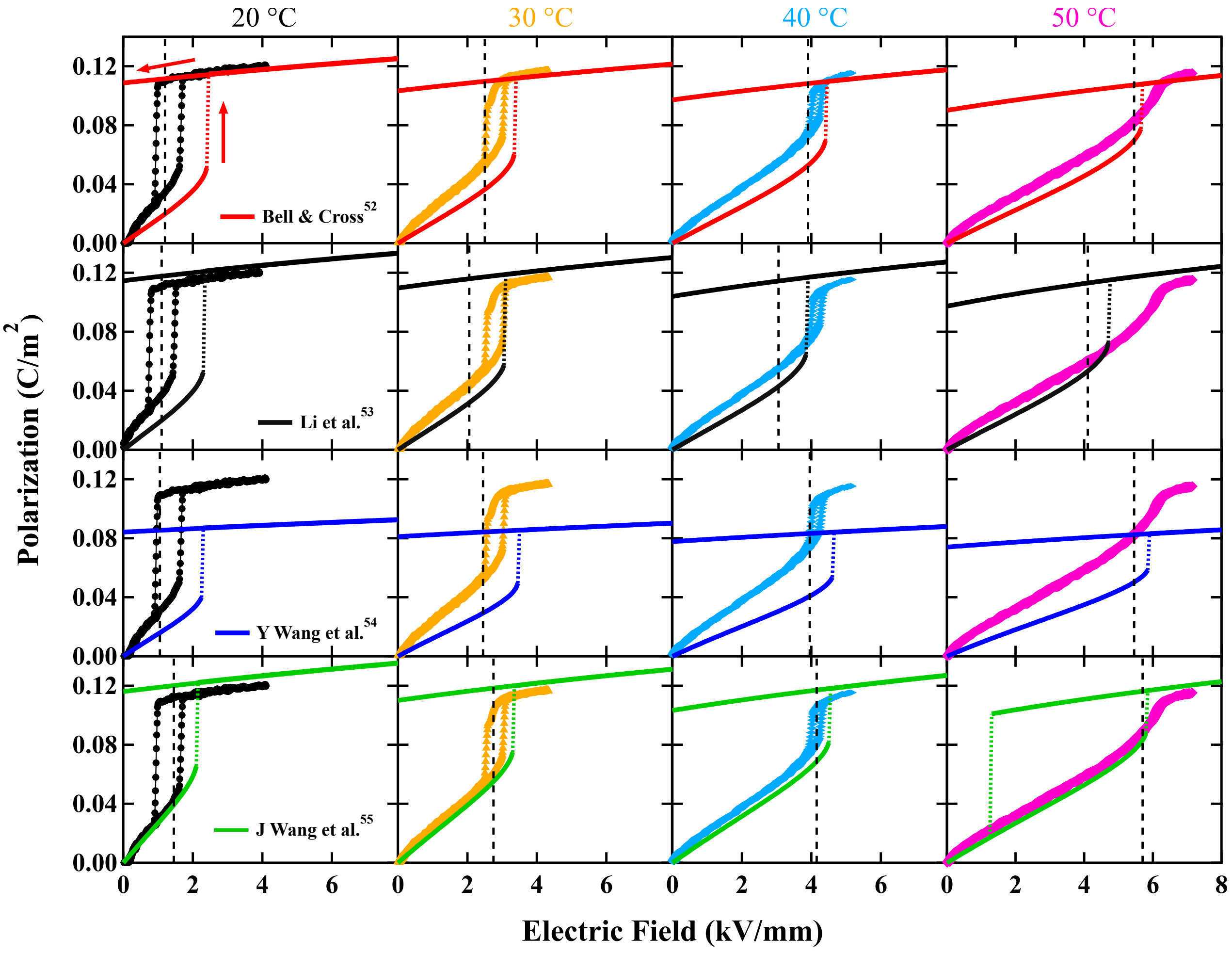

Figure 3.21: Comparison of experimental data and simulations of the macroscopic polarization-electric field behavior at various temperatures [92]. Black dashed lines representing the electric field where the T and O phases have equivalent free energies.

Figure 3.21 shows the calculated polarization responses for the four used Landau potentials at 20 °C, 30 °C, 40 °C, and 50 °C. The evolution equation (Equation 3.3) was solved for each set of Landau coefficients (Table 3.1) and compared to experimental data, with varying degrees of agreement. It is apparent that the principle shape of the T→O transition is predicted by each set of Landau coefficients, although the critical transition field, the jump in polarization during the transition, and the slope of the P-E curve in the T and O regime vary considerably. In contrast to the other three potentials, there is no local minimum in the orthorhombic $\langle 110 \rangle_c$ Landau potential of J. Wang [55] at 50° at zero load, so that a O→T back-transition occurs around 1 $^{\mathrm{kV}}/_{\mathrm{mm}}$. Because no reverse O→T transition was found in the thermodynamic Landau calculations, the equilibrium electric field E_{eq}, which represents the electric field where the T and O phases have equivalent free energies, was also determined and shown in Figure 3.21. If the external orthorhombic electrical load is reduced below E_q, the tetragonal minimum becomes energetically favored, so previously mentioned relaxation processes become possible. From all of the Landau coefficients considered, those of J Wang et al. [55] have the best agreement with the experimental measurements. Typically, the dependence of α_1 on temperature is assumed to follow the Curie-Weiss law, resulting in a linear dependence on temperature [14]. However, following the work of Hayward and Salje [128], J. Wang et al. has included a hyperbolic cotangent dependence of α_1 on temperature to include the influence of quantum effects [55].

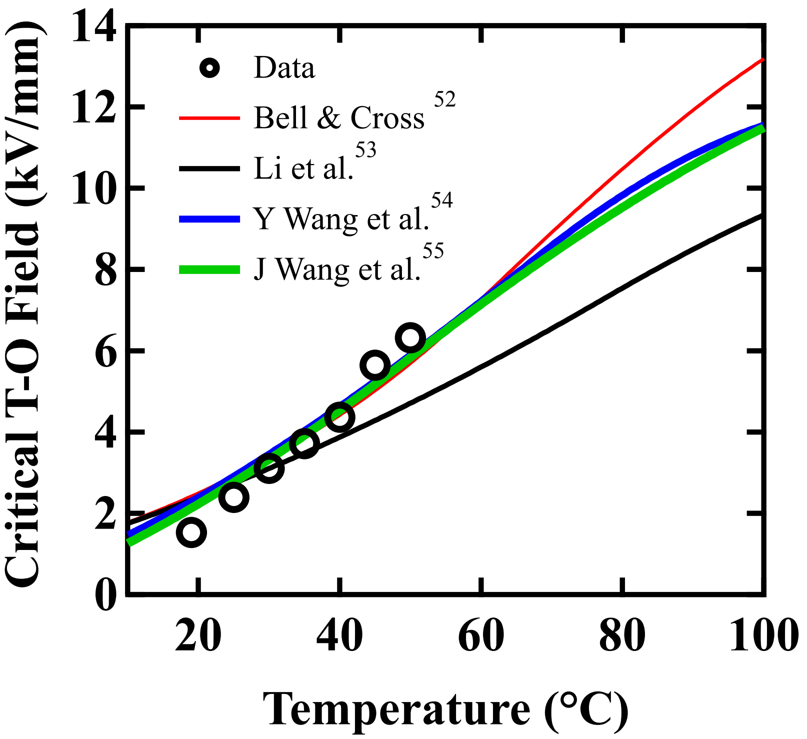

Figure 3.22: Temperature dependence of the critical T→O electric field [92].

For a better comparison of the predictive capabilities of different Landau potentials, the temperature dependence of the critical T→O electric field have been calculated between 10°C and 100°C and plotted together with the results from experimental data in Figure 3.22. It is apparent from Figure 3.22 that the critical T→O electric field displays an approximately linear increase with temperature, which is in good agreement to the predictions from all Landau coefficients except those from Li et al. [53]. These Landau coefficients, only included temperature dependence as a linear effect on the quadratic term α_i. It is likely that a more complex temperature dependency is required to capture the nonlinear behavior.

Additional characteristic values are the slopes of the P-E curves in the tetragonal and orthorhombic phases. An analytical solution for the relative reciprocal susceptibility parallel to the applied electrical field can be directly derived from the second derivative of the free energy function for both the T and O phases:

$$\epsilon_{||} = \frac{1}{\epsilon_0} n_i \cdot \left(\left. \frac{\partial^2 G_{LD}}{\partial P_i \partial P_j} \right|_{\mathbf{P_0}} \right)^{-1} \cdot n_j \tag{3.13}$$

where ϵ_0 is the permittivity of free space and $\mathbf{n}$ is the unit vector along the crystallographic direction of interest. Equation 3.13 can then be solved to find the dependence of the relative permittivity in the $\langle 110 \rangle_c$-direction for the T phase :

$$\epsilon_{||,T} = \frac{1}{\epsilon_0} \cdot \frac{2\alpha_1 + P_T^2 \left(6\beta_{11} + \beta_{12} + (15\gamma_{111} + \gamma_{112}) P_T^2 + (28\delta_{1111} + \delta 1112) P_T^2 \right)}{4 \left(\alpha_1 + 6\beta_{11} P_T^2 + 15\gamma_{111} P_T^4 + 28\delta_{1111} P_T^6 \right) \left(\alpha 1 + \beta_{12} P_T^2 + \gamma_{112} P_T^4 + \delta_{1112} P_T^6 \right)} \tag{3.14}$$

where P_T is the spontaneous polarization of the tetragonal phase and α_i, β_{ij}, γ_{ijk}, and δ_{ijkl} are the Landau coefficients in reduced notation. It should be noted that in this calculation the contributions from linear dielectric background of the $BaTiO_3$ are neglected. The corresponding experimental values were determined from the measured *P*-*E* curves by a linear fit of the low field regime, as shown in Figure 3.23.

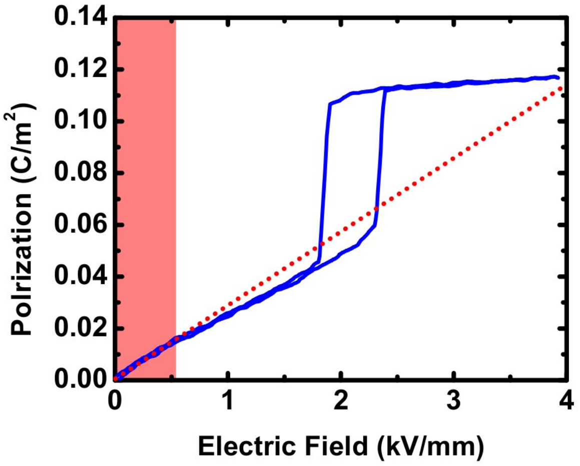

Figure 3.23: Determination of the permittivity of $BaTiO_3$ single crystals in the tetragonal low-field phase along the [011]c direction. The blue line indicates the linear fit of the tetragonal low field part of the experimental *P*-*E* curve, which is highlighted in red.

In Figure 3.24 the measured dielectric susceptibility along the $\langle 110 \rangle_c$ crystallographic orientation is compared to the predictions from different Landau potentials, evaluated at all temperatures between 10°C and 100°C. Decreasing temperature was found to increase the permittivity in the tetragonal phase along the orthorhombic direction. This can be explained by polarization rotation, which is the predominant contribution to the observed susceptibility in this region. A decrease in temperature increases the remanent polarization and therewith the amount of polarization that can be rotated. It is apparent that the coefficients provided by J. Wang et al. [55] show the best results, in terms of representing the exact values as well as the proper temperature dependence of the permittivity in this regime; especially in the strong increase of the susceptibility at lower temperatures. Similar comparisons for the large field susceptibility of the orthorhombic phase of these coefficients could not be performed. Especially at higher temperatures, the applied electric field was not large enough to completely saturate the *P*-*E* loops in the orthorhombic phase.

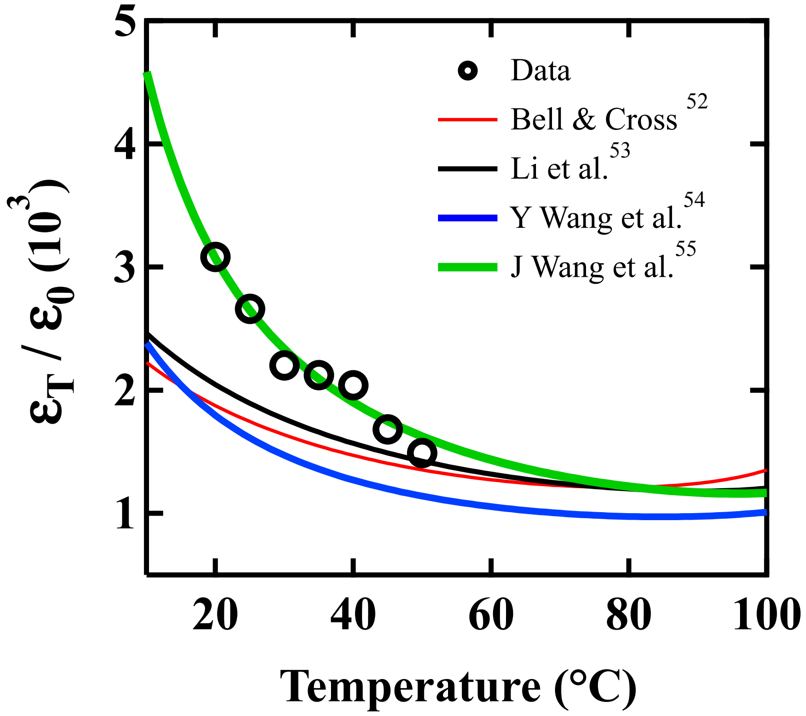

Figure 3.24: Temperature dependence of the susceptibility of the tetragonal phase along the $\langle 110 \rangle_c$ crystallographic orientation [92].

3.4 Conclusions

In this chapter a phenomenological thermodynamic model based on Landau theory is used to predict the dynamic polarization behavior of a ferroelectric single domain under mechanical stress-free boundary conditions in response to an external electrical load that is applied along the polar and nonpolar axis of tetragonal ferroelectric systems. Usually Landau models are used to simulate temperature driven phase transitions or ferroelectric switching including 180° polarization inversion and non-180° polarization rotation. In this model the Gibbs free energy of the system is expanded in terms of the polarization, whereas the expansion (Landau) coefficients can be determined by adjusting to experimental data and symmetry considerations. Interactions to external loads can be included by coupling terms that consequently influence the shape and the symmetry of the free energy distribution. The system is considered stable if the polarization of the system corresponds to a local energy minimum of the energy distribution. The dynamic behavior of a system that is in a non-stable system state, is described by the evolution equation. It was shown that the application of an electric load along a nonpolar $\langle 110\rangle_c$-orthorhombic or $\langle 111\rangle_c$-rhombohedral direction first resulted in a polarization rotation similar to that during 90° polarization rotation. The rotation angle increases with increasing field resulting in an approximately linear increase of the polarization component in field direction. If the applied electric field reaches a critical value the polarization instantly rotates towards the direction of the external field, which is accompanied by a discontinuous jump in the polarization component in field direction. This effect corresponds to the field-induced R→T phase transition via polarization rotation that has been initially proposed by Park and Shrout [75]. Theses field-induced transitions are suspected to be the reason behind the excellent performance of many of today's piezoelectric materials.

In the first part of this chapter, the simplified case of a polarization response of an arbitrary two dimensional material to an electric load along the $\langle 110\rangle_c$-orthorhombic direction is studied. The free energy was represented by a reduced sixth order Landau expansion, where the necessary Landau parameters were chosen according to the tetragonal symmetry of the system, reducing the number of parameters that could be chosen independently. This reduction made it possible to express all non-zero Landau coefficients in terms of the ratio of 90° rotation to 180° inversion energy thresholds G_1/G_0 and a parameter q that characterizes the polarization rotation path, which can be freely chosen out of a empirically determined parameter space. It was shown that field-induced T→O phase transitions can be reproduced by the used thermodynamic Landau model over the whole parameter range. Each tetragonal ferroelectric material that can be described by a reduced sixth order Landau model, exhibits an electric field-induced tetragonal-to-orthorhombic phase transition at a critical electric field E_0 that was always larger than the corresponding coercive field for 180° ferroelectric switching. The respective threshold field E_0 as well as the shape of the T→O phase transition followed directly from the Landau energy landscape and were correlated to the chosen values for G_1/G_0 and q, also providing an alternative explanation approach for the diffuse character of experimentally measured induced phase transitions. Depending on the specific Landau energy landscape, the critical field can reach values up to more than six times the coercive field. Therefore, existing field-induced T→O phase transition might not be possible during experimental measurements if E_0 lies above the value of the electric breakdown field. In addition, the effects of minor crystallographic misorientation were found to have a significant effect on the hysteretic behavior of the phase transition.

In the second part of this chapter, a three dimensional implementation of the previous thermodynamic Landau model was used to study the behavior of a single ferroelectric domain in $BaTiO_3$ for electric loading conditions along the polar $\langle 100\rangle_c$-tetragonal and the nonpolar $\langle 110\rangle_c$-orthorhombic or $\langle 111\rangle_c$-rhombohedral directions. The necessary Landau coefficients of $BaTiO_3$ were taken from literature, where a sixth order representation reported by Bell and Cross [52] and three different eighth order implementations can be found [53–55]. Differences between these values originate from different types of measurement data that was used for the determination and the inclusion of temperature dependence in the respective set of Landau coefficients. At room temperature, the presented Landau model predicted the same fundamental behavior for all four sets of coefficients; only minor differences in the value of the predicted critical field and the slopes of the P-E loops in the different phases were observed. Like in the previous two-dimensional study, electric loads above $2\,{}^{\mathrm{kV}}/_{\mathrm{mm}}$ along the $\langle 110\rangle_c$-orthorhombic direction result in a field-induced T→O phase transitions, for all used sets of coefficients. Along the $\langle 111\rangle_c$-rhombohedral direction, two discontinuous jumps, indicating different induced transitions were observed in the calculated P-E loop in field direction. Considering the respective direction of the polarization these jumps can be identified as an initial T→O transition around $4.5\,{}^{\mathrm{kV}}/_{\mathrm{mm}}$ followed by a second O→R transition around $10\,{}^{\mathrm{kV}}/_{\mathrm{mm}}$ ($17\,{}^{\mathrm{kV}}/_{\mathrm{mm}}$ in case of [54]).

$BaTiO_3$ single crystals are commercially available in different crystal cuts, so large signal measurements along different crystallographic orientations corresponding to the respective calculations could be performed. In accordance to the theoretical prediction discontinuous jumps in the P-E and the S-E loop that were found along the $\langle 110\rangle_c$- and the $\langle 111\rangle_c$-direction indicated T→O phase transitions at similar critical fields to those previously calculated. Unfortunately the electrical breakdown field of the $\langle 111\rangle_c$-oriented crystals was found to be below $10\,{}^{\mathrm{kV}}/_{\mathrm{mm}}$ so that O→R transitions could not be observed in the experiments. Additionally, it was possible to measure the temperature dependence of the T→O phase transition along the $\langle 110\rangle_c$ direction. The two measured temperature dependent characteristic values, i.e., the critical phase transition field and the slope of the P-E loop in the tetragonal regime were compared to the corresponding values determined by the thermodynamic Landau model for all four sets of coefficients. The following important conclusions can be drawn from the comparison of experimental measurements on $BaTiO_3$ crystals and the corresponding simulations:

- Temperature dependence of the Landau coefficients with a higher order than two (β_{ij}, γ_{ijk}, δ_{ijkl}, ...) is not strictly necessary, if the temperature dependence of the first term is chosen correctly.
- The temperature dependence of the quadratic Landau coefficient (α_i) must not be linear, i.e., Curie-Weiss behavior, but can be a nonlinear function;
- When determining or validating a general set of coefficients that should be also accurate for polarization directions between the polar crystallographic axis, field-induced phase transitions should be considered, as they can be found in real materials.

These results have important applications for the prediction of the stable electric field- and stress-dependent phase in ferroelectric thin films and devices, where local electrical and mechanical fields can have a significant impact on device performance.

4 Induced Phase Transitions in Soft Pb(Zr$_{1-x}$Ti$_x$)O$_3$

Ferroelectric lead zirconate titanate, Pb(Zr$_{1-x}$Ti$_x$)O$_3$, is one of the most technologically important piezoelectric materials. It has been widely used in sensor, actuator, and transducer applications because of its outstanding electromechanical properties [14, 129, 130]. Similar to the previously discussed BaTiO$_3$, PZT displays nonlinear ferroelectric and ferroelastic behavior during electrical [131] and mechanical [132, 133] loading, respectively, resulting in the typical hysteretic macroscopic polarization and strain loops. Due to the difficulties in producing single crystal PZT with compositions close to the MPB [134], PZT is exclusively used as a polycrystal. There have been numerous experimental investigations on the nonlinear ferroelastic stress-strain behavior [132, 133, 135–138], on the nonlinear piezoelectric coupling of electrical load and mechanical strain of PZT-based ceramics [14, 139, 140], and on the combined process in a mechanical preloaded piezoelectric actuator [141]. These nonlinear electromechanical properties of PZT were found to be significantly influenced by the composition, dopant type and concentration, and temperature.

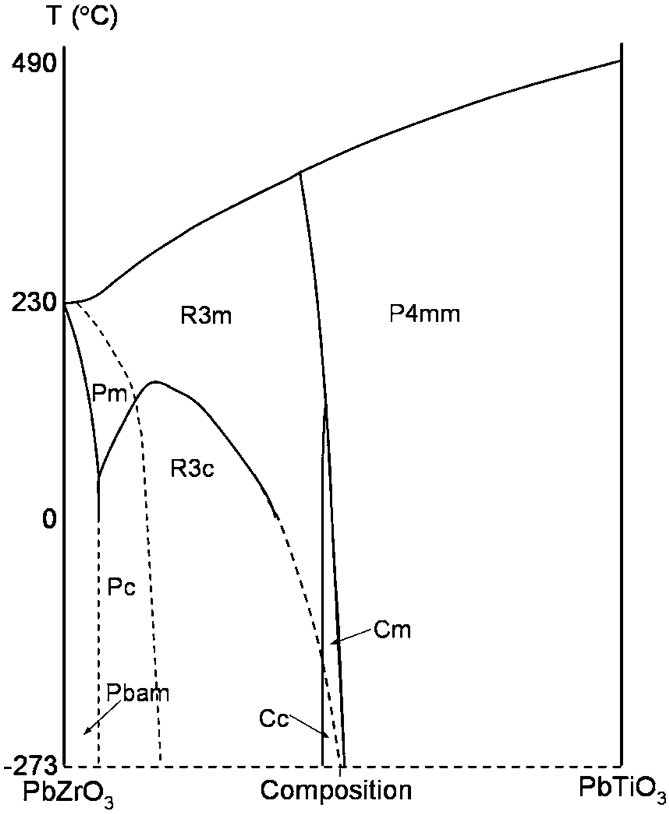

Figure 4.1: Phase diagram of PZT [142].

The stress-strain behavior of hard and soft doped PZT as a function of the PbTiO$_3$ concentrations was presented by Schäufele and Härdtl [136]. Following their work, the minimum coercive stress and maximum remanent strain for both hard and soft doped PZT is found for PbTiO$_3$ concentrations close to the MPB, which separates the ferroelectric rhombohedral and ferroelectric tetragonal phases in the composition-temperature phase diagram, shown in Figure 4.1. This observation is in accordance with earlier investigations that have shown an enhancement in the electrical properties at the MPB [14] that could not be explained by the standard rule of mixtures. Different explanations for this extraordinary behavior at the

MPB have been proposed by various investigators, ranging from the coexistence of the tetragonal and rhombohedral phases [143] to the presence of an additional monoclinic Cm phase [81]. Phenomenological theories have predicted a reduction of domain wall energies for PZT compositions in the vicinity of the MPB [144], which was initially reported by Jin et al., who applied the adaptive state theory of martensites to ferroelectrics. [145, 146]. This energy reduction leads to the formation of nanometer scale domains, called nanopolar regions, which might improve the material properties of these compositions [147, 148]. PZT compositions outside the range of the MPB, either on the tetragonal or the rhombohedral side, show an increase in the coercive stress and a reduction in remanent strain after mechanical loading. These changes increase as the composition moves away from the MPB towards the $PbZrO_3$ or the $PbTiO_3$ side of the phase diagram.

Stress-strain measurements on both hard and soft doped PZT, performed by Cao and Evans [132], have shown that the coercive stress of an acceptor (hard) doped material is larger than that of a donor (soft) doped. Recently, the strong temperature-dependence of the ferroelastic behavior of PZT ceramics in different poling states was investigated by different researchers [137, 138, 149] by characterizing the nonlinear macroscopic constitutive behavior at elevated temperatures. The observed changes in the stress strain behavior with increasing temperature was attributed to a reduction of the spontaneous strain, which leads to a decrease in the energy threshold for ferroelastic switching and obtainable remanent strain. In this context, it is important to mention that the effective modulus of PZT during stress loading is significantly influenced by the anisotropic elastic properties of the perovskite crystal structure [150]. These phenomena also have a significant influence on the fracture behavior of PZT, making them important for the development of various commercial applications that apply electrical, mechanical, and thermal loads to ferroelectric materials. In PZT, most of the material properties depend on the concentration of $PbTiO_3$, e.g., the permittivity [151] and the magnitude of the spontaneous lattice distortion, which is caused by internal stresses appearing during cooling from the paraelectric high temperature phase [152]. Moreover, compositions with different $PbTiO_3$ concentrations show different ferroelectric and ferroelastic responses under electrical and mechanical fields [1]. This behavior is a direct consequence of the different crystallographic phases (Figure 4.1) and lattice distortions that change in the critical energy barrier to switch domains [70, 153]. Additionally, Kungl et al. investigated the nonlinear ferroelectric strain behavior of various PZT compositions at different temperatures that could be explained by the influence of domain switching processes during electric field loading on the piezoelectric effect and confirmed that the ferroelectric-ferroelastic behavior of PZT is both composition and temperature-dependent [154]. However, none of the discussed reports have addressed the influence of external electrical or mechanical loads on the stable phase state in PZT. Following the work by Damjanovic [99], a flattening of the Landau energy landscape for compositions around the MPB results in an increased probability of polarization rotation, which, according to the findings of the previous Chapter 3, reduces the energy thresholds for field-induced phase transitions [90, 91]. It was also noted that field-induced phase transitions can have a significant influence on the macroscopic behavior. According to recent simulations, PZT compositions close to the MPB display an electric field-induced phase transition at electric fields below the dielectric breakdown strength [90]. This is supported by in situ diffraction measurements that showed the existence such induced phase transitions [155]. Despite the previous theoretical and experimental work, the influence of field-induced phase transitions on the macroscopic behavior in polycrystalline PZT is not known. In particular, there has been to date little experimental or theoretical work on the influence of stress or electric field on the phase in PZT.

In this chapter, the mechanical and electrical behavior, in addition to the influence of field-induced phase transitions, in various compositions of soft PZT across the MPB is simulated using a phenomenological thermodynamic analysis. Simulations are contrasted to room temperature data as well as temperature-dependent XRD and ex situ diffraction data. Macroscopic measurements reveal interesting results for rhombohedral compositions close to the MPB that could not be explained by pure ferroelectricity or ferroelasticity. To elucidate the potential contributions from field-induced phase transitions, the phenomenological thermodynamic analysis that was introduced in Chapter 3 was expanded to the polycrystalline nature of the problem. By including electrostriction in the model, it was possible to predict the influence of stress on the stable phase in PZT, allowing for the determination of stress-induced phase transitions. As before, the spontaneous polarization was allowed to evolve in response to an applied load, providing an indirect method of observing the effect of mechanical as well as electrical loading on the stable phase state in polycrystalline PZT. The main results and conclusions of this chapter have been published in Physical Review B [156].

4.1 Measurements of Mechanical and Electrical Load on PZT Ceramics

Recently, the ferroelastic and ferroelectric behavior of Ba and Nb modified PZT solid solution ceramics ($Pb_{0.98}Ba_{0.01}(Zr_{1-x}Ti_x)_{0.98}Nb_{0.02}O_3$) was measured for different $PbTiO_3$-content x of 0.40, 0.47, 0.49, 0.51, 0.53, 0.55 and 0.60. In the following Sections the different compositions are referred to by their $PbTiO_3$-content (mol%), e.g., PZT 40 for $x = 0.40$. The starting powders were produced by using a mixed-oxide route using PbO (Sigma, 99.9 % purity, 211907), TiO_2 (Alfa, 99.8 % purity, 042681), ZrO_2 (TZ-0, Tosoh), Nb_2O_5 (Sigma, 99.9 % purity, 208515) and $BaCO_3$ (Alfa, 99.8 % purity, 014341) as precursors, whereas the powder mixtures were homogenized in isopropyl alcohol (C_3H_7OH) in a planetary mill and calcined twice at 900 °C for 1 h with a heating/cooling rate of 5 °C/min. Each calcination was followed by a milling step. After the final drying and sieving step, the powder mixtures were pressed into pellets and sintered at 1275 °C for 2 h again with a heating/cooling rate of 5 °C/min. The sintered samples were produced by Jurij Koruza and Andreja Benčan from the Jožef Stefan Institute (JSI), Ljubljana, Slovenia, who also performed the X-ray powder diffraction and the XRD analysis that is described in Section 4.1.1. The characterization of the mechanical and electrical behavior presented in this Section were performed by Yohan Seo and Kyle G. Webber from the Technische Universität Darmstadt, Germany.

4.1.1 XRD Analysis

The phase purity of each composition was verified by X-ray powder diffraction that was performed using a PANalytical X'Pert PRO diffractometer (Cu $K\alpha_1/K\alpha_2$ radiation). For the XRD analysis the sintered samples were crushed into powders. The XRD spectra were collected in the 2Θ range from 15° to 80° with a step size of $2.6 \cdot 10^{-4}$ °/s and analyzed by using the JANA2006 software basing on the Rietveld analysis, to determine the lattice parameters of the different PZT compositions [157, 158]. During the analysis of the obtained XRD spectra, the correct zero position was determined by a shift correction refinement. A pseudo-Voigt profile function and Legendre-polynomial background function were used in the refinement of the reflection peaks. The chosen space groups for these refinements were P4mm (SG no 99) and R3m (SG no 160) for the tetragonal and rhombohedral PZT phases, respectively. Six samples of the same composition under identical experimental conditions wee measured to estimate the experimental error of the XRD analysis. After the post-processing that was described above the obtained lattice distortions were compared with each other. For PZT 40 at room temperature a lattice distortion of $7.76 \cdot 10^{-3}$ with a standard deviation of $6.6 \cdot 10^{-5}$ was determined.

The results of the XRD analysis are consistent with the phase predictions from Figure 4.1. At room temperature, the five compositions on the $PbTiO_3$ rich side of the MPB, i.e., PZT 47, 49, 51, 55, and 60, are tetragonal, whereas PZT 40 and 45 was found to be rhombohedral. It is likely that the two compositions close to the MPB, i.e. PZT 45 and 47, also contain a small amount of the tetragonal and rhombohedral phases, respectively [14, 159], but the amount of the minority phases was too small to accurately determine the lattice parameters or volume fraction. Following the results from the XRD analysis, it can be concluded that the MPB of the soft doped PZT material at room temperature is located between PZT 45 and 47, which is closer to the $PbZrO_3$-rich side of the phase diagram than typically found in the undoped PZT system [14]. A similar shift of the MPB concentration was reported for barium doped PZT [160].

The lattice parameter of each composition that was obtained from the XRD analysis, which was used to determine the tetragonal (δ_T) and rhombohedral (δ_R) spontaneous lattice distortion for each composition by using the following two relations:

$$\delta_T = \frac{c}{a} - 1 \tag{4.1}$$

$$\delta_R = \frac{d_{111}}{d_{11\bar{1}}} \tag{4.2}$$

where c and a are the tetragonal lattice parameters and d_{111} and $d_{11\bar{1}}$ are the rhombohedral lattice spacings [161]. The resulting lattice distortions for both phases at room temperature are shown in Figure 4.2 as a function of the $PbTiO_3$-content. It can be seen that the tetragonal lattice distortion of PZT 47, 49, 51, 55, and 60 increases with increasing $PbTiO_3$-content, whereas the lattice distortion for the two rhombohedral composition PZT 40 and 45 seems to be not significantly dependent on the $PbTiO_3$-content. These observations correspond well to previous measurements [14].

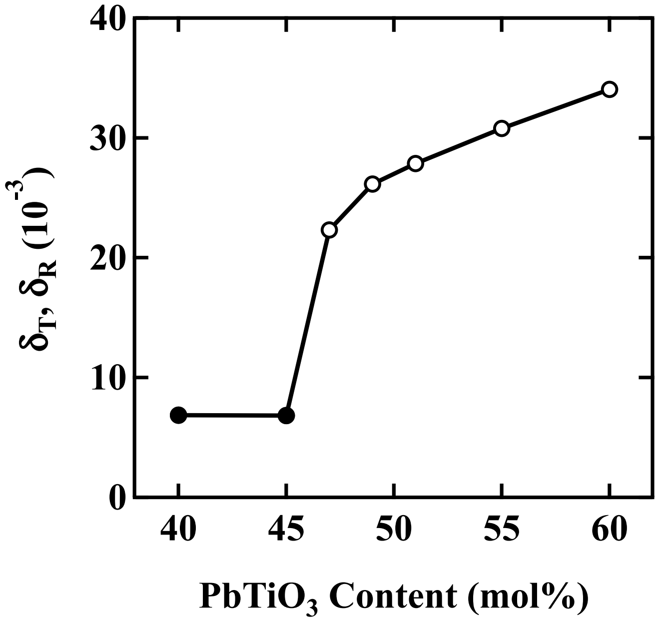

Figure 4.2: Lattice distortion as a function of $PbTiO_3$-content. Open and filled symbols represent the tetragonal and rhombohedral crystal structures, respectively.

4.1.2 Uniaxial compressive stress

The ferroelastic samples from each composition were core drilled from sintered disks with a diameter of 30 mm and a thickness of 7 mm. From this process, cylinders with a diameter of ∼ 5.8 mm and a height of ∼ 6 mm were obtained. The circular surfaces were ground to improve their parallelity. To eliminate potential residual stresses resulting from the drilling process, the samples were annealed at 600 °C for 1 h. To measure the stress-strain behavior, a mechanical compressive stress up to 390 MPa with a rate of 3.7 MPa/s was applied to the specimen by a screw-type load frame. After reaching the maximum compressive stress, the sample was unloaded with the same loading rate. A linear variable differential transformer (LVDT) was used to measure induced uniaxial displacement of the samples parallel to the direction of the applied stress. The experimental error was previously determined as ±2 % for both maximum and remanent strain. In order to ensure reproducibility, at least two ferroelastic measurements were performed for each composition. The experimental setup is described in detail elsewhere [137].

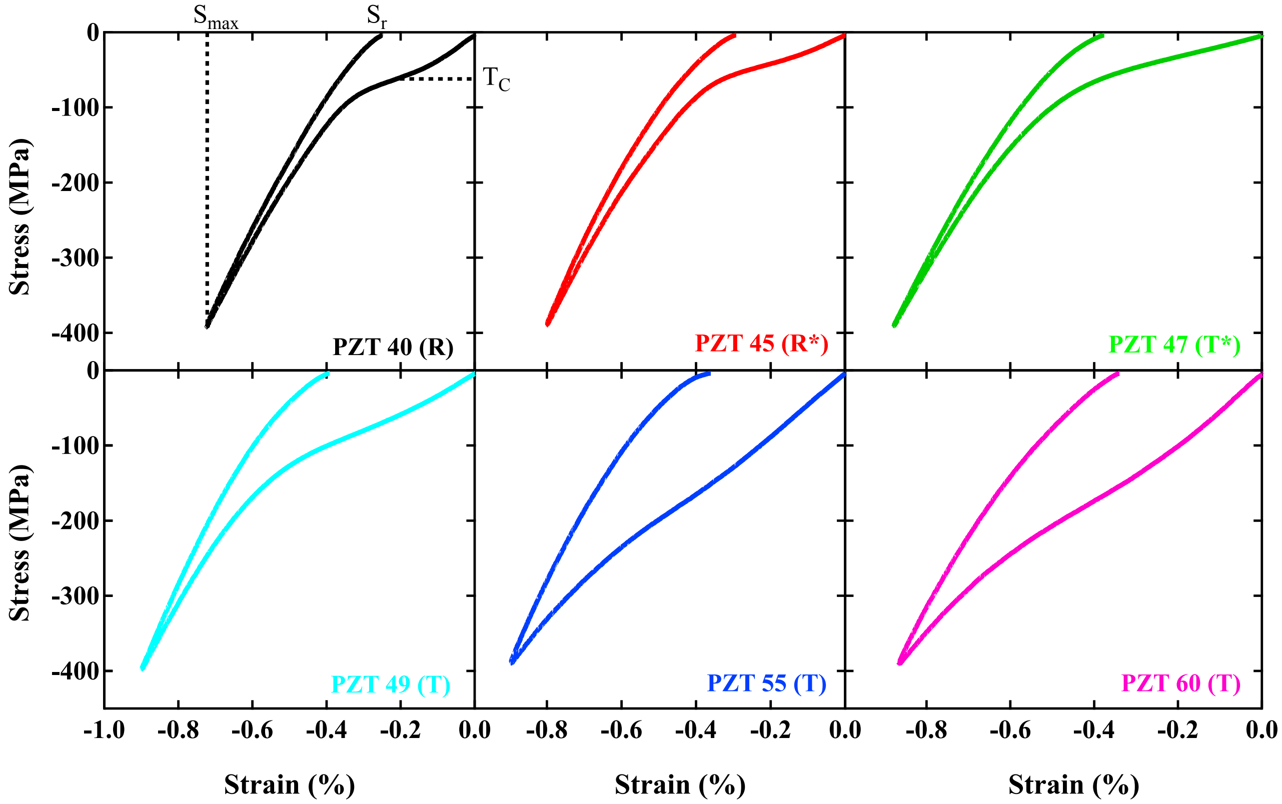

Figure 4.3: Stress-strain curves for PZT with a $PbTiO_3$-content of 40, 45, 47, 49, 55, and 60 % at room temperature. The star denotes that a minority phase was found, although the fraction was too small to accurately determine. The three important characteristic values are exemplary marked in the first plot: T_C indicates the coercive stress at the inflection point on the loading part of the stress-strain curve, S_{max} indicates the maximum compressive strain at the maximum stress, and S_r indicates the remanent strain after the loading cycle [156].

Experimentally measured uniaxial stress-strain curves for representative unpoled tetragonal (PZT 60, 55, 49, and 47) as well as rhombohedral (PZT 45, 40) compositions at room temperature are shown in Figure 4.3. The two compositions close to the MPB (PZT 45 and 47) are marked with a star. As expected for ferroelectric materials (see Section 2.1.4), the stress-strain curves show a distinct non-linear hysteretic behavior, which is caused primarily by irreversible ferroelastic switching. The three characterizing parameters are illustrated for PZT 40. The coercive stress T_C that denotes the inflection point of the loading part of the stress-strain curve, S_{max} indicates the strain at the maximum stress level of 390 MPa, and S_r, which is a measure of non-reversible ferroelastic domain switching processes, indicates the remanent strain after the loading cycle. These characteristic values as well as the shape of the stress-strain hysteresis curve varies as a function of the $PbTiO_3$-content. This is a direct consequence of the crystal phase and lattice distortion, which changes with the $PbTiO_3$-content and defines the ferroelastic characteristic of the ferroelectric sample. It can be seen that the tetragonal compositions display the largest hysteresis, maximum strain S_{max}, and remanent strain S_r. This is expected because of their larger crystal lattice distortion (Figure 4.2). However, in contrast to the evolution of the crystal lattice distortion with increasing $PbTiO_3$-content, S_{max} and S_r do not further increase after crossing the MPB. The initial slope of loading curve decreases for compositions in the vicinity of the MPB. The reason for this flattening is most likely the fact that in compositions around the MPB the coercive stress is minimal, which leads to lower energy thresholds for stress-induced ferroelastic domain wall motion [162] that also influences the macroscopic elastic modulus. Nonlinear plastic processes impact the determination of the material properties at stress levels below the coercive stress T_C as they lead to a softening. However, it can be observed that the slope of the initial unloading curve remains unaffected by composition. The slight flattening of the curve mainly results from back switching of domains that were not completely switched or under the influence of internal fields caused by the ceramic microstructure or defects [163].

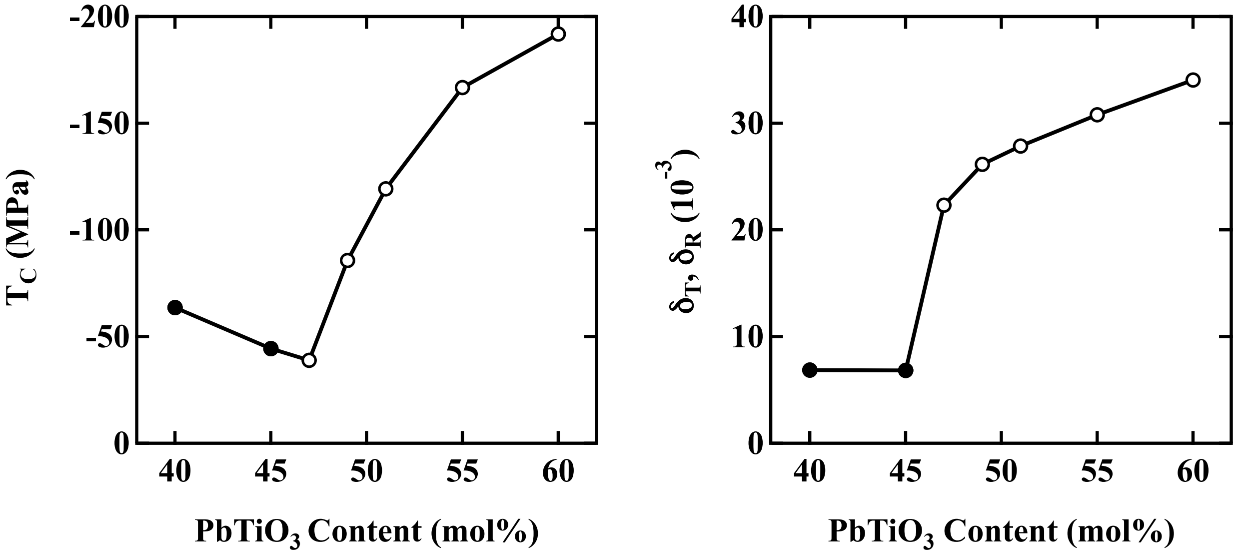

Figure 4.4: Coercive stress and lattice distortion as a function of $PbTiO_3$-content. Open and filled symbols represent tetragonal and rhombohedral crystal structure, respectively [156].

For external mechanical loading above the coercive stress, it is understood that the non-linear hysteretic behavior in PZT ceramics is primarily caused by ferroelastic domain switching [132, 135, 136]. The coercive stress is therefore one of the key properties to characterize the mechanical behavior of ferroelectric materials. In Figure 4.4 the coercive stress T_C of polycrystalline $Pb(Zr_{1-x}Ti_x)O_3$ is presented as a function of the $PbTiO_3$-content. It is apparent that T_C is at a minimum for compositions close to the MPB and increases for the compositions further from the MPB. This increase is far more pronounced in the tetragonal $PbTiO_3$-rich regime, so that tetragonal PZT 60 composition shows the largest coercive stress of all measured compositions. These results are in a good agreement to previous reports [136].

Comparing the trend in T_C for an increasing $PbTiO_3$-content from Figure 4.4 to that of the lattice distortion, shown in Figure 4.2, it can be observed that the increase of the lattice distortion in the tetragonal regime (PZT 47, 49, 51, 55, and 60) is accompanied by an increase in the ferroelastic coercive stress. This correlation can be explained by the increasing amount of internal stresses caused by the larger

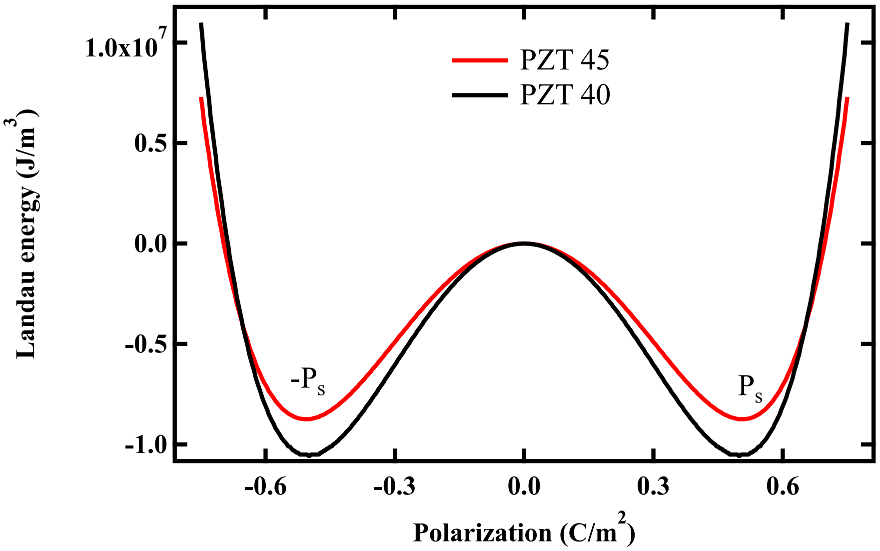

Figure 4.5: Comparison of the Landau energy distribution provided by Haun et al.[56] along the $\langle 111 \rangle_c$ crystallographic axis of rhombohedral PZT 40 and PZT 45.

lattice distortion, which leads to an increase of the energy barrier for ferroelastic domain switching and therefore to a higher coercive stress [164]. The experimental findings are similar to the results of Schäufele and Härdtl [136], who reported that the lowest coercive stress for the compositions near the MPB (PZT 45 and 47). Certainly, it is noticeable that both rhombohedral compositions did not show a similar correlation; PZT 40 exhibited a larger coercive stress than PZT 45, although both composition have a similar lattice distortion. This behavior indicates that the change of the energy threshold for ferroelastic domain reorientation can not be sufficiently explained by the influences from the lattice distortion alone. Additional processes have to occur at the MPB that contribute to the observed mechanical switching behavior, by leading to deeper energy wells in the Landau energy landscape of PZT 40 compared to PZT 45, without changing the position of the minimum, i.e., the value of the spontaneous polarization and polarization. These conclusions are in accordance to the compositional dependent Landau energy landscapes that were provided by Haun et al. [56], which are depicted along the $\langle 111 \rangle_c$ crystallographic axis for PZT 40 and PZT 45. One possible contribution might be the coexistence of tetragonal and rhombohedral phases in the MPB region, proposed by previous investigations [165] to be the reason for improved material properties in this compositional range. XRD results done by the JSI on the PZT compositions from this study indicated that the two compositions closest to the MPB were not single-phase. Unfortunately, the amount of the minor phase, was too small to be accurately measured. Following the recent report from Heitmann and Rossetti, the phase diagram of PZT can be explained by a minimization of the polarization anisotropy energy at the MPB [144]. For their analysis they used a 2-4-6 Landau free energy approach and revealed that a minimization of the polarization anisotropy at the MPB is promoted by an increasingly small energy threshold for polarization reorientation between ferroelectric domains, which could be the origin of the decreased coercive stress observed here. One of the main results from the previous chapter is that lowering the energy threshold increases the probability of the material to undergo induced phase transitions under certain external loading conditions.

For mechanical loads above the saturation level for ferroelastic switching processes, the observed macroscopic remanent strain S_r is the volume average of the spontaneous strain S^0_{ij} of each crystallite in the direction of the applied field [166]. The spontaneous strain of a ferroelectric single crystal is related to its switching strain S_s, which is defined as the achievable strain from each switched domain volume element:

$$S_{ij}^{0} = (3\delta_{3i}\delta_{3j} - \delta_{ij})\left(\frac{S_s}{S_s + 3}\right) \tag{4.3}$$

were δ_{ij} denotes the Kronecker delta. In the case of a single domain crystallite the switching strain is equivalent to the spontaneous lattice distortion, such that $\delta_T = S_s^T$ and $\delta_R = S_s^R$. Following from Equation 4.3, the spontaneous strain can be assumed to be directly proportional to the switching strain, when $S_s \ll 3$, which is typically the case. It is therefore evident that the lattice distortion has to be proportional to the saturated remanent strain, provided that ferroelastic switching is the only irreversible mechanism during mechanical loading that contributes to remanent strain.

If ferroelasticity is the only source of remanent strain or non-reversible process during mechanical loading in a ferroelectric polycrystal, it is possible to predict the theoretical maximum remanent strain-to-switching strain ratio as a function of crystal phase. This was done by previous researchers for the rhombohedral and the tetragonal phases during electrical and mechanical loading [167, 168]. They reported that the maximum S_r/S_s ratio during compressive mechanical loading of polycrystalline samples with initially equally distributed random crystallite orientations was -0.269 and -0.285 for the tetragonal and rhombohedral phases, respectively. These predictions were made under the following assumptions: (i) interactions between the single crystalline grains are weak enough to be neglected, (ii) each crystallite has to remain within its initial crystallographic phase meaning that phase transitions are not allowed, (iii) all grains must have the same lattice distortion and retain it throughout loading, (iv) no domain or domain wall clamping effects; each grain is allowed to ferroelastically switch its polarization direction towards an energetically favored direction if the energy difference lies above a specific threshold value that is the same for all grains, and (v) the external mechanical load is large enough to induce all possible ferroelastic switching processes. The larger rhombohedral value -0.285 relative to the tetragonal -0.269 results from the larger number of possible stable polarization directions, allowing a better overall alignment with the applied mechanical stress.

In Figure 4.6, the maximum theoretical S_s/S_r ratios for the tetragonal and the rhombohedral phase are indicated by dotted blue and dashed black horizontal lines. In reality, lower values are expected because the fracture strength of the samples limits the maximum uniaxial stress that can be applied. In addition, inhomogeneities such as grain boundaries, crystal defects, or internal stresses are able to clamp domain walls and increase the local coercive stress [169, 170]. Interactions between the different grains can be another limiting factor that can lead to domain clamping or backswitching. These effects result in a remanent strain lower than the theoretical ideal during meachanical loading, with an achievable remanent strain that depends on the maximum applied stress. All contributions to the observable macroscopic stress-strain behavior are typically classified into two categories: intrinsic effects that are described by the elastic compliance and extrinsic effects , e.g., ferroelasticity [171]. The maximal extrinsic strain contribution from ferroelasticity is determined by the number of domains that can be switched by the external load as well as the achievable strain from each switched domain volume element, the so called switching strain S_s. The results for S_r/S_s as a function of the $PbTiO_3$-content are shown in Figure 4.6. To reveal contributions from additional non-reversible mechanisms, the measured value of S_r was normalized by the corresponding value of the spontaneous strain S_s of the composition. Clearly, the presented results deviate considerably from the theoretical maxima. All purely tetragonal compositions displayed S_r/S_s ratios below the theoretical maximum with an apparent linear decrease with increasing tetragonality and $PbTiO_3$-content. This linear decrease in S_r/S_s might be due to a reduction in the number of domains that could be ferroelastically reoriented with increasing $PbTiO_3$-content, i.e. increasing T_C, by the maximum applied stress of $-390\,\text{MPa}$.

In tetragonal compositions, the increase in the lattice distortion corresponds to an increase in the ferroelastic coercive stress. In the vicinity of the MPB the maximum stress T_{max} was approximately 8 times

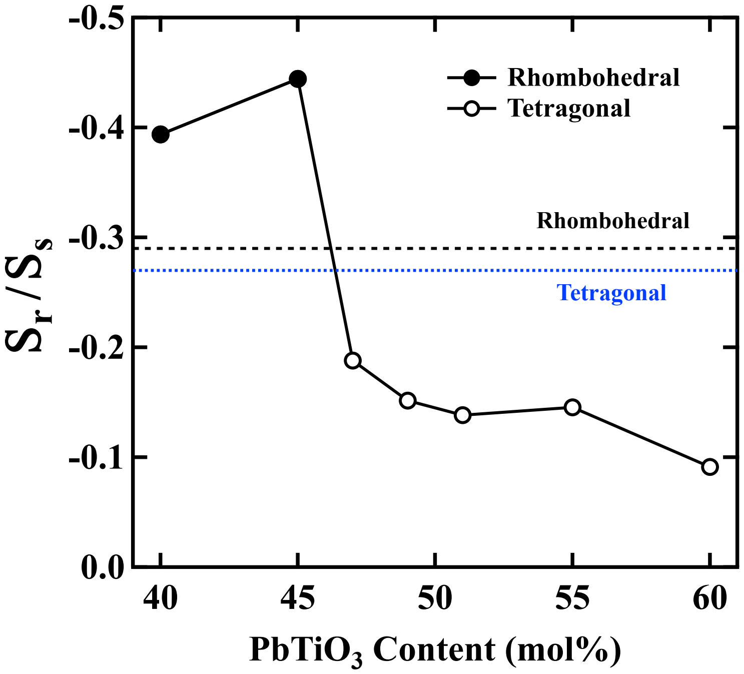

Figure 4.6: Macroscopic remanent strain S_r normalized by the microscopic switching strain S_s as a function of $PbTiO_3$-content for mechanical loading. Open and filled symbols represent tetragonal and rhombohedral crystal structure respectively. The dotted blue and dashed black horizontal lines indicate the maximum theoretical S_s/S_r value for the tetragonal and the rhombohedral phase that can be reached by only ferroelastic domain switching. Data points indicate the average measured value for each composition, whereas the experimental error was estimated to be ±3% [156].

larger than T_c, whereas in PZT 60 the maximum stress was only two times larger. It is likely that a saturated remanent state was not completely achieved in high $PbTiO_3$-content compositions, which was a result of the large T_C. It is expected that the MPB compositions were in an exhausted saturated state relative to the PZT 60 composition. Previous ex situ XRD measurements of MPB PZT specimens mechanically compressed to -385 MPa have revealed that mechanical loading at elevated temperatures does not significantly strengthen the domain texture relative to lower temperatures, indicating that additional domains are not ferroelastically reoriented with a decreased coercive stress at the MPB [137].

Remarkably, the values of S_r/S_s of both rhombohedral compositions lie significantly above the theoretical maximum, well above the measurement uncertainty, which was estimated to be ±3 % from the XRD and ferroelastic measurements. PZT 45, which was shown by XRD to be predominantly rhombohedral, displays a S_r/S_s ratio 50 % larger than the theoretical value. A reduction of the $PbTiO_3$-content was accompanied by a decrease in S_r/S_s for PZT 40, although the observed values were still found to be significantly larger than the theoretically predicted maximum.

4.1.3 Unipolar electrical load

Electric measurements were performed on samples cut from the ferroelastic samples. An electric potential was applied to the parallel electroded surfaces of the samples that resulted in an electric field up to a maximum of 6 kV/mm. The uniaxial displacement parallel to the direction of the electric field was measured with a linear variable differential transformer (LVDT). In order to ensure reproducibility, at least two ferroelastic measurements were performed for each composition.

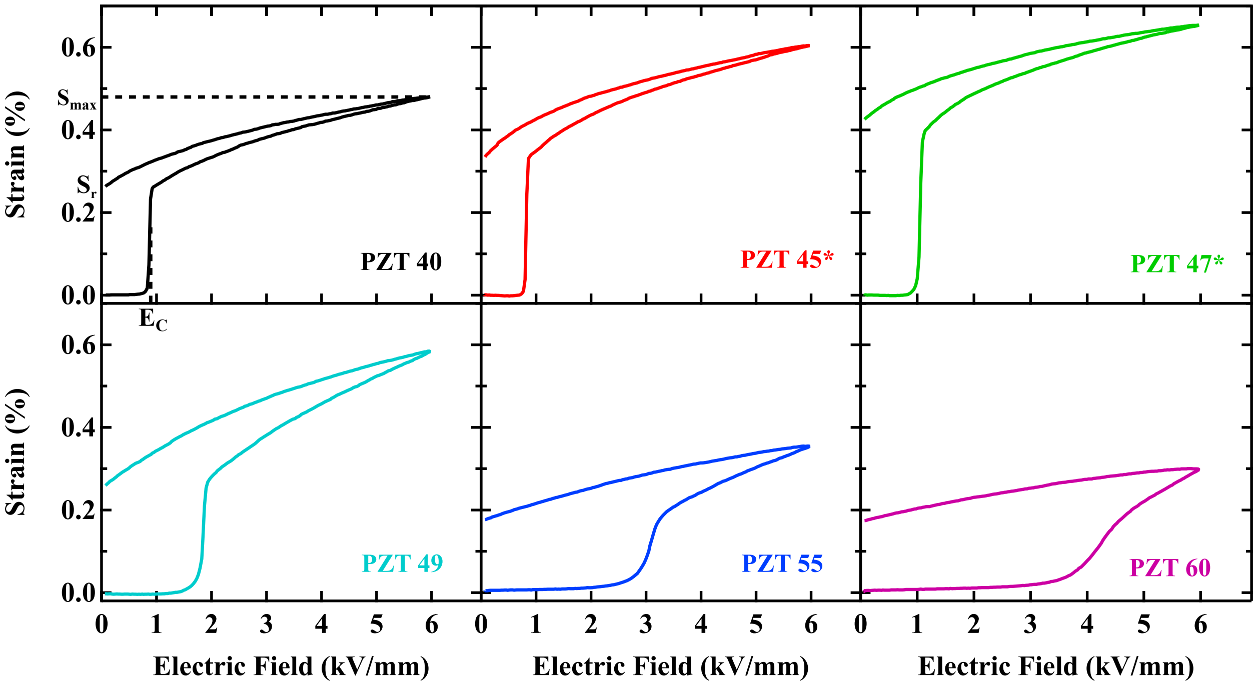

Figure 4.7: Electric field-strain curves for PZT with a $PbTiO_3$-content of 40, 45, 47, 49, 55, and 60 mol% at room temperature.

The measured strain-electric field curves for representative unpoled tetragonal (PZT 60, 55, 49, and 47) as well as rhombohedral (PZT 45, 40) compositions at room temperature are displayed in Figure 4.7. The two compositions in the vicinity of the MPB (PZT 45, 47) contain a small percentage of another phase, which is indicated by a star. All samples showed a distinct non-linear hysteretic behavior, indicating irreversible domain switching processes that were induced by the applied electrical load. Similar to the mechanical case it is possible to define the three important characterizing values of the hysteresis curves: the coercive field E_C that denotes the inflection point of the loading part of the strain-electric field curve, the maximum strain at the maximum field strength S_{max}, and S_r, which is a measure of the non-reversible ferroelestic domain switching processes, indicating the remanent strain after the loading cycle. These three values are illustrated in the first plot in the upper left corner of Figure 4.7. Similarly to the results from the stress-strain measurements, theses characteristic values as well as the shape of the stress-strain hysteresis curve vary with $PbTiO_3$-content. The largest value of the maximum strain S_{max} as well the remanent strain S_r are reached in predominantly tetragonal PZT 47 close to the MPB. Both values decrease with compositional distance from the MPB on the $PbTiO_3$ and $PbZrO_3$ rich sides. This corresponds well to numerous publications that report a significant increase of the electromechanical coupling mechanisms at the MPB [14, 24, 172]. It is apparent from the S-E hysteresis loops (Figure 4.7) that the coercive field increases drastically with an increasing $PbTiO_3$-content for the tetragonal compositions. Similarly to the mechanical case, the maximum applied electric field of $6\,{}^{kV}/_{mm}$ was not large enough to saturate the non-reversible polarization switching processes, particularly for PZT 55 and 60. It is likely that not all polarization domains were aligned by the applied electric field in these samples. Unfortunately, the electrical breakdown strength of polycrystalline PZT prohibited the application of larger fields; electrical measurements performed with $7\,{}^{kV}/_{mm}$ resulted in electrical breakdown. This provides an explanation for the decrease of S_r and S_{max} for an increasing $PbTiO_3$-content that contradicts the increasing trend in the lattice distortion (Figure 4.2).

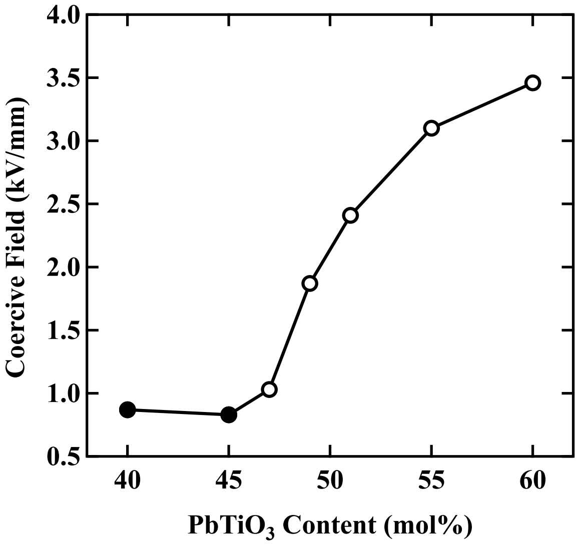

Figure 4.8: Coercive field as a function of $PbTiO_3$-content. Open and filled symbols represent tetragonal and rhombohedral crystal structure, respectively.

A closer look at the dependence of the $PbTiO_3$-content on the coercive field E_c (Figure 4.8) reveals that E_c is nearly constant for the rhombohedral compositions and increases significantly for an increasing $PbTiO_3$-content in the tetragonal compositions, which is in a good agreement with previous reports [173]. It can be seen that the coercive field similar to the coercive stress, is at a minimum for a $PbTiO_3$-content of 45 % close to the MPB. E_c significantly increases with an increasing $PbTiO_3$-content, especially above 47 %. E_c also increases for a lower $PbTiO_3$-content, but with a significantly lower slope. This supports the proposal of Heitmann and Rossetti of a decrease in the energy threshold for polarization reorientation between ferroelectric domains at the MPB that was mentioned in the previous Section [144]. As discussed in Chapter 3, this decrease in switching energy threshold increases the probability of the material to undergo induced phase transitions under certain external loading conditions.

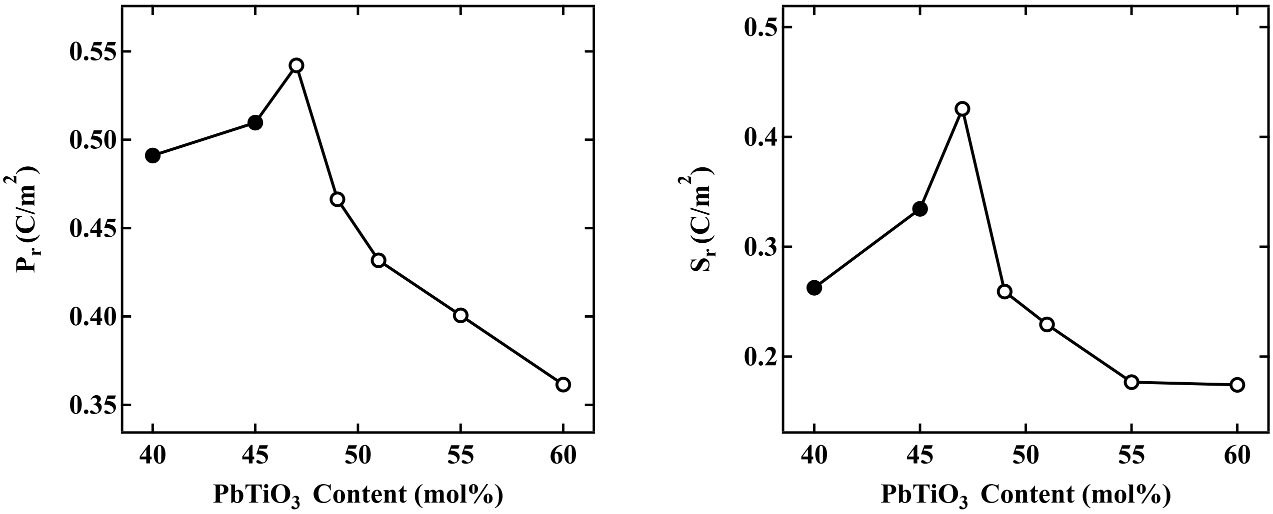

Figure 4.9: Remanent polarization and remanent strain as a function of $PbTiO_3$-content. Open and filled symbols represent tetragonal and rhombohedral crystal structure, respectively.

As expected from previous reports [14, 24, 172], the maximum of the remanent polarization P_r was found for compositions in the vicinity of the MPB, as shown in Figure 4.9. The remanent polarization decreases for compositions that are further away from the MPB. It can be also seen that P_r decreases much faster for compositions on the tetragonal side of the phase-diagram than on the rhombohedral side relative to MPB. This might be explained by the larger number of stable polarization directions in rhombohedral systems, which allow a better alignment of the polarization induced by an external electrical field. Additionally, the significant increase of the coercive field for a higher $PbTiO_3$-content (Figure 4.8) limit the number of domain reorientation processes in these compositions, so that a fully saturate state can not be reached for an applied electric field of 6 kV/mm. Interestingly, the maximum polarization was found for PZT 47, which lies on the tetragonal side of the phase diagram, instead for the rhombohedral PZT 45 that has the smallest coercive field. This effect could be either explained by differences in the spontaneous polarization of both compositions, or might indicate the existence of induced phase transitions. The remanent strain shows a similar dependency on the $PbTiO_3$-content than P_r and the maximum value is again found for PZT 47. Compared to P_r, S_r decreases much faster for compositions on the rhombohedral side of the phase-diagram. Assuming similar electrostrictive coefficients for PZT 45 and 47, the spontaneous strain values would indicate a larger spontaneous polarization in PZT 47 that is responsible for the maximum of P_r in this composition.

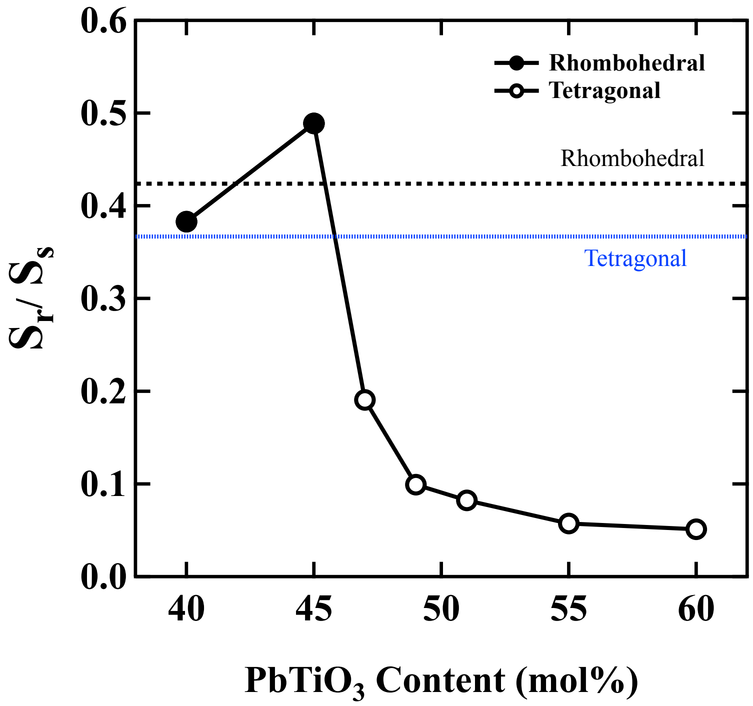

Figure 4.10: Macroscopic remanent strain S_r normalized by the microscopic switching strain S_s as a function of $PbTiO_3$-content for electrical loading. Open and filled symbols represent tetragonal and rhombohedral crystal structure respectively. The dotted blue and dashed black horizontal lines indicate the maximum theoretical S_s/S_r value for the tetragonal and the rhombohedral phase that can be reached by only ferroelastic domain switching. Data points indicate the average measured value for each composition, weras the experimental error was estimated to be $\pm 3\%$

Similarly to the mechanical case, the measured remanent strain of each composition was normalized by the corresponding switching strain (S_r/S_s) and plotted as a function of the $PbTiO_3$-content (Figure 4.6). Again, the maximum theoretical S_s/S_r values for the tetragonal and the rhombohedral phase are indicated by dotted blue and dashed black horizontal lines. These values differ from the values that were determined for the uniaxial compressive loading because the induced domain switching processes are different: uniaxial compressive stress leads to switching of domains that are oriented perpendicular to the external stress, whereas the electric field switches domains parallel to the electric field. For all tetragonal compositions (PZT 47, 49, 51, 55, 60) the measured values lie more that 50 % below the theoretical maximum, with an observed decrease with an increasing $PbTiO_3$-content. This result can be explained with the same arguments from the previous Section: domain pinning by internal defects and stresses, as well as interactions between neighboring grains. Unlike for compressive strain, the decrease seems to be nonlinear, saturating at higher $PbTiO_3$-content. This behavior is comparable to the trend in the coercive field shown in Figure 4.8.

Both rhombohedral compositions (PZT 40, 45) show values of S_r/S_s that are closer to the theoretical maximum. Like the mechanical case, the maximum value of S_r/S_s is found for PZT 45 and is around 20 % larger than the theoretical limit allowed by simple ferroelectric domain switching. This effect is much smaller than for uniaxial compressive stress. An explanation for this effect might be that the maximum applied stress is larger relative to the coercive value T_C, leading to a more saturated state compared to the domain state at maximum electric field. Reducing the $PbTiO_3$-content was again accompanied by a decrease in S_r/S_s for PZT 40. Here, however, the value of S_r/S_s is slightly below the theoretical maximum for the rhombohedral phase.

As shown in Section 4.1, large uniaxial mechanical and electrical loads lead to exceptional remanent strain for $Pb(Zr_{1-x}\ Ti_x)O_3$ ceramics with a predominately rhombohedral composition. This effect cannot be exclusively explained by ferroelastic switching; even the assumption that all domains switch during loading into the energetically favored directions during loading does not lead to such high values. Apparently, additional hysteretic mechanisms that are capable of increasing the amount of plastic strain generated have to be responsible for the increase in the remanent strain. It is believed that the coexistence of tetragonal and rhombohedral phases in materials with compositions close to the MPB can lead to improved ferroelectric and piezoelectric properties because of the increased ease of polarization reorientation during loading [14], although in the present case a minor phase content was found to be too small to be accurately measured in the two compositions closest to the MPB. Recently, Heitmann and Rossetti have shown that a minimization of the polarization anisotropy energy at the MPB is required in order to explain the structure of the PZT phase diagram [144]. They showed that a 2-4-6 Landau free energy polynomial, where the energy barriers for domain reorientation via polarization rotation becoming increasingly small at the MPB, could be the origin of the decrease in coercive stress and coercive field that were observed in the experiments.

One possible explanation for the extraordinary S_r/S_s ratio observed for uniaxial electrical and mechanical loading is an irreversible change of the lattice parameters induced by the applied load. This phenomenon has been previously observed during mechanical compressive loading in PZT with in situ X-ray [174] and neutron diffraction [175]. Recent studies by Hall et al. [174, 176] revealed that mechanical loading can induce irreversible strain incompatibilities between neighboring grains that lead to the formation of local residual stresses in both rhombohedral and tetragonal structured PZT compositions during electrical loading. The magnitude of the local stress fields, however, strongly depends on the anisotropy of the elastic coefficients of each phase. In addition, Jones et al. [175] have estimated the overall contribution of non-ferroelastic remanent strain contributions to account for approximately 25 % of the overall macroscopic remanent strain in a purely tetragonal PZT composition. This phenomenon, however, can not explain why only the rhombohedral compositions display an S_r/S_s ratio significantly larger than the theoretical maximum predicted for ferroelasticity/ferroelectricity alone. It seems likely that this drastic increase would be observed in all compositions if the irreversible changes in the lattice parameters were the primary cause. Moreover, in order for the stress-induced lattice parameter changes to be the only mechanism behind the increase of the S_r/S_s ratio above the theoretical maximum, this phenomenon would need to be nearly 58 % as large as the ferroelastic contribution. It is important to note that an implied assumption here is that all of the domains can ferroelastically switch, which is not physically achievable. Reducing the ferroelastic contribution would necessitate a further increase in the remanent lattice strain contribution. As shown by Jones et al., [175] the remanent lattice strain contribution is only 36 % as large as the ferroelastic effect, considerably smaller than required to account for the experimental observations. In addition, measurements on PZT 45 at elevated temperature, where the composition was found to transform from rhombohedral to tetragonal during heating, displayed a significant decrease in S_r/S_s following the phase transition to tetragonal. This strongly indicates that the effect is directly linked to the rhombohedral phase and cannot solely be explained through stress-dependent hysteretic changes in the spontaneous strain.

An additional possibility is that irreversible stress induces a structural phase transition that could lead to an increase in S_r/S_s for PZT 40 and 45, which is supported by a recent report on in situ synchrotron diffraction measurements that revealed that PZT (PIC 151) undergoes an electric field-induced phase transition that is partially irreversible [155]. Partly reversible field-induced orthorhombic→rhombohedral phase transitions by polarization rotation were reported for PZN-8PT, measured by in situ polarized light microscopy [177]. Unfortunately, PZT single crystals of a sufficient size are not readily available that would allow for the direct characterization of the macroscopic field-induced phase transition behavior.

4.2.1 Model Description

As described in Chapter 3, electric field-induced phase transitions are accompanied by a huge increase in strain, making them a potential explanation for the exceptional high remanent strain. In ferroelectric single crystals this phenomenon can be described by using a phenomenological thermodynamic approach based on Landau theory. In the present case, external mechanical stresses are an additional source of induced phase transitions inside the grains of the PZT ceramic samples. To include the effect resulting from external stresses in the model, an additional term that describes the ferroelastic interactions between the external mechanical load T_{ij} and the polarization of the ferroelectric domain P_i has to be added to the description of the Gibbs free energy of the system (Equation 3.1) [94, 178]:

$$\begin{aligned} G &= G_{LD} - E_i P_i - \frac{1}{2} E_i \epsilon_{ij} E_j - \mathbb{Q}_{ijkl} T_{ij} P_k P_l && (4.4) \\ G_{LD} &= \alpha_{ij} P_i P_j + \beta_{ijkl} P_i P_j P_i P_j + \gamma_{ijklmn} P_i P_j P_k P_l P_m P_n + \text{h.o.t.} && (4.5) \end{aligned}$$

where $\mathbb{Q}_{ijkl}$ denotes the cubic electrostrictive coefficients. As described in the previous Chapter 3 , the stable polarization configurations of a single crystal are given by the minima of G, whereas the evolution of the polarization from unstable configurations is described by the evolution Equation 3.3:

$$\frac{dP_i}{dt} = -M \frac{\delta G}{\delta P_i} \tag{4.6}$$

Unfortunately, the measured PZT ceramics possesses a complex polycrystalline structure consisting of numerous differently oriented grains, each with an individual poly-domain polarization distribution [142], whereas the thermodynamic model is in principle limited to one single ferroelectric domain in a single crystal with a defined crystallographic orientation. In addition, the complex ceramic microstructure also includes defects, inhomogeneities, pores, and internal stresses [179], which are mostly absent in high quality $BaTiO_3$ single crystals. These imperfections can locally influence the domain switching behavior. To use the existing model to describe phase induced transitions in $Pb(Zr_{1-x}Ti_x)O_3$, additional simplifications of the problem and expansions of the model are required.

In Chapter 3, it was shown for $BaTiO_3$ single crystals that a poly-domain microstructure does not necessarily have a significant influence on the quality of the model predictions. For this reason it is assumed that the influence of the domain structure can be neglected in this case as well. This simplification allows the simulation of the dynamic polarization evolution of single grains in reaction to electrical or mechanical loads. If the interactions between individual grains are weak enough to be neglected, it is possible to represent the polycrystalline sample by a distribution of non-interacting single crystals that only differ in their global crystallographic orientation and can be individually represented by the same thermodynamic Landau model. The solution was determined individually for each grain in its local coordinate system, which allowed the usage of the solution algorithm for Equation 4.6 that was previously described in Chapter 3. Therefore, the respective external loads were transformed with a coordinate transition via rotation matrices from the global (sample) coordinate system to the local (grain) coordinate system. The rotation matrices that result in uniformly distributed single crystal polar axis were efficiently constructed, by first performing a random rotation about the vertical axis, followed by a random reflection defined by a Householder-matrix, as suggested by J. Avro [180].

As described in detail in Chapter 3, an induced rotation of the polarization from a polar orientation related to the initial phase of the ferroelectric system towards a direction related with another phase can be interpreted as an induced phase transition. The material properties of PZT, such as the electrostrictive coefficients, depend on the phase of the composition. It is therefore necessary to monitor the respective phase of each grain during the dynamic evolution of the polarization, to adjust the material properties to the instantaneous polar direction, i.e., assumed phase. This was done with the following radial function that describes the proximity of the current polarization orientation to the rhombohedral $\langle 111 \rangle_c$ crystallographic orientation:

$$\xi = \frac{1}{2\|P\|^2}\left(1-\delta_{ij}\right)\left|P_i P_j\right| \tag{4.7}$$

where the radial phase function $\xi = 0$ for polarization vectors along tetragonal $\langle 001 \rangle_c$ crystallographic directions, $\xi = 0.5$ for polarization vectors along orthorhombic $\langle 011 \rangle_c$ crystallographic directions, and $\xi = 1$ for polarization vectors along rhombohedral $\langle 111 \rangle_c$ crystallographic directions, as depicted in Figure 4.11.

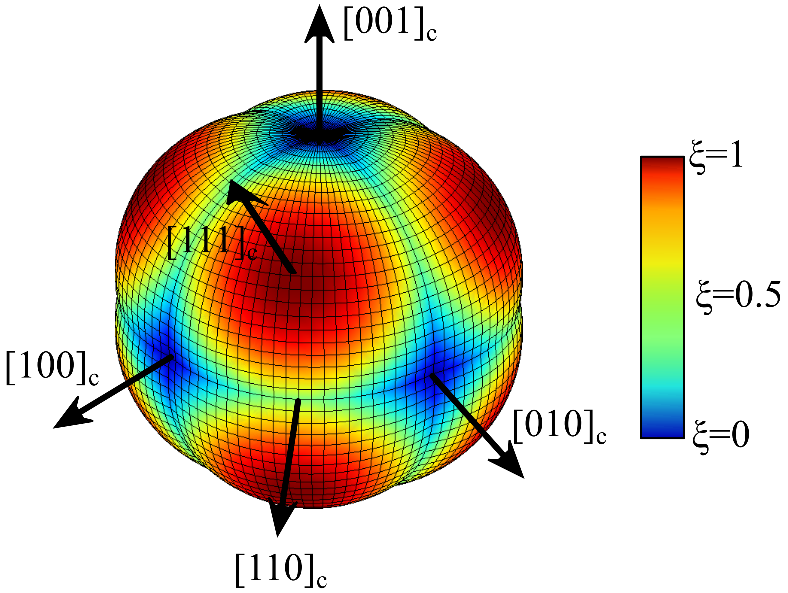

Figure 4.11: Radial phase function ξ to determine the electrostrictive coefficients during an stress-induced phase transition. ξ is 1 along rhombohedral $\langle 111 \rangle_c$, 0.5 along orthorhombic $\langle 011 \rangle_c$, and zero along tetragonal $\langle 001 \rangle_c$ crystallographic directions.

4.2.2 Model Parameters

Haun et al. [56] reported Landau coefficients up to the 6th order for $Pb(Zr_{1-x}Ti_x)O_3$ as a function of the $PbTiO_3$-content in 10 mol%-concentration steps. The necessary coefficients for compositions between these steps were calculated by linear interpolation. The electrostrictive coefficients $\mathbb{Q}_{11}$ and $\mathbb{Q}_{12}$ at room temperature can be determined if the spontaneous strain S_0 and the spontaneous polarization P_s are known, such that:

$$\mathbb{Q}_{11} = \frac{S_s}{P_0^2} \tag{4.8}$$

As described in Equation 4.3 the spontaneous strain can be related to the switching strain S_s. By combining Equations 4.3 and 4.8, it is possible to find expressions for both electrostrictive coefficients $\mathbb{Q}_{11}$ and $\mathbb{Q}_{12}$:

$$\mathbb{Q}_{11} = \frac{1}{P_0^2}\left(\frac{2S_s}{S_s+3}\right) \tag{4.9}$$

$$\mathbb{Q}_{12} = -\frac{\eta}{P_0^2}\left(\frac{2S_s}{S_s+3}\right) \tag{4.10}$$

where η is a parameter used to relate the magnitude of $\mathbb{Q}_{11}$ to $\mathbb{Q}_{12}$. It was previously shown by Yamanda and Rossetti that the application of a hydrostatic stress can shift the Curie temperature of a perovskite ferroelectric [165, 181] if the relation $\mathbb{Q}_{11} > |2\mathbb{Q}_{12}|$ is fulfilled. Moreover η-values of 0.30 - 0.48 were reported for various perovskite ferroelectrics [165, 182]. In particular, Haun et al. have also provided estimates of $\mathbb{Q}_{11}$ and $\mathbb{Q}_{12}$ for various PZT compositions [56] with η-values between 0.30 to 0.48, depending on the respective $PbTiO_3$-content. The maximum value $\eta = 0.48$ was found for the composition closest to the MPB. Due to the limited and varying data available, it was assumed during simulations that $\eta = 0.45$ for all compositions and phases. As a consequence of the differences in the spontaneous strain and spontaneous polarization values between the rhombohedral and tetragonal phases, the electrostrictive coefficients do not only depend on composition, but also on the phase of the material. The electrostrictive coefficients $\mathbb{Q}_{11}$ and $\mathbb{Q}_{12}$ for each phase were estimated by combining results from experimental measurements and calculations based on the Landau-potential. The spontaneous polarization P_0 of the rhombohedral and tetragonal phase for a $PbTiO_3$-content between 40 mol% and 60 mol% was determined by minimizing the systems free energy (Equation 4.5) for a load-free condition. The results are shown in Figure 4.12 and are in a reasonable agreement with previous estimates for MPB compositions of PZT [183]. The $\mathbb{Q}_{44}$ coefficient, which describes the effect of shear stresses on the free energy density, can be determined from $\mathbb{Q}_{11}$ and $\mathbb{Q}_{12}$ using the isotropy condition [48, 184]:

$$\mathbb{Q}_{44} = 2\left(\mathbb{Q}_{11} - \mathbb{Q}_{12}\right) \tag{4.11}$$

An overview of the complete model parameters for each composition is provided in Table 4.1. These coefficients were implemented into Equation 4.5. To visualize the resulting three-dimensional energy landscapes, Equation 4.5 was minimized in the three-dimensional polarization space $\{P_1P_2P_3\}$. Here, both the shape and the color indicate the free energy, with blue and red being the energetic minimum and maximum, respectively. In the first column of Figure 4.13 and 4.14, this minimized energy for a load-free state is shown as a three dimensional surface plot. Interestingly, it can be seen that local energy minima along the polarization orientations of both phases were found in the stress-free state, regardless of the composition. However, while both phases were stable, only one represented the global energetic minimum. This indicates that field-induced phase transitions can lead to stable or meta stable changes of the phase even after the inducing field is no longer applied. The stability of this ”induced phase state” depends on the height of the potential barrier between the local and the global maximum and on the amount of thermal fluctuations in the system. It should be remarked that crystal defects and other domain pinning centers, will have an additional influence on the stability of these induced phases. It can be seen in Figure 4.13 and 4.14 that in compositions with a higher $PbTiO_3$-content the global minimum lies along the $\langle 001\rangle_c$ directions, while in compositions with a lower $PbTiO_3$-content the global minimum is found along the $\langle 111\rangle_c$ directions. At approximately 52 mol% $PbTiO_3$, the magnitude of the spontaneous polarization reverses, indicating a change in the globally stable phase. The spontaneous strain for each composition, which is necessary for the determination of the electrostrictive coefficients was determined with XRD analysis (Figure 4.12 b). Due to the peak overlap in the MPB compositions the spontaneous strains could not be directly measured for both phases. To determine the necessary spontaneous strain values for both phases, the measured data was extrapolated in the PZT 40, 45, 47, and 49 compositions. The data points that were determined by extrapolation are indicated as open symbols in Figure 4.12b.

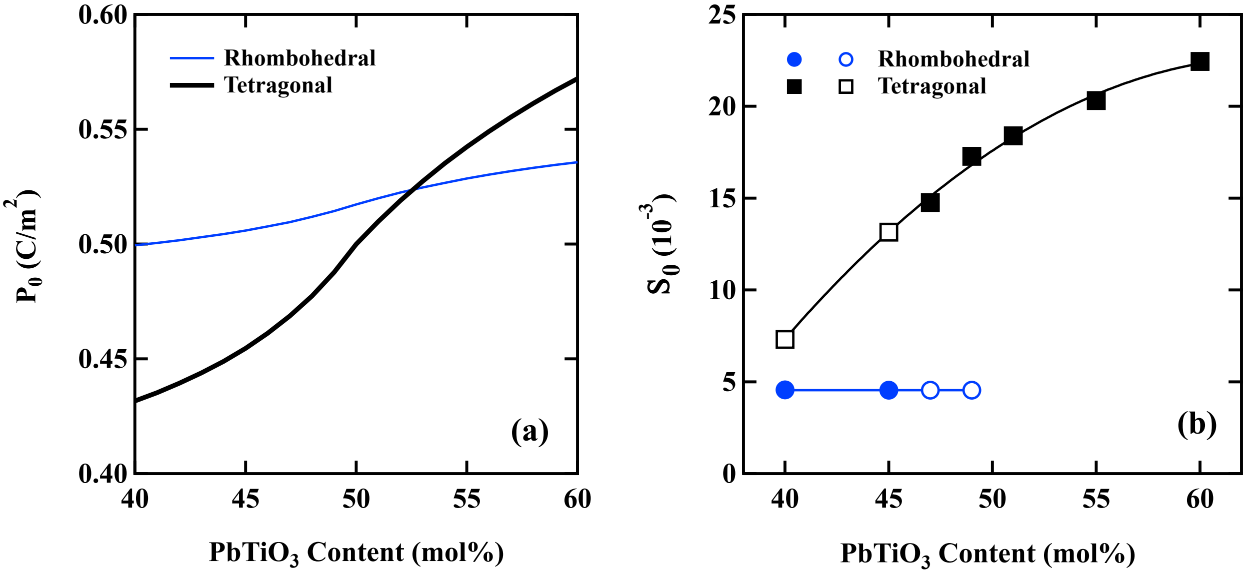

Figure 4.12: The calculated spontaneous polarization and the measured spontaneous strain of PZT as a function of the $PbTiO_3$-content [156]. The filled symbols indicate experimental measurements, while the open symbols indicate extrapolated values.

Applied stresses and electric fields change the shape of the free energy landscape. During the simulation of a polycrystal, the load, which is applied to each grain has a different direction depending on the global grain orientation. In Figure 4.13 and 4.14 the effects of an uniaxial compressive stress of −200 MPa and an electric field of 4 $^{\mathrm{kV}}/_{\mathrm{mm}}$ is illustrated for loading along a tetragonal $\langle 001\rangle_c$ (middle column) and a rhombohedral $\langle 111\rangle_c$ (right column) crystallographic orientation. As expected the uniaxial compressive stress favors a polarization direction perpendicular to the loading axis. It can be seen that the free energy in the direction of the applied stress is increased, whereas the energy of all directions that are perpendicular are decreased. Applying an electric field, however, decreases the free energy in field direction, whereas the energy in the opposite direction is increased. Directions perpendicular to the field remain unchanged, which is, unfortunately, not clearly visible in the graphs because the size and color of the different landscapes is scaled. In PZT 40, which is purely rhombohedral, it can be clearly seen that the energetic minima, denoted by the blue indents, lie along the $\langle 111\rangle_c$ orientations in the unstressed state (Figure 4.13 and 4.14 left column), while the PZT 60 composition, which is purely tetragonal, clearly shows energetic minima along the $\langle 001\rangle_c$ orientations. The stress free free energy landscapes for the intermediate compositions display the evolution of energy landscape, where the energy stable polarization direction indicated by the global energetic minimum along the $\langle 111\rangle_c$ directions increases with respect to the local minimum along the $\langle 001\rangle_c$ orientations with increasing $PbTiO_3$-content. Between PZT 47 and 49 the energy of the minimum along the $\langle 001\rangle_c$ orientation drops below the value along the $\langle 111\rangle_c$ orientations. In all presented compositions it is apparent that both the tetragonal and the rhombohedral phases are stable, with one being the global minimum (stable configuration) and the other the local minimum (metastable configuration). The distortion of the energy landscape during the application of an external load also influences the relation between the different minima and leads to a break in the symmetry of the system, i.e., all minima related to one phase are no longer energetically equivalent and can be shifted from their initial positions. Interestingly, in some cases, especially for compositions around the MPB the external load is able to decrease the value of a local minimum below the global minimum value, which can be interpreted as a field-induced phase transition [90]. For example in PZT 45, the globally stable polarization direction, which was originally along the $\langle 111 \rangle_c$ orientation, was found to transition to the $\langle 001 \rangle_c$orientation perpendicular to the applied stress, indicating a simulated stress-induced R→T phase transition. When the external load is applied along an arbitrary off-axis direction, the free energy landscape will distort accordingly and allow for complex polarization evolution paths that may result in ferroelectric/ferroelastic switching or induced phase transitions. Following unloading, the polarization axis in the model will be located along a principal crystallographic direction (for PZT this means $\langle 001 \rangle_c$or $\langle 111 \rangle_c$), which may be either globally or locally stable depending on the rotation path and applied local stress field.

Table 4.1: Landau coefficients for Pb(Zr$_{1-x}$Ti$_x$)O$_3$ [56]

	PbTiO$_3$-content (mol%)							
Coefficients	40	45	47	49	51	55	60	Units
α_1	−7.9040	−6.3955	−5.7921	−5.1887	−5.2323	−6.6135	−8.3400	10^7 m^{2}N/C^2
β_{11}	1.3620	0.9192	0.7421	0.5650	0.4649	0.4189	0.3614	10^7 m^{6}N/C^4
β_{12}	2.3910	2.0630	1.9318	1.8006	1.8848	2.4840	3.2330	10^8 m^{6}N/C^4
γ_{111}	2.7130	2.0245	1.7491	1.4737	1.3883	1.5975	1.8590	10^8 m^{10}N/C^6
γ_{112}	1.2130	0.9129	0.7929	0.6728	0.6365	0.7316	0.8503	10^8 m^{10}N/C^6
γ_{123}	−5.6900	−4.2920	−3.7328	−3.1736	−3.0109	−3.4785	−4.0630	10^9 m^{10}N/C^6
$\mathbb{Q}^T_{11}$	3.9390	6.3650	6.7220	7.2650	7.0771	6.9052	6.8568	10^{-2} m^4/C^2
$\mathbb{Q}^T_{12}$	−1.7726	−2.8643	−3.0249	−3.2693	−3.1847	−3.1073	−3.0855	10^{-2} m^4/C^2
$\mathbb{Q}^T_{44}$	11.4231	18.4585	19.4938	21.0685	20.5235	20.0250	19.8846	10^{-2} m^4/C^2
$\mathbb{Q}^R_{11}$	1.8280	1.7770	1.7500	1.7150	1.6773	1.6196	1.5726	10^{-2} m^4/C^2
$\mathbb{Q}^R_{12}$	−0.8226	−0.7996	−0.7875	−0.7717	−0.7548	−0.7288	−0.7077	10^{-2} m^4/C^2
$\mathbb{Q}^R_{44}$	5.3012	5.1533	5.0750	4.9735	4.8641	4.6967	4.5604	10^{-2} m^4/C^2

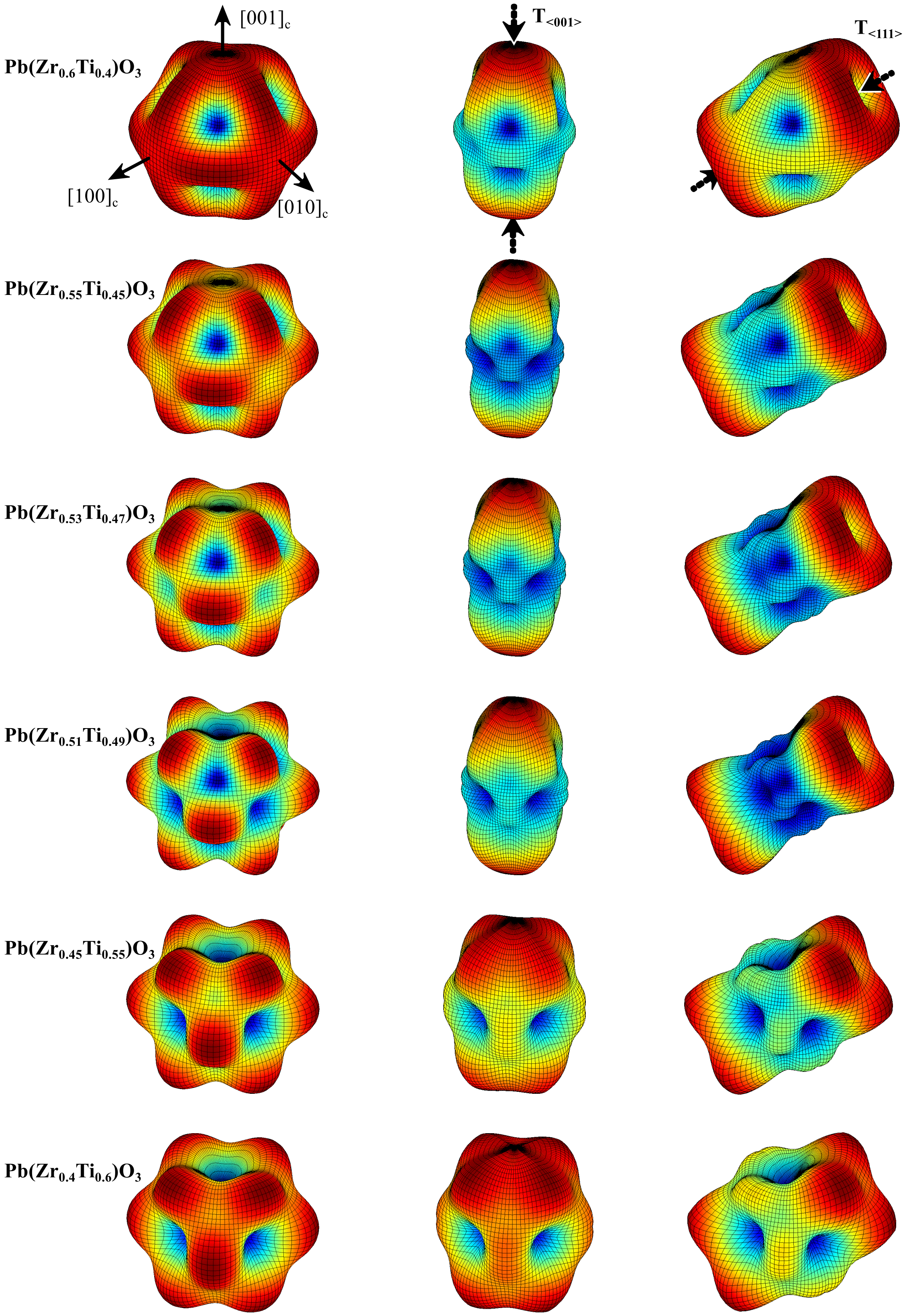

Figure 4.13: Three-dimensional free energy landscapes for PZT with a $PbTiO_3$-content of 40, 45, 47, 49, 55, and 60 mol% in the unstressed state and with an applied compressive stress ($T_{\langle 001\rangle} = T_{\langle 111\rangle} = -200\,\mathrm{MPa}$) along the $\langle 001\rangle_c$ as well as the $\langle 111\rangle_c$ direction. The crystallographic axes are shown for the unstressed PZT 40 and apply to all figures.

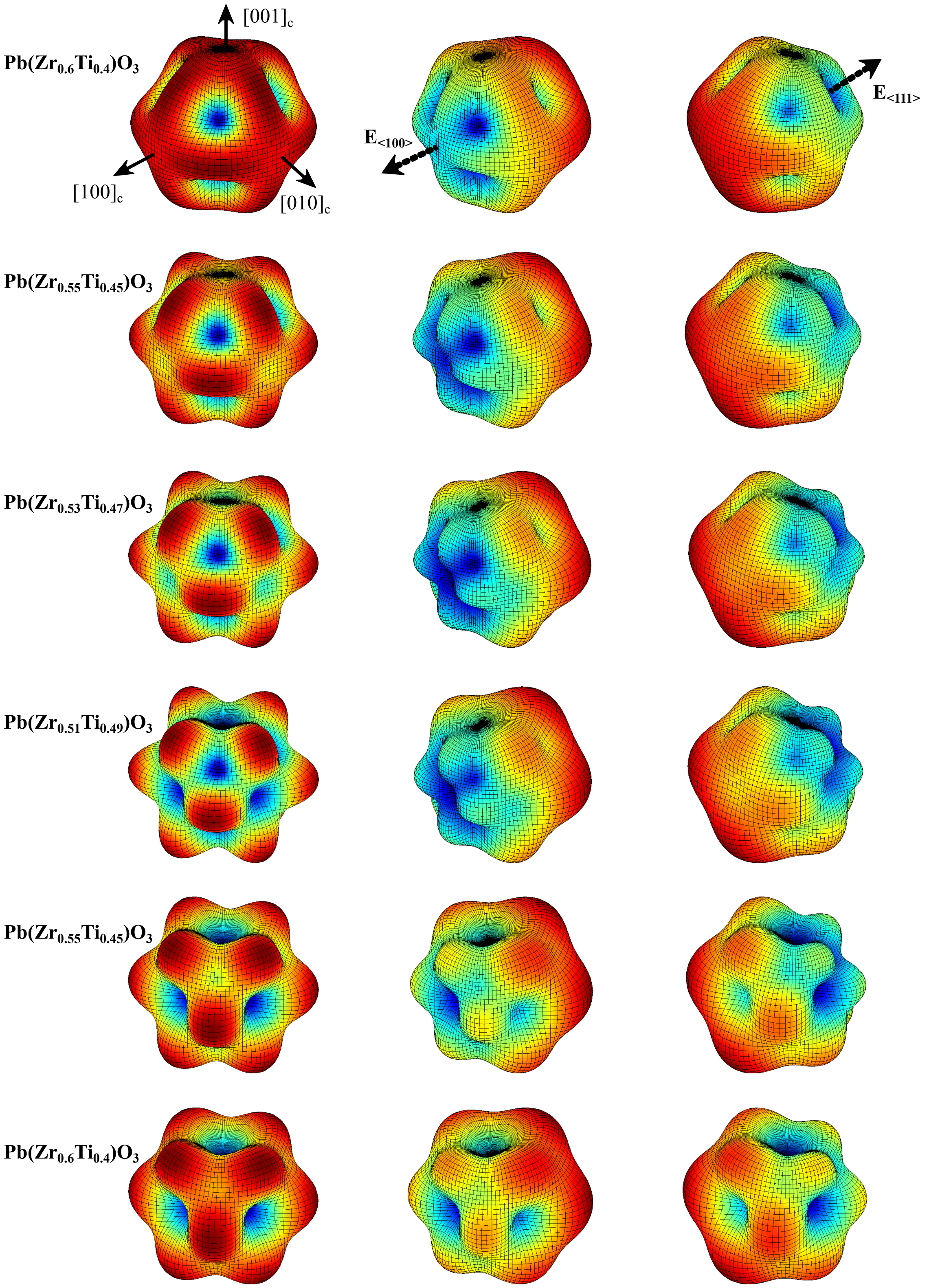

Figure 4.14: Three-dimensional free energy landscapes for PZT with a $PbTiO_3$-content of 40, 45, 47, 49, 55, and 60 mol% in the unstressed state and with an applied electric field ($E_{\langle 100 \rangle} = E_{\langle 111 \rangle} = 4\,^{\mathrm{kV}}/_{\mathrm{mm}}$) along the $\langle 001 \rangle_c$ as well as the $\langle 111 \rangle_c$ direction. The crystallographic axes are shown for the unloaded PZT 40 and apply to all figures.

4.2.3 Results and Discussion

During the simulation of each grain, the applied external fields in an off-axis crystallographic orientation resulted in the stable polarization direction, which follows the local energy minimum, by rotating through non-principal orientations. This has been previously shown in Chapter 3 for a tetragonal variant that was electrically loaded in the $[110]_c$-orientation. The polarization was predicted to rotate from the tetragonal $[100]_c$ direction to the orthorhombic $[110]_c$ direction through an intermediate phase, where the stable polarization vector does not lie along one of the principal axes [92]. At each time step the effective electrostrictive coefficient was calculated by the linear combination of the rhombohedral and tetragonal electrostrictive coefficients following from Equation 4.7:

$$\mathbb{Q} = \mathbb{Q}^R \xi + \mathbb{Q}^T (1 - \xi) \tag{4.12}$$

The evolution Equation 4.6 that describes the dynamic behavior of a single ferroelectric domain was solved numerically for $3 \cdot 10^5$ individual, non-interacting single domain ”grains”, using the solution algorithm described in Chapter 3. Because each grain could be solved individually, it was possible to parallelize the solution-algorithm and therefore to decrease the necessary computation time. During calculations the mobility parameter M was chosen to be $2.5 \cdot 10^{-9}\,\mathrm{A/Vm}$ with a time step size of $1 \cdot 10^{-3}$ s for all compositions and loading scenarios. The size of the time step was found to be sufficiently small to allow for program convergence and smooth polarization evolution. Simulations were performed for PZT 40, 45, 47, 49, 51, 55, and 60 using the material parameters in Table 4.1. During calculations an arbitrarily large uniaxial compressive stress of 50 GPa and an electric field of $30\,\mathrm{kV/mm}$ were utilized to ensure a saturated remanent state, which was defined as the stress or electric field above which no further increase in remanent strain was found. As a starting condition, it was assumed that the polarization of each grain was consistent with its local coordinate system with the position of a minimum of the Landau energy in either a tetragonal or rhombohedral crystallographic direction, depending on the phase of the respective compositions that were determined by XRD measurements. In PZT 47 and 49, the two compositions that were found to have a minority phase content 5 % were randomly set to the respective metastable phase as the initial condition. All calculations were performed in the local (”grain”) coordinate system, with the identical Landau potential only dependent on the chosen composition. The mechanical or electrical load was transformed into this local coordinate system via the corresponding rotation matrix. After applying the load, the system was allowed to relax, where changes in the polarization below $1 \cdot 10^{-13}\,\mathrm{C/m^2}$ between two sequential time steps were used as a criterion that indicated a stable polarization configuration. The unloading process was realized by 100 consecutive steps. After each reduction, the system was allowed to relax. The strain S_{ij} of each grain was determined from the solution of the polarization P_i and the electrostrictive coefficients $\mathbb{Q}_{ijkl}$ of the current phase (Equation 4.12) [185]:

$$S_{ij} = \mathbb{Q}_{ijkl} P_k P_l \tag{4.13}$$

Each local solution of strain and polarization was back-transformed to the global system and averaged over all calculated grains to determine the solution for the full polycrystalline system.

Uniaxial Compressive Stress

Model results for the $PbTiO_3$-content dependent macroscopic S_r/S_s ratio during a uniaxial compressive loading condition are shown in Figure 4.15 and compared to experimental measurements. It is apparent that the model is able to accurately predict the important features of S_r/S_s as a function of composition. The maximum value is found on the rhombohedral side of the MPB (PZT 45), with significantly decreasing values on either side. In general, the model predicted S_r/S_s values in good agreement with experimental data. However, in the case of PZT 40 the theoretical prediction was significantly smaller than the experimental value. The Landau coefficients used have a significant impact on the simulation results, which is expected to be a primary cause for variations between model and experimental results. In addition, it is anticipated that local fields in the polycrystalline material also act to hinder the motion of domain walls and interphase boundaries and could lead to differences to simulation results.

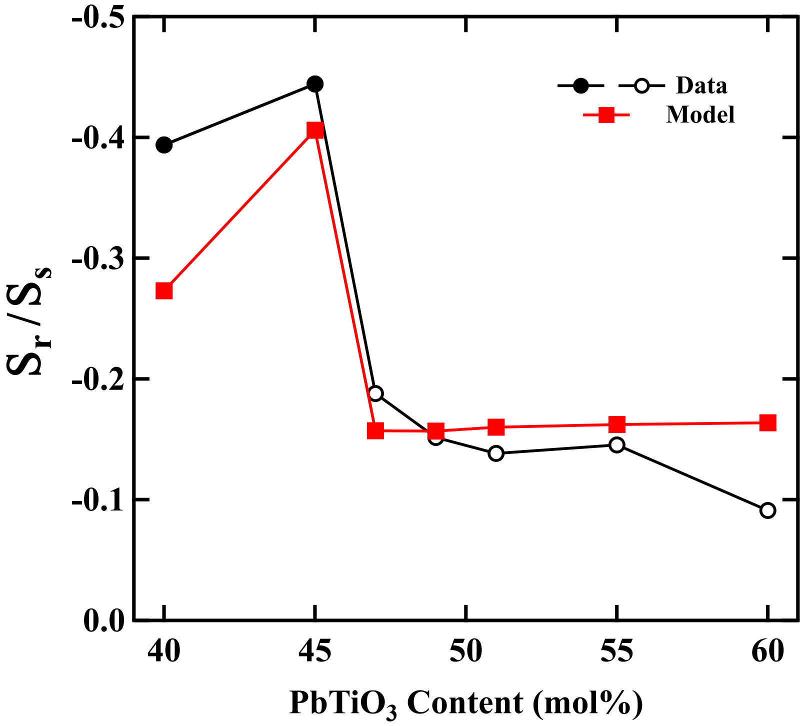

Figure 4.15: Comparison of experimental measurements and model results at room temperature. Filled symbols indicate compositions that were originally rhombohedral, while open symbols were originally tetragonal.

It stands to reason that stress-induced phase transitions via polarization rotation, similar to those that were described in Chapter 3, from an initial rhombohedral to the metastable tetragonal orientation are the primary reason for the exceptional remanent strain. This hypothesis can be directly verified by checking the phase distribution of the grain system in the equilibrium state after mechanical unloading. This was done by evaluating the polarization orientation in the respective local ("grain") coordinate system with the radial phase function ξ (Equation 4.7), where $\xi = 0$ means a polarization orientation along the $\langle 100 \rangle_c$ direction, $\xi = 1$ a polarization along the $\langle 111 \rangle_c$ direction and $\xi = 0.5$ is a polarization along the $\langle 100 \rangle_c$ direction. All other ξ values indicate a monoclinic phase, which should be unstable in the unloaded state (Figure 4.11). The ξ values, i.e., phase distribution, of the six PZT compositions 40, 45, 47, 49, 55, and 60 are shown in Figure 4.16 as blue bars. Because the Landau energy landscapes (first column in Figure 4.13 and 4.14) only possesses minima along the tetragonal $\langle 100 \rangle_c$ and rhombohedral $\langle 111 \rangle_c$ orientations, it was expected that each composition shows only two sharp peaks at the corresponding values of the phase function $\xi = 0$ and $\xi = 1$. Instead, it is apparent that compositions with a low $PbTiO_3$-content display a broad distribution around the tetragonal minimum $\xi = 0$. The size of distribution, however, becomes narrower for compositions with a higher $PbTiO_3$-content and nearly vanishes for PZT 55 and 60. This phenomena can be explained on the base of the used solution algorithm with regard to the different shapes of the corresponding Landau energy landscapes.

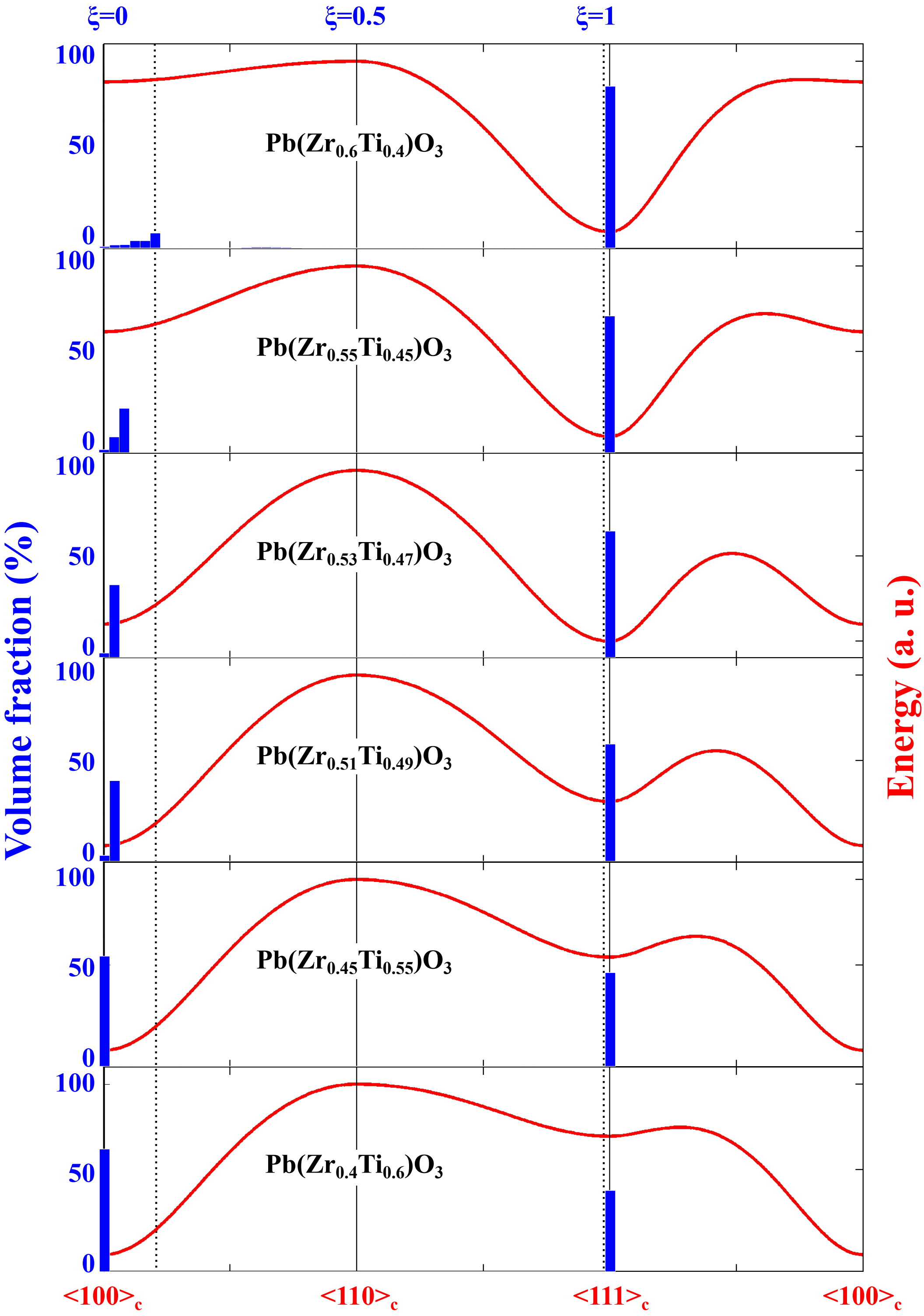

Figure 4.16: Minimal Landau energy between the tetragonal, rhombohedral, and orthorhombic crystallographic direction as explained in Figure 4.17 (red). History plot of the calculated phase distribution of PZT 40, 45, 47, 49, 55, and 60 in the equilibrium state after mechanical unloading (blue). Black dashed lines indicate the chosen intervals, in which the grain is treated as to be tetragonal $[0, 0.1]$ or rhombohedral $[0.99, 1]$.

For this purpose, it is helpful to use a two dimensional visualization of the different Landau energy landscapes along a path that passes through all important polarization directions ($\langle 100\rangle_c$, $\langle 110\rangle_c$, and $\langle 111\rangle_c$) as explained in Figure 4.17 and to compare these curves with the corresponding phase distribution. In each direction only the minimal energy in the radial direction is used, analogue to the three-dimensional visualizations. An example of such a graph for PZT 40 is shown in Figure 4.17. This graph illustrates the free energy ratio between the absolute rhombohedral minimum, the local tetragonal minimum, and the maximum in the orthorhombic crystallographic direction, as well as the slope of the free energy in between. As expected the curve shows an absolute minimum at $\langle 111\rangle_c$ as well as a local minimum along $\langle 100\rangle_c$. For clarification, the path along which the (radial minimalized) Landau energy is shown as a red line on the surface of the blue unit-sphere as well as the corresponding three dimensional minimum Landau energy surface in Figure 4.17.

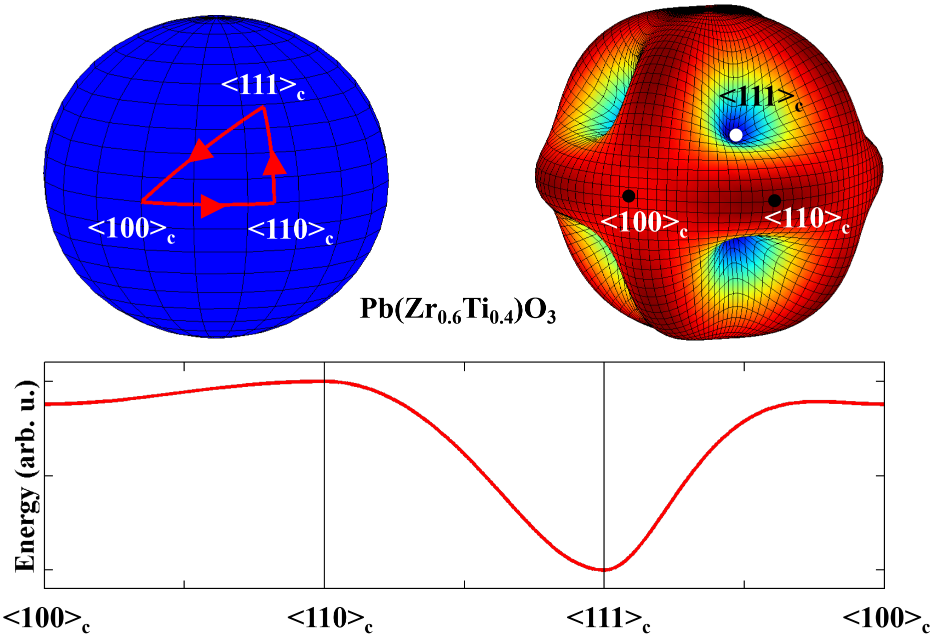

Figure 4.17: Minimal Landau energy for PZT 40 along a path that passes through all important polarization directions ($\langle 100\rangle_c$, $\langle 110\rangle_c$, and $\langle 111\rangle_c$). As expected the curve shows an absolute minimum at $\langle 111\rangle_c$ as well as a local minimum at $\langle 100\rangle_c$. The red line on the surface of the blue unit-sphere in the upper left part of the Figure indicates the path along which the Landau energy was plotted. For comparison, the three dimensional minimal Landau energy is depicted in the upper right part of the Figure.

According to the evolution Equation 4.6, the slope of the free energy serves as a driving force and therefore determines the relaxation time for different initial polarization values. The deeper the minima of the Landau energy are, the faster the relaxation will take place, meaning that the flatness of the $\langle 100\rangle_c$ minima in PZT 40 allows the polarization direction to remain artificially stable along a non-principle crystallographic orientation. To put the phase distribution into the context of the corresponding Landau energy landscapes, both plots were combined in Figure 4.16. It is clear that the slope of the Landau energy in the $\langle 100\rangle_c$ direction affects the phase volume fraction. It can be also seen that the local rhombohedral minimum of PZT 60 is more distinct than the local tetragonal minimum in PZT 40, which results in a larger volume fraction of a second phase in PZT 60 compared to PZT 40. In addition, the shallow slope around the local minimum of PZT 40 along the $\langle 100\rangle_c$ direction leads to a broader distribution of the phase volume fraction than the much sharper absolute minimum at $\langle 111\rangle_c$. This is because polarization changes below $1 \cdot 10^{-13}\,\mathrm{C/m^2}$ between adjacent time steps of $1 \cdot 10^{-3}\,\mathrm{s}$ were interpreted a stable configuration. This means that a polarization evolving towards a $\langle 100\rangle_c$ direction will experience a weak driving force allowing, for example, pinning centers to easily stabilize a non-principle polarization direction.

Between these extreme cases the shape of the Landau energy changes continuously. The evolution of the minima along the tetragonal $\langle 100 \rangle_c$ and rhombohedral $\langle 111 \rangle_c$ directions for different $PbTiO_3$-content is clearly observable. In PZT 40 and 45 the absolute minimum lies in the rhombohedral direction, whereas the tetragonal local minimum is flat. In PZT 47, both minima are nearly energetically equivalent. In all compositions with a higher $PbTiO_3$-content (PZT 49, 55, 60) the absolute minimum lies in the tetragonal direction. Interestingly, although the rhombohedral minimum becomes shallower, the phase distribution around the rhombohedral minimum is still very sharp (Figure 4.16). To account for the broadening of the tetragonal peak in some compositions, it was assumed that the simulated grains in this region ($0 \leq \xi \leq 0.1$) belonged to the tetragonal phase. Because no such polarization clustering was observed along the rhombohedral directions the range $0.99 \leq \xi \leq 1$ was taken to be rhombohedral. These intervals are indicated by dotted lines in Figure 4.16. Interestingly, the model still predicted a small non-tetragonal and non-rhombohedral volume fraction in the remanent state of the rhombohedral compositions, which corresponds to the flat energy distribution between $\langle 100 \rangle_c$ energy minima and the $\langle 110 \rangle_c$ energy maxima.

The phase volume fraction in the saturated remanent state predicted by the model is depicted in Figure 4.18. It can be seen that the rhombohedral compositions increased in tetragonal composition by 19 to 31 % for PZT 40 and PZT 45, respectively, while the tetragonal compositions were predicted to increase in the rhombohedral content by 62 to 40 % for PZT 47 to PZT 60, respectively. With an applied compressive stress, the rhombohedral phase was more favorable due to the smaller electrostrictive coefficients, which resulted in a higher rate of stress-induced tetragonal→rhombohedral phase transitions. Moreover, it was found that the electrostrictive shear constant $\mathbb{Q}_{44}$ had a significant influence on the final predicted S_r/S_s ratio predicted by the model; at lower values of $\mathbb{Q}_{44}$ the rate of induced R→T transitions was increased, leading to a larger value of the obtained saturated remanent strain. Although this seems counterintuitive, it helps answer why a maximum on the rhombohedral side of the MPB is observed.

Previous idealized models for the maximum S_r/S_s ratio of the compositions only considered the initial switching strain of the sample from an unloaded (virgin) state [167, 168]. Following the results of the present model, the macroscopic observable remanent strain contains contributions from ferroelastic switching as well as from stress-induced phase transitions that seem to significantly increase the predicted S_r/S_s ratio in rhombohedral compositions. However, it should be kept in mind that the remanent strain is normalized only by the switching strain of the initial phase; the influence of other phases, i.e., stress-induced phase transition contribution, are not considered. Due to the larger spontaneous strain of the tetragonal phase relative to the rhombohedral phase, the S_r/S_s ratio in rhombohedral compositions can be significantly increased by induced R→T transitions. The remanent strain of the tetragonal phase is also a combination of both contributions from ferroelastic domain reorientation and induced T→R phase transitions. In this case, however, the stress-induced phase transition leads to an increase in the volume fraction of the rhombohedral phase, which has a smaller spontaneous strain than the original tetragonal phase. Even though the rhombohedral domain may be more favorably aligned to the applied compressive stress, the smaller rhombohedral spontaneous strain reduces the final composite remanent strain and decreases the S_r/S_s ratio. This also explains the smaller S_r/S_s ratio in PZT 40 compared to PZT 45. In PZT 40 the tetragonal phase is less stable than in PZT 45, evidenced by the increased shallowness of the $\langle 100 \rangle_c$ energy wells in the unstressed state (Figure 4.17). In PZT 40, this results in a reduction in the number of R→T phase transitions occurring during simulated mechanical compression (Figure 4.18). In addition, the spontaneous strain of the tetragonal phase is smaller for PZT 40 than PZT 45, meaning that the contribution of each R→T phase transition to the composite remanent strain is also diminished. Both of these effects result in a smaller S_r/S_s ratio for PZT 40 than PZT 45.

The maximum theoretical S_r/S_s ratio predicted by the present model for tetragonal compositions was smaller than the theoretical maximum of a ferroelasticity-only model, indicating a negative contribution from stress-induced T→R phase transitions on the maximum achievable remanent strain. Stress-induced T→R phase transitions and the increase in the spontaneous strain in the tetragonal phase were found to work counteractive against one another. The simulations predicted that during mechanical loading the rate of stress-induced T→R phase transitions is much larger in tetragonal compositions than the rate of stress-induced R→T phase transitions in rhombohedral compositions (Figure 4.18). The linear decrease in S_r/S_s with increasing tetragonality that was found in the present experimental measurements was not reproduced by the model predictions. This can be partly explained by the absence of local fields and interactions in the model that influence the reorientation ability of all domains. These local interaction effects are expected to make significant contributions to the achievable saturated state, with some effects such as intergranular stresses increasing with $PbTiO_3$-content. For example, local spontaneous strain-induced stresses have been shown to have a significant influence on the domain wall motion in various PZT compositions [186]. As a result, it was found that the Rayleigh parameters were significantly larger in the rhombohedral phase than in the tetragonal phase, which was attributed to local stresses originating from the increased spontaneous lattice distortions in the tetragonal phase exerting a clamping effect on the irreversible displacement of domain walls. A second possibility is the unsaturated remanent state in $PbTiO_3$-rich compositions due to the large coercive stresses. Interestingly, however, simulations showed the existence of stress-induced phase transition behavior to the metastable phase for an uniaxial compressive mechanical load far above the coercive stress in all materials. Although the predicted volume fraction of material that underwent a stress-induced phase transition, particularly on the tetragonal side of the MPB, seems unrealistically high, the simulations indicate that such transitions are possible and that they can provide an explanation for the extraordinary S_r/S_s values of the rhombohedral phase.

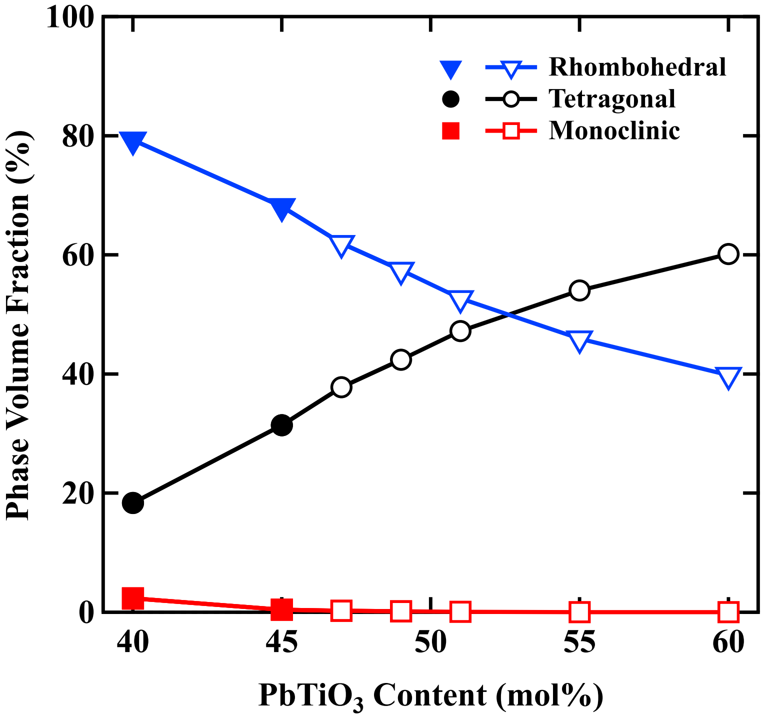

Figure 4.18: Predicted phase volume fraction in the saturated remanent state for PZT 40, 45, 47, 49, 55, and 60 after removing the uniaxial compressive strain. Filled symbols indicate compositions that were originally rhombohedral, while open symbols were originally tetragonal.

In real ceramic materials there are additional non-reversible processes to the high quality single crystals that were examined in the previous Chapter 3. These perturbations were not considered in the model and significantly limit the number of domains that can reorient or change their phase by an external load or may lead to back-switching processes of oriented domains during unloading. On the other hand, these additional factors can lead to a clamping of domains in their orientation and phase at maximum load. Moreover, irreversible changes of the lattice parameters induced by the applied load can contribute to the observed behavior of the samples and are not included in the model. All these factors may explain the observable imprecision of the model predictions with respect to the experimental observations. Despite this, the model is able to accurately predict the value and the change in the S_r/S_s ratio as a function of composition. Again, the importance of induced phase transitions on the observed nonlinear behavior of ferroelectric materials became apparent. The model showed that a small volume fraction of grains that undergo a non-reversible stress-induced R→T phase transition can significantly increase the experimentally measured S_r/S_s ratio in rhombohedral PZT with compositions in the vicinity of the MPB. Due to differences in the electrostrictive coefficients, T→R phase transitions were predicted to occur more easily than the converse R→T transitions, increasing the likelihood that the stress-induced phase transitions can be directly observed using laboratory (i.e., low-energy) X-rays where the penetration depths can cause surface measurements to significantly vary in comparison to bulk behavior.

As seen in the experiments, electrical loads also lead to an increase of the remanent strain for rhombohedral PZT compositions close to the MPB. The results are similar to that for the uniaxial compressive stress, and most of the previous discussion also applies to present results. However, there are some significant differences in the observed behavior that will be addressed in the following section. Firstly, the difference between the measured value and the theoretical maximum for ferroelectric switching is not as large as for the uniaxial compressive mechanical load. The comparison between the experimental values and the prediction by the model can be found in Figure 4.19 as a function of the $PbTiO_3$-content. It is apparent that the model again predicts the correct trend including the important features of S_r/S_s as a function of composition. The simulated points represent the new theoretical maximum values when both ferroelectricity and electric field-induced phase transitions are allowed during electrical loading. Again, the maximum value is found on the rhombohedral side of the MPB (PZT 45), with significantly decreasing values on either side. In general, the model also predicted S_r/S_s values in good agreement with the experimental data. The false trend at higher $PbTiO_3$-content may be due to the maximum applied field of 6 $^{kV}/_{mm}$, which was likely not large enough to reach a saturated state. It should be again emphasized that the used Landau coefficients have a significant impact on the simulation results, which is expected to be a primary cause for variations between model and experimental results and that local fields in the polycrystalline material also act to hinder the motion of domain walls and interphase boundaries and could lead to differences with simulations.

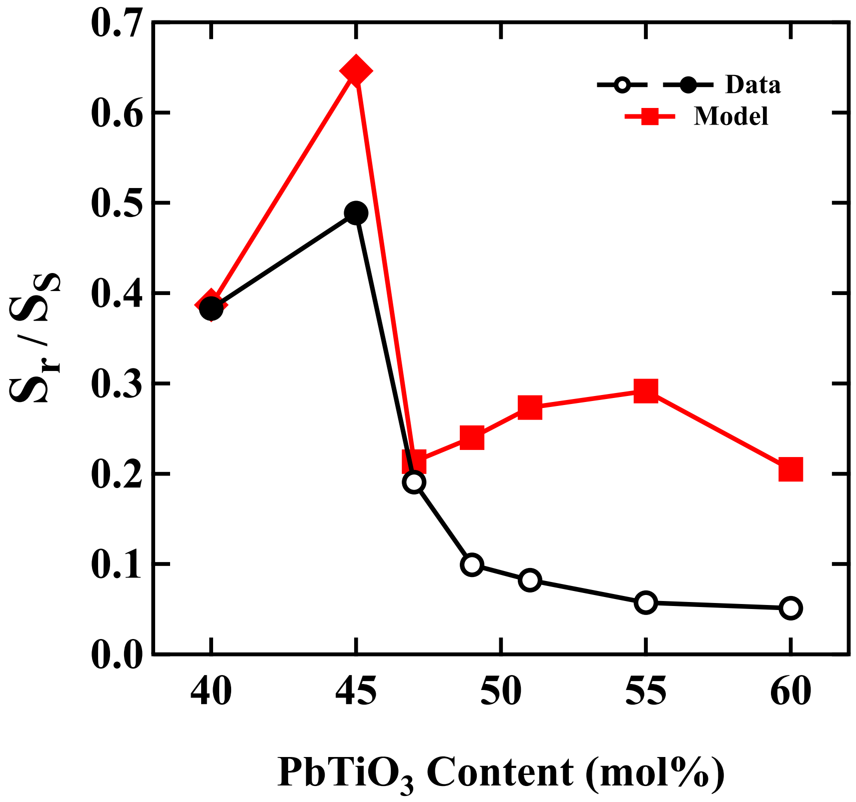

Figure 4.19: Comparison of experimental measurements and model results at room temperature. Filled symbols indicate compositions that were originally rhombohedral, while open symbols were originally tetragonal.

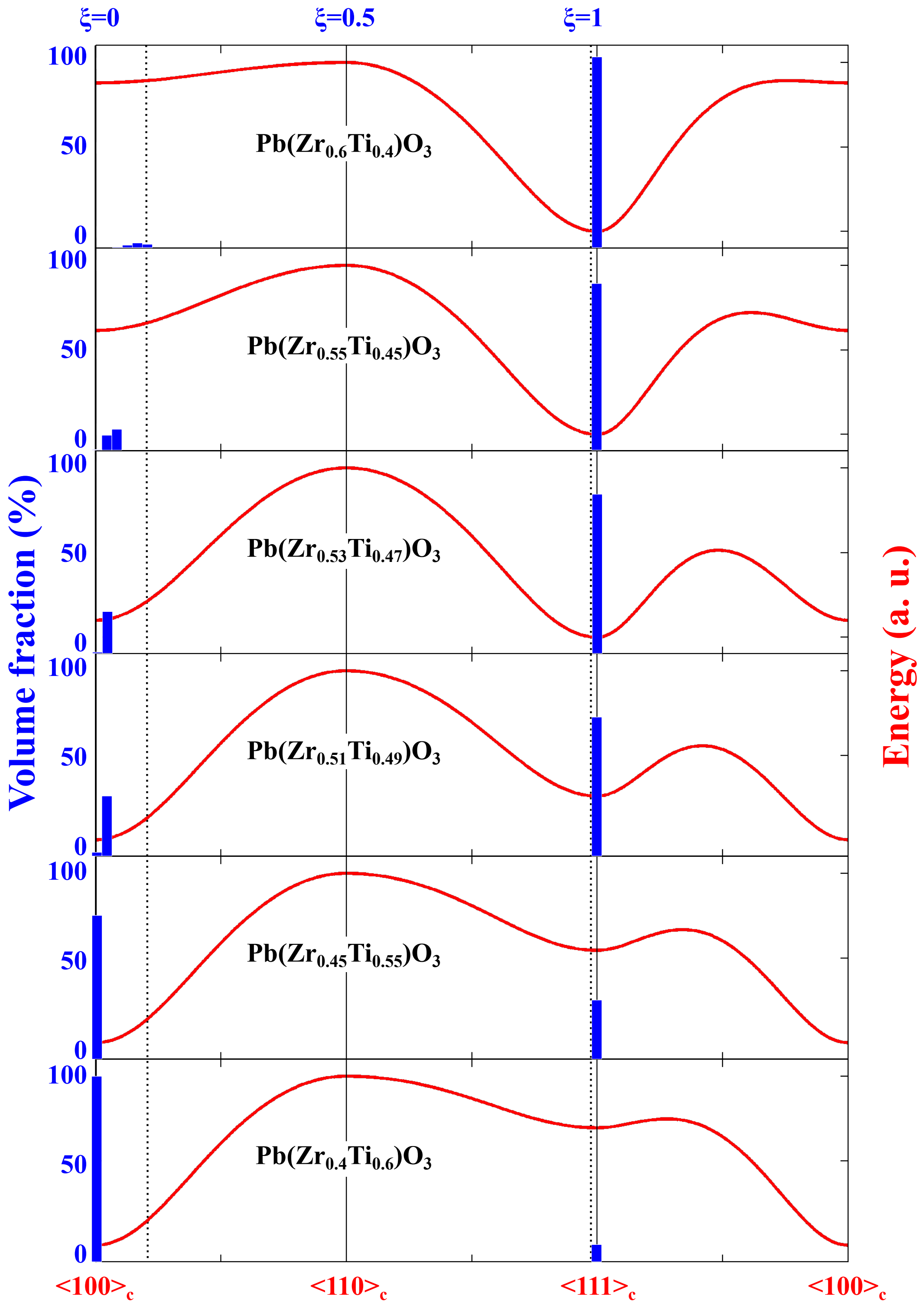

Figure 4.20: Minimal Landau energy between the tetragonal, rhombohedral, and orthorhombic crystallographic direction as explained in Figure 4.17 (red). History plot of the calculated phase distribution of PZT 40, 45, 47, 49, 55, and 60 in the equilibrium state after electrical unloading (blue). Black dashed lines indicate the chosen intervals in which the grain is treated as to be tetragonal $[0, 0.1]$ or rhombohedral $[0.99, 1]$.

The fraction of each phase after electrical unloading is illustrated with history graphs in Figure 4.20. Again the shallow tetragonal minimum in the rhombohedral compositions led to a broadening of the corresponding peak around $\xi = 0$. To account for the broadening of the tetragonal peak and to allow for comparisons with the results for mechanical loading the phase intervals for ξ were chosen according to the previous section: $0 \leq \xi \leq 0.1$ equates to the tetragonal phase phase and $0.99 \leq \xi \leq 1$ to the rhombohedral. Like before, a small non-tetragonal and non-rhombohedral volume fraction in the remanent state of the rhombohedral compositions was identified in the model predictions for PZT 40 that was an order of magnitude smaller than during mechanical loading. Interestingly, in all other compositions no monoclinic phase fraction was found.

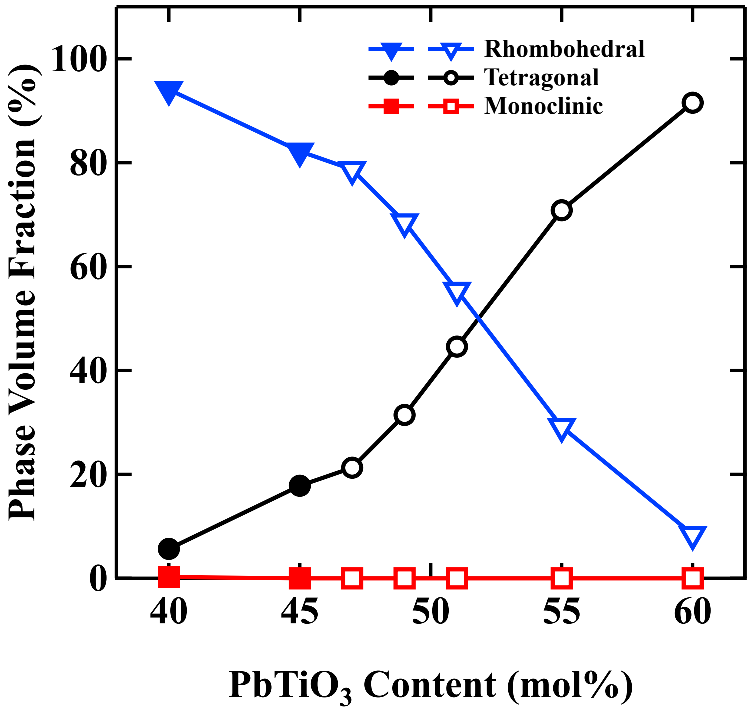

Figure 4.21: Predicted phase volume fraction in the saturated remanent state for PZT 40, 45, 47, 49, 55, and 60 after removing the electric field. Filled symbols indicate compositions that were originally rhombohedral, while open symbols were originally tetragonal.

The predicted phase volume fraction in the saturated remanent state for PZT 40, 45, 47, 49, 55, and 60 is shown in Figure 4.21. Like in the mechanical case, the flat local minima at the $\langle 100 \rangle_c$ crystallographic orientation of compositions with a low $PbTiO_3$-content lead to a broader phase distribution. This is, however, not as distinct as in the mechanical case because the total amount of tetragonal phase content in these compositions is much lower. By comparing the remanent phase content for mechanical and electrical loading (Figure 4.18 and 4.21), one can see that the rhombohedral compositions (PZT 40 and 45) increased in tetragonal content by 5 to 20 %, whereas the tetragonal compositions (PZT 47 to 49) increased in rhombohedral content by 68 to 80 %. Comparing these results with those for the mechanical loading (Figure 4.18) reveal differences in the rate of induced phase transitions of the particular compositions. It is apparent that the rate of the induced R→T transitions in both rhombohedral compositions (PZT 40, 45) is significantly lower (6 % and 18 %) than for mechanical loading (18 % and 31 %), as well as the rate of the induced T→R transitions in the tetragonal compositions with the highest $PbTiO_3$ (PZT 55, 60; 29 % and 8 % for electrical loading vs 46 % and 39 % for mechanical loading). Unlike electrical fields, which energetically favor only one direction, compressive stress energetically favors all directions perpendicular to the loading direction and therefore increases the possibility to switch into the direction of the opposite phase. Especially for PZT 60 the probability of T→R phase transitions is extremely low for electrical loading, which is also expected because differences in the electrostrictive coefficients between the teragonal and the rhombohedral phase that were proposed as the explanation for the higher rate of T→R phase transitions during mechanical loading do not influence the coupling between the electric field and the polarization. As previously stated, the small amount of a non-tetragonal and non-rhombohedral volume fraction that was found for compositions with a small $PbTiO_3$-content is much higher for mechanical than for electrical loading. It can be concluded that the differences in the electrostrictive coefficients lead to a different induced phase transition characteristic for electrical and mechanical loading. Interestingly, the rate of T→R phase transitions is nearly identical 50 % for compositions with a $PbTiO_3$-content around 52 %.

4.3 Conclusions

The ferroelectric and ferroelastic behavior of soft PZT with regard to the remanent strain as a function of composition was investigated. Experiments showed that the remanent state was strongly influenced by the spontaneous switching strain, which was determined by XRD measurements for PZT compositions from 40 to 60 mol% $PbTiO_3$-content around the MPB. It was found for some compositions that the remanent-to-switching strain ratio of the rhombohedral materials was significantly above the theoretical maximum for pure ferroelectric/ferroelastic realignment of domains. This behavior indicated the existence of additional non-linear irreversible processes that contribute to the electric field-strain/stress-strain behavior of these compositions. Electric field and stress-induced phase transitions were proposed as the key mechanism behind the observed behavior, motivated by the results from Chapter 3. To verify the hypothesis, the thermodynamic phenomenological model from Chapter 3 was expanded to account for the polycrystalline nature of the material system. This was done by neglecting the interactions between the individual single-crystal grains so that each grain could be solved individually. The necessary Landau potentials were taken from literature, whereas the electrostrictive coefficients were deduced from XRD measurements and predicted spontaneous polarization values. By extrapolating the measured spontaneous switching strain over the MPB it was possible to determine the electrostrictive coefficients of the tetragonal phase in rhombohedral compositions and vice versa. The predicted theoretical maximum remanent-to-switching strain values are in good agreement with those observed in the experimental measurements. The analysis of the stable phases of the remanent state after unloading revealed that a significant amount of induced phase transitions took place in every composition. Due to differences in the spontaneous strain and the electrostrictive coefficients between the tetragonal (T) and rhombohedral (R) phase, T→R phase transitions were predicted to occur more easily than the converse R→T transitions for the application of an uniaxial compressive stress. Deviations of the model results from the experimental results are due to the numerous approximations, i.e., neglecting domain pinning and back-switching induced by defects, phase boundaries, grain-to-grain interactions, etc. These results indicate that phase transitions may potentially play an important role in the ferroelastic and ferroelectric behavior of rhombohedral PZT at the MPB.

Due to their excellent electromechanical properties and relative thermal stability, lead based ferroelectric materials, such as lead zirconate titanate ($Pb(Zr_{1-x}Ti_x)O_3$, PZT), have been extensively used during the past 60 years in actuator and transducer applications [14]. An often cited example of such an application is a multi-layer stack actuator that can be integrated into novel diesel fuel injection systems [187]. The piezo-actuator provides an improved precision in the regulation of the fuel mass injection compared to the currently used electromagnetic solenoid systems, leading to a better fuel efficiency and a reduction of CO_2 emissions as well as engine noise [188, 189]. Unlike the traditional injection systems, the piezoelectric stack actuators show an exceptional response time that facilitates a nozzle needle reaction time on the order of micro-seconds [187], increasing the number of fuel injections per cycle [190]. It is believed that the transition to piezo-fuel injection systems in the automotive-industry could lead to a demand of about 10^8 actuators per year [187].

However, the use of lead-containing materials is today discouraged, due to their negative environmental impact. Recent EU regulations limit the use of lead and other toxic materials, as soon as a technologically equivalent alternative is available [191, 192]. Equivalent forms of this legislation have also been enacted in the United States (California), Korea, China, and Japan [193–196]. These regulations stimulate the scientific search for an alternative lead-free material that shows piezoelectric properties and ideally utilizes the well established solid-state processing route similar to PZT. To date, many of the large manufacturing firms are hesitant to invest heavily into the development of materials that may be banned in the near future, so that an implementation of this technology is still out of reach.

Numerous recent studies on lead-free BNT (bismuth sodium titanate) based ceramics revealed the exceptional piezoelectric properties of this class of materials. The reports on $(1\text{-}x\text{-}y)(Bi_{1/2}Na_{1/2})TiO_3\text{-}xBaTiO_3\text{-}y(K_{1/2}Na_{1/2})NbO_3$ (BNT-BT-KNN) [197], Ta- and Li-doped $Bi_{1/2}(Na_{0.82}K_{0.18})_{1/2}TiO_3$ (BNT-BKT) [198], $(1\text{-}x\text{-}y)(Bi_{1/2}Na_{1/2})TiO_3\text{-}xBi_{1/2}K_{1/2}TiO_3\text{-}y(K_{0.5}Na_{0.5})NbO_3$ (BNT-BKT-KNN) [199] and $(1\text{-}x\text{-}y)(Bi_{1/2}Na_{1/2})TiO_3\text{-}xBaTiO_3\text{-}y(K_{0.5}Na_{0.5})NbO_3$ (BNT-6BT-2KNN) [8] display unipolar strains that ever surpass that of PZT [154, 200]. The origin of this behavior has been found to be an electric field-induced transformation from the initial macroscopically nonpolar phase (NP) to an ordered macroscopically polar state (P) [201, 202]. The terms nonpolar and polar system states have been previously introduced by Jo et al. [203] in the original rationalization of the large strain materials. All materials are basically solid solutions of a rhombohedral ($(Bi_{1/2}Na_{1/2})TiO_3$, bismuth sodium titanate) and a tetragonal ($BaTiO_3$, barium titanate) phase. The addition of dopants like $K_{1/2}Na_{1/2}Nb)_3$ (potassium sodium niobate) allows the adjustment of the field-induced NP→P phase transition. By the initial application of an external electrical field, the NP material undergoes an electric field-induced NP→P transition. The fact that NP and P states are energetically similar, leads to a transition field that is significantly lower than the dielectric breakdown strength. Similar to the previously discussed field-induced transition between two ferroelectric phases, the NP→P transition is accompanied by an extraordinary unipolar strain. In the case of a fully reversible transition, this unipolar strain can be recovered during the removal of the electric field. The reversibility of the NP→P transition is influenced by the dopant concentration, because it destabilizes the long range order of the polar phase. Unfortunately, the electric fields required to generate the NP→P transition in KNN doped BNT-BT are lager than $4\,{}^{\mathrm{kV}}/_{\mathrm{mm}}$ [204], which is too large for actuator applications. One approach to overcome this drawback are hetero-structures, in which the high-strain nonpolar material is combined with chemically compatible polar materials with a coercive field below the transformation field [205]. Such a structure is also called composite material. The principle idea is that the polar grains influence the electric field, mechanical strain, and polarization of the nonpolar matrix in their direct vicinity and therewith serve as ”crystallization seeds” for the field induced NP→P phase transition. Different approaches for the realization of such structures are possible. A common approach for ferroelectric composite materials are so called core-shell structures, where each main material grain (in our case the nonpolar material) of the polycrystalline composite contains a smaller core of the seed material (in our case the polar material), as illustrated in Figure 5.1. Composite materials of this type were often used to tailor the phase transition behavior of ferroelectric materials [206–208]. These types of structures are manufactured by mixing the calcined starting powders with a different particle size distribution of both materials before the final sintering step, whereas the sintering temperature is chosen, to avoid diffusion between both materials and therewith a formation of a mixed phases during sintering.

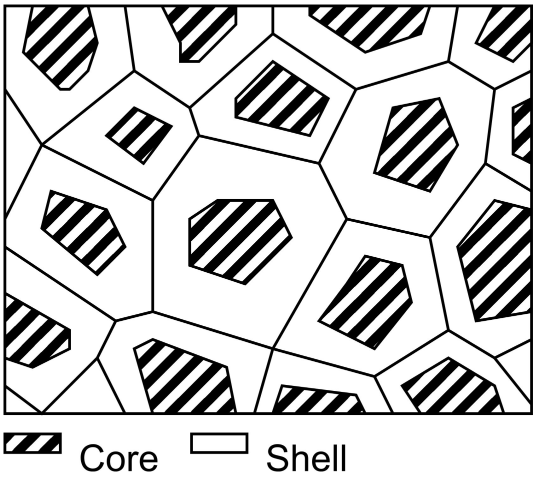

Figure 5.1: Scheme of a composite core-shell structure. The black striped regions represent the polar core ("seed"), the white regions represents the nonpolar grain shell ("matrix").

A good candidate for such a material is undoped BNT-BT that undergoes a non-reversible NP→P transition during the initial electric field loading cycle, at which the long range order remains stable during unloading [88, 204]. It was shown that the inclusion of BNT-BT seed grains into a polycrystalline BNT-BT-KNN matrix results in an effective reduction of the transition nucleation energy, allowing for the exceptional NP→P poling strain to be re-harnessed with each electric field cycle at lower electric fields ($< 4\,^{\mathrm{kV}}/_{\mathrm{mm}}$). By varying the volume fraction of the polar material, the composition can be tailored for optimum electromechanical properties. According to the literature, BNT-BT materials with a fully reversible induced NP→P phase transition may also be termed a nonergodic relaxor, whereas the KNN doped material BNT-BT-KNN with a stable polar phase can be described as an ergodic relaxor [89].

The piezoelectric properties of $(1\text{-}x)(Bi_{1/2}Na_{1/2})TiO_3\text{-}xBaTiO_3$ (BNT-BT) systems were shown more than 20 years ago [209]. Due to the worldwide inaction of regulations [191–196] strictly limiting the use of toxic lead-containing materials, the search for alternative lead-free piezo-materials brought these materials back into the scientific focus in recent years. The solid solution of the rhombohedral BNT and the tetragonal BT end members is found to form a morphotropic phase boundary (MPB) at approximately 6-7 mol% BT, where a maximum in piezoelectric properties is found [209–213]. However, this increase in the piezoelectric properties is accompanied by a decrease in the depolarization temperature at the MPB, limiting the usefulness in high temperature sensor applications [214].

Recent diffraction investigations with electrons [202, 215], X-rays [188, 216, 217], and neutrons [73, 218] revealed that BNT-BT compositions near the MPB possess a pseudo-cubic crystal structure at room temperature. Furthermore, it was shown by in situ structural investigations that the application of external fields, leads to the induction of an irreversible structural phase transformation from pseudo-cubic to a lower symmetry phase [73, 88, 204, 215–219]. These field induced structural phase transitions were identified to be responsible for the enhanced strain capabilities of BNT-based ceramics [220] and single crystals [221], in addition to large poling strains [204]. Unfortunately, in some compositions the poling process leads to a stable polar phase content that results in a large remanent strain and corresponding decrease in the effective usable strain that can be repeatedly produced for unipolar working cycles after poling. The irreversibility of the electric field-induced phase transformation is affected by the stability of the ferroelectric order. It was shown that the remanent polar phase of a perovskite ferroelectric can be destabilized by a substitution with right dopant material, like $K_{0.5}Na_{0.5}NbO_3$ [222]. This can significantly increase the effective usable strain because poling strain remains relatively unaffected by the KNN-doping [203].

Moreover, significant unipolar strains of lead-free piezoelectrics have been reported for aged single crystal BT [223], Mn-doped BST [224], and KNN [225], where the aging-induced point defect structure destabilizes the remanent polarization state during unloading, which allows essentially for the poling strain to be obtained during each electric field cycle. This effect, however, is highly sensitive to temperature and loading, reducing the usability of these materials for applications. The maximum usable strain in BNT-BT-KNN was found for the composition of approximately 0.92BNT-0.06BT-0.02KNN at room temperature [197]. In compositions with a lower KNN content the polar phase is no longer completely destabilized resulting in a decrease in the effective usable strain as well as a decrease in the coercive field. When the KNN content is increased the polar phase is excessively destabilized, which results in a decrease in the effective strain and an increase in NP→P transition-field [216]. Similar large unipolar strain behavior has been observed in numerous other BNT-based lead-free compositions, such as $Bi_{1/2}Na_{1/2}TiO_3$-$(Bi_{1/2}Li_{1/2})TiO_3$-$Bi_{1/2}K_{1/2}TiO_3$ (BNT-BLT-BKT) [226], $Bi_{1/2}Na_{1/2}TiO_3$-$SrTiO_3$ (BNT-ST) [227], $Bi_{0.5}(Na_{0.75}K_{0.25})_{0.5}TiO_3$-$BiAlO_3$ (BNKT-BA) [205], and Mn-doped $Bi_{1/2}Na_{1/2}TiO_3$-$Bi_{1/2}Li_{1/2}TiO_3$-$BaTiO_3$ (BNT-BLT- BT) [228] as well as KNN-based lead-free compositions, such as textured $(K_{1/2}Na_{1/2})NbO_3$- $LiTaO_3$ (KNN-LT) [222].

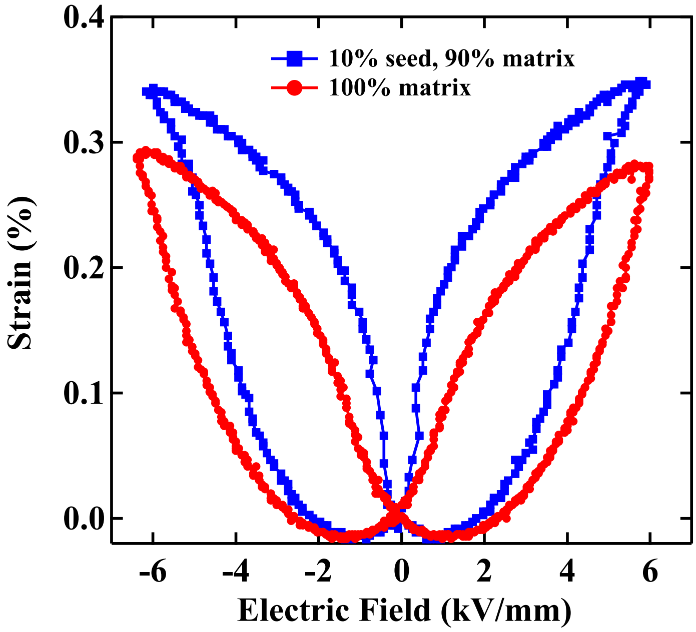

Figure 5.2: Large signal *S-E* curves of pure nonpolar matrix material (BNT-6BT-2KNN, red) and a composite material consisting of the same matrix material with 10% ferroelectric (BNT-7BT, blue) material*. The electric field, which is necessary to reach similar strain values is lowered by approximately 20% by the polar seeds. Therefore higher maximum strains can be realized.

Recent large signal measurements performed by Groh et al. (Figure 5.2) on non-polar (1-x-y)$(Bi_{1/2}Na_{1/2})TiO_3$-x$BaTiO_3$-y$(K_{0.5}Na_{0.5})NbO_3$ (BNT-6BT-2KNN) again demonstrated the suitability of the composite approach. By including different amounts of polar seed grains (1-x)$(Bi_{1/2}Na_{1/2})TiO_3$-x$BaTiO_3$ (BNT-7BT) into the BNT-6BT-2KNN it was possible to significantly decreases the poling field, which is necessary to create reasonable mechanical strains. At the same time, the incorporation of seed material leads to the formation of a remanent state that decrease the effective usable strain that can be repeatedly produced for unipolar working cycles. Both effects were shown to strongly depend on the volume fraction of polar seed material. The maximum value of the effective piezoelectric coefficient $d_{33}^{\star}$ at 4 kV/mm was found for a seed content of 10 %. New model approaches are necessary to understand the relation between the seed content and the observable piezoelectric coefficient $d_{33}^{\star}$ for different maximum fields. These models can also help to further improve the electro-mechanical properties of composite materials by identifying optimal material combinations and optimizing the microstructure for the next generation of composite materials. In the following chapter, a macroscopic equivalent circuit model approach is presented in detail. The predictive capability of the model is validated by a comparison of the model results to available experimental data. A subsequent study of seed material characteristic is presented to predict optimal material combinations and the resulting optimal seed concentrations. The results from the presented study are part of a manuscript that is submitted for publication in Advanced Functional Materials [229].

---

[*] Experiments were performed by Claudia Groh and Wook Jo, TU Darmstadt

The electromechanical response of a composite material to the application of an external electrical field is a complex process, even if the response of both constituent materials are known. Actually, one could presume that the difference in the large signal polarization hysteresis of the nonpolar matrix and the polar seed material leads to an inhomogeneous polarization distribution inside the composite under an external electrical load. An inhomogeneous polarization distribution, however, would lead to the formation of internal charge distributions and an increase in the internal energy of the system, if the resistivity of both materials and the grain boundaries is large enough to be neglected. It is, therefore, more likely that each material experiences a different field caused by the formation of local fields, reducing the formation of internal charges and the differences in the local polarization. A theoretical description of these local fields is very difficult because of the complex microstructure of composites. A possibility to decrease the complexity of a composite material, allowing for the study of the electrostatic interactions between both materials, is to represent the complex microstructure of the composite material by an equivalent capacitor circuit. Such equivalent circuit models have been previously used to interpret impedance spectroscopy data from ferroelectric materials [27] and to model the interaction between the surface and the polycrystalline microstructure of PZT [230] and the behavior of ferroelectric switching devices [231]. In 1996, Dausch et al. [232] used an equivalent circuit model to simulate the field enhancement in ferroelectric/antiferroelectric PLZT-based composites. Due to the lack of computation power they were only able to solve the minimization problem graphically. A necessary prerequisite for the applicability of such a model is that a mixed phase at the grain boundary between grains of the different base materials is not formed during sintering and that the mechanical and short-range interaction between the unit-cell polarizations are negligibly low.

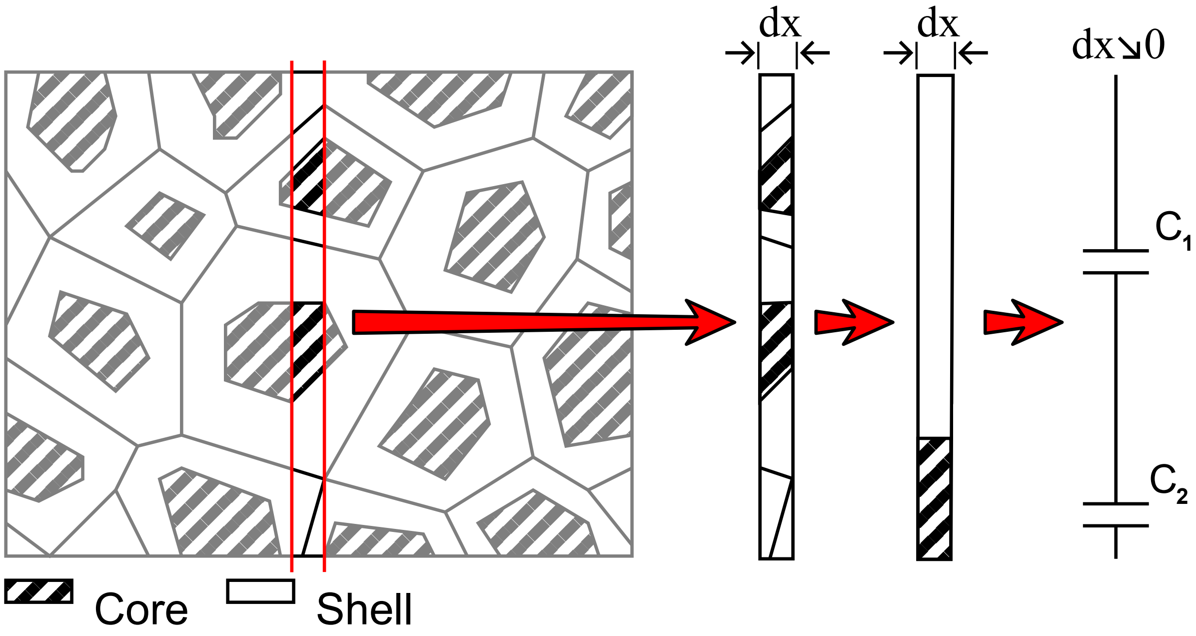

Figure 5.3: Equivalent circuit simplification scheme. The material is divided into thin sections dx. Each section can be represented by two nonlinear capacitors in series configuration for the limit $dx \searrow 0$.

To obtain an appropriate equivalent circuit representation of the composite, the sample is divided into small sections perpendicular to the electrodes, as described in Figure 5.3. As the thickness of the chosen section decreases to zero, it can be assumed that the grain boundaries are perpendicular to the slicing directions. By neglecting the interactions between neighboring sections each part can be represented by a capacitor with nonlinear history dependent constitutive behavior, defined by the NP and P materials. The capacitor thickness can be determined by the ratio of the respective volume fractions of both materials assuming unit area. Because of the stochastic spacial distribution of both materials in the composite, statistical fluctuations of the plate separation distance of the capacitors in each section is expected. It should be pointed out that a more robust equivalent circuit representation of the composite material is a parallel connection of multiple series connections, each representing one section of the material, consisting of two capacitors with a stochastic distributed plate separation distance. The standard deviation of this stochastic distributed plate separation distance is a function of the sample thickness and the average grain size. The standard deviation for most macroscopic samples is very small, meaning that the result is nearly identical to the simplification of only one series connection with a plate separation distance proportional to the composition ratio of the composite material. If the polarization response of both materials is known, it is possible to estimate the total system polarization by using Kirchhoff's second law:

$$\sum_{k=1}^{n} U_k = U_{applied}, \tag{5.1}$$

which reads as that the total applied voltage $U_{applied}$ distributed between both capacitors so that the connection between the matrix-capacitor (U_1 is distributed to C_1) and the seed-capacitor (U_2 is distributed to C_2) remains charge free. In other words, the polarization of both materials must remain identical for all external electrical loads. In this work, the respective large signal response of a composite material with a known matrix-seed ratio to a given electric loading scenario is calculated by dividing the loading path into smaller monotonic loading steps. Starting from an arbitrary initial external electrical load and the corresponding voltage distribution that fulfills Kirchhoff's second law, a binary search algorithm minimizes the difference in polarization of both materials in order to determine the voltage distribution of the next loading step.

The necessary information about the change in polarization due to the change in the external field of the pure base materials can be directly obtained from dielectric large signal measurements of both materials. However, it is not possible to use the experimental data without proper post-processing; the binary search requires a monotonically increasing (decreasing) polarization with increasing (decreasing) voltage without any noise, which is always present in experiments. Smoothing algorithms can be used to convert the experimental data into the right form, but one must be careful to ensure that the shape of the P-E loop is not significantly changed by the smoothing algorithm. A far more serious problem is that the electric loading conditions for each material that occur in the composite during a defined loading cycle are unknown. P-E loops of a nonpolar or polar material consist of different reversal and irreversible processes [233], which makes it difficult to deduce the exact shape of a large signal *P-E* or *S-E* hysteresis from a single known loop, measured for a different maximum/minimum electric loading [234]. This problem also occurs in the optimal control of ferroelectric actuators, which makes control-loops [235] or complex hysteresis models necessary [236, 237]. These models, however, require a number of measurements with different maximum/minimum electric loading conditions to predict the exact polarization response of both initial materials.

5.1.1 Linear Hysteresis Model

An approach to model the nonlinear polarization response of both materials is to use a piecewise linear model of the large signal hysteresis loop of both initial materials. Furthermore, it is possible in this approach to vary the characteristic key values, e.g., the coercive field E_C or the remanent polarization P_r of the polar material, of both curves to study their influence on the physical properties of the composite, and therewith identify optimal materials for the next generation composite materials. The respective *P-E* behavior divided into different segments that can be linearly fit without loosing too much information about the shape of the experimental curve. The scheme of this approximation of both materials can be seen in Figure 5.4 and 5.5.

Polar Material Model

In the case of a polar material, the connection points between the different linear segments are referred to as (A), (B), (D), (E), (M), and (F). The coordinates of each of this points, e.g., (E_A, P_A) for point (A), are the model parameters that are adjusted to the experimental data and define the shape of the P-E loop. ϵ_n, ϵ_p, ϵ_g, ϵ_f, and ϵ_s denote the slopes of the different segments. They are determined directly from the coordinates of the two connection points of the corresponding segment, e.g.:

$$\epsilon_p = \frac{P_B - P_A}{E_B - E_A} \tag{5.2}$$

A piecewise linear approximation of full bipolar polarization hysteresis cycle of a polar material is shown in Figure 5.4 (a). A full hysteresis curve is reached, if the amplitude of the applied electric load E^{max} lies above E_D. In the initial state, the material begins at point 0, found at the origin. Here, the polarization and the applied field are zero. When the applied electric field is increased for the first time, the sample shows a virgin curve behavior. As long as the applied external field remains smaller that E_A the polarization response is just linear with a slope of ϵ_n and no hysteresis. This corresponds to the dielectric behavior of real polar systems, where a small electric field is not able to induce any non-reversible domain switching or domain-wall movement. Above E_A, the slope increases significantly $\epsilon_p > \epsilon_n$. This segment is called the poling curve, were most of the domains are irreversibly oriented into the direction of the external field. When E_B is reached, most of these irreversible poling processes have taken place. However, some domains of the polycrystalline polar material are clamped by defects, or other inhomogeneities, so that a small amount of domains can still be reoriented by higher fields. The slope of this high field poling segment ϵ_g is significantly smaller than ϵ_p. Point (M) denotes the polarization at maximum field that was applied during the measurement. This value is only necessary to determine ϵ_g and the slope for the linear decrease, when the field is reduced (ϵ_f). It is assumed that above E_F all of the high field domain reorientation processes have taken place. In most cases, the maximum applied field during measurement E^{max} is not large enough to induce all possible polarization reorientation processes and the sample is still inside the high field poling segment. In such cases, E_F can only be roughly estimated. The behavior for electric field amplitudes above the experimental measurements are indicated by dashed lines in Figure 5.4 (a). When the field is reduced back to zero only reversible polarization changes take part. In this reversible segment, the polarization decreases with a slope of ϵ_f. For $E^{max} \leq E_F$, the value of the remanent polarization P_r at $E = 0$ is a function of E^{max}:

$$P_r = P^{max} - \epsilon_f E^{max} \tag{5.3}$$

For decreasing electrical field it is assumed that above E_E no irreversible ferroelectric switching processes take place. Ferroelectric switching, meaning a reorientation the majority of domains happens between E_E and E_D, which is accompanied by a much steeper switching slope ϵ_s. The coercive field is given by the following relation:

$$E_C = \frac{P_E}{\epsilon_s} + E_E = \frac{E_D - E_E}{P_E - P_P} P_E + E_E \tag{5.4}$$

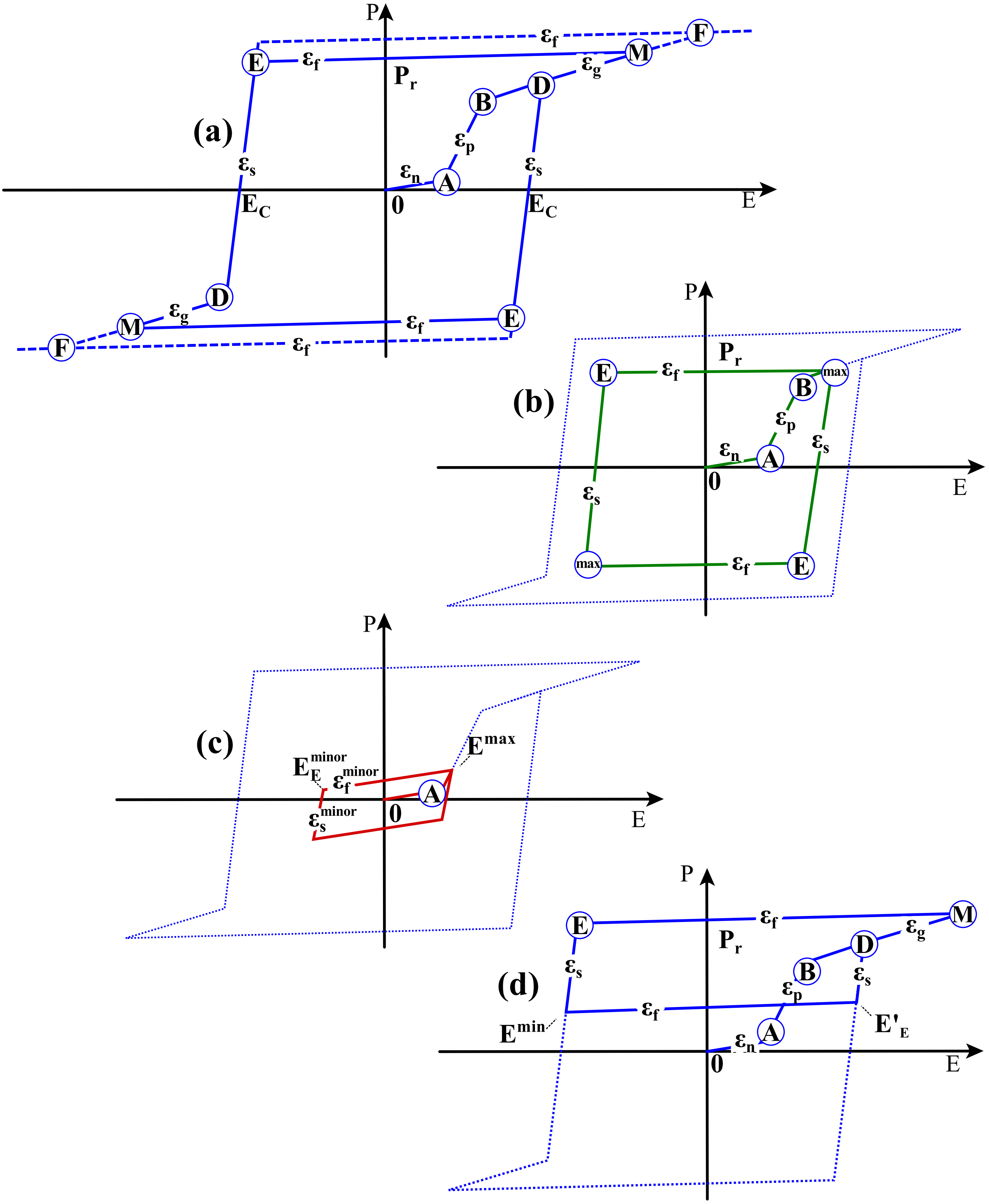

Figure 5.4: Piece-wise linear approximation of a polar large signal P-E hysteresis curve, including a description of all important model parameters and slopes. The connecting points between the different linear segments are referred to (A), (B), (D), (E), (M), and (F). ϵ_n, ϵ_p, ϵ_g, ϵ_f, and ϵ_s denote the slopes of each segment. (a) is a full bipolar polarization hysteresis curve, (b) and (c) are bipolar polarization hysteresis curves for smaller maximum electrical fields. (d) is an unsymmetrical polarization hysteresis that appears for sesquipolar loading scenarios. The dotted lines indicate the course of the full hysteresis.

It should be remarked that E_E in Figure 5.4 (a) is marked for field amplitudes that are the same as in the experimental data. For different field amplitudes, E_E depends on the maximum electrical field that was previously applied to the polar system, e.g., in case of higher fields (dashed lines) it can be seen in Figure 5.4 (a) that P_E increases, whereas E_E decreases. Both values are given by:

$$E_E = \frac{-P_D - P^{max} + E^{max}\epsilon_f + E_D\epsilon_s}{\epsilon_s - \epsilon_f} \tag{5.5}$$

$$P_E = -P_D + (E_D - E_E)\epsilon_s \tag{5.6}$$

where P^{max} is the maximum polarization that is reached at $E = E^{max}$. For amplitudes above E_F, E_E and P_E no longer change. It is important to mention that in the case of a full hysteresis the value of the coercive field does not depend on E^{max}. If the electrical field is below E_D, the slope ϵ_g becomes again flatter, as all domains that are not clamped by defects or inhomogeneities have switched into the direction of the external electrical field. The system is again in the high field poling segment. Without the virgin poling curve, a symmetric bipolar loading results in a symmetric hysteresis curve.

In Figure 5.4 (b), a minor hysteresis is shown that results from a bipolar electric load with an amplitude E^{max} below E_D, but still above E_B. The poling curve of the virgin system and all slopes ϵ_n, ϵ_p, ϵ_g, ϵ_f, and ϵ_s remain the same. The main difference to the previously described full hysteresis is that the apparent coercive field is no longer independent from E^{max}. E_E, P_E, and E_C are given by:

$$E_E = \frac{-2P^{max} + E^{max}(\epsilon_f + \epsilon_s)}{\epsilon_s - \epsilon_f} \tag{5.7}$$

$$P_E = -P^{max} + (E^{max} - E_E)\epsilon_s \tag{5.8}$$

$$E_C = E^{max} + \frac{P^{max}}{\epsilon_s} \tag{5.9}$$

If the amplitude E^{max} is smaller than E_D the electrical field is not able to align all unclamped domains inside the polar system, which drastically influence the characteristic values. This is shown in In Figure 5.4 (c). The switching slope ϵ_s^{minor} becomes a linear combination of the original value ϵ_s and the poling slope ϵ_p and the slope of the reversible segment ϵ_f^{minor} becomes a linear combination of the original value ϵ_f and the linear low field response ϵ_n:

$$\epsilon_s^{minor} = f \cdot \epsilon_s + (1 - f) \cdot \epsilon_p \tag{5.10}$$

$$\epsilon_f^{minor} = f \cdot \epsilon_f + (1 - f) \cdot \epsilon_n \tag{5.11}$$

The factor f that determines both slopes is determined by the maximum absolute electric field, which was reached during the loading path:

$$f = \frac{||E||^{max} - E_A}{E_B - E_A} \tag{5.12}$$

The other characteristic values are given by:

$$E_E^{minor} = \frac{-2P^{max} + E^{max}(\epsilon_f^{minor} + \epsilon_s^{minor})}{\epsilon_s^{minor} - \epsilon_f^{minor}} \tag{5.13}$$

$$P_E = -P^{max} + (E^{max} - E_E)\epsilon_s^{minor} \tag{5.14}$$

$$E_C = E^{max} + \frac{P^{max}}{\epsilon_s^{minor}} \tag{5.15}$$

The linear model is also able to represent the polarization for unipolar or sesquipolar loading scenarios. In Figure 5.4 (d) an example of a hysteresis loop for sesquipolar loading is shown. When the field is first increased the P-E loop is identical to the full hysteresis case that was described before. This time, however, the field is not fully reversed. In the example depicted in Figure 5.4 (d) the minimum applied field E^{min} lies below E_E and above E_D, in the middle of the ferroelectric switching process. When the field is increased again, the polarization increases with ϵ_f until E'_E an the P-E returns to the previous high-field behavior. If E^{min} lies above E_E, no switching takes place. In this case the polarization curve that is provided by the model is a linear line:

$$P(E) = P_r + \epsilon_f E \tag{5.16}$$

These sesquipolar loading scenarios are assumed to occur during unipolar loading of a composite material, where the remanent polarization of the polar seed leads to a stabilize the loading field in the matrix material, that is macroscopically compensated by a negative field in the seed material. Other unipolar/sesquipolar P-E loops for E^{min} below E_D or E_B are determined analogously.

Nonpolar Material Model

For the representation of the nonpolar material, a similar model of the large signal hysteresis can be implemented. In the ideal case, the NP→P phase transition that is induced by the external field is completely reversible if the external electric field is reduced to zero, which would lead to a vanishing remanent polarization. Most nonpolar materials, however, show a remanent polarization; the induced polar phase does not completely decay [238]. Measuring at higher temperatures or at lower frequencies results in a significant decrease in the remanent polarization. These conditions, however, do not match those of potential applications. This remanent polarization has to be included in the model. A scheme of the model representation of full bipolar P-E double loop hysteresis of a nonpolar material can be found in Figure 5.5 (a). The connecting points between the different linear segments are referred to as (A), (B), (C), (D), (E), (M), and (F). Like before, the coordinates of each of these points, e.g., $(\tilde{E}_B, \tilde{P}_B)$* for point (B), are the model parameters that have to be adjusted to the experimental data and define the shape of the P-E loop.

Applied electrical fields below $\tilde{E}_A$ result in a non-hysteretic linear dielectric response with a slope of $\tilde{\epsilon}_p$. Above $\tilde{E}_A$, the material is still in the nonpolar phase. However, since we are dealing with a polycrystal that contains defects and inhomogeneities, a small volume fraction is already polar and can be irreversibly aligned by the applied electrical field. This irreversible reorientation leads to a larger slope $\tilde{\epsilon}_n$ and the formation of a remanent polarization P_r:

$$\tilde{P}_r = \tilde{P}^{max} - \tilde{E}^{max} \cdot \tilde{\epsilon}_p, \tag{5.17}$$

whereas the maximum value of the remanent polarization is given by:

$$\tilde{P}_r = \tilde{P}_E - \tilde{E}_E \tilde{\epsilon}_p, \tag{5.18}$$

Between $\tilde{E}_B$ and $\tilde{E}_C$ the applied electrical field induces a NP→P phase transition. This leads to a significant increase of the slope of the P-E curve $\tilde{\epsilon}_t$. The poling field of the nonpolar material E_{pol} can be defined as the average of $\tilde{E}_B$ and $\tilde{E}_C$:

$$E_{pol} = \frac{1}{2}(\tilde{E}_B + E_C) \tag{5.19}$$

Above $\tilde{E}_C$, the slope again decreases as the majority volume fraction is in the polar phase. The slope in this high field segment includes NP→P phase transitions from regions with higher critical fields caused by defects and inhomogeneities or domain reorientation processes of already polar regions. Again, it is assumed that above a certain electrical field $\tilde{E}_F$ all of these high field processes have taken place and the slope of the P-E curve decreases again ($\tilde{\epsilon}_f$). This point is often not achieved in measurement, as the maximum applied field E^{max} is not large enough; $\tilde{E}_F$ can only be estimated. The assumed high field behavior is indicated by dashed lines in Figure 5.5 (a).

When the electrical field is reduced the polarization decreases with the high field slope $\tilde{\epsilon}_f$. A characteristic value for the spontaneous polarization P_S of the polar phase can be determined by extrapolating the linear trend to $E = 0$:

$$P_S = \tilde{P}_M - \tilde{\epsilon}_f \tilde{E}_m \tag{5.20}$$

---

* ˜ is used to distinguish between the material parameters of the polar and the nonpolar model.

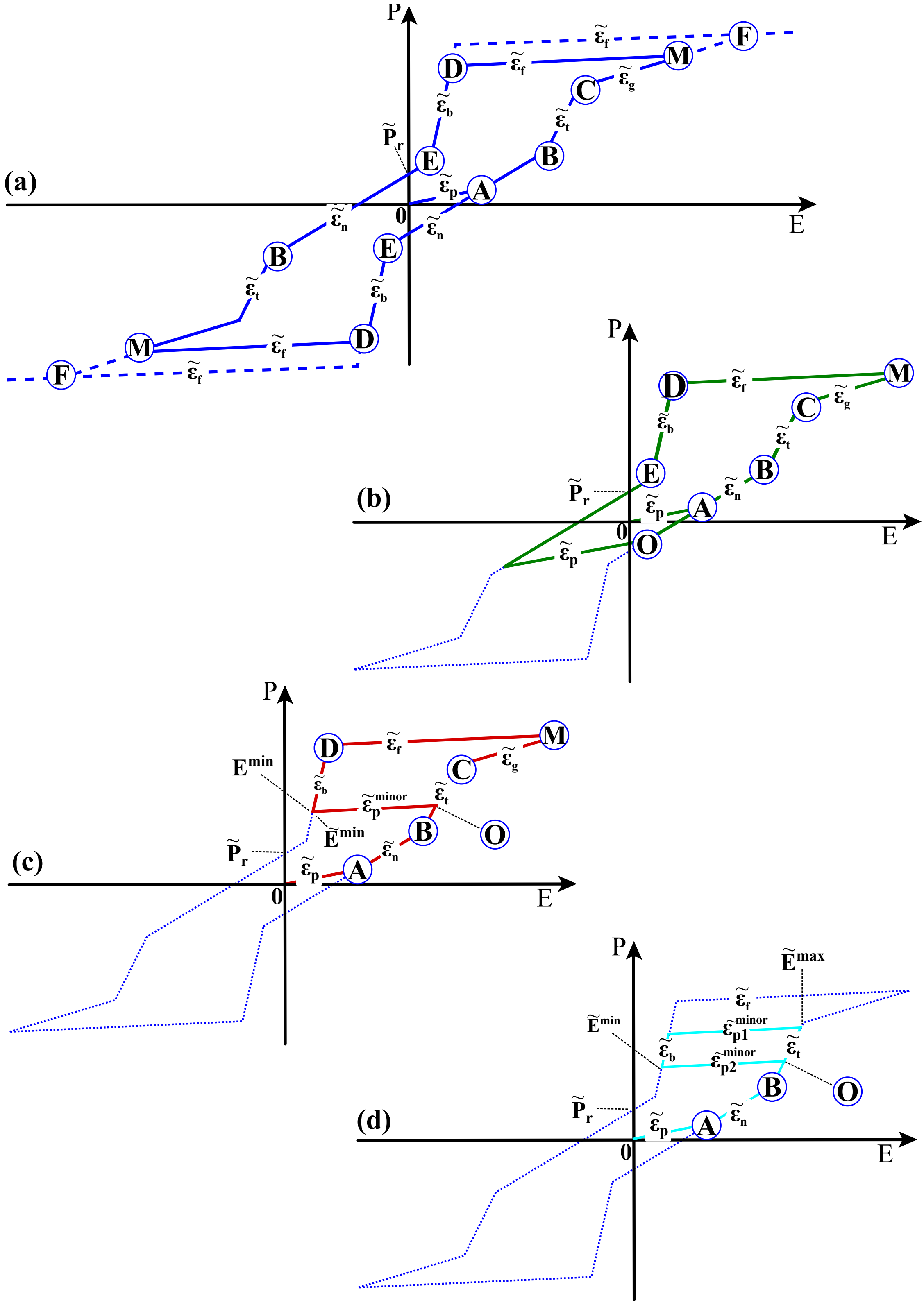

Figure 5.5: Piece-wise linear approximation of the large signal P-E double loop hysteresis curve of the nonpolar material, including a description of all important model parameters and slopes. The connecting points between the different linear segments are referred to (A), (B), (C), (D), (E), (M), and (F). $\tilde{\epsilon}_p$, $\tilde{\epsilon}_n$, $\tilde{\epsilon}_t$, $\tilde{\epsilon}_f$, $\tilde{\epsilon}_g$, and $\tilde{\epsilon}_b$ denotes the slopes of each segment. (a) is a full bipolar polarization hysteresis curve, (b), (c), and (d) are polarization hysteresis curves for sesquipolar loading scenarios with different minimum and maximum electrical fields, whereas the dotted lines indicates the course of the full hysteresis.

Below $\tilde{E}_D$ the system undergoes a phase transition to its nonpolar phase. This results in a much steeper slope $\tilde{\epsilon}_b$. It should be mentioned that the connection point (D) in Figure 5.5 (a) is marked for the maximum field that was applied during the experiment. The maximum electrical field that is applied to the system E^{max} influences the field at which the back-transition processes start. The position of (E) as well as the slope of the back-transition segment were kept constant:

$$\begin{aligned}\tilde{E}_D &= \frac{1}{\tilde{\epsilon}_b - \tilde{\epsilon}_f}\left(\tilde{E}_E\tilde{\epsilon}_b - E^{max}\tilde{\epsilon}_f + P^{max} - \tilde{P}_E\right) && (5.21)\\ \tilde{P}_D &= (\tilde{E}_D - \tilde{E}_E)\tilde{\epsilon}_b + \tilde{P}_E && (5.22)\end{aligned}$$

where P^{max} is the maximum polarization that is reached at $E = E^{max}$. At $\tilde{E}_E$ all reversible regions have transformed to the nonpolar phase. As mentioned above, the NP→P phase transition is not fully reversible, so a remanent polarization value can be observed at $E = 0$. In this nonpolar segment the polarization slope is again $\tilde{\epsilon}_n$. In addition to the virgin part between $E = 0$ and $\tilde{E}_A$, which only occurs during the first loading cycle, the hysteresis curve for a bipolar loading scenario is symmetric.

Different sesquipolar loading scenarios are possible that have to be addressed in the model. In Figure 5.5 (b) the maximum electric field that is applied in the negative direction E^{min} is still above $-\tilde{E}_B$ so no NP→P phase transition can be observed. When the electric field is increased, the polarization increases with the slope $\tilde{\epsilon}_p$ until it reaches the full hysteresis curve (O). As mentioned in the description of the linear hysteresis model of the polar material, a unipolar electric load applied on a composite material will lead to an internal field distribution at $E^{external} = 0$. Because of the remanent polarization of the polar seed material the local field inside the nonpolar matrix material will not be reduced to zero. Such a loading scenario is depicted in Figure 5.5 (c), where E^{min} is positive and lies between $\tilde{E}_E$ and $\tilde{E}_D$, meaning that the P→NP back-transition was not complete. In this case, the polarization increases with a slope $\tilde{\epsilon}_p^{minor}$ for an increase in the electrical field that is a linear combination of $\tilde{\epsilon}_p$ and $\tilde{\epsilon}_f$, depending on E^{min}:

$$\tilde{\epsilon}_p^{minor} = (1-f)\cdot\tilde{\epsilon}_p + f\cdot\tilde{\epsilon}_f, \quad f = \frac{E^{min} - \tilde{E}_E}{\tilde{E}_D - \tilde{E}_E} \qquad (5.23)$$

When the P-E reaches the NP→P phase transition section (B)−(C) at (O), it continues along the original path. In some cases, even the maximum applied electrical field is not large enough to fully induce the polar phase. An exemplary P-E curve for this type of sesquipolar loading is depicted in Figure 5.5 (d). Because the system never reaches the fully transformed polar state, the polarization slope for decreasing field $\tilde{\epsilon}_{p1}^{minor}$ is a linear combination of $\tilde{\epsilon}_p$ and $\tilde{\epsilon}_f$, depending on E^{max}:

$$\tilde{\epsilon}_{p1}^{minor} = (1-f)\cdot\tilde{\epsilon}_p + f\cdot\tilde{\epsilon}_f, \quad f = \frac{E^{max} - \tilde{E}_B}{\tilde{E}_C - \tilde{E}_P} \qquad (5.24)$$

This also has an influence on the determination of the back-transition field $\tilde{E}_D$:

$$\tilde{E}_D = \frac{1}{\tilde{\epsilon}_b - \tilde{\epsilon}_{p1}^{minor}}\left(\tilde{E}_E\tilde{\epsilon}_b - E^{max}\tilde{\epsilon}_{p1}^{minor} + P^{max} - \tilde{P}_E\right) \qquad (5.25)$$

The polarization slope for an increasing electrical field ϵ_{p2}^{minor} is determined like $\tilde{\epsilon}_p^{minor}$ in Equation 5.23. For the development of new applications for composite materials, the usable strain $S_{33}^{\star}(E^{max})$, meaning the difference between the strain at maximum electric field $S(E^E)$ and the remanent strain at zero field $S_R = S(E = 0)$, is of primary interest, not the polarization. Fortunately, the mechanical strain at each loading condition can be determined by using their appropriate electrostrictive coefficients. If the electrostrictive coefficient Q_{33} is unknown, it can be derived by fitting experimental large signal $S - E$ measurements. If both large signal loops (P-E, and S-E) are available, they can be used to determine the model parameters as well as the electrostrictive coefficient simultaneously.

5.1.2 Model Verification

A model system consisting of nonpolar and polar end members of BNT-6BT-2KNN and BNT-7BT, respectively, was used to prove the predictive capabilities of the equivalent circuit model, based on the linearizion of the polarization hysteresis of the nonpolar matrix and the polar seed, respectively. 10 independent material parameters are necessary in the linear hysteresis model to fully define the P-E curve of the polar material, E_A, P_A, E_B, P_B, E_E, P_E, E_M , P_M, E_D, and E_F. In case of the nonpolar material 12 independent material parameters are necessary in this model to fully define the double loop hysteresis, $\tilde{E}_A$, $\tilde{E}_F$, $\tilde{E}_B$, $\tilde{P}_B$, $\tilde{E}_C$, $\tilde{P}_C$,$\tilde{E}_D$, $\tilde{P}_D$, $\tilde{E}_E$, $\tilde{P}_E$, $\tilde{E}_M$, and $\tilde{P}_M$. These parameters are determined by fitting experimentally measured large signal P-E loops. The model material parameters for the matrix and the seed were derived from bipolar large signal polarization and strain measurements of BNT-6BT-2KNN and BNT-7BT measured with a field amplitude of 6 kV/mm (Figure 5.6). The determined coefficients of both materials can be found in Table 5.1. A comparison of the linearized hysteresis plots with the corresponding measured large signal data of both materials is shown in Figure 5.6. It can be seen that the model is able to capture all of the main features of both hysteresis loops of each material.

Table 5.1: Model parameters of the hysteresis model for BNT-6BT-2KNN and BNT-7BT for an electric field amplitude of 6 kV/mm

Matrix BNT-6BT-2KNN			Seed BNT-7BT		
Parameter	Value	Unit	Parameter	Value	Unit
$\tilde{E}_A$	1.5	kV/mm	E_A	1.75	kV/mm
$\tilde{E}_B$	3.8	kV/mm	E_B	1.9	kV/mm
$\tilde{E}_C$	4.6	kV/mm	E_D	3.0	kV/mm
$\tilde{E}_D$	0.7	kV/mm	E_E	2.0	kV/mm
$\tilde{E}_E$	0.1	kV/mm	E_M	6.0	kV/mm
$\tilde{E}_M$	6.0	kV/mm	E_F	10.0	kV/mm
$\tilde{E}_F$	10.0	kV/mm			
$\tilde{P}_B$	0.22	C/cm^2	P_A	0.06	C/cm^2
$\tilde{P}_C$	0.35	C/cm^2	P_B	0.3	C/cm^2
$\tilde{P}_D$	0.33	C/cm^2	P_E	0.3	C/cm^2
$\tilde{P}_E$	0.085	C/cm^2	P_M	0.41	C/cm^2
$\tilde{P}_M$	0.41	C/cm^2			
$\tilde{Q}_{33}$	$2.4 \cdot 10^{-2}$	m^4/C^2	Q_{33}	$2.65 \cdot 10^{-2}$	m^4/C^2

By inserting the determined material parameters into the corresponding piecewise linear polarization models, it was possible to calculate the large signal behavior of BNT-6BT-2KNN matrix composites with different BNT-7BT seed concentration, using the minimization algorithm previously described. The calculated P-E- and S-E hysteresis curves of composites with a seed concentration of 10%, 20%, 30%, and 50% for a bipolar electric load with an amplitude of 6 kV/mm are shown in Figure 5.7 and 5.8, together with the respective measurement data from the corresponding composites. The shape of the calculated P-E- and S-E hysteresis curves are in a good agreement with the respective experimental measurements, particularly during the loading. This indicates the accuracy of the proposed model. However, unipolar loading scenarios with maximum field amplitudes below 4 kV/mm are far more important for the majority of actuator applications. Additionally, the differences between the proposed equivalent circuit model and a simple averaging of both hysteresis curves on bases of the rule of mixtures decrease for fields far

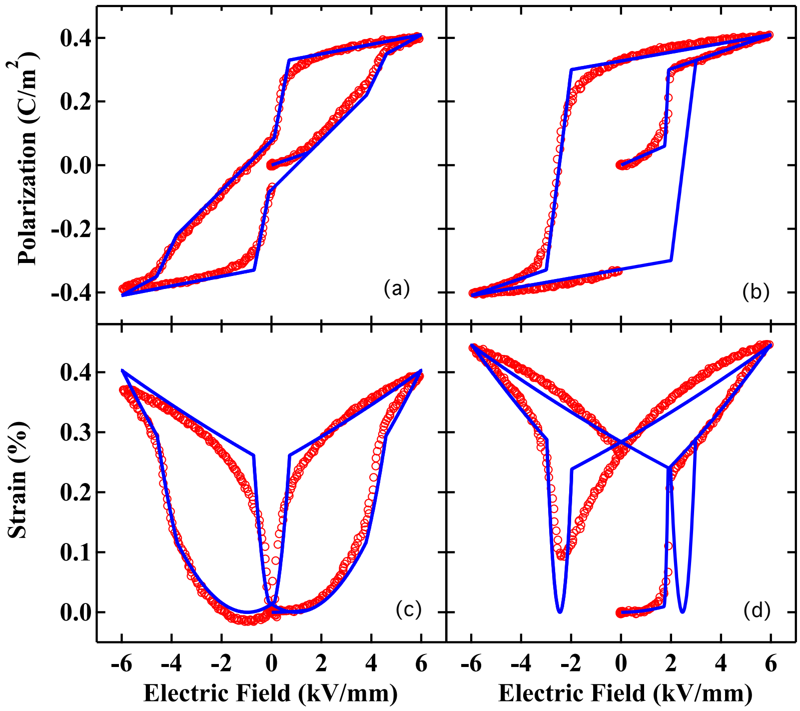

Figure 5.6: Comparison between the measured large signal P-E- and S-E hysteresis curves of the single-phase matrix (a) and (c) and seed material (b) and (d), respectively, represented by the red dots and the corresponding piecewise linear hysteresis model represented by the blue lines, for a bipolar loading with an amplitude of $6\,{}^{\mathrm{kV}}/_{\mathrm{mm}}$. The parameters used in the linear model can be found in table 5.1.

above the poling-, coercive-, and phase transition fields. In this high field region, the polarization curves of both materials show a similar trend and absolute value, so that the differences in the local fields of both materials vanish. It is, therefore, of great importance to examine the accuracy of the predicted hysteresis under low field unipolar loading conditions, especially from the point of the predicted poling/depoling field and the effective piezoelectric coefficient, which are the key benchmark parameters in the development of modern piezo-applications.

The unipolar response of the composite materials was calculated as described above. Initially, both materials were assumed to be in their virgin states. For each composition the unipolar electric load was simulated for three unipolar cycles to ensure that the hysteresis and therefore the remanent polarization and the remanent strain of the sample is fully saturated. The usable strain $S_{33}^{\star}$ of each composition was calculated from the unipolar large signal strain curve. $S_{33}^{\star}(E^{max}, c)$ is defined as the difference between the maximum strain that occurs at maximum load E^{max} and the remanent strain for zero load. Typically $S_{33}^{\star}$ is a function of E^{max}. In this case, $S_{33}^{\star}$ also depends on the seed concentration c. The effective piezoelectric coefficient $d_{33}^{\star}$ is given by:

$$d_{33}^{\star}(E^{max}, c) = \frac{S_{33}^{\star}(E^{max}, c)}{E^{max}} \tag{5.26}$$

$d_{33}^{\star}$ was determined for a variety of maximum fields in 1% concentration steps using the model nonpolar and polar end members. The results of these calculations can be found in Figure 5.9, together with experimental data measured under the same conditions. Unfortunately, there was no experimental data

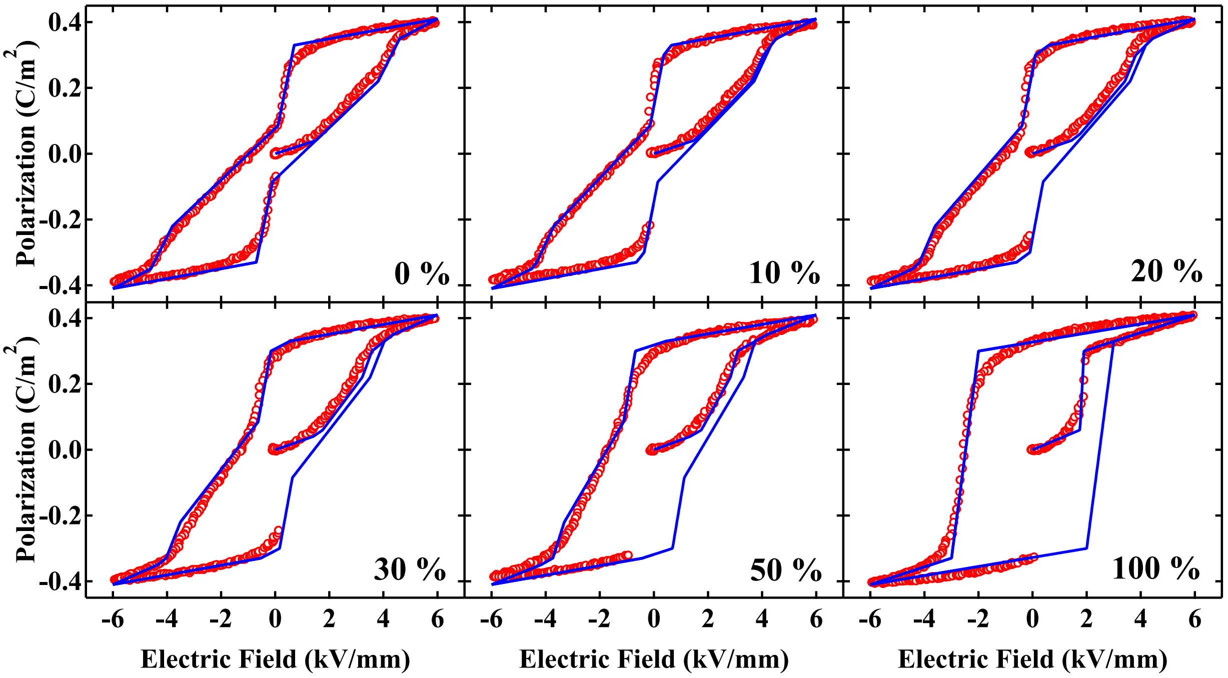

Figure 5.7: Comparison between the measured large signal *P*-*E* hysteresis curves of composite materials with a seed concentration of 10%, 20%, 30%, and 50% and the corresponding hysteresis curves calculated with the equivalent circuit model, for a bipolar load with an amplitude of 6 kV/mm.

available for 3 kV/mm and 5 kV/mm. Looking at the results for 6 kV/mm (blue curve) one finds that the composite material has no advantage over the pure matrix material in terms of the large field piezoelectric constant. The value of $d_{33}^{\star}$ decreases with an increasing seed content. The shape of the experimental curve differs from a simple rule of mixture and is closely reproduced by the theoretical results from the equivalent circuit model. Only at the seed rich side, the theoretical results are lower than the experiment. This can be explained by the fact that the ferroelectric strain hysteresis differs more from its linear representation than in the case of the polar material. The trend, however, is still well reproduced by the model. At 5 kV/mm the theoretical predictions show a similar behavior, so that a composite material again has no advantages over the pure matrix material. At 4 kV/mm the situation changes drastically. For lower seed content below 20 % the composite shows a higher $d_{33}^{\star}$ than the pure matrix material. The maximum $d_{33}^{\star}$ is about 10 % higher in the experiments with a 10 % seed content. This trend agrees well with the theoretical results from the equivalent circuit model, where the maximum $d_{33}^{\star}$ appears for 12 % seed content. The enhancement of $d_{33}^{\star}$ is even 3 times larger than in the experimental measurements. At lower field amplitudes the maximum of $d_{33}^{\star}$ shifts to higher seed concentrations. At 3 kV/mm the maximum of $d_{33}^{\star}$, is still 33 % or 22 % larger than for the pure matrix or pure seed material, respectively, and lies at a seed concentration of 54 %. The maximum value of $d_{33}^{\star}$, however, is much smaller than for 4 kV/mm.

From Figure 5.9 it is apparent that the absolute value of $d_{33}^{\star}$ for 4 kV/mm is approximately 40 % overpredicted by the model. This difference can be explained by the fact that the material parameters used in the equivalent circuit model were determined for 6 kV/mm and that the piecewise linear model has weaknesses in the prediction of the minor hysteresis loops of nonpolar materials. To check this explanation, the parameters where determined from experimental data for unipolar loads with a field amplitude of 4 kV/mm. An updated version of the coefficients can be found in Table 5.2. A comparison of the large signal polarization and strain curves for the piecewise linear model using the updated parameters and the

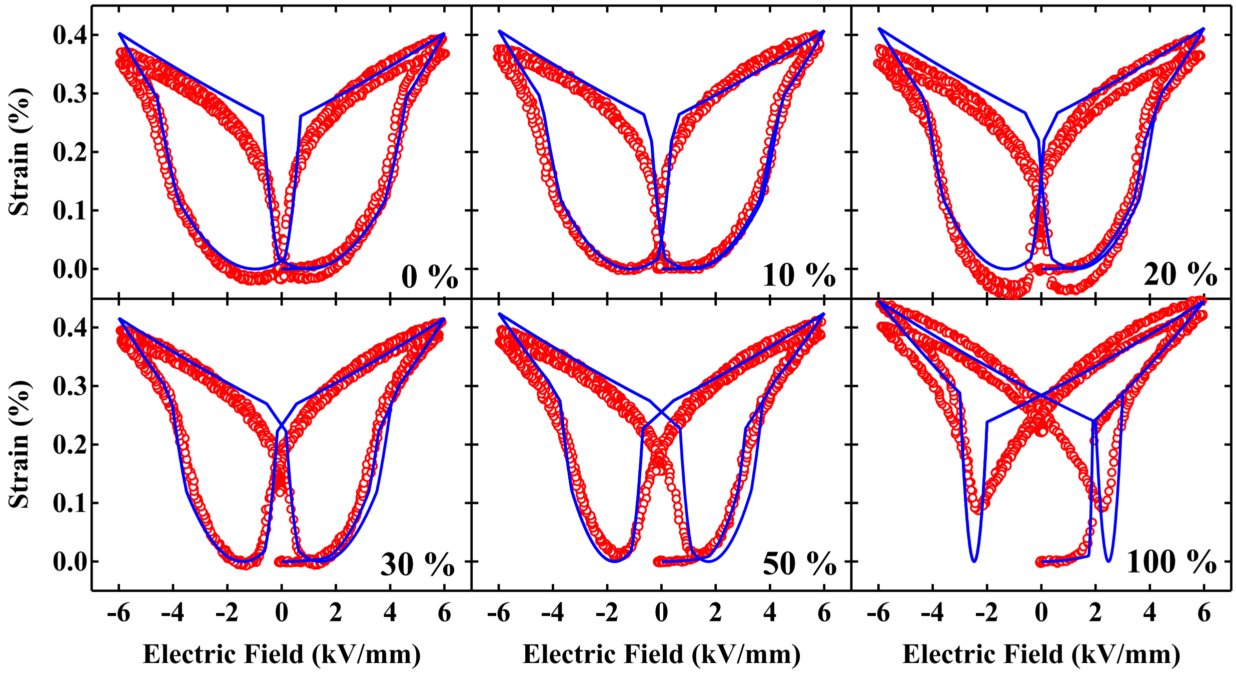

Figure 5.8: Comparison between the measured large signal $S - E$ hysteresis curves of composite materials with a seed concentration of 10%, 20%, 30%, and 50% and the corresponding hysteresis curves calculated with the equivalent circuit model, for a bipolar load with an amplitude of $6\,{}^{\mathrm{kV}}/_{\mathrm{mm}}$.

experimental data that was used to determine the material model parameters is shown in Figure 5.10. The dependence of $d^{\star}_{33}$ on the concentration for unipolar loads with an amplitude of $4\,{}^{\mathrm{kV}}/_{\mathrm{mm}}$ was then recalculated with the updated parameters. Comparing these new results to the experimental data (Figure 5.11), one can see that the difference has decreased by a factor of 5. Again, the trend of $d^{\star}_{33}$ is well reproduced by the equivalent circuit model.

As shown in Figures 5.7 and 5.8, the equivalent circuit model can accurately predict the seed concentration-dependent behavior of composite materials for different load amplitudes. This requires, however, experimental knowledge of the large signal P-E and S-E hysteresis behavior of the nonpolar and polar end members. The accuracy of the absolute value of $d^{\star}_{33}$ can be improved, by adjusting the material parameters to the large signal hysteresis curves of both raw materials for the same loading conditions, at which the composite material is to be investigated. For a given material combination, it is possible to predict the optimum seed content and therefore avoid large series of measurements. Moreover, the equivalent circuit model serves as a powerful tool to study the influences of the different material parameters on the composite effect and to identify optimal material combinations for new composite systems.

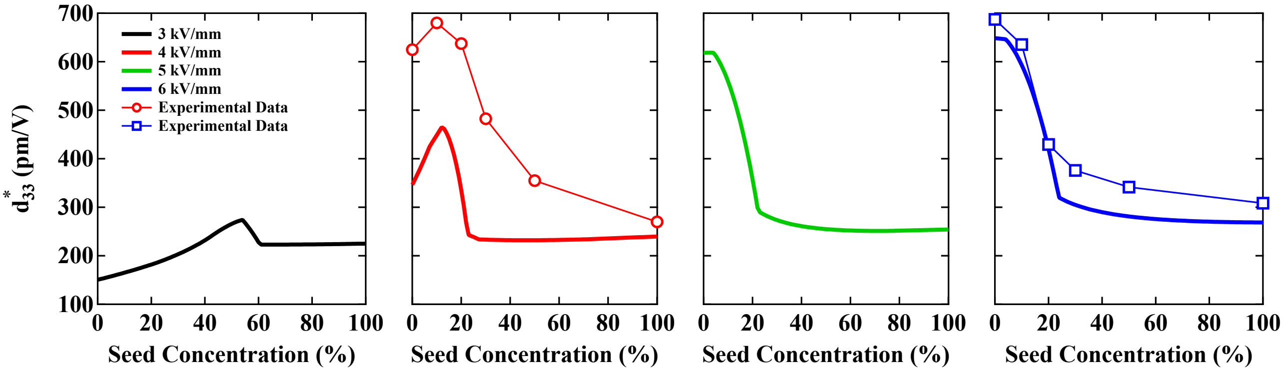

Figure 5.9: $d_{33}^{\star}$ as a function of the seed concentration for unipolar load with different amplitude (thick lines). The thin lines represents $d_{33}^{\star}$ calculated from experimental measurements under the same conditions.

Table 5.2: Model parameters of the hysteresis model for BNT-6BT-2KNN and BNT-7BT for an electric field amplitude of $6\,\mathrm{kV/mm}$ and for BNT-6BT-2KNN or an electric field amplitude of $4\,\mathrm{kV/mm}$

Matrix BNT-6BT-2KNN				Seed BNT-7BT		
Parameter	Value ($6\,\mathrm{kV/mm}$)	Value ($4\,\mathrm{kV/mm}$)	Unit	Parameter	Value	Unit
$\tilde{E}_A$	1.5	0.9	$\mathrm{kV/mm}$	E_A	1.75	$\mathrm{kV/mm}$
$\tilde{E}_B$	3.8	3.38	$\mathrm{kV/mm}$	E_B	1.9	$\mathrm{kV/mm}$
$\tilde{E}_C$	4.6	3.8	$\mathrm{kV/mm}$	E_D	3.0	$\mathrm{kV/mm}$
$\tilde{E}_D$	0.7	1.2	$\mathrm{kV/mm}$	E_E	2.0	$\mathrm{kV/mm}$
$\tilde{E}_E$	0.1	0.13	$\mathrm{kV/mm}$	E_M	6.0	$\mathrm{kV/mm}$
$\tilde{E}_M$	6.0	no change	$\mathrm{kV/mm}$	E_F	10.0	$\mathrm{kV/mm}$
$\tilde{P}_B$	0.22	0.25	$\mathrm{C/cm^2}$	P_A	0.06	$\mathrm{C/cm^2}$
$\tilde{P}_C$	0.35	0.31	$\mathrm{C/cm^2}$	P_B	0.3	$\mathrm{C/cm^2}$
$\tilde{P}_D$	0.33	0.35	$\mathrm{C/cm^2}$	P_E	0.3	$\mathrm{C/cm^2}$
$\tilde{P}_E$	0.085	0.083	$\mathrm{C/cm^2}$	P_M	0.41	$\mathrm{C/cm^2}$
$\tilde{P}_M$	0.41	0.50	$\mathrm{C/cm^2}$			
$\tilde{E}_F$	10.0	no change	$\mathrm{kV/mm}$			
$\tilde{Q}_{33}$	$2.4 \cdot 10^{-2}$	no change	$\mathrm{m^4/C^2}$	Q_{33}	$2.65 \cdot 10^{-2}$	$\mathrm{m^4/C^2}$

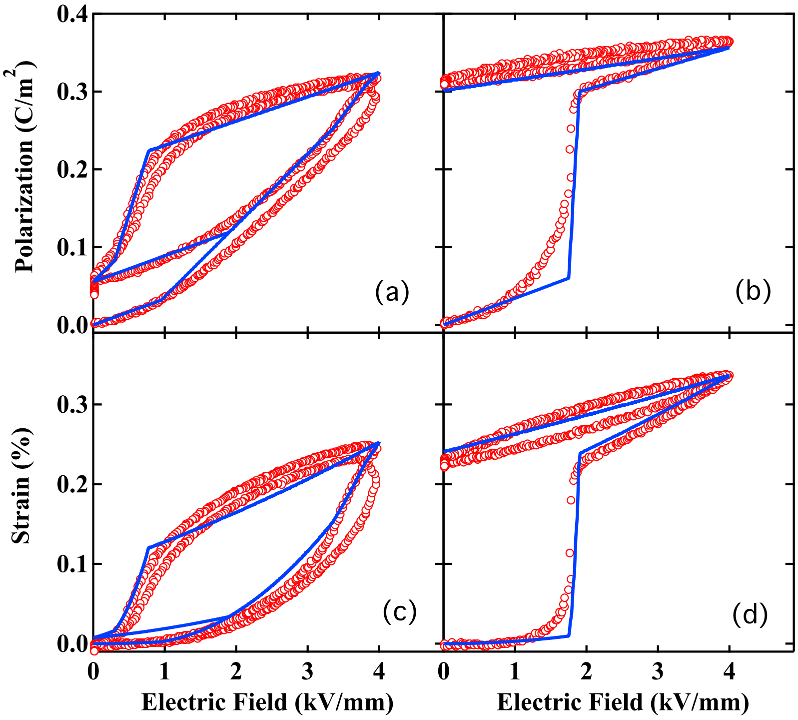

Figure 5.10: Comparison between the measured large signal P-E- and S-E hysteresis curves of the single-phase matrix (a) and (c) and seed material (b) and (d), respectively, represented by the red dots and the corresponding piecewise linear hysteresis model represented by the blue lines, for a unipolar loading with an amplitude of $4\,{}^{\mathrm{kV}}\!/\!{}_{\mathrm{mm}}$.

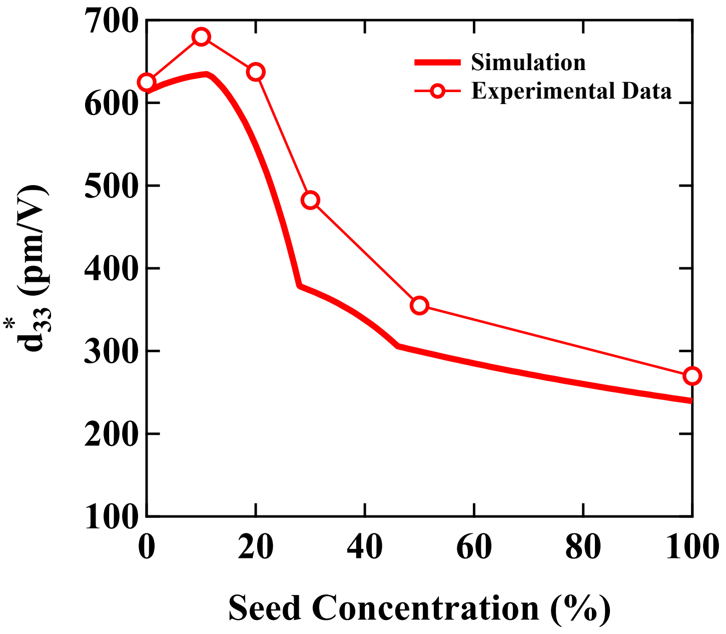

Figure 5.11: $d^\star_{33}$ as a function of the seed concentration for unipolar load with an amplitude of $4\,{}^{\mathrm{kV}}\!/\!{}_{\mathrm{mm}}$ (thick lines). In the simulation the updated version of the coefficients for $4\,{}^{\mathrm{kV}}\!/\!{}_{\mathrm{mm}}$ was used that can be found in Table 5.2. The thin lines represents $d^\star_{33}$ calculated from experimental measurements under the same conditions.

5.1.3 Parameter Study

The previously described equivalent circuit model is used in this section to optimize the unipolar strain through an adjustment of the material parameters to examine their influence on the predicted $d_{33}^{\star}$. The hope is to identify optimal parameter combinations and potentially optimal marix- and seed materials for new composite materials. Unfortunately, there are in total 13 independent parameters for the matrix and 11 independent parameters for the seed material, which represents a large parameter space for possible examinations. To reduce the number of free parameters, all parameters of the matrix material will initially be kept constant and the parameter study will be limited to the seed material. It can be shown that the electrostrictive coefficient Q_{33} has no influence on the overall shape of the hysteresis curves; there is only a linear influence on the predicted $d_{33}^{\star}$. Obviously, a large Q_{33} value is always desirable for both the matrix- and seed materials. It should be mentioned that all model parameters are not typically used to characterize polar and nonpolar materials in the literature and that specific combinations of matrix- or seed parameters do not necessarily correspond to any real material. To achieve a better comparison of the theoretical findings to electro-mechanical characterization data of potential materials from literature, the important characteristic values remanent polarization P_r and coercive field E_C of the seed material were varied independently during the parameter study. Therefore, it was necessary to relate the 10 remaining free model parameters of the seed material to these characteristic values. In Equation 5.3 and 5.4 the dependency of P_r and E_C on P_F, E_F, ϵ_f, and E_D, P_D, ϵ_s, respectively, was already shown. In the first study, the value of the remanent polarization P_r was varied between half and twice the original remanent polarization, i.e. $P_r \rightarrow \alpha P_r$ with $0.5 \leq \alpha \leq 2$. Regarding Equation 5.3, a variation of P_r can be implemented by the following change in the position of the connection point (F):

$$P_F \rightarrow P_F + (\alpha - 1) P_r \tag{5.27}$$

$$E_F \rightarrow E_F \tag{5.28}$$

In order to keep the slopes of all segments constant during the variation of P_r, some model parameters must change as well:

$$P_B \rightarrow P_B + (\alpha - 1)\frac{P_r \epsilon_p}{\epsilon_p - \epsilon_g} \tag{5.29}$$

$$E_B \rightarrow E_B + (\alpha - 1)\frac{P_r}{\epsilon_p - \epsilon_g} \tag{5.30}$$

$$P_D \rightarrow P_D + (\alpha - 1)\frac{P_r \epsilon_s}{\epsilon_s - \epsilon_g} \tag{5.31}$$

$$E_D \rightarrow E_D + (\alpha - 1)\frac{P_r}{\epsilon_s - \epsilon_g} \tag{5.32}$$

$$P_E \rightarrow P_E + (\alpha - 1)\frac{P_r \epsilon_s}{\epsilon_s - \epsilon_f} \tag{5.33}$$

$$E_E \rightarrow E_E - (\alpha - 1)\frac{P_r}{\epsilon_s - \epsilon_f} \tag{5.34}$$

In the second study the coercive field of the polar material was varied ($E_C \rightarrow \beta E_C$) with $0.5 \leq \beta \leq 2$, whereas the remanent polarization was fixed at its original value. A change in the coercive field means that the energy threshold for domain reorientation processes changes, which also influences the poling process of a virgin material. In order to address this correlation in the model, the poling field, defined as $\frac{1}{2}(E_A + E_B)$ was varied by using the same factor $\frac{1}{2}(E_A + E_B) \rightarrow \beta \frac{1}{2}(E_A + E_B)$. Similar to the previous case, none of the segment slopes were changed during the variation. Therefore some of the material parameters must be changed as well:

$$E_A \rightarrow E_A + (\beta - 1)\frac{E_A - E_B}{2} \tag{5.35}$$

$$P_A \rightarrow P_A + (\beta - 1)\frac{(E_A - E_B)\epsilon_p}{2} \tag{5.36}$$

$$E_B \rightarrow E_B + (\beta - 1)\frac{(E_A - E_B)\epsilon_p}{\epsilon_p - \epsilon_g} \tag{5.37}$$

$$P_B \rightarrow P_B + (\beta - 1)\frac{(E_A - E_B)\epsilon_p\epsilon_g}{\epsilon_p - \epsilon_g} \tag{5.38}$$

$$E_D \rightarrow E_D + (\beta - 1)\frac{E_C\epsilon_s}{\epsilon_s - \epsilon_g} \tag{5.39}$$

$$P_D \rightarrow P_D + (\beta - 1)\frac{E_C\epsilon_g\epsilon_s}{\epsilon_s - \epsilon_g} \tag{5.40}$$

$$E_E \rightarrow E_E + (\beta - 1)\frac{E_C\epsilon_s}{\epsilon_s - \epsilon_f} \tag{5.41}$$

$$P_E \rightarrow P_E + (\beta - 1)\frac{E_C\epsilon_s\epsilon_f}{\epsilon_s - \epsilon_f} \tag{5.42}$$

The large signal hysteresis curves of the polar material under the variation of P_r and E_C are shown in Figure 5.12. By varying α and β, it is possible to use the equivalent circuit model to calculate $d_{33}^{\star}$ as a function of the varied seed material parameters.

In the first study the remanent polarization of the seed material was varied. Simulation results for $d_{33}^{\star}$ of composite materials with different seed concentrations from 5 % to 25 % are shown in Figure 5.13, as a function of the remanent polarization of the polar material P_r, normalized with P_S, which is a measure of the remanent polarization of the polar phase of the matrix material. Simulations were done for a unipolar cyclic load with an amplitude of 4 kV/mm and 6 kV/mm, respectively. It can be seen that the overall trend of all calculated curves does not depend on the seed concentration. For each loading amplitude and seed concentration, there is a critical value of P_r/P_S, below which $d_{33}^{\star}$ drops drastically. Above this critical ratio the value of $d_{33}^{\star}$ remains nearly constant. Dashed blue line marks the $d_{33}^{\star}$ value of the pure matrix material. $d_{33}^{\star}$ values below this line indicate that the corresponding composite materials have a lower performance than the matrix material alone.

For a loading amplitude of 4 kV/mm a maximum improvement of $d_{33}^{\star}$ is 27 % compared to the nonpolar matrix material. This value is reached for seed concentrations between 10 % and 20 % and a P_r/P_S ratio above 1.2. At this ratio the polarization of the seed material no longer reaches the point (B) (compare Figure 5.4), which results in a smaller coercive and back-switching field E_E. The local electrical field that is induced in the seed material E^{seed} is large enough ($\|E^{seed}\| > \|E_E\|$) to lead to a partial back-switching of the domains in the seed, which results in a significant decrease in the remanent strain and polarization of the composite material. Above the critical P_r/P_S ratio the steep slope of the (A)−(B) segment prohibits a further decrease of E_E. There is an optimum of $d_{33}^{\star}$ around 15 % seed content, only available for composite materials with a 5 % larger P_r/P_S-ratio. Regarding the results for the original composite material indicated by the black dashed line, the ratio P_r/P_S of the original composite lies above the critical ratio for seed concentrations below 10 %. This explains the $d_{33}^{\star}$ maximum in this material system around 12 % seed content, which can be also seen in the experiments. For higher load amplitudes of 6 kV/mm the same trends can be seen in Figure 5.13. However, the maximum improvement of $d_{33}^{\star}$ decreases to 5 % and the required ratios shift to higher values around 1.5. The reason for the

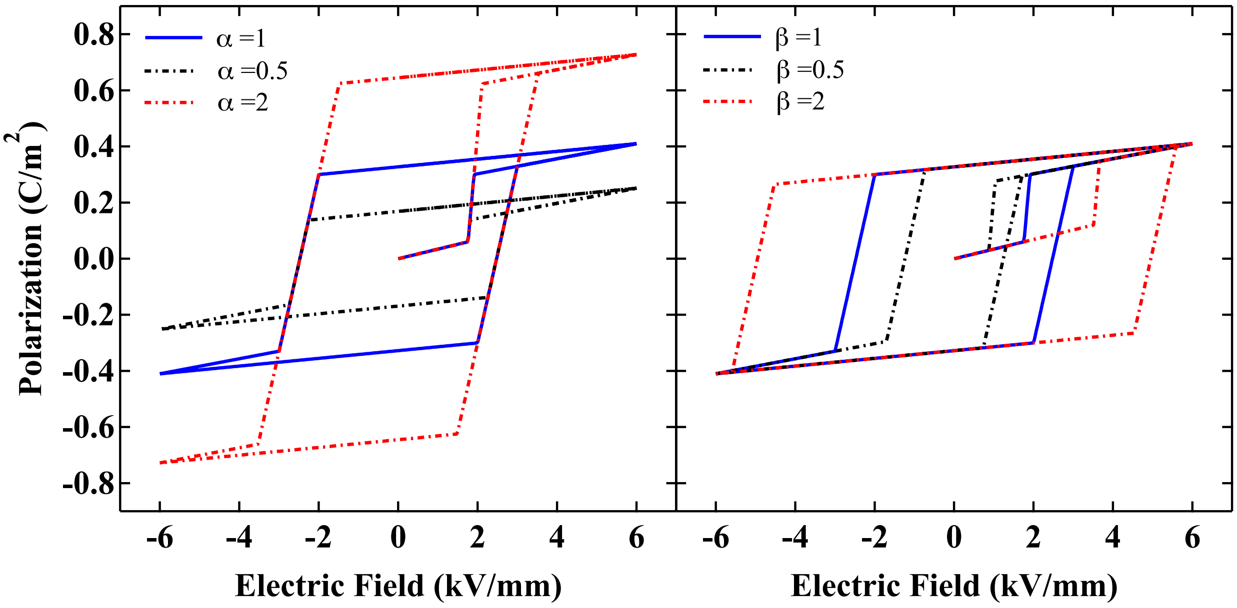

Figure 5.12: Large signal polarization hysteresis curves for the polar seed material (blue straight line) for a variation of P_r on the left side and a variation of E_C on the right (red and black dashed lines).

trend is the same as before, but the higher amplitude of the applied electrical field requires a larger P_B to keep the coercive field of the seed low. The increase in $d_{33}^{\star}$ is lower because the increased local field at the seed material has no longer a significant influence as soon as the seed has completed its NP→P transition.

It can be concluded that the composite effect can be further improved by using seed materials with a higher remanent polarization. These seed materials will also shift the optimum seed concentration to higher seed contents. If a certain maximum value is reached, seeds with even higher remanent polarization values will show no additional effect on the maximum $d_{33}^{\star}$ of the composite system. For a higher loading amplitude of 6 kV/mm only a small increase of $d_{33}^{\star}$ can be expected from the composite approach. Moreover the necessary P_r/P_S-ratio is around 50 % larger than in the previously studied model system.

In the second study the coercive field of the seed material was varied. $d_{33}^{\star}$ was again determined from the simulated large signal polarization and strain hysteresis curves for a unipolar electrical load with an amplitude of 4 kV/mm and 6 kV/mm. The results are shown for different seed contents in Figure 5.14 as a function of the normalized coercive field $E_C^{seed}/E_{pol}^{matrix}$, where E_{pol}^{matrix} denotes the poling field of the matrix material, i.e., the electrical field in the middle of the poling segment (B)−(C) (compare Figure 5.5):

$$E_{pol}^{matrix} = (\tilde{E}_C + \tilde{E}_B)/2 \tag{5.43}$$

In general, a larger $E_C^{seed}/E_{pol}^{matrix}$ ratio leads to a decrease in $d_{33}^{\star}$ of the composite. This trend can be observed in all compositions and for each electrical loading amplitude. In case of a maximum applied electrical field of 4 kV/mm, $d_{33}^{\star}$ of the composite material can be improved up to 69 % for a seed content of 25 % at the lowest $E_C^{seed}/E_{pol}^{matrix}$ ratio of 0.17. Depending on the $E_C^{seed}/E_{pol}^{matrix}$ ratio, different seed contents lead to an optimal $d_{33}^{\star}$, e.g., 10 % seed content leads to a maximum $d_{33}^{\star}$ for $0.4 \leq E_C^{seed}/E_{pol}^{matrix} \leq 0.8$ and 15 % seed content $0.3 \leq E_C^{seed}/E_{pol}^{matrix} \leq 0.4$. Again, the experimental results that showed

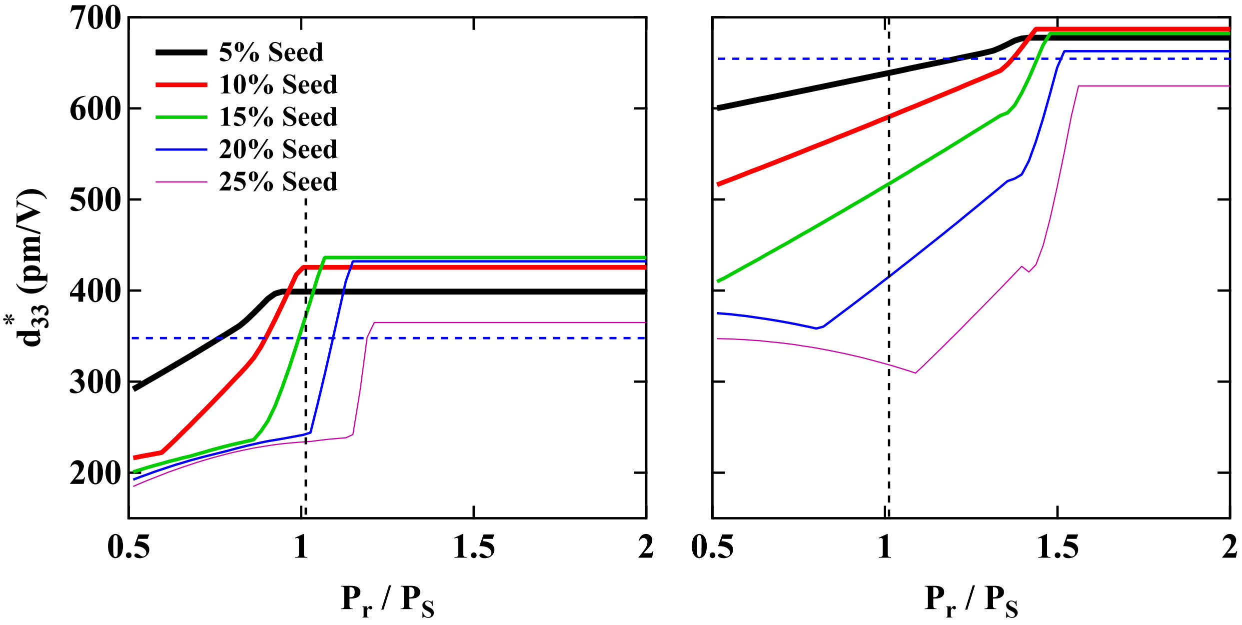

Figure 5.13: $d^\star_{33}$ for seed concentrations of 5% to 25% , and unipolar cyclic load with an amplitude of $4\,{}^{\mathrm{kV}}/_{\mathrm{mm}}$ on the right hand and $6\,{}^{\mathrm{kV}}/_{\mathrm{mm}}$ on the left hand side, as a function of the ratio between the remanent polarization of the seed P_r and the extrapolated polarization of the polar phase of the matrix material $P_S = 0.319\,{}^{\mathrm{C}}/_{\mathrm{cm}^2}$ (compare Equation 5.20). The dashed black line indicate the ratio of the initially examined composite $P_r/P_S = 1.03$ (BNT-6BT-2KNN matrix, BNT-7BT seed), whereas the blue dashed line indicate the value of $d^\star_{33}$ for the pure matrix material

a maximum $d^\star_{33}$ for a 10% seed content are in accordance with the presented results (the measured composite is indicated by the vertical black dashed line in Figure 5.14). The exact trend of $d^\star_{33}$ at $4\,{}^{\mathrm{kV}}/_{\mathrm{mm}}$ is a complex function of the model parameters. In summary, finding a seed material with a lower coercive field always increases $d^\star_{33}$ for a load amplitude of $4\,{}^{\mathrm{kV}}/_{\mathrm{mm}}$. Moreover, the seed concentration for a maximum $d^\star_{33}$ shifts to higher seed contents for lower coercive fields of the seed material.

At a higher maximum electrical loading field of $6\,{}^{\mathrm{kV}}/_{\mathrm{mm}}$, $d^\star_{33}$ of all compositions is smaller than or equal to the matrix material. As mentioned before, when the applied electrical field is large enough to fully induce the NP→P phase transition in the matrix material, the voltage enhancement from the seed no longer improves the composite $d^\star_{33}$. A larger seed content will rather increase the remanent polarization and strain of the composite and lower the high field $d^\star_{33}$ of the composite.

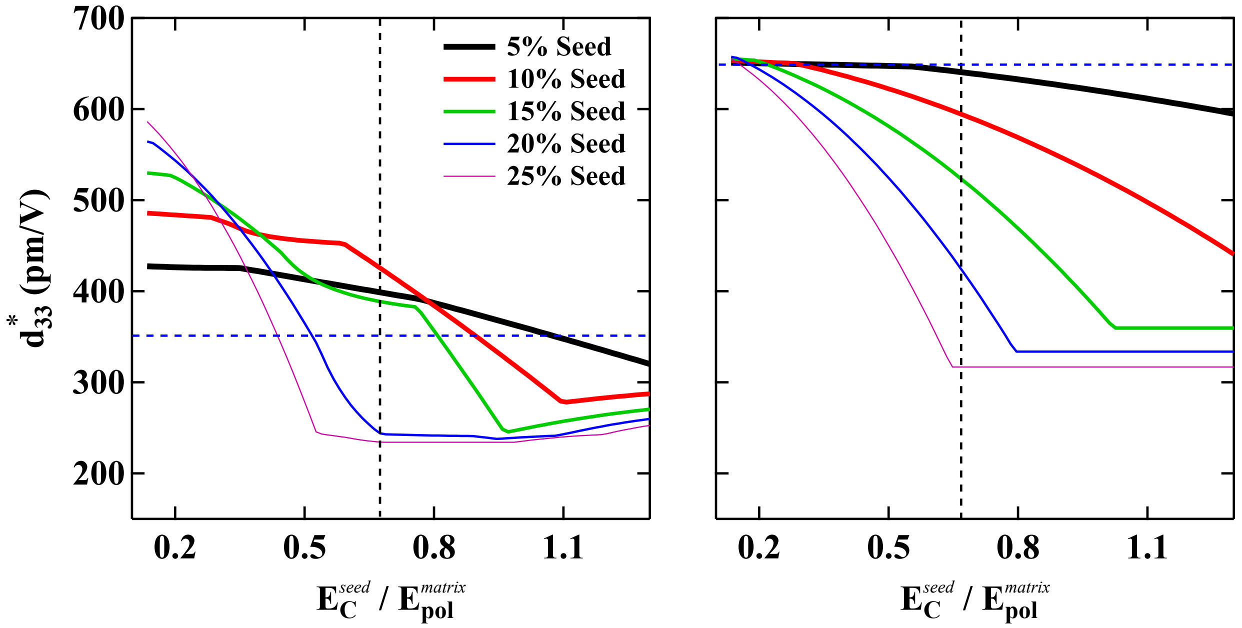

Figure 5.14: $d_{33}^{\star}$ for seed concentrations of 5% to 25% , and unipolar cyclic load with an amplitude of $4\,{}^{\mathrm{kV}}/_{\mathrm{mm}}$ on the right hand and $6\,{}^{\mathrm{kV}}/_{\mathrm{mm}}$ on the left hand side, as a function of the ratio between the coercive field of the seed E_C and the poling field of the matrix material $E_{pol} = 3.67\,{}^{\mathrm{kV}}/_{\mathrm{mm}}$ (compare Equation 5.19). The dashed black line indicate the ratio of the initially examined composite (BNT-6BT-2KNN matrix, BNT-7BT seed), whereas the blue dashed line indicates the value of $d_{33}^{\star}$ for the pure matrix material.

5.2 Conclusions

In this chapter it was shown that the large signal polarization and strain behavior of NP-P composite materials can be predicted for different bipolar and unipolar electrical load by an equivalent circuit model of two nonlinear capacitors in series configuration. The nonlinear P-E characteristic of both capacitors is a piecewise linear approximation of the experimentally measured polarization hysteresis of the polar and nonpolar material. Some rules were introduced to predict the P-E curves for different loading scenarios. The strain is directly derived from the polarization by using electrostrictive coefficients that were determined from the measurement data. The voltage at each capacitor was determined by an algorithm that minimized the polarization difference between both capacitors. With this model it was possible to calculate the usable strain and effective piezoelectric constant as a function of the seed content to predict the optimal seed concentration.

The simulated P-E and S-E curves, as well as the optimal seed concentration, were in good agreement with experimental measurements. However, the calculated effective piezoelectric constant was too large for lower field amplitudes than those used to determine the model parameters. The quality of the results for $d_{33}^{\star}$ were significantly improved by using model parameters for the matrix material determined from measurements at lower fields. Therefore ten out of the total twelve parameters had to be changed by 2-70%. This indicates that the rules that were proposed to predict the large signal polarization and strain behavior of the nonpolar matrix at lower fields were not sufficiently accurate. The accuracy of the piecewise linear fit can be improved by adding additional linear parts to the model. However, increasing the number of linear parts, as well as a better model for minor loops significantly increases the model complexity. In this case it might be better to replace the piecewise linear representation by more advanced models for the hysteretic behavior of polar and nonpolar materials. A promising approach based on the Preisach theory of hysteresis [239], which already proved its suitability in the prediction of minor hysteresis loops in ferroelectric materials [240]. An adaption of the Preisach model to nonpolar systems, however, is still pending.

In the second part of the chapter, the P-E curve of the seed material was varied to study the influence of P_r and E_C of the polar seed on the performance of composites with different compositions. At 6 kV/mm no interesting phenomena were observed. The applied electrical field is large enough to fully induce the NP→P phase transition in the matrix material, the voltage enhancement from the seed no longer leads to an enhanced $d_{33}^{\star}$ of the composite. A variation of the remanent polarization or coercive field of the seed material influences $d_{33}^{\star}$, but in most cases $d_{33}^{\star}$ of the composite is below or equal to $d_{33}^{\star}$ of the nonpolar material. At 4 kV/mm a change in the coercive field or remanent polarization of the seed can significantly improve the maximum $d_{33}^{\star}$. In the case of the remanent polarization an increase will result in an increase in $d_{33}^{\star}$. However, for each composition there is a critical value above which $d_{33}^{\star}$ remains constant for a further increase in P_r. This critical value is close to that of the seed material that was used in the experiments for all tested compositions. P_r also influences the optimal seed concentration. A decrease in the coercive field will always improve $d_{33}^{\star}$. Moreover, the seed concentration for a maximum $d_{33}^{\star}$ shifts to higher seed contents for lower coercive fields of the seed material.

6 Phase Field Model for Composite Materials

6.1 Introduction

Nonpolar-polar (NP-P) composite materials are a promising class of materials for the replacement of lead containing piezoelectric materials in actuator and sensor applications. Numerous reports have demonstrated enhanced piezoelectric properties for a variety of different NP material systems, e.g., BNT-6BT-2KNN [8], BNT-BKT-KNN [199], and BNT-ST [238]. Unfortunately, large electric fields, often larger than desirable in applications, are required to archive large unipolar strains [8]. A promising method for reducing the required electric fields is the inclusion of polar seeds, which can decrease the necessary electric fields significantly [205]. The basic structure and enhanced piezoelectric properties of bismuth based NP-P composite materials were discussed in Chapter 5 in detail. To date, the fundamental mechanisms responsible for the observed reduction in the electric field are still unknown and no reports on potential theoretical models for NP-P composite materials have been reported. Such models, which could investigate the influence of various material parameters, could aid the optimization of NP-P composites and give insight in the search for potentially useful NP oor P end members. In Chapter 5 a simple equivalent circuit model was proposed, in which the complex microstructure of the composite material was replaced by a series configuration of two non-linear, loading-history dependent capacitors. It was shown that this model was capable of predicting the optimal polar seed concentration in the composite. Additionally, it was possible to vary some of the key properties of the seed material, such as the remanent polarization and coercive field, to study their influence on the optimal seed concentrations and the overall large field piezoelectric properties of the composite material. Studies like this can help in the search for optimal polar and nonpolar material combinations. However, the equivalent-circuit model does not include effects from the grain boundaries, grain sizes, grain shapes, grain distribution, and the inter- and intra-granular electrical and mechanical interactions. It is assumed that these factors have a significant influence on the observed NP→P phase transition. In addition to the identification of optimal NP and P material combinations, understanding the influence of local interactions can help to increase the performance of composite materials by optimizing the microstructure. The experimental data that are used in this chapter in order to determine the model parameters and to evaluate the predictive capabilities of the presented model are the same as in Chapter 5. The measurements were performed by Claudia Groh and Wook Jo.

6.2 Model Description

Numerous theoretical models have been proposed to understand and predict the nonlinear behavior of polar ferroelectric materials caused by ferroelectric switching of the unit cell dipole moments [50, 241–247]. Typically, thermodynamic approaches are based on switching energy criteria for the spontaneous polarization and the particular switching region is usually assumed to be an entire domain. A prominent example was published by Huber et al. [245]. They proposed a nonlinear constitutive model with an extension of the self-consistent crystal plasticity scheme to simulate the non-linear switching of tetragonal ferroelectric materials under the influence of electrical and mechanical loads. The nonlinear P-E hysteresis loops [248] and T-S curves [246] of polycrystal ferroelectrics have also been simulated by using a switching energy criteria for the spontaneous polarization and a finite element approach for the solution of the electric potential or the mechanical displacement. In this approach individual crystallites were represented by finite elements with a randomly chosen crystallographic orientation and polarization direction. The macroscopic response to electric and mechanical loads were determined by averaging over the individual solutions for each grain. The results of this model capture some of the characteristic features of ferroelectric materials such as the shapes of the dielectric hysteresis and the butterfly loop and the depolarization of a polycrystalline by compressive stresses that are observed in experiments. Most analytical material models of domain switching do not take the interactions between domains during the switching process or partial switching of domains into account. Furthermore, the electric characteristics, such as the electric boundary conditions between domains, are ignored. Phase field simulations of the nonlinear behavior of ferroelectrics, however, are able to give detailed insights into the microscopic switching mechanism by domain nucleation and domain wall movement.

Phase field theory is based on the fundamental principles of thermodynamics and kinetics. Related material models are well established in different fields of material science, e.g. alloy solidification [249], and provide a powerful method for predicting the evolution of microstructures in materials. Thermodynamic energies are described in terms of a set of continuous order parameters. The temporal evolution of a microstructure is given by kinetics equations that describe the time dependence of the spatially inhomogeneous order parameters. Landau type approaches are often used to describe the free energy density of a ferroelectric system in phase field models [126, 250, 251]. In these approaches the polarization is treated as the primary order parameter. Strain, and in later implementations also the electric potential [252, 253], are secondary order parameters whose time dependence is defined by the primary order parameter. The calculated phase transitions are direct consequences of the minimization process of the free energy integrated over the whole volume of the simulated system.

In this chapter, a phenomenological phase field model for composite materials based on Ginzburg-Landau theory is presented. The polar seed material shows a remanent polarization and a typical ferroelectric switching behavior. It can be therefore assumed that the polar seed material can be treated like a regular ferroelectric material, i.e., represented by a two dimensional implementation of a conventional phase field approach that was previously used to study various phenomena in ferroelectric single crystals [21, 41, 98, 104–106, 201, 214]. A three dimensional implementation is possible, but the required computation effort is extensive and not required for this work. In the phase field approach it is assumed that the state of a ferroelectric body occupying a region $\mathscr{B}$ with a boundary $\partial\mathscr{B}$ can be sufficiently described by continuous fields (degrees of freedom): the mechanical displacement u_{ij}, the electric potential ϕ, and the spontaneous polarization P_i. The electric field E_i and the linearized strain S_{ij} can be directly deduced from the degrees of freedom:

$$S_{ij} = \frac{1}{2}(u_{i,j} + u_{j,i}) \tag{6.1}$$

$$E_i = -\nabla\phi \tag{6.2}$$

The spontaneous polarization is taken as an order parameter that determines the time evolution of the entire system. Most electro-mechanical processes in ferroelectrics evolve relatively slowly compared to the speed of sound in the ferroelectric medium [254]. Therefore, the stress T_{ij} and the dielectric displacement D_i can be assumed as quasi-static and fulfill the following balance equations

$$D_{i,j} = 0 \tag{6.3}$$

$$T_{ij,j} = 0 \tag{6.4}$$

if inertia terms, body forces, and volume charges are neglected. For each equation two types of boundary conditions can be considered: The Dirichlet boundary condition

$$\phi = \phi^* \quad \text{on } \partial\mathscr{B} \tag{6.5}$$

$$u_i = u_i^* \quad \text{on } \partial\mathscr{B} \tag{6.6}$$

that corresponds to an electrode with a defined electric potential ϕ^* and a mechanical bearing with a predefined mechanical displacement u_i^*, or the Neumann boundary condition

$$\begin{aligned} D_i n_i &= -\sigma^* \quad \text{on } \partial\mathscr{B} && (6.7)\\ T_{ij} n_i &= t_j \quad \text{on } \partial\mathscr{B} && (6.8)\end{aligned}$$

where n_i is the outer unit normal vector to the surface $\partial\mathscr{B}$ that corresponds to a defined surface charge density σ^* and the surface traction t_j. A crucial part in the formulation of this phase field model is the free energy density $\mathscr{H}$, which is used as the phase field potential of the ferroelectric system as a function of the order parameter P_i. Here, $\mathscr{H}(P_i)$ consists of three parts: the classical electric enthalpy $\mathscr{H}^{ent}$, the domain separation energy $\mathscr{H}^{sep}$, also called Landau-type energy G_{LD}, which describes the domain orientations that are energetically favored by the crystallographic symmetry of the ferroelectric material, and the interface energy $\mathscr{H}^{int}$, such that:

$$\mathscr{H}(P_i, \mathrm{grad}P_i, S_{ij}, E_i) = \mathscr{H}^{ent}(P_i, S_{ij}, E_i) + \mathscr{H}^{sep}(P_i) + \mathscr{H}^{int}(P_i, j) \tag{6.9}$$

The classical electric enthalpy is given by:

$$\mathscr{H}^{ent}(P_i, S_{ij}, E_i) = \frac{1}{2}\Delta S_{ij}\left[\mathbb{C}_{ijkl}(\Delta S)_{kl}\right] - (\Delta S)_{ij}\left[\mathbb{e}^T_{ijk}(P_i)E_k\right] - \frac{1}{2}E_i\left(\epsilon_{ij}E_j\right) - P_iE_i \tag{6.10}$$

where $\mathbb{C}_{ijkl}$ is the elastic stiffness, $\mathbb{e}^T_{ijk}$ is the transposed piezoelectric coupling constant, and ϵ_{ij} is the dielectric constant. $(\Delta S)_{ij}$ is the strain difference between the strain S_{ij} relative to the paraelectric reference configuration and the spontaneous strain $S^0_{ij}(P_i)$ that correlates with the amount of spontaneous polarization P_i ($(\Delta S)_{ij} = S_{ij} - S^0_{ij}(P_i)$). Following relationship between the S^0_{ij} and P_i can be found [255]:

$$S^0_{ij}(P_k) = \frac{3}{2}S^0\frac{||P_k||}{P_0}\left(e_ie_j - \frac{1}{3}\delta_{ij}\right) \tag{6.11}$$

where P_0 is the equilibrium spontaneous polarization*, S_0 is the equilibrium spontaneous strain, δ_{ij} is the Kronecker delta and e_i is the unit vector in the direction of the spontaneous polarization:

$$e_i = \frac{P_i}{||\mathbf{P}||} \tag{6.12}$$

The mechanical stiffness, the piezoelectric tensor, and dielectric tensor are assumed to be independent of P_i. As previously noted, the phase separation energy corresponds to the Landau energy function that was previously used in Chapter 3 and 4 to describe the free energy of a single ferroelectric domain. In the case of the polar material, the lowest order approach, a reduced, two dimensional (2-4-6) function was used for $\mathscr{H}^{sep}$ that is still able to capture the main characteristics of a ferroelectric material (compare Equation 3.9):

$$\mathscr{H}^{sep} = G_{LD}(P_1, P_2) = \frac{G_0\kappa_s}{\lambda}\left[1 + \alpha_1(P_1^2 + P_2^2) + \beta_{11}(P_1^4 + P_2^4) + \beta_{12}P_1^2P_2^2 + \gamma_{111}(P_1^6 + P_2^6)\right] \tag{6.13}$$

where G_0 and λ are the specific energy and the width of a 180° domain wall, respectively, and κ_s is a calibration constant. The Landau coefficients α_1, β_{11}, β_{12}, and γ_{111} are determined in a way that the local minima of the domain separation energy lie at the four polarization variants $(\pm P_0, 0)$ and $(0, \pm P_0)$.

---

* $P_0 = \mathbf{P}_0$, were $\mathbf{P}_0$ is the minimum of the Landau energy function (domain separation energy)

The solution of the coefficients can be found in Equation 3.10 in Chapter 3. The interface energy is given by:

$$\mathscr{H}^{int} = \frac{G_0 \lambda \kappa_i}{P_0^2} \|P_{i,j}\| \tag{6.14}$$

where κ_i is a calibration constant. More detailed description of the different parameters can be found in [21, 256].

From the free energy density, the constitutive relation for the stress T_{ij} and the electric displacement D_i field can be derived by using standard thermodynamic arguments:

$$T_{ij} = \frac{\partial \mathscr{H}}{\partial S_{ij}} = \mathbb{C}_{ijkl}(\Delta S)_{kl} - \mathbb{e}_{kij} E_k \tag{6.15}$$

$$D_i = -\frac{\partial \mathscr{H}}{\partial E_i} = \mathbb{e}_{ijk}(\Delta S)_{jk} + \epsilon_{ij} E_j + P_i \tag{6.16}$$

The time evolution of the order parameter P_i is given by the evolution equation:

$$\frac{\delta P_i}{\delta t} = -M \frac{d\mathscr{H}}{dP_i} = -M \left(\frac{\partial \mathscr{H}^{ent}}{\partial P_i} + \frac{\partial G_{LD}(P_j)}{\partial P_i} - 2 \frac{G_0 \lambda \kappa_i}{P_0^2} P_{i,kk} \right) \tag{6.17}$$

where M is the mobility parameter. The partial differential field Equations 6.3, 6.4, and 6.17 can be solved using the finite element method [257]. Plane 4-node elements were used for discretization. Each degree of freedom (P_1, P_2, ϕ, u_1, u_2) was represented by a standard bilinear shape function; for area integrals a 4-point Gauss integration was used. To ensure numerical stability, an implicit time integration was utilized. One drawback of the presented implementation is that even in two dimensions the required computation costs for the finite element solution algorithm of a full loading cycle limits the maximum size of the ferroelectric body to sizes in the order of 10-100 domain wall widths. This size limitation affects the complexity of the microstructures that can be represented in the model. Only a few smaller grains can be represented by the model so that a simulation of a macroscopic polycrystal is currently still out of reach.

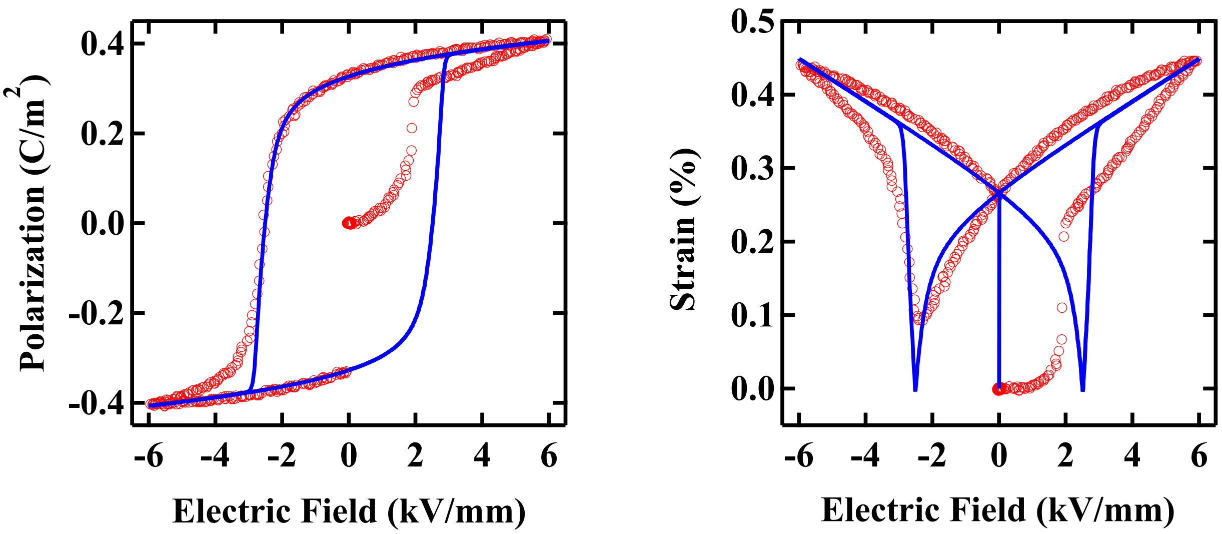

Figure 6.1: Experimentally measured P-E and S-E bipolar hysteresis loops (red circles) and the corresponding results from the phase field model (blue curves).

Most of the required model parameters for the polar material were determined by fitting experimental *P*-*E* and *S*-*E* behavior, shown in Figure 6.1. The red circles are experimental *P*-*E* and *S*-*E* bipolar hysteresis curves for polar BNT-7BT, whereas the blue curves are the corresponding fit from the phase field model. The model results were obtained for a simple two dimensional square-shaped ferroelectric body with an edge size of $1 \cdot 10^{-7}$ m, which is an appropriate approach for describing a crystal with mechanical free boundary conditions [105]. Periodic boundary conditions are assumed on the edges. The domain wall width λ was chosen to be $2 \cdot 10^{-9}$ m, so that a discretization with square-shaped elements with an edge size of elem $1 \cdot 10^{-9}$ m provides a sufficient resolution. Electrodes on the top and bottom edge were represented in the model by Dirichlet boundary conditions for the electric potential. A scheme of the mesh is depicted in Figure 6.2. The potential difference between both electrodes was varied stepwise following the triangular bipolar voltage distribution with a frequency of 1 Hz and a maximum voltage that corresponds to an applied electric field of 6 V/mm, which corresponds to the experimental conditions. Depending on the complexity of the occurring domain wall structure, a full hysteresis cycle of this 100 × 100 mesh can be calculated within 24 h to 240 h. The ferroelectric material was oriented with a 1° angle mismatch between the stable polarization direction and the direction of the applied electric field to break the symmetry of the system and therefore facilitate 180° polarization switching by polarization rotation that can be often observed in real ferroelectric materials [76, 102].

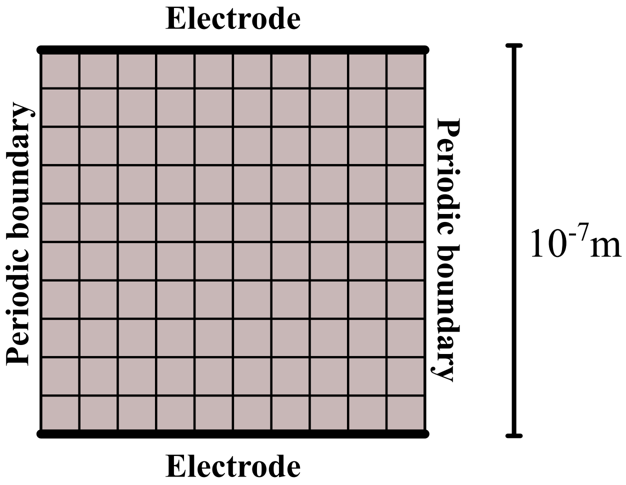

Figure 6.2: Scheme of the finite element mesh that was used to determine the material parameters.

It is apparent from Figure 6.1 that some characteristics of the measured behavior cannot be fully reproduced by the model. This is because the phase field model represents the behavior of a pure tetragonal single-crystal, whereas the model parameters are chosen to mimic the behavior of a ceramic material. As mentioned before, the numerical complexity of the model and the available computation power does not allow the simulation of multiple grains nor include the effects from defects. Moreover, a three dimensional implementation is necessary to investigate effects from out-of-plane polarization rotation processes in crystallographic symmetries, for example, rhombohedral or orthorhombic. The model is therefore more suited to study some of the fundamental physical relationships of the composite effect, rather than to be an exact representation of the experimental measurements.

The main challenge in the simulation of NP-P composite materials lies in finding a material model for the nonpolar matrix material. At high temperatures these materials are paraelectric, like ferroelectric materials above their Curie temperature. Upon cooling below the so-called Burns temperature they undergo a phase transition into an ergodic relaxor state. This phase transition cannot be considered a structural phase transition because it is not accompanied by any change of crystal structure on the macroscopic or mesoscopic scale. On the microscopic scale, however, the unit cells develop a spontaneous polarization, which influences the physical properties of the crystal [258]. Unlike ferroelectric materials, relaxors typically exhibit a significant compositional disorder, meaning a disorder in the ion arrangement on the crystallographic equivalent sites. This compositional disorder is believed to induce local random fields [259] that can destabilize the long range coupling of the order parameter P_i [260]. Instead of macroscopic domains, the polarization exists in a highly uncorrelated nano domain state [261]. These local fluctuations of the polarization cannot be effectively represented by a phase field model. In addition, the compositional disorder causes difficulties in implementing an appropriate material model.

Instead of finding a precise material model of the relaxor system, a simplified phenomenological approximation is used. It is assumed that the relaxor can be sufficiently described by using the same degrees of freedom used for the polar seed (P_1, P_2, ϕ, u_1, u_2) allowing the previous theoretical framework, e.g., Equations 6.3, 6.4, 6.15, 6.16, and 6.17, to be used. The key difference to the polar material model is the phase separation energy $\mathscr{H}^{sep}$. It was shown in Chapter 3 and 4 that the right set of $\mathscr{H}^{sep}$-coefficients is able to predict the trend of field-induced phase transitions between different polarization variants. In the case of a nonpolar material, however, the field-induced, reversible transition is from a nonpolar to a polar phase, which results in the characteristic double loop behavior in the P-E curve under bipolar loading conditions (compare Figure 5.2). The determination of appropriate $\mathscr{H}^{sep}$-coefficients that can reproduce the shape of the observed polarization double loop is required to phenomenologically describe the nonpolar material behavior. In a temperature range in the vicinity of a temperature driven first oder paraelectric-to-ferroelectric phase transition the Landau energy landscape allows the formation of a double loop polarization hysteresis [59, 185, 262].

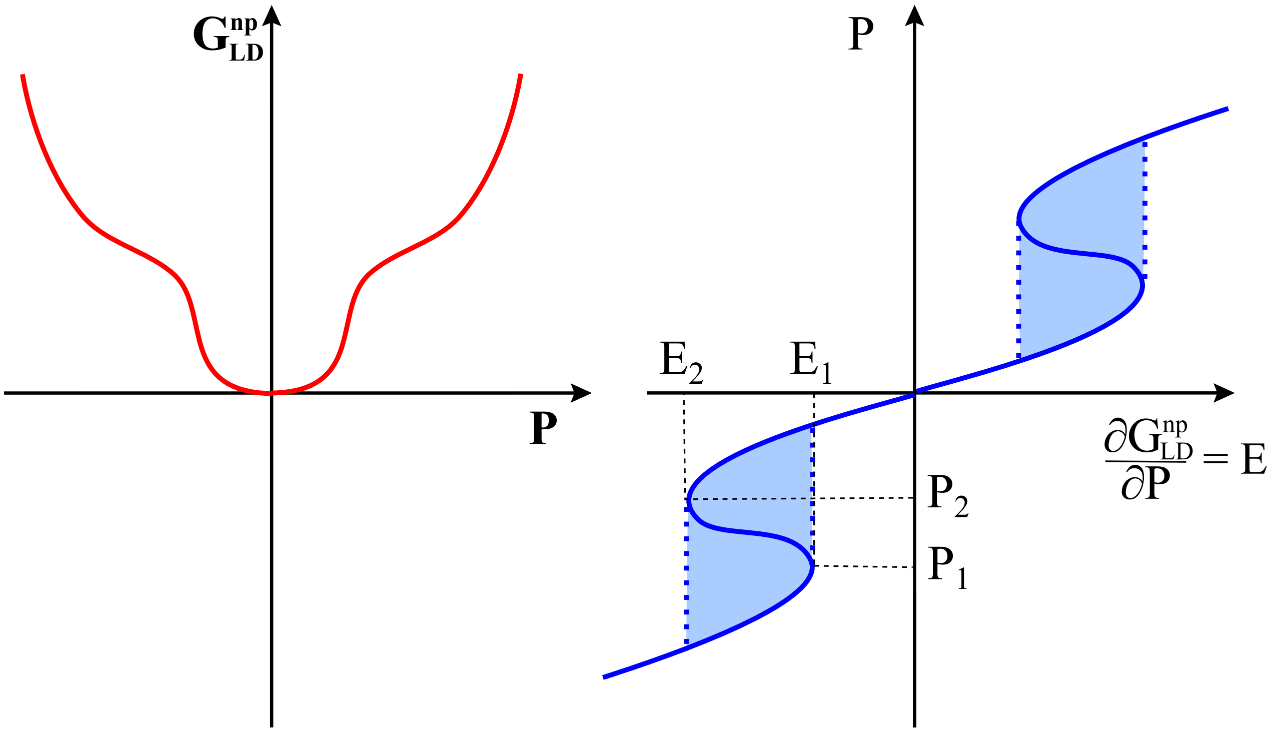

Figure 6.3: Right: "Landau-like" energy ($G^{np}(P)$) scheme of a nonpolar material with a double hysteresis (red) and the corresponding curve of the first derivative (blue). Left: Double hysteresis, which results from the first derivative curve, defined by the values for E_1, E_2, P_1, and P_2

In Figure 6.3 the scheme of the one dimensional "Landau-like" energy $G_{LD}^{np}(P)$ and the resulting double loop hysteresis are shown. To simplify the discussion, the dimension of the Landau energy is reduced.

Results can be later easily transferred to the two- or three dimensional case. The steady state P-E curve of a domain in a pure ferroelectric single crystal that corresponds to a specific Landau energy landscape can be derived from the first derivative of the free energy with respect to the order parameter P.

As depicted in Figure 6.3, Two characteristic points (E_1, P_1) and (E_2, P_2) define the size and width of the double loop hysteresis, where $E_1 < E_2$ and $P_1 > P_2$. These two points are extrema of the first derivative curve of $G(P)^{np}_{LD}$, i.e., the inflection points of the Landau curve. This results in the following four criteria that the Landau energy must fulfill:

$$\left.\frac{\partial G^{np}_{LD}}{\partial P}\right|_{P_1} = E_1 \qquad (6.18)$$

$$\left.\frac{\partial G^{np}_{LD}}{\partial P}\right|_{P_2} = E_2 \qquad (6.20)$$

$$\left.\frac{\partial^2 G^{np}_{LD}}{\partial P^2}\right|_{P_1} = 0 \qquad (6.19)$$

$$\left.\frac{\partial^2 G^{np}_{LD}}{\partial P^2}\right|_{P_2} = 0 \qquad (6.21)$$

Similar to the polar material, the measurable polarization behavior of the nonpolar material is point-symmetrical with respect to the coordinate origin, which prohibits the appearance of odd terms in G^{np}_{LD}. It can also be shown that G^{np} has to be at least of the eighth order (2-4-6-8 "Landau-like" free energy potential) to determine all model parameters E_1, E_2, P_1, P_2 independently from each other:

$$G^{np}_{LG}(P) = G_0 + \alpha'_1 P^2 + \beta'_{11} P^4 + \gamma'_{111} P^6 + \delta'_{1111} P^8 \qquad (6.22)$$

where α'_1, β'_{11}, γ'_{111}, and δ'_{1111} are the dielectric stiffness coefficients, and G_0 is an arbitrary energy offset that does not influence the P-E-characteristic of the material. Inserting Equation 6.22 into the criteria functions (Equation 6.20, 6.19, and 6.21) lead to a system of four linear equations:

$$\left.\frac{\partial G^{np}_{LD}}{\partial P}\right|_{P_1} = 2\alpha'_1 P_1 + 4\beta'_{11} P_1^3 + 6\gamma'_{111} P_1^5 + 8\delta'_{1111} P_1^7 = E_1 \qquad (6.23)$$

$$\left.\frac{\partial G^{np}_{LD}}{\partial P}\right|_{P_2} = 2\alpha'_1 P_2 + 4\beta'_{11} P_2^3 + 6\gamma'_{111} P_2^5 + 8\delta'_{1111} P_2^7 = E_2 \qquad (6.24)$$

$$\left.\frac{\partial^2 G^{np}_{LD}}{\partial P^2}\right|_{P_1} = 2\alpha'_1 + 12\beta'_{11} P_1^2 + 30\gamma'_{111} P_1^4 + 56\delta'_{1111} P_1^6 = 0 \qquad (6.25)$$

$$\left.\frac{\partial^2 G^{np}_{LD}}{\partial P^2}\right|_{P_2} = 2\alpha'_1 + 12\beta'_{11} P_2^2 + 30\gamma'_{111} P_2^4 + 56\delta'_{1111} P_2^6 = 0 \qquad (6.26)$$

The Landau coefficients in terms of the four characteristic parameters E_1, P_1, E_2, and P_2 are given by the solution of the Equations 6.23, 6.24, 6.25, and 6.26 :

$$\alpha'_1 = \frac{3E_1P_2^7 + 7E_1P_1^2P_2^5 - 7E_2P_1^5P_2^2 - 3E_2P_1^7}{4P_1P_2(P_2^2 - P_1^2)} \qquad (6.27)$$

$$\beta'_{11} = \frac{E_2P_1^5(P_1^4 + P_1^2P_2^2 - 14P_2^4) - E_1(P_2^9 + P_1^2P_2^7 - 14P_1^4P_2^5)}{8P_1^3P_2^3(P_2^2 - P_1^2)} \qquad (6.28)$$

$$\gamma'_{111} = \frac{2E_1P_2^7 - 7E_1P_1^2P_2^5 + 7E_2P_1^3P_2^4 - 7E_1P_1^4P_2^3 + 7E_2P_1^5P_2^2 - 2E_2P_1^7}{12P_1^3P_2^3(P_2^2 - P_1^2)} \tag{6.29}$$

$$\delta'_{1111} = \frac{-E_1P_2^5 + 5E_1P_1^2P_2^3 - 5E_2P_1^3P_2^2 + E_2P_1^5}{16P_1^3P_2^3(P_2^2 - P_1^2)} \tag{6.30}$$

It should be noted that G_{LD}^{np} is assumed to have only 5 extrema, $\pm P_1$, $\pm P_2$ and at $P = 0$. Because G is an eighth order polynomial, it can additionally have two symmetric real extrema for certain values of E_1, P_1, E_2, and P_2. Therefore, not every combination of E_1, P_1, E_2, and P_2 results in a realistic energy distribution. Unlike the measured P-E curves (Figure 5.2), the results from the model (Figure 6.3) show very sharp transitions from NP to P at E_2 and from P to NP at E_2 and no remanent polarization. The reason for this small remanent polarization and the more continuous transitions in the experiments is that real materials do not react instantaneously to the change of the external field, i.e., the experimentally determined P-E curves are not the steady-state reaction of the system. In the phase field model, these inertia effects are taken into account by the evolution relationship (Equation 6.17). A local clamping of the polar phase by strong local fields that leads to a stable remanent polarization for some compositions in the experiments is not considered in the model. To study the influence of the mobility parameter M on the shape of the resulting P-E hysteresis curve, the Equation 6.17 was solved with an implicit time integration scheme for a bipolar triangular electric load. For simplicity, a stress free mono-domain single crystal, similar to that described in Chapter 3 and 4 was assumed, which reduces the free energy function of the nonpolar system to contributions from the phase separation energy and the coupling of the polarization to the external field. Inserting this free energy density into Equation 6.17 leads to:

$$\frac{dP}{dt} = -M\frac{d(G_{LD}^{np}(P) - P \cdot E(t))}{dP} \tag{6.31}$$

where $E(t)$ denotes the time dependent external electrical field that changes the total system energy and leads to the system dynamic. The solutions of Equation 6.31 for different values of M are shown in Figure 6.4 for a constant frequency of the applied electric field. It can be observed that smaller values of M lead to a more continuous NP→P and P→NP phase transition behavior and the formation of a remanent polarization comparable to the experimental observations. Moreover, the critical electric fields for NP→P and P→NP phase transitions are shifted to higher and lower values with larger M, respectively. This demonstrates that the system mobility must be taken into account during the determination of the separation energy coefficients of the nonpolar material.

Assuming that no preferred direction for the induction of a polar phase exists, the presented "Landau-like" function can be expanded to two or three dimensions by replacing P^2 with $||P||^2$:

$$G_{LD}^{np}(\mathbf{P}) = G_0 + \alpha'_1||\mathbf{P}||^2 + \beta'_{11}||\mathbf{P}||^4 + \gamma'_{111}||\mathbf{P}||^6 + \delta'_{1111}||\mathbf{P}||^8 \tag{6.32}$$

This results in an energy landscape with rotational symmetry. Different expansions resulting in energy landscapes with lower symmetries, e.g. tetragonal, are also possible. To date, there are no reports available on the directional dependent P-E behavior of BNT-6BT-2KNN. This new developed two dimensional expansion of the phase separation energy function was implemented into the finite element ferroelectric material model. Again, most of the required model parameters for the polar material could be determined by fitting experimental P-E and S-E curves.

The comparison between the model results and the experimental data is shown in Figure 6.5. The red circles show the experimental P-E and S-E bipolar hysteresis curves of polar BNT-6BT-2KNN, whereas the blue curves are show the corresponding fit from the phase field model. The numerical setup was identical to that used for the polar material described above, namely a 100×100 mesh with an edge size of $1 \cdot 10^{-7}$ m. The domain wall width λ was chosen to be the same as in the polar material ($2 \cdot 10^{-9}$ m).

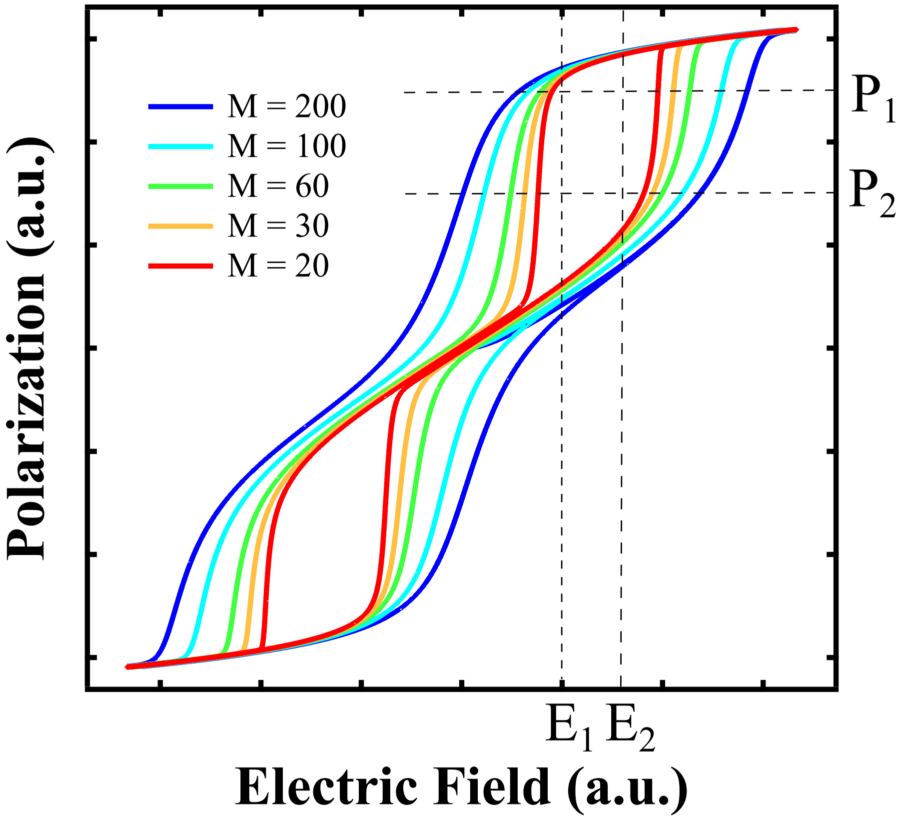

Figure 6.4: P-E hysteresis curves of the nonpolar material calculated by an implicit solution of the evolution equation for different mobility parameters M.

Electrodes on the top and bottom edge were represented in the model by Dirichlet boundary conditions for the electric potential, periodic boundary conditions were assumed on the sides, and traction free boundary conditions were assumed for the polarization and displacement on the top and bottom edge (compare Figure 6.2). The polarization hysteresis can be well reproduced by the material model. Unfortunately, the agreement is not as good for the strain hysteresis curve. Interestingly, the measurement curve shows a significant remanent polarization but a negligible remanent strain, which is not reflected by the model. Moreover, the initial gradient of the S-E curve is more shallow than the prediction from the material model. More complex electromechanical coupling mechanisms have to be included in the model in order to improve the representation of the S-E of the nonpolar material. However, the principle trend, as well as the high-field behavior of of the S-E, can be predicted with a sufficient accuracy to use this model to study some of the fundamental physical relationships of the composite effect, and to serve as a good starting point for future investigations.

An overview of the model parameters for the polar and the nonpolar material can be found in Table 6.1. Due to the lack of necessary material parameters, most of the previously described material parameters were determined by fitting the experimental P-E and S-E macroscopic behavior. Material constants and their relations of BNT-BT, BT and PZT (only for domain wall parameters) were used as starting points for the fitting process or as values for the parameters that can not be determined from uniaxial large signal P-E and S-E curves [21, 263–265]. Tensorial quantities are referred to by their typical names from three

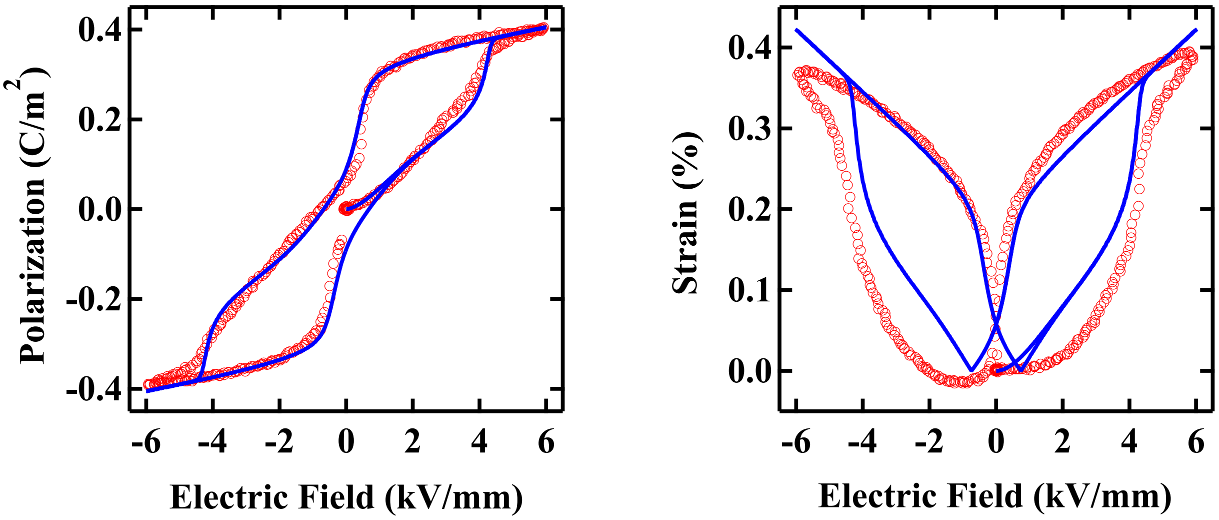

Figure 6.5: Experimentally measured P-E and S-E bipolar hysteresis loops (red circles) of the nonpolar material and the corresponding results from the phase field model (blue curves).

dimensional systems. The corresponding tensors in Voigt notation used in the two dimensional model are:

$$\mathbb{C}_{ij} = \begin{bmatrix} \mathbb{C}_{11} & \mathbb{C}_{12} & 0 \\ \mathbb{C}_{12} & \mathbb{C}_{11} & 0 \\ 0 & 0 & \mathbb{C}_{44} \end{bmatrix} \tag{6.33}$$

$$\mathbb{e}_{ij} = \begin{bmatrix} 0 & 0 & \mathbb{e}_{15} \\ \mathbb{e}_{31} & \mathbb{e}_{33} & 0 \end{bmatrix} \tag{6.34}$$

$$\epsilon_{11} = \begin{bmatrix} \epsilon_{11} & 0 \\ 0 & \epsilon_{11} \end{bmatrix} \tag{6.35}$$

Table 6.1: Model parameters for the nonpolar matrix (BNT-6BT-2KNN) and the polar seed (BNT-7BT) material used in the phase field model

Nonpolar Matrix			Polar Seed		
Parameter	Value	Unit	Parameter	Value	Unit
M	$3 \cdot 10^{-6}$	A/Vm	M	$7 \cdot 10^{-6}$	A/Vm
P_1	0.22	C/m^2	G_0	$0.7\ 0.76 \cdot 10^{-3}$	J m^2/C^2
P_2	0.19	C/m^2	G_1/G_0	0.7	C/cm^2
E_1	1.4	kV/mm	q	0.508	
E_2	3	kV/mm	κ_s	0.7	
$\mathbb{C}_{11}$	$2.06 \cdot 10^{10}$	N/m^2	$\mathbb{C}_{11}$	$1.18 \cdot 10^{10}$	N/m^2
$\mathbb{C}_{12}$	$1.55 \cdot 10^{10}$	N/m^2	$\mathbb{C}_{12}$	$0.89 \cdot 10^{10}$	N/m^2
$\mathbb{C}_{44}$	$0.85 \cdot 10^{10}$	N/m^2	$\mathbb{C}_{44}$	$0.49 \cdot 10^{10}$	N/m^2
$\mathbb{e}_{31}$	-0.02	C/m^2	$\mathbb{e}_{31}$	-0.2	C/m^2
$\mathbb{e}_{33}$	0.08	C/m^2	$\mathbb{e}_{33}$	0.8	C/m^2
$\mathbb{e}_{15}$	0.059	C/m^2	$\mathbb{e}_{15}$	0.59	C/m^2
ϵ_{11}	$8.8 \cdot 10^{-9}$	C/Vm	ϵ_{11}	$1.6 \cdot 10^{-11}$	C/Vm
P_0	0.96	C/m^2	P_0	0.362	C/m^2
S_0	0.58	%	S_0	0.262	%
κ_i	0.17		κ_i	0.17	
λ	$2 \cdot 10^{-9}$	m	λ	$2 \cdot 10^{-9}$	m

6.3 Simulation and Discussion

6.3.1 Two-Layer Model

The simplest representation of a composite ferroelectric is a two-layer structure; a phase field representation of the equivalent circuit model that was discussed in the previous chapter. The mesh was again a square shaped 100×100 mesh with an edge size of $1 \cdot 10^{-7}$ m that was vertically separated into two parts. A scheme of the mesh can be found in Figure 6.6. The boundary conditions were the same as in the previous simulations (Dirichlet boundary conditions for the electric potential, periodic boundary conditions are assumed at the sides, and traction free boundary conditions for the polarization and displacement on the top and bottom edge). At the inner interface between both materials, representing the grain boundary, continuous boundary conditions are assumed for all degrees of freedom. Other boundary conditions for the grain boundary are also possible, but not addressed in this work. The exact structure in the real material, however, is still unknown. Macroscopic P-E and S-E curves were calculated for triangular bipolar and unipolar loading scenarios with an electric load amplitude of $6\,\mathrm{kV/mm}$. The spontaneous polarization in each node in both materials was assumed to be zero in the initial state. Again, an angular mismatch of 1 ° between the stable polarization direction of the polar material and the vertical coordinate axis was chosen to break the symmetry of the system to facilitate 180° polarization switching by polarization rotation.

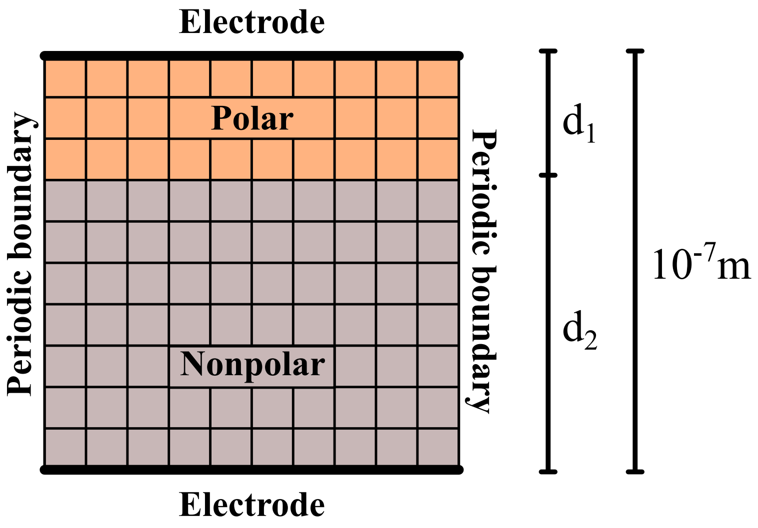

Figure 6.6: Scheme of the finite element mesh representing a double layer NP-P layer structure. The thickness of the polar material layer is given by the seed concentration $c = d_1/(d_1 + d_2)$.

The polarization was found to be nearly homogeneous in both parts, meaning that no domains were formed during switching. Interestingly, the external field-free poled state of the structure, i.e., a poled polar material and the nonpolar material with a vanishing polarization is stable. The depolarizing fields that results from the spontaneous polarization of the polar material are not strong enough to lead to a depolarization through the formation of domains upon the removal of the external electrical field. In Figure 6.7 an exemplary distribution of the electric field in the remanent state of a NP-P composite layer structure with a NP volume fraction of 20 % is shown in a contour plot. The electric field was initially applied in the negative y direction and completely removed. As expected from the results of the previous chapter, the nonpolar region (lower part) retains a remanent electric field of $-0.26\,\mathrm{kV/mm}$ that is macroscopically compensated by an electric field in the opposite direction in the polar region (upper part) of 1.02 $^{\mathrm{kV}}/_{\mathrm{mm}}$. A continuous transition is observable at the internal interface that has a thickness of about $2 \cdot 10^{-9}$ m corresponding exactly to the chosen domain wall width.

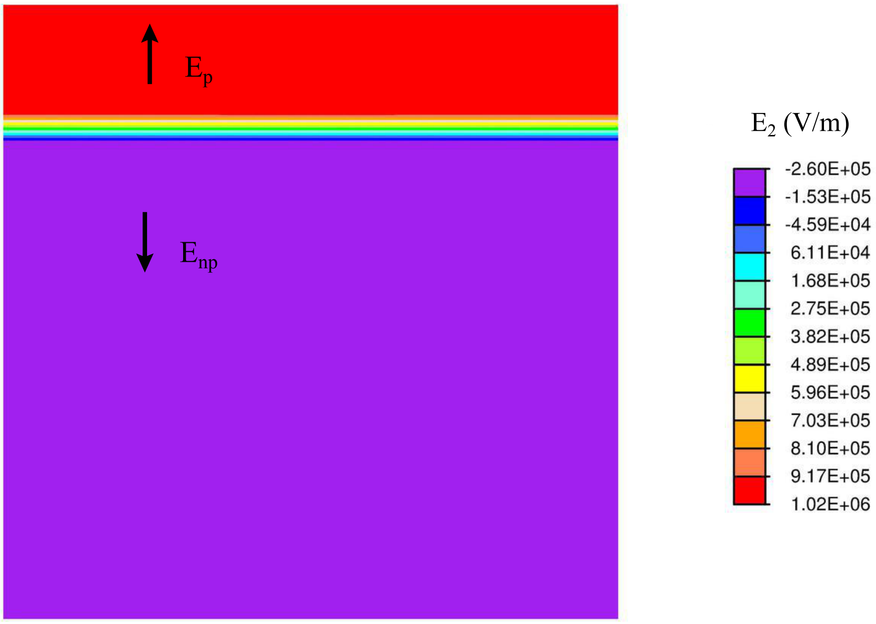

Figure 6.7: Calculated electric field distribution in vertical direction in the remanent state of a double layer structure.

The calculated macroscopic P-E and S-E hysteresis curves of the two-layer structure for a triangular bipolar electric loading with an amplitude of $6\,\mathrm{kV/mm}$ are shown in Figure 6.8 and 6.9. Calculations were performed for polar volume fractions of 50 %, 30 %, 20 %, and 10 %. It can be seen that the general trends of the experimental curves are well represented by the simulation results, particularly for lower amounts of polar phases (10 % and 20 %). Differences in the polarization curve occur in particular when the absolute field is increased above $4\,\mathrm{kV/mm}$. This behavior can be explained by the limitations of the model. In this field range the shape of the P-E and S-E curve of the polar material is influenced by its polycrystalline microstructure and can be only poorly represented by the single crystal model. This explanation is supported by the fact that the difference in this field regime between the simulation and the experiment increases with a higher volume fraction of the polar material, suggesting that the reasons for this difference are mainly due to the non optimal representation of the polar material by the model. As mentioned during the model explanation, the polar material is treated as a single crystal with a coercive field and a remanent polarization of the polycrystalline seed material. Differences in the P-E and S-E hysteresis curves were visible during the determination of the model parameters (compare Figure 6.1). Significantly improving the representation of the polar seed material is not straightforward. Multiple randomly oriented seed crystals have to be implemented in the microstructure. Unfortunately, these complex models would require new Landau parameters for the seed material to better represent the single crystal behavior, i.e., anisotropic material properties, instead of mimicking the polycrystalline properties. In addition, the numerical effort, which is necessary to solve such a complex structure, is much larger than for the presented examples and lies beyond the scope of this work. However, the general trends of the experimental curves are predicted and allow for further study of the influence of the microstructure on the observed macroscopic material behavior.

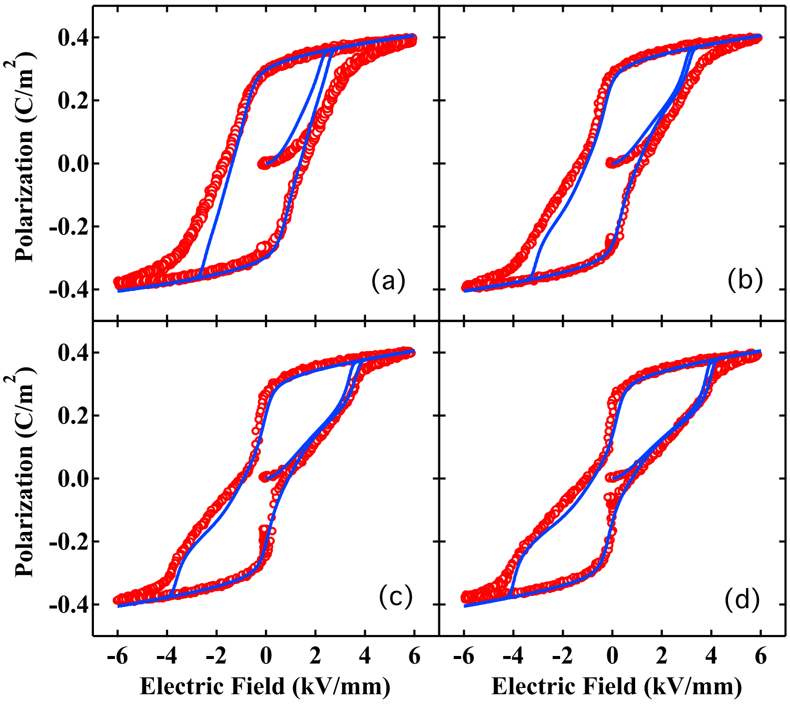

Figure 6.8: Experimentally measured macroscopic P-E bipolar hysteresis loops of NP-P composite materials with a seed concentration of 50 % (a), 30 % (b), 20 % (c), and 10 % (d) (red circles) and the corresponding results from the two-layer phase field model (blue curves).

Similar trends are observed in the simulated *S*-*E* behavior (Figure 6.9) of composite ferroelectrics as that observed in the calculated *P*-*E* behavior. The general trend of the experimental curves is represented by the simulations with a good agreement; deviations increase for an increasing volume fraction of polar material. The best agreement can be found for the unloading process, where the slope and the remanent strain value is accurately predicted by the model. Deviations between the simulations and the experimental curves are particularly evident during the loading path. Again the steep ferroelectric switching of the ”single-crystal” polar material influences properties of the simulated composite.

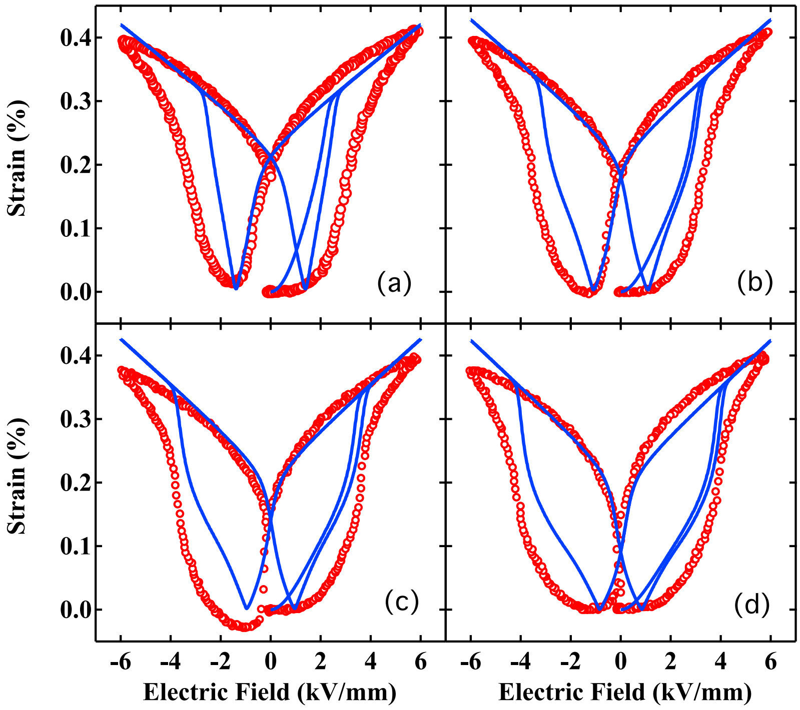

Figure 6.9: Experimentally measured macroscopic *S*-*E* bipolar hysteresis loops of NP-P composite materials with a seed concentration of 50 % (a), 30 % (b), 20 % (c), and 10 % (d) (red circles) and the corresponding results from the two-layer phase field model (blue curves).

More important for actuator applications is the unipolar behavior. The results from the phase field simulations of the macroscopic *P*-*E* and *S*-*E* curves are shown in Figure 6.10 and 6.11 together with experimental measurements. Similar to the bipolar results the best agreement can be found for the unloading process and fields above 6 kV/mm. For the composition with a polar volume fraction of 50 %, the remanent polarization and strain as well as the small hysteresis of the *P*-*E* and the *S*-*E* curve are in good agreement with the experimental data. During unipolar loading the polar seed material does not ferroelectrically switch, so that the steep switching curve of the single crystal seed model does not influence the results of the simulation like in the bipolar case. For compositions with a lower polar volume fraction of 20 % and 30 % the prediction of the high field behavior is still very good. During unloading the P→NP back-transformation begins around 0.5 kV/mm in the model, whereas the P→NP back-transformation in the experimental curves is not as distinct and is only observed below 0.1 kV/mm. This results in an underestimation of the remanent polarization and strain in these compositions. A possible explanation for this behavior might be the more complex microstructure of real materials, which includes defects that can stabilize the polar phase and decrease the amount of usable strain. The prediction of the macroscopic *P*-*E* and *S*-*E* improves for the composite with a polar volume fraction of 10 %. Again, the depolarization in the model appears already at higher fields below 1 kV/mm than in the real material (0.2 kV/mm). However, the remanent polarization and especially the remanent strain is much closer to the predicted values. This composition is the only one where a distinct depolarization for decreasing electric fields is observable. The density of seed grains in the material is obviously low enough to prevent a clamping of the polar phase in matrix material.

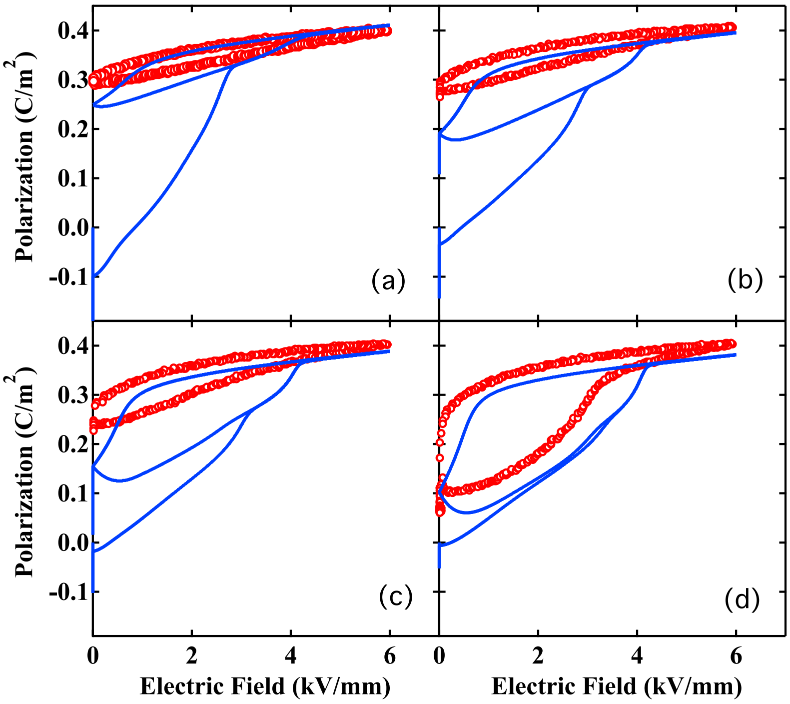

Figure 6.10: Experimentally measured macroscopic *P*-*E* unipolar hysteresis loops of NP-P composite materials with a seed concentration of 50 % (a), 30 % (b), 20 % (c), and 10 % (d) (red circles) and the corresponding results from the two-layer phase field model (blue curves).

It should be mentioned that the polarization and strain in the model decrease even further when the field is raised again. This originates from the system inertia. At $E = 0$ the system has not reached its equilibrium position. Even at higher fields this equilibrium position is above the current value so that polarization and strain decrease even for an increasing field. This effect can be observed in each simulation and especially stands out in case of the composite with 30 % seed content. A closer look at the experimental data reveals that this effect is also visible in the experimental data, since they are also not in their equilibrium state when the field is decreased to zero. This effect is particularly evident in the curves of the composite with a 10 % seed content, were the depolarization is especially pronounced.

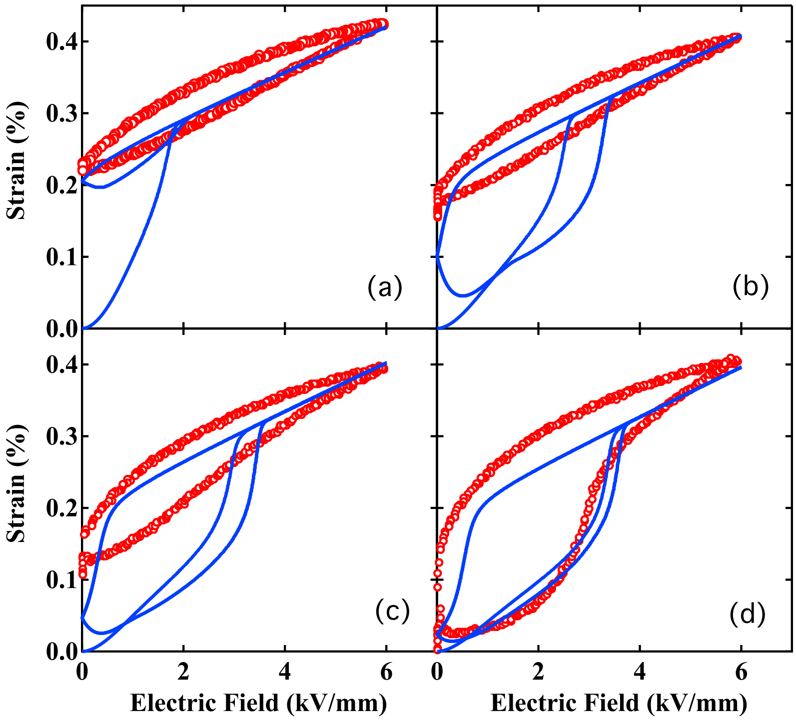

Figure 6.11: Experimentally measured macroscopic S-E unipolar hysteresis loops of NP-P composite materials with a seed concentration of 50 % (a), 30 % (b), 20 % (c), and 10 % (d) (red circles) and the corresponding results from the two-layer phase field model (blue curves).

6.3.2 Simple Grain Model

A first step into the direction of the representation of a complex polycrystalline microstructure of a NP-P composite material is the simulation of a single polar seed-grain inside a nonpolar matrix. For simplicity, a single square-shaped grain was assumed. In Figure 6.12 scanning electron microscopy images show the actual grain structure of BNKT-BA and BNKT-BA-BNT [205]. Especially in compositions with BNT content, red colored cuboid-shaped grains can be observed in the enlarged cutout, matching the proposed microstructure. The grain is completely surrounded by nonpolar material; the edge length of the seed crystal in each composition was derived from the respective volume fraction of polar material. An angular mismatch of 1 ° between the stable polarization direction of the polar material and the vertical coordinate axis was chosen to break the symmetry of the system. A scheme of the mesh that was used for the simulations can be seen in Figure 6.13. The number of elements discretizing each structure was reduced to 80 × 80. In order to maintain the element size, the edge size of each structure was reduced to $8 \cdot 10^{-8}$ m. This reduction was necessary because the complex domain structure of the polar seed drastically increased the necessary computation time. Calculations were performed for polar volume fractions of 50 %, 30 %, 20 %, and 10 %.

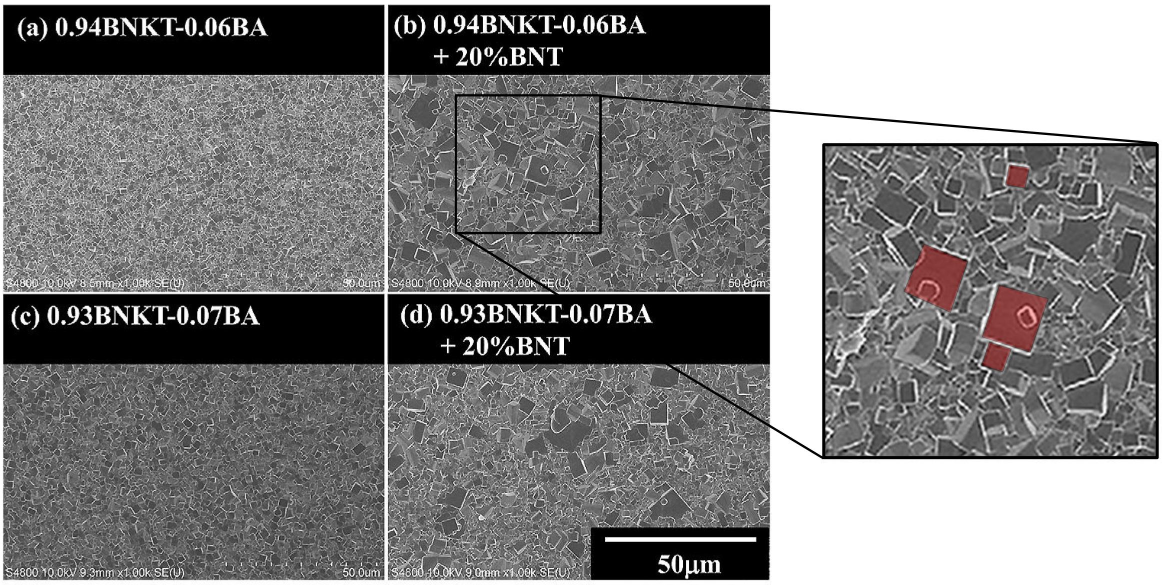

Figure 6.12: Scanning electron microscopy images showing the surface of 0.94BNKT-0.06BA without (a) and with (b) BNT and 0.93BNKT-0.07BA without (c) and with (d) BNT. Large BNT grains are observed [205]. Some exemplary square-shaped grains are colored in red.

In the initial state, the nodes of the polar material were homogeneously set to $P_i = (0, P_S)$, whereas the nodes of the nonpolar material were set to $P_i = (0, 0)$. Unlike in the previous two-layer geometry, this initial polarization in the seed material was not stable. With no external electric field applied, the polar seed decreases its net polarization and the corresponding depolarization field by the formation of a stripe-like domain structure. For different grain sizes, grain geometries, and boundary conditions, different domain patterns are expected [35, 266]. The stable domain structure for 50 % and 10 % volume fraction of polar material after relaxing from the initial condition can be found in Figure 6.14. In both cases, one central domain is formed (blue) with a polarization orientation in the opposite direction of the initial polarization direction, flanked by two domains pointing in the opposite direction. This can be explained by the slower seed dynamic that is clamping the polarization of the seed at the right and

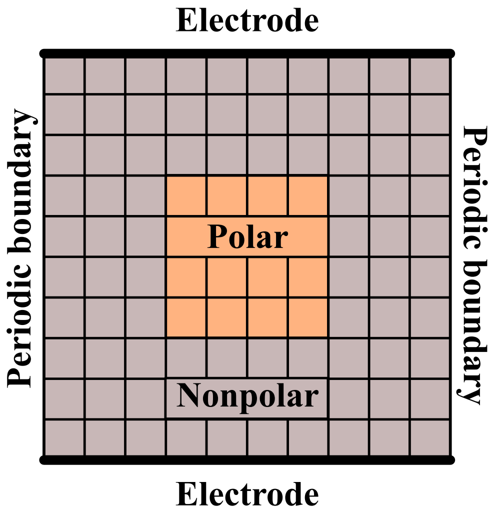

Figure 6.13: Scheme of the finite element mesh representing a simple grain NP-P layer structure. The size of the polar material layer is given by the seed concentration.

left edges. The central domain is formed in order to decrease the total net polarization and therewith decrease the internal depolarizing field. The polarization perpendicular to the grain boundary is further decreased by the formation of the triangular shaped horizontal domains (yellow, green).

When the external field of $(0, -E)$ is applied the domain structure evolved gradually (Figure 6.15). Instead of a homogeneous switching of the whole polar material, the domain walls are moved by the external field. The size of the energetically favored (blue) domain increases at the expense of the neighboring unfavored (red) domains as well as the neighboring triangular horizontal domains (yellow, green). In this process, the 180° domain walls are pushed through the right and left grain boundaries out of the seed crystal. Moreover, at the corner of the seed crystal triangular horizontal domains start rotating into the direction of the electric field. Interestingly, the shape of the domain-structures is identical for both seed concentrations, i.e., seed crystal sizes. Future studies will have to show how the observable domain-structure and domain switching behavior is influenced by the seed crystal orientation, the boundary conditions, the shape of the seed grain, as well as by the interaction of multiple seed grains.

The domain-structure of the composite with a 50% seed content is shown in Figure 6.16 for the first unipolar loading cycle at five selected load levels. For comparison, the macroscopic polarization curve is shown as well. The initial domain configuration (1) is the same as in Figure 6.14. The unipolar electrical load was applied in the negative vertical direction. As previously described, with an increase in the applied electrical field the central domain that is oriented in field direction (blue) grows at the expense of neighboring, oppositely oriented domains (red). This results in the corresponding 180° domain walls being pushed towards the edges of the grain (2). Initially, the horizontal domains (green, yellow) also grow at the expense of the energetically unfavored domains (red), pushing them towards the corners of the square shaped grain. When the electric field is further increased, the domains are primarily oriented parallel to the field direction (3). Interestingly, both 180° domain walls were not completely driven out of the crystal. Instead the polarization at the edges of the seed crystal switched by 180°, leaving a small stripe with a reduced polarization at the former position of the domain wall. Two switching mechanisms can be observed that reduce the size of the vertical domains. On the one hand the 90° domain wall between the vertical and the downwardly oriented domain shifts towards the corners of the seed grains, on the other hand the polarization at the corners rotate into the direction of the applied electric field, forming new downwardly oriented domains. Moreover, the matrix starts to develop a spontaneous

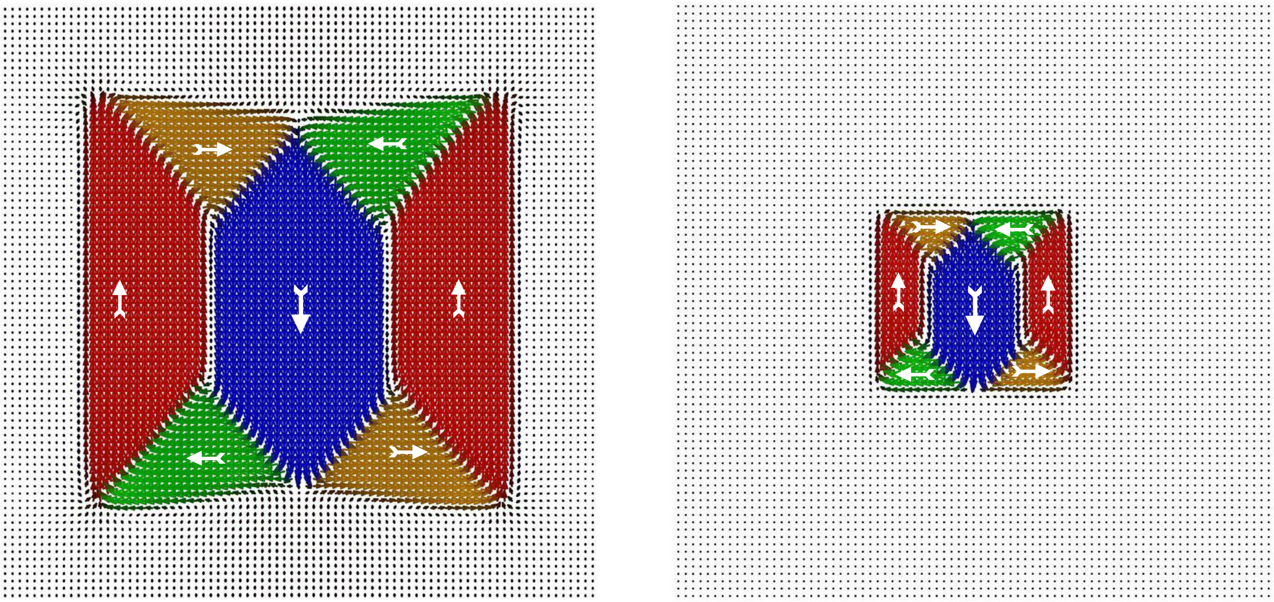

(a) 50 % seed

(b) 10 % seed

Figure 6.14: Stable domain structure for 50 % and 10 % volume fraction of polar material after relaxing from the initial condition. Red and blue areas are representing a polarization direction of $(0, P)$ and $(0, -P)$ respectively, whereas yellow and green areas are representing a polarization direction of $(P, 0)$ and $(-P, 0)$, respectively.

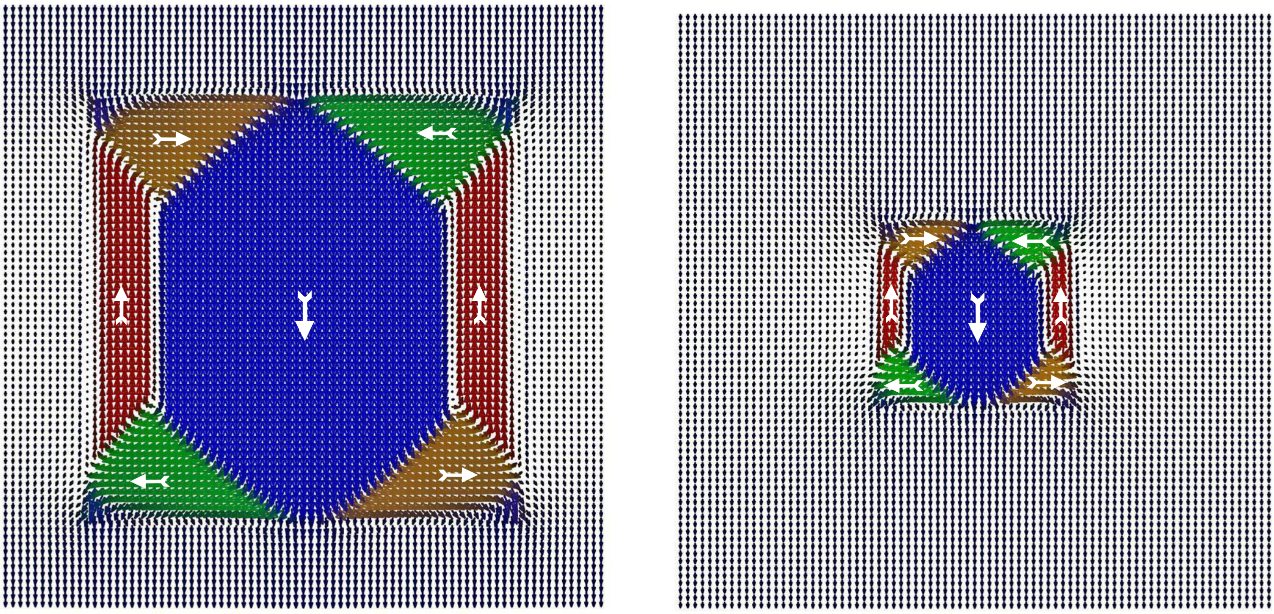

(a) 50 % seed

(b) 10 % seed

Figure 6.15: Domain structure for 50 % and 10 % volume fraction of polar material for the application of $1.8\,{}^{\mathrm{kV}}/_{\mathrm{mm}}$. Red and blue areas are representing a polarization direction of $(0, P)$ and $(0, -P)$ respectively, whereas yellow and green areas are representing a polarization direction of $(P, 0)$ and $(-P, 0)$, respectively.

polarization, which is completely parallel to the applied electric field. It can be seen that the polarization matrix material above and below the seed crystal is larger than on that side of the seed crystal. Moreover, the polarization of the seed is increased in areas where the seed polarization is oriented perpendicular to the grain boundary.

At maximum electric field (4), the domain-structure vanishes completely; the polarization of the seed and the matrix is homogeneously oriented in field direction. The absolute value of the seed polarization is, however, approximately 10 % larger than the polarization of the seed. Even in the remanent state the single domain state of the seed crystal remains stable. At the sides of the seed crystal the polarization of the matrix material decreases drastically, whereas above and below the seed the polarization remains stable, with a remanent value equivalent to the seed crystal.

In Figure 6.17 the electric field in the vertical direction inside the composite during the unipolar loading is shown at the same five load levels. In the initial state, large field values between -0.52 and $0.87\,{}^{\mathrm{kV}}/_{\mathrm{mm}}$ can be seen in the seed material and in the matrix material above and below the grain boundary. It should be noted that because of the $1\,^{\circ}$ angle mismatch in the orientation of the seed crystal the field distribution has no central vertical axis of symmetry. The electric field values inside the seed and matrix materials are predominately negative and positive, respectively. This is primarily due to the non-zero net polarization in the negative vertical direction of the seed material in the initial state. This polarization leads to a positively charged lower grain boundary and a negatively charged upper grain boundary, which induce charge densities with an opposite sign in the nearby electrode on top and bottom of the composite. The fields, caused by these local charge densities, are maximum along the central axis, which corresponds to the position of the central domain that is oriented in the direction of the initial net polarization of the seed crystal. The strong inhomogeneities in the electric field are caused by the polarization gradients of the domain structure inside the seed crystal.

When the external electric field of $1.5\,{}^{\mathrm{kV}}/_{\mathrm{mm}}$ is applied the field distribution becomes more homogeneous. It can be seen that the electric field inside the seed and the lateral parts of the matrix material is in general lower ($\sim 1\,{}^{\mathrm{kV}}/_{\mathrm{mm}}$) than the field in the matrix above and below the seed material ($\sim 2\,{}^{\mathrm{kV}}/_{\mathrm{mm}}$)). This effect is similar to the equivalent circuit model of the double layer structure. However, the lateral parts of the matrix material do not benefit from the seed material. Future studies will have to show if this "neutral" volume fraction of the seed material is reduced for more complex domain-structure with multiple randomly oriented seed crystals. There are still some inhomogeneities in the electric field at the corners and the central axis of the seed crystal, where the field is even further increased in the matrix material (up to $2.75\,{}^{\mathrm{kV}}/_{\mathrm{mm}}$). At this point the polarization of the seed is oriented perpendicular to the grain boundary, so that the interface term $\mathscr{H}^{int}$ locally supports the composite effect. These contributions are still visible for higher applied field of $3\,{}^{\mathrm{kV}}/_{\mathrm{mm}}$ (3) and $6\,{}^{\mathrm{kV}}/_{\mathrm{mm}}$ (5) along the whole horizontal grain boundaries, resulting from the vanishing domain structure and the increasingly homogeneous polarization of the seed. Even at maximum field (4) there is still a strong field enhancement in the matrix material.

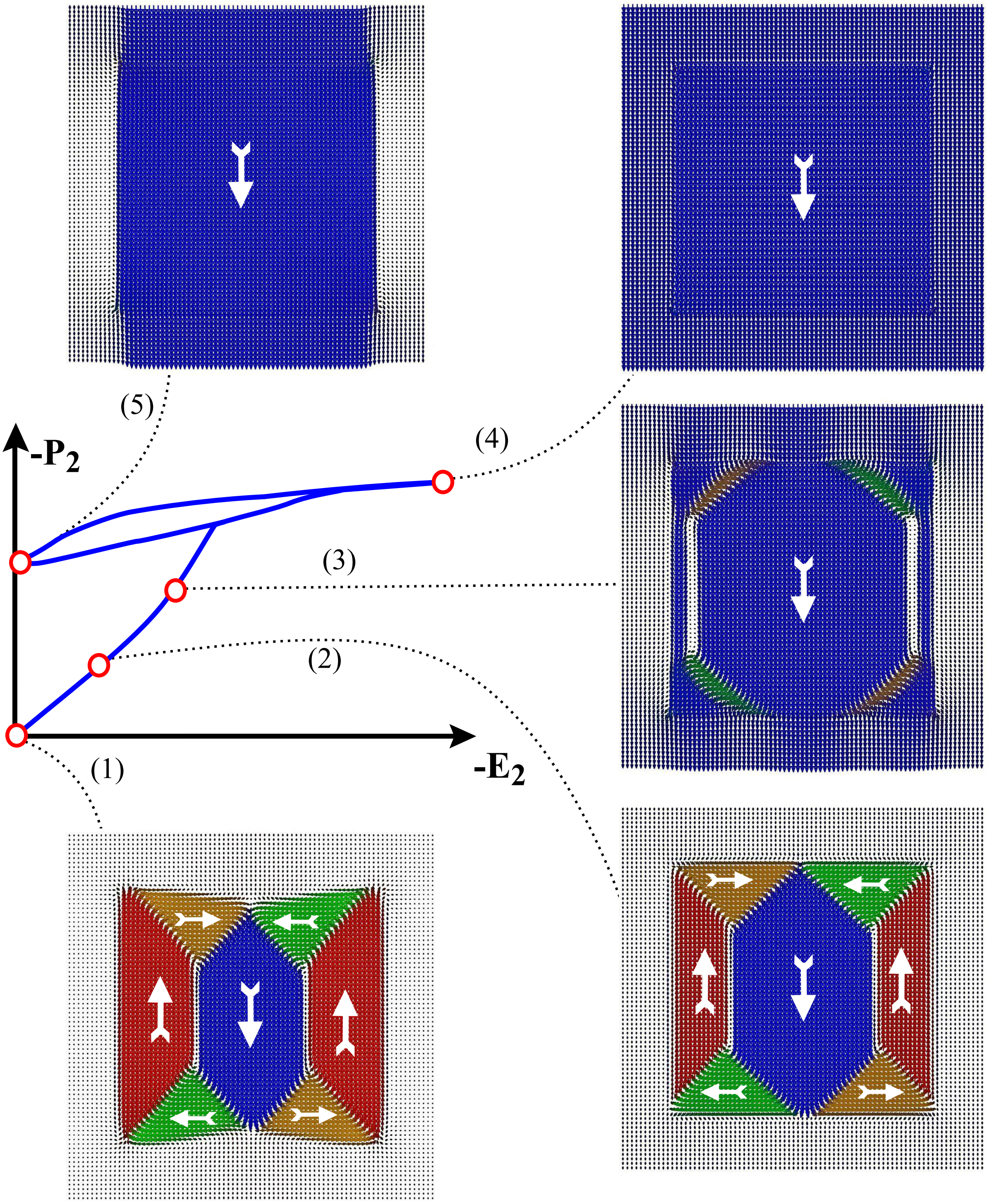

Figure 6.16: Unipolar P-E hysteresis calculated with the simple grain approach for a composite material with a seed concentration of 50 %. The polarization distribution is presented at five points during the first loading cycle.

In the remanent state (5), a depolarizing field of 0.9 kV/mm is formed in the opposite direction of polarization. This is compensated by an electric field of 2 kV/mm in the matrix material above and below the seed crystal that stabilizes the polarization in these areas. In the "neutral" lateral matrix areas the electric field is not large enough to induce any significant polarization.

The internal mechanical stress in the vertical direction inside the composite during the unipolar loading is shown at the same five load levels in Figure 6.18. In the initial state, most of the observed stresses arise from the domain-structure of the seed material. The four tensile stress maxima correspond to the connection points of three domains (up, down, horizontal). There are six compressive stress maxima visible in the seed material, each at a position where a vertical domain impinges on the grain boundary. Moreover, a tensile stress distribution in the matrix material and a corresponding compressive stress distribution in the seed material in vicinity of the lateral grain boundaries can be observed. In this region the seed polarization is oriented parallel to the grain boundary so that the stress distribution can be due to the differences in the spontaneous strain of both materials. When the field is increased (2), (3), and (4) the stress distribution homogenizes and the maximum stresses drop by 40 % (compressive) and 24 % (tensile). The disappearances of the vertical domains reduce the tensile stresses in the seed material. In addition, the electric field induces a significant polarization in the matrix material that is accompanied by a spontaneous strain. This reduces the strain mismatch in the vertical direction between the matrix and the seed and lead to the decrease in compressive stress. However, the seed material experience compression from the surrounding matrix from the maximum applied field of even at 6 kV/mm (4) to the remanent state (5), which generally influences the physical properties of polar materials [42, 267, 268].

Figure 6.16, 6.17, and 6.18 illustrate the advantages of the phase field method to simpler material models for composites. With this method it is not only possible to include effects from the microstructure, but to monitor the behavior of the polarization and other internal fields during loading.

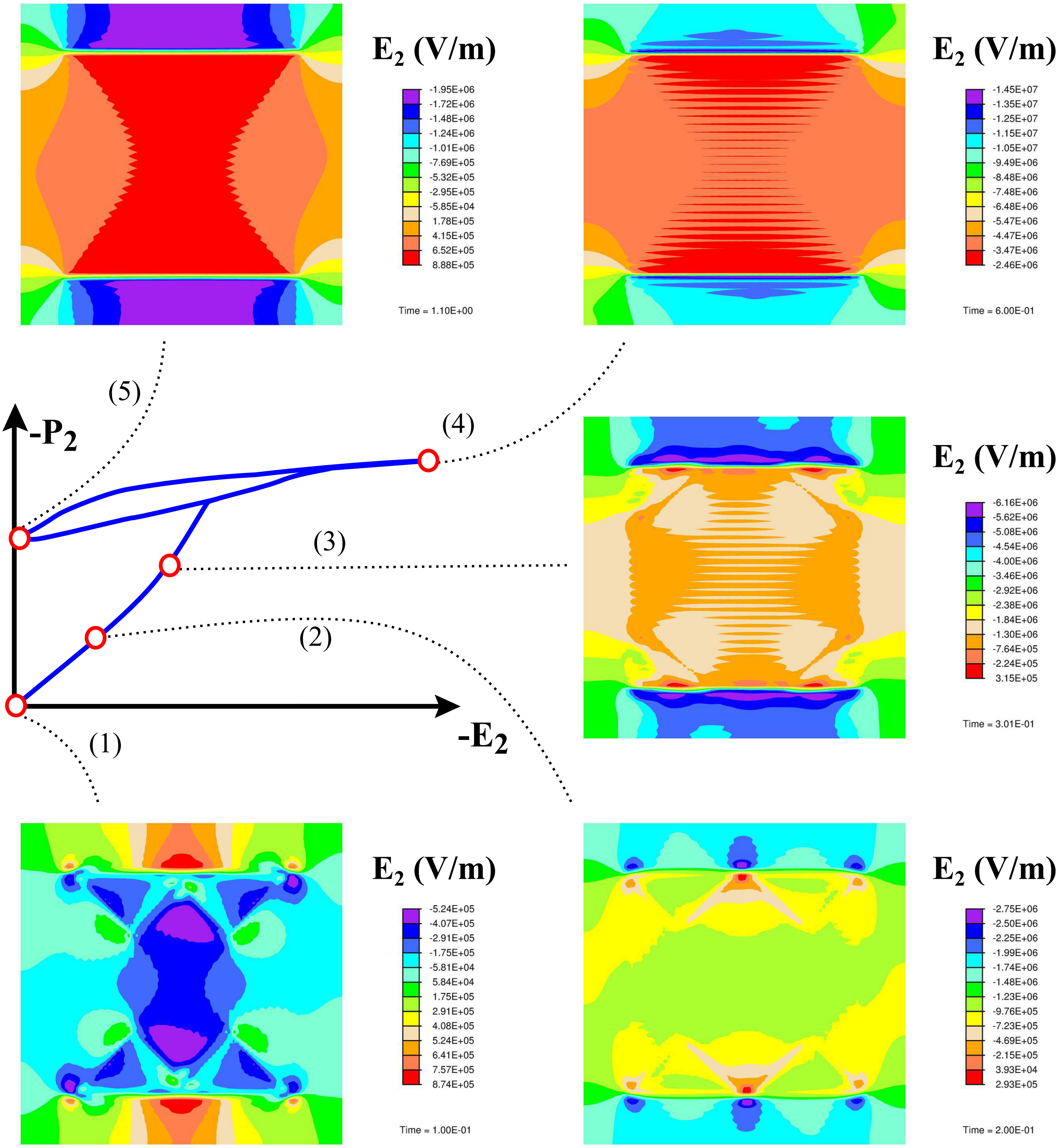

Figure 6.17: Unipolar P-E hysteresis calculated with the simple grain approach for a composite material with a seed concentration of 50 %. The distribution of the electric field is presented at five points during the first loading cycle.

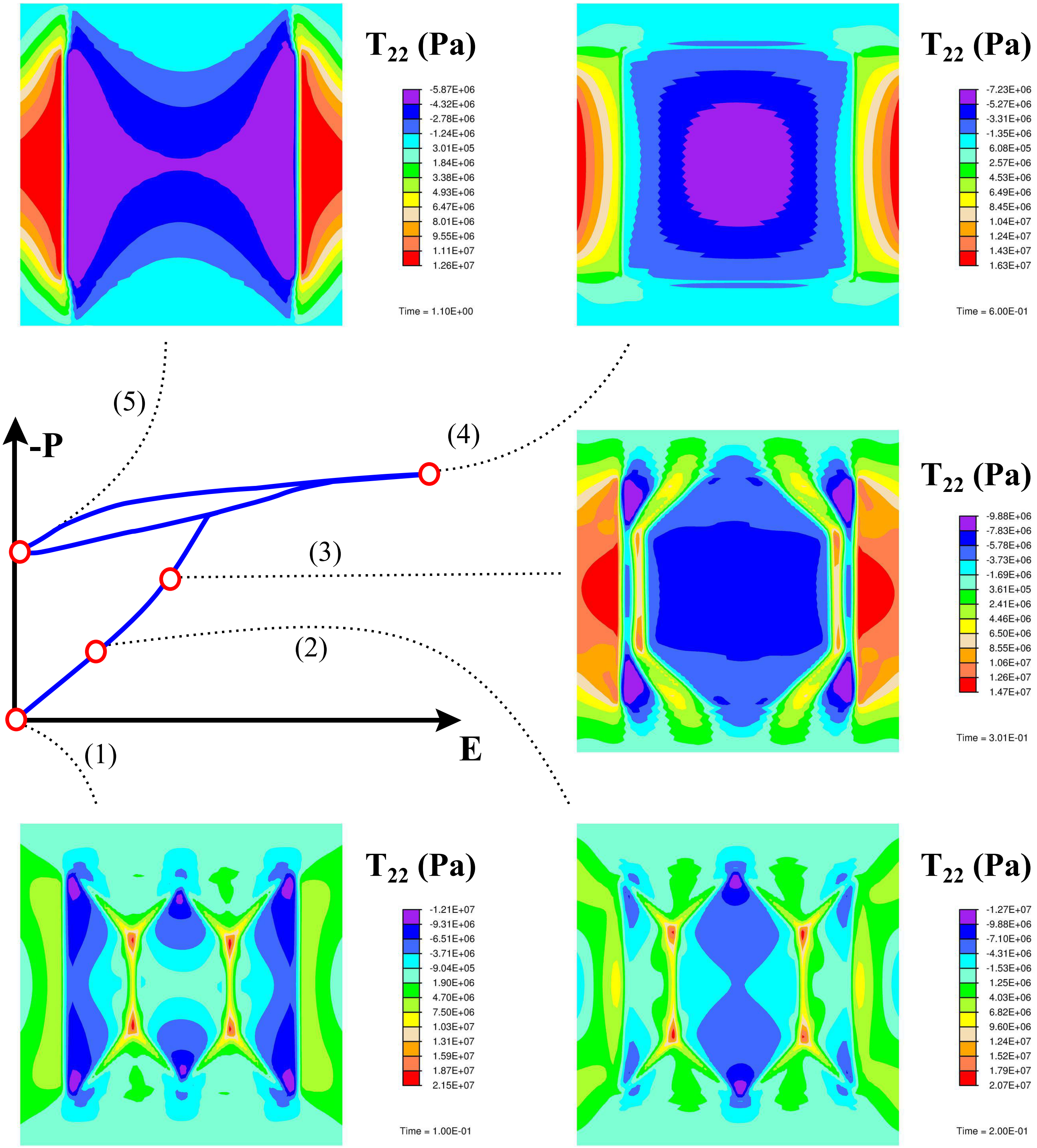

Figure 6.18: Unipolar P-E hysteresis calculated with the simple grain approach for a composite material with a seed concentration of 50 %. The distribution of the mechanical stress is presented at five points during the first loading cycle.

The simulated macroscopic *P*-*E* and *S*-*E* hysteresis curves of the two-layer structure for a triangular bipolar electric loading with an amplitude of 6 $^{\mathrm{kV}}/_{\mathrm{mm}}$ are shown in Figure 6.19 and 6.20 and compared to experimental measurements. At the beginning and the end of each plot the relaxation process can be observed. Compared to the previous two-layer model the shape of the hysteresis matches the experimental data more closely. The depolarizing process starts at the same fields found in the simplified two-layer model, which are larger than that found in experiments. However, the estimation of the remanent polarization and strain has been significantly improved. It appears that the greater interface between polar and the nonpolar material leads to a stronger phase clamping effect, comparable to that in real materials. Further simulations including multiple grains should be able to address this question. Unfortunately, the accuracy of the predictions of the slopes and absolute values of the *S*-*E* at higher fields decreases for the single grain microstructure. This may be caused by inaccurate model parameters, which were derived from experimental data and represent essentially one-dimensional coefficients. In the current simulations we find more complex polar structures that necessitate anisotropic material properties. This is especially apparent in the simulated *S*-*E* behavior. Here, the electrostrictive coefficients were assumed to be isotropic, due to lack of available material properties. It is anticipated that these coefficients have lower symmetry, which can adversely affect simulated behavior. In these previous cases no formation of domains or switching by domain wall movement occur and influence the calculated macroscopic *P*-*E* and *S*-*E* hysteresis curves.

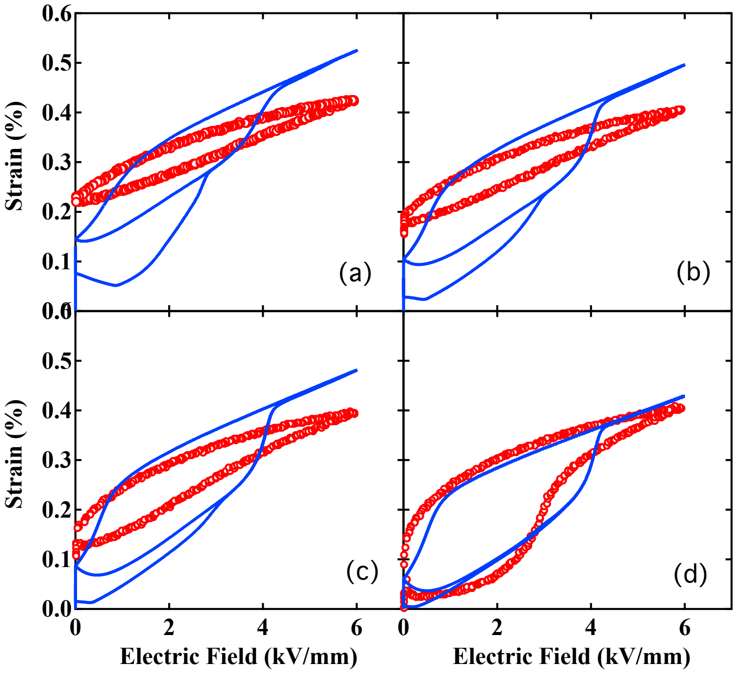

Figure 6.19: Experimentally measured macroscopic *P*-*E* unipolar hysteresis loops of NP-P composite materials with a seed concentration of 50 % (a), 30 % (b), 20 % (c), and 10 % (d) (red circles) and the corresponding results from the simple grain phase field model (blue curves).

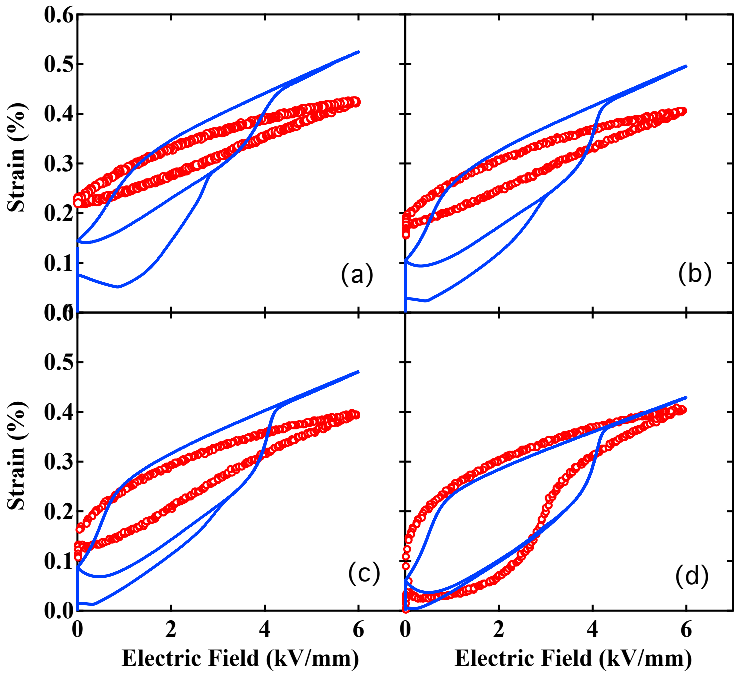

Figure 6.20: Experimentally measured macroscopic S-E unipolar hysteresis loops of NP-P composite materials with a seed concentration of $50\,\%$ (a), $30\,\%$ (b), $20\,\%$ (c), and $10\,\%$ (d) (red circles) and the corresponding results from the simple grain phase field model (blue curves).

6.4 Conclusions

In this chapter a phase field model based on Ginzburg-Landau theory for polar-nonpolar composite materials was presented. Both materials were described with the same degrees of freedom, whereas the spontaneous polarization is used as the primary order parameter that determines the dynamics of each system. The main difference between the material models is the form of the phase separation energy that describes the free energy density as a function of the magnitude and direction of the spontaneous polarization. The polar material was treated as a regular ferroelectric material with a 2-4-6-Landau potential with four minima along the axis of coordinates $(\pm P_S, 0)$ and $(0, \pm P_S)$. Numerous reports on similar models for ferroelectric materials can be found in the literature [21, 41, 98, 104–106, 201, 214]. For the nonpolar material a rotationally symmetrical phenomenological energy function was used, which leads to the typical double-loop P-E- hysteresis curve that is observed in the experiments. The necessary model parameters for both phase separation energies were determined by fitting the calculated macroscopic P-E- hysteresis curve to experimental observations. With this material model, two examples of potential NP-P composite microstructures were simulated. First a double layer structure that corresponds to the equivalent circuit model that was presented in the previous chapter. The second structure was a single, square-shaped polar seed crystal inside a nonpolar matrix.

The quality of the calculated results was further limited by the lack of knowledge of the appropriate material parameters that were not accessible by the fitting method. However, the main scope of this work was reached. It was demonstrated that the presented material model approach is able to simulate the basic characteristics of NP-P composite materials. In order to improve the predictive capabilities of the phase field model it is necessary to implement more complex microstructures, including multiple seed grains with different crystallographic orientations. In addition, special attention should be given to the implementation of the NP-P boundary condition. So far the physical structure of the grain boundary is still unknown; recent bright field measurements on related EDX spectra suggest the formation of mixed material between the grains of different materials [229]. However, complex structures can be no longer effectively handled on conventional single-processor CPUs. It is necessary to implement a parallel solver to execute calculations on more powerful mainframe computers. A second important point that can be improved is the accuracy of the model parameters. Currently, only the parameters that directly influence the macroscopic P-E and S-E hysteresis curves are determined by fitting corresponding experimental data. All other parameters were estimated from related materials. Moreover, the Landau coefficients of the seed material were directly determined from experimental data measured on polycrystalline samples and therefore include the effects of the polycrystalline nature of the sample material. Phase field models that are complex enough to sufficiently represent polycrystalline structures will require Landau coefficients that correspond to the behavior of a single crystal. To obtain these values additional experimental data, ideally from single crystal samples are required. Alternatively, some of the required parameters could be determined by ab initio calculations [17, 19]. An interesting test case for the described material model would be NP-P multilayer thin-films, made by either magnetron sputtering [269] or pulse laser deposition [270]. These films have typically single crystal characteristics and the structures are thin enough to be represented by the model.

7 Summary and Outlook

Field-induced phase transitions between different ferroelectric phases are important phenomena as they are typically accompanied by discontinuous increases in polarization and strain. In the first part of this work, field-induced tetragonal→orthorhombic phase transitions of ferroelectric single crystals were theoretically studied with a thermodynamic Landau model for an arbitrary material. It was shown that during the transition the direction of the spontaneous polarization rotates from a polar axis of the initial tetragonal phase towards the metastable direction that is energetically favored by the applied electric field. The height of the critical electric field at which the transition takes place as well as the magnitude of the discontinuous jump in the polarization is determined by the shape of the Landau energy landscape. In all studied cases the critical field was larger than the coercive field for 180° switching. Moreover, the critical field decreased for a flattening of the energy landscape between two equivalent tetragonal crystallographic orientations. The findings were consistent with previous work by Bell [90] and Damjanovic [72] and were published in Applied Physics Letters [91].

The optimal model system to measure electrical field-induced phase transitions is $BaTiO_3$. High quality single crystals are commercially available and the phase transition temperature for a tetragonal→orthorhombic lies close to room temperature at $8\,^\circ C$, suggesting a flat Landau energy landscape and a lower critical field. Bipolar and unipolar large signal P-E and S-E curves were measured along the $\langle 100\rangle_c$, $\langle 110\rangle_c$, and $\langle 111\rangle_c$ crystallographic axes. Field-induced tetragonal→orthorhombic phase transitions were found along the $\langle 110\rangle_c$ crystallographic axis at critical fields of about $2.5\,{}^{\mathrm{kV}}/_{\mathrm{mm}}$ at room temperature. For higher temperatures that are further away from the T→O transition temperature, the critical field increases significantly. This material behavior was compared to predictions from the thermodynamic model, using various Landau energy landscapes that were reported from different researchers [52–55]. It turned out that the Landau parameters proposed by J. Wang [55] were the most appropriate to estimate the exact trend of the P-E curve for an electrical load along the $\langle 110\rangle_c$ crystallographic axis. Moreover, the calculated temperature dependence of the critical field as well as the permittivity along $\langle 110\rangle_c$ of the tetragonal phase was in a good agreement with the measurement results. T→R were not found along the $\langle 111\rangle_c$ crystallographic axis. The critical fields that were predicted by the Landau model were larger than the breakdown strength of the measured samples. However, it was possible to identify the T→O in polarization curves measured at the lower temperature of $15\,^\circ C$. The temperature dependent measurements along $\langle 110\rangle_c$ as well as the comparison with the predictions by the thermodynamic model calculated for four different Landau potentials were published in Applied Physics Letters [92].

Recent measurements by Seo et al. [156] revealed a pronounced increase in the remanent strain for unipolar mechanical and electrical loading of virgin $Pb(Zr_{1-x}Ti_x)O_3$ with compositions close to the morphotropic phase boundary (MPB) that could not sufficiently be explained by ferroelastic/ferroelectric switching or plastic deformation. Damjianovic proposed that a flattening of the Landau energy landscape could be an important reason for the improved ferroelectric properties for materials with a composition close to the MPB [99]. It is therefore reasonable to assume that non-reversible phase transitions, induced by the applied load are the origin of this behavior. A statistical method was used to expand the thermodynamic model to predict the behavior of polycrystalline ferroelectric materials. Moreover an electrostrictive coupling term was added to allow the application of mechanical loads. The advantage of this method, compared to to other statistical models that are based on fixed switching energy criteria for the spontaneous polarization, is that the possibility of induced phase transitions is already included in the shape of the Landau energy landscape. This expanded model was used to simulate the polarization and strain response of $Pb(Zr_{1-x}Ti_x)O_3$-compositions for mechanical and electrical loading scenarios. The Landau parameters were previously reported by Haun et al. [93] and the electrostrictive coefficients were determined from fitting of experimental values. The resulting remanent strain was normalized by the switching strain of the respective compositions to prevent contributions from the ferroelastic/ferroelectric switching. It was also possible to monitor the current phase of each grain during the simulation. The model predicted a final tetragonal volume fraction of 31 % and 18 % after mechanical and electrical unloading in PZT45 that showed the highest remanent strain in relation to its switching strain in the measurements. The predicted remanent strain of this composition is in good agreement with the experimental results, suggesting that induced phase transitions are very likely to contribute to the high remanent strain in $Pb(Zr_{1-x}Ti_x)O_3$ compositions close to the MPB. This theory could be further supported by in situ XRD measurements that can determine the phase content of a sample during mechanical or electrical loading. The experimental data as well as the model description and results were for mechanical loading were published in Physical Review B [156].

In the last two parts of this work, two material models are introduced for novel lead-free NP-P composite materials that are a promising class of materials to replace conventional lead containing materials in piezoelectric applications. The physical mechanism that leads to the large value of usable strain and effective piezoelectric properties is an induced nonpolar→polar phase transition of the nonpolar material that is mostly reversible during reduction of the applied field. Therefore, the discontinuous jump in strain that accompanies the field-induced transition can be used in each loading cycle. The main drawback is that the required field to induce the NP→P phase transition is too large for most applications. This problem is solved by forming a heterostructure with a chemically compatible polar material, which serves as seed crystal for the NP→P phase transition and decreases the critical field. The aim for both of the material models was to gain insight into the dependency of the critical field as well as the effective piezoelectric coefficient $d_{33}^{\star}$ from the composition of the composite and the material constants of the polar seed and nonpolar matrix.

In the first model the complex microstructure of the composite material is drastically simplified and represented by a series configuration of two nonlinear capacitors. Polarization and strain responses of the capacitors to the application of an external field corresponds to that of the nonpolar matrix and polar seed material. Both P-E curves were transferred to a piecewise linear representation, in order to define a limit set of material parameters and to predict the polarization hysteresis for different loading amplitudes. S-E curves were calculated from the polarization curve by using electrostrictive coefficients that were determined by a fit of the S-E curves of both end members. The composite effect, i.e., an increase of $d_{33}^{\star}$ compared to the matrix material, is a direct consequence of the different P-E curves of the matrix and the seed material together with the fact that the polarization of each capacitor in the series configuration has to be the same. This is achieved by the formation of internal electric fields in each capacitor. As result, the lower poling field of the seed material leads to a field enhancement at the matrix material. On the other hand, if the external field is reduced the matrix material results in a negative field enhancement for the seed material that leads to backswitching processes and reduces the remanent polarization of the composite material. The P-E and S-E curves of the composite materials calculated with the equivalent circuit model were in a good agreement with experimental measurements. Moreover, the model was able to predict the optimum seed concentration for a maximum $d_{33}^{\star}$. The absolute values of $d_{33}^{\star}$ were overestimated by the model at lower electric field values, because the piecewise linear representation of the nonpolar material is not sufficiently precise in the prediction of the P-E curve for a lower field amplitude. Improved hysteresis models will improve the predictive capabilities of the equivalent circuit model. In addition it was possible to vary the remanent polarization and coercive field of the seed material and to study the influence on the optimum seed content and maximum $d_{33}^{\star}$. It was found that an optimum seed material combines a low coercive field and a high remanent polarization. However, there exists a maximum remanent polarization above which $d_{33}^{\star}$ no longer increases, whereas a decrease in the coercive field always improves the accessible $d_{33}^{\star}$. These results can be helpful in the search process for an optimum matrix-seed combination. The results of this Chapter are part of a manuscript that was submitted for publication in Advanced Functional Materials [229].

In the last chapter a phenomenological two-dimensional Landau-type phase field representation of the nonpolar matrix material is suggested, which can be easily combined with existing phase field models for polar materials. In contrast to the equivalent circuit model, it is possible to simulate parts of the microstructure in the model to study the influence of the grain boundaries, the grain sizes, the grain shapes, the grain distribution, and the inter- and intra-granular electrical and mechanical interactions on the macroscopic polarization and strain. The phase separation energy, i.e., the part of the free energy density that depends on the polarization, is phenomenologically chosen to create the typical double loop polarization hysteresis curve of a nonpolar material. Necessary material parameters were determined from measurements or reports on similar materials. With this model it was possible to compare the behavior of a two layer composite, which is a representation of the equivalent circuit, to a simple grain model of an individual polar grain surrounded by matrix material. It was found that the boundary conditions at the grain boundary between both materials have a significant influence on the domain structure inside the polar seed material and a direct influence on the macroscopic strain and polarization of the composite. However the presented studies are only a proof of concept. Future studies have to address the influence of the character and shape of the grain boundary in more detail. The implementation of a parallelized solver will allow the simulation of more complex microstructures and the expansion of the model to three dimensions. This will allow for the study of interactions between different seed grains. An important point that should be addressed in future studies is the accuracy of the model parameters.

Moreover, recent in situ transmission electron microscopy measurements revealed that the electric fields required for the nonpolar material to transform into its polar phase are actually smaller than the coercive field of the polar phase [271]. At the phase transition field the material transforms from the nonergodic relaxor state to a poly-domain polar state similar to that of a ferroelectric material. With further increasing electric fields these domains begin switching and continue until the material is fully poled. This is not predicted by the presented phase field model. Only transitions from nonpolar to a poled polar state are possible, domain walls can only occur at grain boundaries or highly spatially fluctuating electric fields. More advanced approaches are necessary to consider this experimental observation in the phase field model, for example the introduction of a new order parameter that describes polar or nonpolar phase of the material and couples to the electric field.

In each chapter it could be seen that phase transitions induced by mechanical or electrical loads significantly influence the behavior of the different types of ferroelectric materials and composites. Typically, large electric fields or mechanical stresses have to be applied to reach the critical point. However, these critical loads decrease in the vicinity of a phase transition temperature or a morphotropic phase boundary. Moreover, the appropriate combination of materials in different phases can lead to a further decrease of the critical loads. The presented models help to understand the fundamental correlations at these critical points and to make field-induced phase transitions usable for ferroelectric applications.

Bibliography

[1] H. Jaffe, “Piezoelectric ceramics,” Journal of the American Ceramic Society, vol. 41, no. 11, pp. 494–498, 1958.

[2] G. Haertling, “Ferroelectric ceramics: history and technology,” Journal of the American Ceramic Society, vol. 82, no. 4, pp. 797–818, 1999.

[3] J. Im, O. Auciello, and S. K. Streiffer, “Layered $(Ba_xSr_{1-x})Ti_{1+y}O_{3+z}$ thin films for high frequency tunable devices,” Thin Solid Films, vol. 413, no. 1-2, pp. 243 – 247, 2002.

[4] D. Dimos and C. Mueller, “Perovskite thin films for high-frequency capacitor applications,” Anual Review of Materials Science, vol. 28, pp. 397–419, 2003.

[5] L.-Y. Vicki Chen, R. Forse, D. Chase, and R. York, “Analog tunable matching network using integrated thin-film BST capacitors,” Agile Mater. & Technol., Goleta, CA, USA, vol. 1, pp. 261–264, 2004.

[6] J. F. Scott and C. A. Paz de Araujo, “Ferroelectric memories,” Science, vol. 246, no. 4936, pp. 1400–1405, 1989.

[7] G. Binnig, C. F. Quate, and C. Gerber, “Atomic force microscope,” Physial Review Letters, vol. 56, pp. 930–933, Mar 1986.

[8] W. Jo, R. Dittmer, M. Acosta, J. Zang, C. Groh, E. Sapper, K. Wang, and J. Rödel, “Giant electric-field-induced strains in lead-free ceramics for actuator applications - status and perspective,” Journal of Electroceramics, vol. 29, pp. 71–93, 2012. 10.1007/s10832-012-9742-3.

[9] “Piezoelectric actuators and motors - global markets and market trends,” tech. rep., Innovative Research and Products, Inc (Stamford, CT, USA), 2010.

[10] J. Valasek, “Dielectric anomalies in rochelle salt crystals,” Physial Review, vol. 24, pp. 560–568, Nov 1924.

[11] J. Valasek, “Piezo-electric and allied phenomena in rochelle salt,” Physial Review, vol. 17, pp. 475–481, Apr 1921.

[12] B. Wul and I. Goldman, “Dielectric constants of titanates of metals of the second group,” in Dokl. Akad. Nauk SSSR, vol. 46, pp. 154–57, 1945.

[13] G. Shirane, E. Sawaguchi, and Y. Takagi, “Dielectric properties of lead zirconate,” Physial Review, vol. 84, pp. 476–481, Nov 1951.

[14] B. Jaffe, J. R. Cook, and H. Jaffe, Piezoelectric Ceramics. R.A.N, 1971.

[15] B. Meyer and D. Vanderbilt, “Ab initio study of ferroelectric domain walls in $PbTiO_3$,” Physial Review B, vol. 65, p. 104111, Mar 2002.

[16] W. Duan and Z.-R. Liu, “Theoretical modeling and simulations of perovskite ferroelectrics: From phenomenological approaches to ab initio,” Current Opinion in Solid State and Materials Science, vol. 10, no. 1, pp. 40 – 51, 2006.

[17] A. Dal Corso, M. Posternak, R. Resta, and A. Baldereschi, “*Ab initio* study of piezoelectricity and spontaneous polarization in ZnO,” Physial Review B, vol. 50, pp. 10715–10721, Oct 1994.

[18] Y. Umeno, J. M. Albina, B. Meyer, and C. Elsässer, "*Ab initio* calculations of ferroelectric instability in $PbTiO_3$ capacitors with symmetric and asymmetric electrode layers," Phys. Rev. B, vol. 80, p. 205122, Nov 2009.

[19] M. Gröting, Ab-initio Calculations of the Relaxor Ferroelectric $Na_{1/2}Bi_{1/2}TiO_3$ and its Solid Solutions. PhD thesis, TU Darmstadt, 2013.

[20] J. Huber, "Micromechanical modelling of ferroelectrics," Current Opinion in Solid State and Materials Science, vol. 9, no. 3, pp. 100 – 106, 2005.

[21] D. Schrade, B.-X. Xu, R. Müller, and D. Gross, "On phase field modeling of ferroelectrics: parameter identification and verification," in Proceedings of SMASIS08 ASME conference of smart materials, adaptive structures and intelligent systems, 2008.

[22] J. Wang, S.-Q. Shi, L.-Q. Chen, Y. Li, and T.-Y. Zhang, "Phase-field simulations of ferroelectric/ferroelastic polarization switching," Acta Materialia, vol. 52, no. 3, pp. 749 – 764, 2004.

[23] W. Cady, Piezoelectricity. McGraw-Hill New York, 1946.

[24] A. Moulson and J. Herbert, Electroceramics: materials, properties, applications. John Wiley & Sons Inc, 2003.

[25] J. Nye, Physical properties of crystals. Clarendon Press, 1957.

[26] W. Nolting, Grundkurs theoretische Physik: Elektrodynamik. Springer, 2007.

[27] A. R. West, D. C. Sinclair, and N. Hirose, "Characterization of electrical materials, especially ferroelectrics, by impedance spectroscopy," Journal of Electroceramics, vol. 1, pp. 65–71, 1997. 10.1023/A:1009950415758.

[28] N. Ottosen and M. Ristinmaa, The mechanics of constitutive modeling. Elsevier Amsterdam, 2005.

[29] L. E. Malvern, Introduction to the Mechanics of a Continuous Medium. Prentice-Hall, 1969.

[30] D. Damjanovic and R. Newnham, "Electrostrictive and piezoelectric materials for actuator applications," Journal of intelligent material systems and structures, vol. 3, no. 2, p. 190, 1992.

[31] D. Berlincourt, D. Curran, and H. Jaffe, "Piezoelectric and piezomagnetic materials and their function in transducers," Physical acoustics: principles and methods, vol. 1, 1964.

[32] A. Sonin and B. Strukow, Einführung in die Ferroelektrizität. Vierweg Braunschweig, 1974.

[33] I. Boerasu, L. Pintilie, and M. Kosec, "Ferroelectric properties of $Pb_{1-3y/2}La_y(Zr_{0.4}Ti_{0.6})$O[sub 3] structures with La concentration gradients," Applied Physics Letters, vol. 77, no. 14, pp. 2231–2233, 2000.

[34] Y. S. Luh, R. S. Feigelson, M. M. Fejer, and R. L. Byer, "Ferroelectric domain structures in $LiNbO_3$ single-crystal fibers," Journal of Crystal Growth, vol. 78, no. 1, pp. 135 – 143, 1986.

[35] A. Schilling, D. Byrne, G. Catalan, K. Webber, Y. Genenko, G. Wu, J. Scott, and J. Gregg, "Domains in ferroelectric nanodots," Nano letters, vol. 9, no. 9, pp. 3359–3364, 2009.

[36] J. Wittborn, C. Canalias, K. Rao, R. Clemens, H. Karlsson, and F. Laurell, "Nanoscale imaging of domains and domain walls in periodically poled ferroelectrics using atomic force microscopy," Applied Physics Letters, vol. 80, p. 1622, 2002.

[37] Y. G. Wang, W. L. Zhong, and P. L. Zhang, "Surface and size effects on ferroelectric films with domain structures," Physial Review B, vol. 51, pp. 5311–5314, Feb 1995.

[38] W. Cao and C. A. Randall, “Grain size and domain size relations in bulk ceramic ferroelectric materials,” Journal of Physics and Chemistry of Solids, vol. 57, no. 10, pp. 1499 – 1505, 1996. Proceeding of the 3rd Williamsburg Workshop on Fundamental Experiments on Ferroelectrics.

[39] S. Hong, E. Colla, E. Kim, D. Taylor, A. Tagantsev, P. Muralt, K. No, and N. Setter, “High resolution study of domain nucleation and growth during polarization switching in $Pb(Zr_x,Ti_{1-x})O_3$ ferroelectric thin film capacitors,” Journal of Applied Physics, vol. 86, p. 607, 1999.

[40] T. J. Yang, V. Gopalan, P. J. Swart, and U. Mohideen, “Direct observation of pinning and bowing of a single ferroelectric domain wall,” Physial Review Letters, vol. 82, pp. 4106–4109, May 1999.

[41] D. Schrade, R. Mueller, D. Gross, T. Utschig, V. Shur, and D. Lupascu, “Interaction of domain walls with defects in ferroelectric materials,” Mechanics of Materials, vol. 39, no. 2, pp. 161 – 174, 2006.

[42] A. B. K. Njiwa, E. Aulbach, T. Granzow, and J. Rödel, “Influence of radial stress on the poling behaviour of lead zirconate titanate ceramics,” Acta Materialia, vol. 55, no. 2, pp. 675 – 680, 2007.

[43] J. Mendiola, C. Alemany, B. Jimenez, and E. Maurer, “Poling strategy of PLZT ceramics,” Ferroelectrics, vol. 54, no. 1, pp. 195–198, 1984.

[44] W. Rodel, K. Seifert, E. Anton, T. Granzow, and D. Damjanovic, “Perspective on the development of lead-free piezoceramics,” Journal of the American Ceramic Society, vol. 92, no. 6, pp. 1153–77, 2009.

[45] C. Kittel, “Theory of antiferroelectric crystals,” Physial Review, vol. 82, pp. 729–732, Jun 1951.

[46] W. Pan, Q. Zhang, A. Bhalla, and L. E. Cross, “Field-forced antiferroelectric-to-ferroelectric switching in modified lead zirconate titanate stannate ceramics,” Journal of the American Ceramic Society, vol. 72, no. 4, pp. 571–578, 1989.

[47] L. Valenta, “A derivation of the curie-weiss and weiss laws from heisenberg’s theory of ferromagnetism,” Czechoslovak Journal of Physics, vol. 3, pp. 188–192, 1953. 10.1007/BF01687123.

[48] V. Sundar and R. Newnham, “Electrostriction and polarization,” Ferroelectrics, vol. 135, no. 1, pp. 431–446, 1992.

[49] L. Cross, S. Jang, R. Newnham, S. Nomura, and K. Uchino, “Large electrostrictive effects in relaxor ferroelectrics,” Ferroelectrics, vol. 23, no. 1, pp. 187–191, 1980.

[50] S. Hwang, C. Lynch, and R. McMeeking, “Ferroelectric/ferroelastic interactions and a polarization switching model,” Acta Metallurgica et Materialia, vol. 43, no. 5, pp. 2073 – 2084, 1995.

[51] L. Landau, “On the theory of phase transitions,” Pisma v Zhurnal Eksperimentalnoi i Teoreticheskoi Fiziki, vol. 7, p. 19âĂŞ32, 1937.

[52] A. J. Bell and L. E. Cross, “A phenomenological gibbs function for batio3 giving correct e field dependence of all ferroelectric phase changes,” Ferroelectrics, vol. 59, no. 1, pp. 197–203, 1984.

[53] Y. L. Li, L. E. Cross, and L. Q. Chen, “A phenomenological thermodynamic potential for $BaTiO_3$ single crystals,” Journal of Applied Physics, vol. 98, no. 6, p. 064101, 2005.

[54] Y. L. Wang, A. K. Tagantsev, D. Damjanovic, N. Setter, V. K. Yarmarkin, A. I. Sokolov, and I. A. Lukyanchuk, “Landau thermodynamic potential for $BaTiO_3$,” Journal of Applied Physics, vol. 101, no. 10, p. 104115, 2007.

[55] J. J. Wang, P. P. Wu, X. Q. Ma, and L. Q. Chen, “Temperature-pressure phase diagram and ferroelectric properties of $BaTiO_3$ single crystal based on a modified landau potential,” Journal of Applied Physics, vol. 108, no. 11, p. 114105, 2010.

[56] M. J. Haun, Z. Q. Zhuang, E. Furman, S. J. Jang, and L. E. Cross, “Thermodynamic theory of the lead zirconate-titanate solid solution system, part III: Curie constant and sixth-order polarization interaction dielectric stiffness coefficients,” Ferroelectrics, vol. 99, no. 1, pp. 45–54, 1989.

[57] J. Iniguez, S. Ivantchev, J. M. Perez-Mato, and A. Garclia, “Devonshire-landau free energy of $BaTiO_3$ from first principles,” Physical Review B, vol. 63, p. 144103, Mar 2001.

[58] I. A. Sergienko, Y. M. Gufan, and S. Urazhdin, “Phenomenological theory of phase transitions in highly piezoelectric perovskites,” Physical Review B, vol. 65, p. 144104, Mar 2002.

[59] M. Lines and A. Glass, Principles and applications of ferroelectrics and related materials. Clarendon Press Oxford, 2001.

[60] K. M. Rabe, C. H. Ahn, and J.-M. Triscone, Physics of ferroelectrics: a modern perspective, vol. 105. Springer, 2007.

[61] S.-J. Kim, “A one-dimensional continuum model for thermoelectric phase transformations in ferroelectrics,” International Journal of Solids and Structures, vol. 37, no. 8, pp. 1145 – 1164, 2000.

[62] Q. Jiang, “On modeling of phase transformations in ferroelectric materials,” Acta Mechanica, vol. 102, pp. 149–165, 1994.

[63] I. Fritz and J. Keck, “Pressure-temperature phase diagrams for several modified lead zirconate ceramics,” Journal of Physics and Chemistry of Solids, vol. 39, no. 11, pp. 1163 – 1167, 1978.

[64] M. K. Durbin, E. W. Jacobs, J. C. Hicks, and S.-E. Park, “In situ x-ray diffraction study of an electric field induced phase transition in the single crystal relaxor ferroelectric, 92% $Pb(Zn_{1/3}Nb_{2/3})O_3$-8% $PbTiO_3$,” Applied Physics Letters, vol. 74, no. 19, pp. 2848–2850, 1999.

[65] M. K. Durbin, J. C. Hicks, S.-E. Park, and T. R. Shrout, “X-ray diffraction and phenomenological studies of the engineered monoclinic crystal domains in single crystal relaxor ferroelectrics,” Journal of Applied Physics, vol. 87, no. 11, pp. 8159–8164, 2000.

[66] B. Noheda, D. E. Cox, G. Shirane, S.-E. Park, L. E. Cross, and Z. Zhong, “Polarization rotation via a monoclinic phase in the piezoelectric 92% $PbZn_{1/3}Nb_{2/3}O_3$-8% $PbTiO_3$,” Physial Review Letters, vol. 86, pp. 3891–3894, Apr 2001.

[67] K.-P. Chen, X.-W. Zhang, and H.-S. Luo, “Electric-field-induced phase transition in ⟨001⟩-oriented $Pb(Mg_{1/3}\ Nb_{2/3}\ )O_3$ -$PbTiO_3$ single crystals,” Journal of Physics: Condensed Matter, vol. 14, no. 29, p. L571, 2002.

[68] C.-S. Tu, I.-C. Shih, V. H. Schmidt, and R. Chien, “E-field-induced polarization rotation in $Pb(Mg_{1/3}Nb_{2/3})_{1-x}Ti_xO_3$ crystals,” Applied Physics Letters, vol. 83, no. 9, pp. 1833–1835, 2003.

[69] D. Viehland and J. F. Li, “Stress-induced phase transformations in ⟨001⟩-oriented $Pb(Mg_{1/3}Nb_{2/3})O_3$ -$PbTiO_3$ crystals: Bilinear coupling of ferroelastic strain and ferroelectric polarization,” Philosophical Magazine, vol. 83, no. 1, pp. 53–59, 2003.

[70] M. J. Hoffmann and H. Kungl, “High strain lead-based perovskite ferroelectrics,” Current Opinion in Solid State and Materials Science, vol. 8, no. 1, pp. 51 – 57, 2004.

[71] R. R. Chien, V. H. Schmidt, C.-S. Tu, L.-W. Hung, and H. Luo, “Field-induced polarization rotation in (001)-cut $Pb(Mg_{1/3}Nb_{2/3})_{0.76}Ti_{0.24}O_3$,” Physical Review B, vol. 69, p. 172101, May 2004.

[72] D. Damjanovic, “Contributions to the piezoelectric effect in ferroelectric single crystals and ceramics,” Journal of the American Ceramic Society, vol. 88, no. 10, pp. 2663–2676, 2005.

[73] H. Simons, J. Daniels, W. Jo, R. Dittmer, A. Studer, M. Avdeev, J. Rödel, and M. Hoffman, “Electric-field-induced strain mechanisms in lead-free 94%$(Bi_{1/2}Na_{1/2})TiO_3$-6%$BaTiO_3$,” Applied Physics Letters, vol. 98, no. 8, p. 082901, 2011.

[74] M. Davis, “Picturing the elephant: Giant piezoelectric activity and the monoclinic phases of relaxor-ferroelectric single crystals,” Journal of Electroceramics, vol. 19, pp. 25–47, 2007.

[75] S.-E. Park and T. R. Shrout, “Ultrahigh strain and piezoelectric behavior in relaxor based ferroelectric single crystals,” Journal of Applied Physics, vol. 82, no. 4, pp. 1804–1811, 1997.

[76] Z. Zhang, D. Fang, and A. Soh, “A new criterion for domain-switching in ferroelectric materials,” Mechanics of Materials, vol. 38, no. 1-2, pp. 25 – 32, 2006. Macro-, Meso-, Micro- and Nano-Mechanics of Materials.

[77] M. Davis, D. Damjanovic, and N. Setter, “Electric-field-, temperature-, and stress-induced phase transitions in relaxor ferroelectric single crystals,” Physical Review B, vol. 73, p. 014115, Jan 2006.

[78] D. Viehland, “Effect of uniaxial stress upon the electromechanical properties of various piezoelectric ceramics and single crystals,” Journal of the American Ceramic Society, vol. 89, no. 3, pp. 775–785, 2006.

[79] K. G. Webber, R. Zuo, and C. S. Lynch, “Ceramic and single-crystal (1-x)PMN-xPT constitutive behavior under combined stress and electric field loading,” Acta Materialia, vol. 56, no. 6, pp. 1219 – 1227, 2008.

[80] B. Noheda, J. A. Gonzalo, L. E. Cross, R. Guo, S.-E. Park, D. E. Cox, and G. Shirane, “Tetragonal-to-monoclinic phase transition in a ferroelectric perovskite: The structure of $PbZr_{0.52}Ti_{0.48}O_3$,” Physial Review B, vol. 61, pp. 8687–8695, Apr 2000.

[81] R. Guo, L. E. Cross, S.-E. Park, B. Noheda, D. E. Cox, and G. Shirane, “Origin of the high piezoelectric response in $PbZr_{1-x}Ti_xO_3$,” Physial Review Letters, vol. 84, pp. 5423–5426, Jun 2000.

[82] F. Bai, N. Wang, J. Li, D. Viehland, P. M. Gehring, G. Xu, and G. Shirane, “X-ray and neutron diffraction investigations of the structural phase transformation sequence under electric field in 0.7 $Pb(Mg_{1/3}Nb_{2/3})$ - 0.3 $PbTiO_3$ crystals,” Journal of Applied Physics, vol. 96, no. 3, pp. 1620–1627, 2004.

[83] H. Fu and R. Cohen, “Polarization rotation mechanism for ultrahigh electromechanical response in single-crystal piezoelectrics,” Nature, vol. 403, pp. 281–282, 2000.

[84] S. Wada, S. Suzuki, T. Noma, T. Suzuki, M. Osada, M. Kakihana, S.-E. Park, L. E. Cross, and T. R. Shrout, “Enhanced piezoelectric property of barium titanate single crystals with engineered domain configurations,” Japanese Journal of Applied Physics, vol. 38, no. Part 1, No. 9B, pp. 5505–5511, 1999.

[85] J. Haeni, P. Irvin, W. Chang, R. Uecker, P. Reiche, Y. Li, S. Choudhury, W. Tian, M. Hawley, B. Craigo, et al., “Room-temperature ferroelectricity in strained $SrTiO_3$,” Nature, vol. 430, no. 7001, pp. 758–761, 2004.

[86] K. J. Choi, M. Biegalski, Y. L. Li, A. Sharan, J. Schubert, R. Uecker, P. Reiche, Y. B. Chen, X. Q. Pan, V. Gopalan, L.-Q. Chen, D. G. Schlom, and C. B. Eom, “Enhancement of ferroelectricity in strained $BaTiO_3$ thin films,” Science, vol. 306, no. 5698, pp. 1005–1009, 2004.

[87] W. D. Dong, P. Finkel, A. Amin, and C. S. Lynch, "Giant electro-mechanical energy conversion in $[011]_c$ cut ferroelectric single crystals," Applied Physics Letters, vol. 100, no. 4, p. 042903, 2012.

[88] J. E. Daniels, W. Jo, J. Rödel, and J. L. Jones, "Electric-field-induced phase transformation at a lead-free morphotropic phase boundary: Case study in a 93%$(Bi_{0.5}Na_{0.5})TiO_3$-7% $BaTiO_3$ piezoelectric ceramics," Applied Physics Letters, vol. 95, no. 3, p. 032904, 2009.

[89] V. Bobnar, Z. Kutnjak, R. c. v. Pirc, and A. Levstik, "Electric-field−temperature phase diagram of the relaxor ferroelectric lanthanum-modified lead zirconate titanate," Physical Review B, vol. 60, pp. 6420–6427, Sep 1999.

[90] A. J. Bell, "On the origin of the large piezoelectric effect in morphotropic phase boundary perovskite single crystals," Applied Physics Letters, vol. 76, no. 1, pp. 109–111, 2000.

[91] D. J. Franzbach, B.-X. Xu, R. Mueller, and K. G. Webber, "The effects of polarization dynamics and domain switching energies on field induced phase transformations of perovskite ferroelectrics," Applied Physics Letters, vol. 99, no. 16, p. 162903, 2011.

[92] D. J. Franzbach, Y. J. Gu, L. Q. Chen, and K. G. Webber, "Electric field-induced tetragonal to orthorhombic phase transitions in $[110]_c$-oriented $BaTiO_3$ single crystals," Applied Physics Letters, vol. 101, no. 23, p. 232904, 2012.

[93] M. J. Haun, E. Furman, S. J. Jang, H. A. McKinstry, and L. E. Cross, "Thermodynamic theory of $PbTiO_3$," Journal of Applied Physics, vol. 62, no. 8, pp. 3331–3338, 1987.

[94] A. Devonshire, "Theory of barium titanate l," Philosophical Magazine, vol. 40, no. 309, pp. 1040–1063, 1949.

[95] N. A. Pertsev, A. K. Tagantsev, and N. Setter, "Phase transitions and strain-induced ferroelectricity in $SrTiO_3$ epitaxial thin films," Physical Review B, vol. 61, pp. R825–R829, Jan 2000.

[96] A. K. Tagantsev, E. Courtens, and L. Arzel, "Prediction of a low-temperature ferroelectric instability in antiphase domain boundaries of strontium titanate," Physical Review B, vol. 64, p. 224107, Nov 2001.

[97] S. M. Allen and J. W. Cahn, "A microscopic theory for antiphase boundary motion and its application to antiphase domain coarsening," Acta Metallurgica, vol. 27, no. 6, pp. 1085–1095, 1979.

[98] B. Xu, D. Schrade, R. Müller, D. Gross, T. Granzow, and J. Rödel, "Phase field simulation and experimental investigation of the electro-mechanical behavior of ferroelectrics," ZAMM - Journal of Applied Mathematics and Mechanics / Zeitschrift für Angewandte Mathematik und Mechanik, vol. 90, no. 7-8, pp. 623–632, 2010.

[99] D. Damjanovic, "A morphotropic phase boundary system based on polarization rotation and polarization extension," Applied Physics Letters, vol. 97, no. 6, p. 062906, 2010.

[100] J. Paul, T. Nishimatsu, Y. Kawazoe, and U. V. Waghmare, "Polarization rotation, switching, and electric-field temperature phase diagrams of ferroelectric $BaTiO_3$: A molecular dynamics study," Physial Review B, vol. 80, p. 024107, Jul 2009.

[101] W. Lu, D.-N. Fang, C. Li, and K.-C. Hwang, "Nonlinear electrical/mechanical behavior and micromechanics modelling of ferroelectric domain evolution," Acta Materialia, vol. 47, no. 10, pp. 2913 – 2926, 1999.

[102] B. Jiang, Y. Bai, W. Chu, Y. Su, and L. Qiao, "Direct observation of two 90° steps of 180° domain switching in $BaTiO_3$ single crystal under an antiparallel electric fields," Applied Physics Letters, vol. 93, no. 15, p. 152905, 2008.

[103] K. S. Lee, Y. K. Kim, S. Baik, J. Kim, and I. S. Jung, “In situ observation of ferroelectric 90°-domain switching in epitaxial Pb(Zr,Ti)O_3 thin films by synchrotron x-ray diffraction,” Applied Physics Letters, vol. 79, no. 15, pp. 2444–2446, 2001.

[104] D. Schrade, Microstructural modeling of ferroelectric material behavior. PhD thesis, TU Kaiserslautern, 2011.

[105] D. Schrade, R. Mueller, B. Xu, and D. Gross, “Domain evolution in ferroelectric materials: A continuum phase field model and finite element implementation,” Computer Methods in Applied Mechanics and Engineering, vol. 196, no. 41-44, pp. 4365 – 4374, 2007.

[106] B. Xu, D. Schrade, R. Mueller, and D. Gross, “Micromechanical analysis of ferroelectric structures by a phase field method,” Computational Materials Science, vol. 45, no. 3, pp. 832 – 836, 2009.

[107] K. G. Webber, H. C. Robinson, G. A. R. Jr., and C. S. Lynch, “A distributed step-like switching model of the continuous field-driven phase transformations observed in (1-x)PMN–xPT relaxor ferroelectric single crystals,” Acta Materialia, vol. 56, no. 12, pp. 2744 – 2749, 2008.

[108] A. Herklotz, J. D. Plumhof, A. Rastelli, O. G. Schmidt, L. Schultz, and K. Dörr, “Electrical characterization of PMN-28%PT(001) crystals used as thin-film substrates,” Journal of Applied Physics, vol. 108, no. 9, p. 094101, 2010.

[109] T. Liu and C. Lynch, “Ferroelectric properties of [110], [001] and [111] poled relaxor single crystals: Measurements and modeling,” Acta Materialia, vol. 51, no. 2, pp. 407 – 416, 2003.

[110] O. Noblanc, P. Gaucher, and G. Calvarin, “Structural and dielectric studies of $Pb(Mg_{1/3}Nb_{2/3})O_3$-$PbTiO_3$ ferroelectric solid solutions around the morphotropic boundary,” Journal of Applied Physics, vol. 79, no. 8, pp. 4291–4297, 1996.

[111] Z.-G. Ye and M. Dong, “Morphotropic domain structures and phase transitions in relaxor-based piezo-/ferroelectric (1 - x)$Pb(Mg_{1/3}Nb_{2/3})O_3$ - x$PbTiO_3$ single crystals,” Journal of Applied Physics, vol. 87, no. 5, pp. 2312–2319, 2000.

[112] V. Westphal, W. Kleemann, and M. D. Glinchuk, “Diffuse phase transitions and random-field-induced domain states of the “relaxor” ferroelectric $PbMg_{1/3}Nb_{2/3}O_3$,” Physial Review Letters, vol. 68, pp. 847–850, Feb 1992.

[113] G. Goodman, “Electrical conduction anomaly in samarium-doped barium titanate,” Journal of the American Ceramic Society, vol. 46, no. 1, pp. 48–54, 1963.

[114] G. Godefroy, P. Lompré, C. Dumas, and H. Arend, “Pure and doped barium titanate. crystal growth and chemical composition,” Materials Research Bulletin, vol. 12, no. 2, pp. 165 – 169, 1977.

[115] C. Turner, N. Mason, and A. Morris, “The growth of barium titanate single crystals by the travelling solvent zone technique,” Journal of Crystal Growth, vol. 56, no. 1, pp. 137 – 140, 1982.

[116] J. Yuh, J. C. Nino, and W. M. Sigmund, “Synthesis of barium titanate ($BaTiO_3$) nanofibers via electrospinning,” Materials Letters, vol. 59, no. 28, pp. 3645 – 3647, 2005.

[117] W. J. Merz, “Double hysteresis loop of $BaTiO_3$ at the curie point,” Physical Review, vol. 91, pp. 513–517, Aug 1953.

[118] C. J. Johnson, “Some dielectric and electro-optic properties of batio[sub 3] single crystals,” Applied Physics Letters, vol. 7, no. 8, pp. 221–223, 1965.

[119] Y. Yoneda, T. Okabe, K. Sakaue, H. Terauchi, H. Kasatani, and K. Deguchi, “Structural characterization of $BaTiO_3$ thin films grown by molecular beam epitaxy,” Journal of Applied Physics, vol. 83, no. 5, pp. 2458–2461, 1998.

[120] J. Y. Jo, D. J. Kim, Y. S. Kim, S.-B. Choe, T. K. Song, J.-G. Yoon, and T. W. Noh, “Polarization switching dynamics governed by the thermodynamic nucleation process in ultrathin ferroelectric films,” Physial Review Letters, vol. 97, p. 247602, Dec 2006.

[121] B. Jiang, Y. Bai, J.-L. Cao, Y. Su, S.-Q. Shi, W. Chu, and L. Qiao, “Delayed crack propagation in barium titanate single crystals in humid air,” Journal of Applied Physics, vol. 103, no. 11, p. 116102, 2008.

[122] E. A. Little, “Dynamic behavior of domain walls in barium titanate,” Physical Review, vol. 98, pp. 978–984, May 1955.

[123] E. Burcsu, G. Ravichandran, and K. Bhattacharya, “Large electrostrictive actuation of barium titanate single crystals,” Journal of the Mechanics and Physics of Solids, vol. 52, no. 4, pp. 823 – 846, 2004.

[124] R. Landauer, D. R. Young, and M. E. Drougard, “Polarization reversal in the barium titanate hysteresis loop,” Journal of Applied Physics, vol. 27, no. 7, pp. 752–758, 1956.

[125] L. Eng, M. Abplanalp, and P. Günter, “Ferroelectric domain switching in tri-glycine sulphate and barium-titanate bulk single crystals by scanning force microscopy,” Applied Physics A, vol. 66, pp. S679–S683, 1998.

[126] R. Ahluwalia and W. Cao, “Influence of dipolar defects on switching behavior in ferroelectrics,” Physical Review B, vol. 63, p. 012103, Dec 2000.

[127] M. Stewart, M. Cain, and D. Hall, “Ferroelectric hysteresis measurement and analysis,” Report CMMT (A), vol. 152, 1999.

[128] S. A. Hayward and E. K. H. Salje, “The pressure-temperature phase diagram of $BaTiO_3$: A macroscopic description of the low-temperature behaviour,” Journal of Physics: Condensed Matter, vol. 14, no. 36, p. L599, 2002.

[129] K. Uchino, “Materials issues in design and performance of piezoelectric actuators: an overview,” Acta Materialia, vol. 46, no. 11, pp. 3745 – 3753, 1998.

[130] K. Uchino, Ferroelectric devices. Marcel Dekker (New York), 2000.

[131] D. Damjanovic, “Ferroelectric, dielectric and piezoelectric properties of ferroelectric thin films and ceramics,” Reports on Progress in Physics, vol. 61, no. 9, p. 1267, 1998.

[132] H. Cao and A. G. Evans, “Nonlinear deformation of ferroelectric ceramics,” Journal of the American Ceramic Society, vol. 76, no. 4, pp. 890–896, 1993.

[133] J. Li, R. Rogan, E. Üstündag, and K. Bhattacharya, “Domain switching in polycrystalline ferroelectric ceramics,” Nature materials, vol. 4, no. 10, pp. 776–781, 2005.

[134] A. A. Bokov, X. Long, and Z.-G. Ye, “Optically isotropic and monoclinic ferroelectric phases in $Pb(Zr_{1-x}Ti_xO_3$ (PZT) single crystals near morphotropic phase boundary,” Physical Review B, vol. 81, p. 172103, May 2010.

[135] C. Lynch, “The effect of uniaxial stress on the electro-mechanical response of 8/65/35 PLZT,” Acta Materialia, vol. 44, no. 10, pp. 4137 – 4148, 1996.

[136] A. B. Schäufele and K. Heinz Härdtl, “Ferroelastic properties of lead zirconate titanate ceramics,” Journal of the American Ceramic Society, vol. 79, no. 10, pp. 2637–2640, 1996.

[137] K. Webber, E. Aulbach, T. Key, M. Marsilius, T. Granzow, and J. Rödel, “Temperature-dependent ferroelastic switching of soft lead zirconate titanate,” Acta Materialia, vol. 57, no. 15, pp. 4614 – 4623, 2009.

[138] Y. W. Li, X. L. Zhou, and F. X. Li, “Temperature-dependent mechanical depolarization of ferroelectric ceramics,” Journal of Physics D: Applied Physics, vol. 43, no. 17, p. 175501, 2010.

[139] D. Damjanovic, “Stress and frequency dependence of the direct piezoelectric effect in ferroelectric ceramics,” Journal of Applied Physics, vol. 82, no. 4, pp. 1788–1797, 1997.

[140] A. Endriss, M. Hammer, M. Hoffmann, A. Kolleck, and G. Schneider, “Microscopic and macroscopic ferroelectric-ferroelastic and piezoelectric behavior of PZT ceramics,” Journal of the European Ceramic Society, vol. 19, no. 6-7, pp. 1229 – 1231, 1999.

[141] D. Fang and C. Li, “Nonlinear electric-mechanical behavior of a soft PZT-51 ferroelectric ceramics,” Journal of Materials Science, vol. 34, pp. 4001–4010, 1999.

[142] D. I. Woodward, J. Knudsen, and I. M. Reaney, “Review of crystal and domain structures in the $\mathrm{PbZr}_x\mathrm{Ti}_{1-x}\mathrm{O}_3$ solid solutions,” Physical Review B, vol. 72, p. 104110, Sep 2005.

[143] W. Cao and L. E. Cross, “Theoretical model for the morphotropic phase boundary in lead zirconate-lead titanate solid solution,” Physical Review B, vol. 47, pp. 4825–4830, Mar 1993.

[144] A. Heitmann and G. Rossetti, “Thermodynamics of polar anisotropy in morphotropic ferroelectric solid solutions,” Philosophical Magazine, vol. 90, no. 1-4, pp. 71–87, 2010.

[145] Y. M. Jin, Y. U. Wang, A. G. Khachaturyan, J. F. Li, and D. Viehland, “Conformal miniaturization of domains with low domain-wall energy: Monoclinic ferroelectric states near the morphotropic phase boundaries,” Physial Review Letters, vol. 91, p. 197601, Nov 2003.

[146] Y. M. Jin, Y. U. Wang, A. G. Khachaturyan, J. F. Li, and D. Viehland, “Adaptive ferroelectric states in systems with low domain wall energy: Tetragonal microdomains,” Journal of Applied Physics, vol. 94, no. 5, pp. 3629–3640, 2003.

[147] K. A. Schönau, L. A. Schmitt, M. Knapp, H. Fuess, R.-A. Eichel, H. Kungl, and M. J. Hoffmann, “Nanodomain structure of $\mathrm{Pb}[\mathrm{Zr}_{1-x}\mathrm{Ti}_x]\mathrm{O}_3$ at its morphotropic phase boundary: Investigations from local to average structures,” Physical Review B, vol. 75, p. 184117, May 2007.

[148] R. Theissmann, L. A. Schmitt, J. Kling, R. Schierholz, K. A. Schönau, H. Fuess, M. Knapp, H. Kungl, and M. J. Hoffmann, “Nanodomains in morphotropic lead zirconate titanate ceramics: On the origin of the strong piezoelectric effect,” Journal of Applied Physics, vol. 102, no. 2, p. 024111, 2007.

[149] M. Marsilius, K. G. Webber, E. Aulbach, and T. Granzow, “Comparison of the temperature-dependent ferroelastic behavior of hard and soft lead zirconate titanate ceramics,” Journal of the American Ceramic Society, vol. 93, no. 9, pp. 2850–2856, 2010.

[150] T. Fett, D. Munz, and G. Thun, “Young’s modulus of soft PZT from partial unloading tests,” Ferroelectrics, vol. 274, no. 1, pp. 67–81, 2002.

[151] Z. Q. Zhuang, M. Haun, S.-J. Jang, and L. Cross, “Composition and temperature dependence of the dielectric, piezoelectric and elastic properties of pure PZT ceramics,” Ultrasonics, Ferroelectrics and Frequency Control, IEEE Transactions on, vol. 36, no. 4, pp. 413–416, 1989.

[152] A. E. Glazounov, H. Kungl, J.-T. Reszat, M. J. Hoffmann, A. Kolleck, G. A. Schneider, and T. Wroblewski, “Contribution from ferroelastic domain switching detected using x-ray diffraction to r-curves in lead zirconate titanate ceramics,” Journal of the American Ceramic Society, vol. 84, no. 12, pp. 2921–2929, 2001.

[153] M. Hoffmann, M. Hammer, A. Endriss, and D. Lupascu, “Correlation between microstructure, strain behavior, and acoustic emission of soft PZT ceramics,” Acta Materialia, vol. 49, no. 7, pp. 1301 – 1310, 2001.

[154] H. Kungl and M. J. Hoffmann, “Temperature dependence of poling strain and strain under high electric fields in lasr-doped morphotropic pzt and its relation to changes in structural characteristics,” Acta Materialia, vol. 55, no. 17, pp. 5780 – 5791, 2007.

[155] M. Hinterstein, J. Rouquette, J. Haines, P. Papet, M. Knapp, J. Glaum, and H. Fuess, “Structural description of the macroscopic piezo- and ferroelectric properties of lead zirconate titanate,” Physical Review Letters, vol. 107, p. 077602, Aug 2011.

[156] Y.-H. Seo, D. J. Franzbach, J. Koruza, A. Benčan, B. Malič, M. Kosec, J. L. Jones, and K. G. Webber, “Nonlinear stress-strain behavior and stress-induced phase transitions in soft $Pb(Zr_{1-x}Ti_x)O_3$ at the morphotropic phase boundary,” Physical Review B, vol. 87, p. 094116, Mar 2013.

[157] V. Petricek and M. Dusek, The Crystallographic Computing System JANA 2006. Institute of Physics, Academy of Sicences of the Czech Republic, Praha, 2006.

[158] H. M. Rietveld, “Line profiles of neutron powder-diffraction peaks for structure refinement.,” Acta Crystallographica, vol. 22, pp. 151–152, 1967.

[159] W.-F. Rao and Y. U. Wang, “Grain size effect of phase coexistence around morphotropic phase boundary in ferroelectric polycrystalline ceramics,” Applied Physics Letters, vol. 92, no. 10, p. 102905, 2008.

[160] K. Ramam and M. Lopez, “Ferroelectric and piezoelectric properties of Ba modified lead zirconium titanate ceramics,” Journal of Physics D: Applied Physics, vol. 39, no. 20, p. 4466, 2006.

[161] N. Uchida and T. Ikeda, “Studies on $Pb(Zr_xTi_{1-x})O_3$ ceramics with addition of cr_2o_3,” Japanese Journal of Applied Physics, vol. 6, no. 11, pp. 1292–1299, 1967.

[162] J. Muõz Saldaña, G. G.A. Schneider, and L. Eng, “Stress induced movement of ferroelastic domain walls in $BaTiO_3$ single crystals evaluated by scanning force microscopy,” Surface Science, vol. 480, pp. L402 – L410, 2001.

[163] A. Gruverman, B. J. Rodriguez, A. I. Kingon, R. J. Nemanich, J. S. Cross, and M. Tsukada, “Spatial inhomogeneity of imprint and switching behavior in ferroelectric capacitors,” Applied Physics Letters, vol. 82, no. 18, pp. 3071–3073, 2003.

[164] T. Leist, K. G. Webber, W. Jo, T. Granzow, E. Aulbach, J. Suffner, and J. Rödel, “Domain switching energies: Mechanical versus electrical loading in la-doped bismuth ferrite–lead titanate,” Journal of Applied Physics, vol. 109, no. 5, p. 054109, 2011.

[165] G. A. Rossetti, W. Zhang, and A. G. Khachaturyan, “Phase coexistence near the morphotropic phase boundary in lead zirconate titanate ($PbZrO_3$-$PbTiO_3$) solid solutions,” Applied Physics Letters, vol. 88, no. 7, p. 072912, 2006.

[166] S. C. Hwang, J. E. Huber, R. M. McMeeking, and N. A. Fleck, “The simulation of switching in polycrystalline ferroelectric ceramics,” Journal of Applied Physics, vol. 84, no. 3, pp. 1530–1540, 1998.

[167] J. L. Jones, M. Hoffman, and K. J. Bowman, “Saturated domain switching textures and strains in ferroelastic ceramics,” Journal of Applied Physics, vol. 98, no. 2, p. 024115, 2005.

[168] F. Li, D. Fang, and A. Soh, “Theoretical saturated domain-orientation states in ferroelectric ceramics,” Scripta Materialia, vol. 54, no. 7, pp. 1241 – 1246, 2006.

[169] U. Robels and G. Arlt, “Domain wall clamping in ferroelectrics by orientation of defects,” Journal of Applied Physics, vol. 73, no. 7, pp. 3454–3460, 1993.

[170] J. Nuffer, D. Lupascu, and J. Rödel, "Damage evolution in ferroelectric PZT induced by bipolar electric cycling," Acta Materialia, vol. 48, no. 14, pp. 3783 – 3794, 2000.

[171] A. Pramanick, D. Damjanovic, J. E. Daniels, J. C. Nino, and J. L. Jones, "Origins of electro-mechanical coupling in polycrystalline ferroelectrics during subcoercive electrical loading," Journal of the American Ceramic Society, vol. 94, no. 2, pp. 293–309, 2011.

[172] J. Herbert, Ferroelectric Transducers and Sensors. Gordon and Breach Science, New York, 1982.

[173] H. D. Chen, K. R. Udayakumar, C. J. Gaskey, and L. E. Cross, "Electrical properties' maxima in thin films of the lead zirconate–lead titanate solid solution system," Applied Physics Letters, vol. 67, no. 23, pp. 3411–3413, 1995.

[174] D. Hall, A. Steuwer, B. Cherdhirunkorn, T. Mori, and P. Withers, "Analysis of elastic strain and crystallographic texture in poled rhombohedral PZT ceramics," Acta Materialia, vol. 54, no. 11, pp. 3075 – 3083, 2006.

[175] J. L. Jones, M. Hoffman, and S. C. Vogel, "Ferroelastic domain switching in lead zirconate titanate measured by in situ neutron diffraction," Mechanics of Materials, vol. 39, no. 4, pp. 283 – 290, 2007.

[176] D. Hall, A. Steuwer, B. Cherdhirunkorn, P. Withers, and T. Mori, "Micromechanics of residual stress and texture development due to poling in polycrystalline ferroelectric ceramics," Journal of the Mechanics and Physics of Solids, vol. 53, no. 2, pp. 249 – 260, 2005.

[177] M. Davis, D. Damjanovic, and N. Setter, "Electric-field-induced orthorhombic to rhombohedral phase transition in $[111]_c$-oriented $0.92Pb(Zn_{1/3}Nb_{2/3})O_3$ - $0.08PbTiO_3$," Journal of Applied Physics, vol. 97, no. 6, p. 064101, 2005.

[178] M. J. Haun, E. Furman, S. J. Jang, and L. E. Cross, "Thermodynamic theory of the lead zirconate-titanate solid solution system, part I: Phenomenology," Ferroelectrics, vol. 99, no. 1, pp. 13–25, 1989.

[179] S. O. Kramarov, A. V. Beliayev, Y. V. Dashko, N. Y. Yegorov, and L. M. Katsnelson, "Localization of internal mechanical stresses in polycrystalline ferroelectrics," Ferroelectrics, vol. 100, no. 1, pp. 101–110, 1989.

[180] J. Avro, "Fast random rotation matrices," Graphics Gems III Academic Press, London, pp. 117–120, 1992.

[181] T. Yamada, "Electromechanical properties of oxygen-octahedra ferroelectric crystals," Journal of Applied Physics, vol. 43, no. 2, pp. 328–338, 1972.

[182] G. A. Samara, "Pressure and temperature dependences of the dielectric properties of the perovskites $BaTiO_3$ and $SrTiO_3$," Physial Review, vol. 151, pp. 378–386, Nov 1966.

[183] J. Frantti, S. Ivanov, S. Eriksson, H. Rundlöf, V. Lantto, J. Lappalainen, and M. Kakihana, "Phase transitions of $PbZr_xTi_{1-x}O_3$ ceramics," Physial Review B, vol. 66, p. 064108, Aug 2002.

[184] A. Devonshire, "Theory of barium titanate II," Philosophical Magazine, vol. 42, p. 1065, 1951.

[185] D. Jonah, F. Shirane, Ferroelectric Crystals. Pergamon Press, 1962.

[186] D. Damjanovic and M. Demartin, "Contribution of the irreversible displacement of domain walls to the piezoelectric effect in barium titanate and lead zirconate titanate ceramics," Journal of Physics: Condensed Matter, vol. 9, no. 23, p. 4943, 1997.

[187] C. Randall, A. Kelnberger, G. Yang, R. Eitel, and T. Shrout, "High strain piezoelectric multilayer actuators–a material science and engineering challenge," Journal of Electroceramics, vol. 14, no. 3, pp. 177–191, 2005.

[188] J. Benajes, S. Molina, R. Novella, R. Amorim, H. Ben Hadj Hamouda, and J. Hardy, "Comparison of two injection systems in an HSDI diesel engine using split injection and different injector nozzles," International Journal of Automotive Technology, vol. 11, no. 2, pp. 139–146, 2010.

[189] P. Tennison and R. Reitz, "An experimental investigation of the effects of common-rail injection system parameters on emissions and performance in a high-speed direct-injection diesel engine: Internal combustion engines," Journal of engineering for gas turbines and power, vol. 123, no. 1, pp. 167–174, 2001.

[190] B. Oh, S. Oh, K. Lee, and M. Sunwoo, "Development of an injector driver for piezo actuated common rail injectors," in 14th Asia Pacific Automotive Engineering Conference Hollywood. California, vol. 528, 2007.

[191] E.-D. 2002/95/EC, "Restriction of the use of certain hazardous substances in electrical and electronic equipment (RoHS).," Official Journal of the European Union, vol. 46(L37), pp. 19–23, 2003.

[192] E.-D. 2002/96/EC, "Waste electrical and electronic equipment (WEEE).," Official Journal of the European Union, vol. 46 (L37), pp. 24–38, 2003.

[193] USA, "Electronic waste recycling act of 2003, sb 20/sb 50," Department of Toxic Substances Control, California, USA, 2003.

[194] Environment and L. C. of the National Assembly of Korea, "Act for resource recycling of electrical and electronic equipment and vehicles," Bill Nr. 6319, 2007.

[195] C. Ministry of Information Industry, "Measures for the administration on pollution control of electronic information products," Order of the Ministry of Information Industry No 39, 2007.

[196] T. Minister of Economy and J. Industry, "Law for promotion of effective utilization of resources," JIS C 0950, 2001.

[197] S.-T. Zhang, A. B. Kounga, E. Aulbach, H. Ehrenberg, and J. Rödel, "Giant strain in lead-free piezoceramics $Bi_{0.5}Na_{0.5}TiO_3$–$BaTiO_3$–$K_{0.5}Na_{0.5}NbO_3$system," Applied Physics Letters, vol. 91, no. 11, p. 112906, 2007.

[198] V.-Q. Nguyen, H.-S. Han, K.-J. Kim, D.-D. Dang, K.-K. Ahn, and J.-S. Lee, "Strain enhancement in $Bi_{1/2}(Na_{0.82}K_{0.18})_{1/2}TiO_3$ lead-free electromechanical ceramics by co-doping with li and ta," Journal of Alloys and Compounds, vol. 511, no. 1, pp. 237 – 241, 2012.

[199] A. Singh and R. Chatterjee, "Structural, electrical, and strain properties of stoichiometric 1-x-y$(Bi_{0.5}Na_{0.5})TiO_3$ - x$(Bi_{0.5}K_{0.5}TiO_3)$ - y$(Na_{0.5}K_{0.5})NbO_3$ solid solutions," Journal of Applied Physics, vol. 109, no. 2, p. 024105, 2011.

[200] P. M. Chaplya, M. Mitrovic, G. P. Carman, and F. K. Straub, "Durability properties of piezoelectric stack actuators under combined electromechanical loading," Journal of applied physics, vol. 100, no. 12, pp. 124111–124111, 2006.

[201] G. Xu, Z. Zhong, Y. Bing, Z.-G. Ye, and G. Shirane, "Electric-field-induced redistribution of polar nano-regions in a relaxor ferroelectric," Nature Materials, vol. 5, pp. 134–140, Feb. 2006.

[202] J. Kling, X. Tan, W. Jo, H.-J. Kleebe, H. Fuess, and J. Rödel, "In situ transmission electron microscopy of electric field-triggered reversible domain formation in bi-based lead-free piezoceramics," Journal of the American Ceramic Society, vol. 93, no. 9, pp. 2452–2455, 2010.

[203] W. Jo, T. Granzow, E. Aulbach, J. Rödel, and D. Damjanovic, “Origin of the large strain response in $(K_{0.5}Na_{0.5})NbO_3$-modified $(Bi_{0.5}Na_{0.5})TiO_3$–$BaTiO_3$ lead-free piezoceramics,” Journal of Applied Physics, vol. 105, no. 9, p. 094102, 2009.

[204] W. Jo and J. Rödel, “Electric-field-induced volume change and room temperature phase stability of $(Bi_{0.5}Na_{0.5})TiO_{0.5}$-x mol.% $BaTiO_{0.5}$ piezoceramics,” Applied Physics Letters, vol. 99, no. 4, p. 042901, 2011.

[205] D. S. Lee, D. H. Lim, M. S. Kim, K. H. Kim, and S. J. Jeong, “Electric field-induced deformation behavior in mixed $Bi_{0.5}Na_{0.5}TiO_3$ and $Bi_{0.5}(Na_{0.75}K_{0.25})_{0.5}TiO_3$-$BiAlO_3$,” Applied Physics Letters, vol. 99, no. 6, p. 062906, 2011.

[206] G. Arlt, “The influence of microstructure on the properties of ferroelectric ceramics,” Ferroelectrics, vol. 104, no. 1, pp. 217–227, 1990.

[207] H.-Y. Lu, J.-S. Bow, and W.-H. Deng, “Core-shell structures in ZrO_2-modified $BaTiO_3$ ceramics,” Journal of the American Ceramic Society, vol. 73, no. 12, pp. 3562–3568, 1990.

[208] C. Huber, M. Treguer-Delapierre, C. Elissalde, F. Weill, and M. Maglione, “New application of the core-shell concept to ferroelectric nanopowders,” Journal of Materials Chemistry, vol. 13, pp. 650–653, 2003.

[209] T. Takenaka, K.-I. Maruyama, and K. Sakata, “$(Bi_{1/2}Na_{1/2})TiO)_3$- $BaTiO_3$ system for lead-free piezoelectric ceramics,” Japanese journal of applied physics, vol. 30, no. 9B, pp. 2236–2239, 1991.

[210] B.-J. Chu, D.-R. Chen, G.-R. Li, and Q.-R. Yin, “Electrical properties of $Na_{1/2}Bi_{1/2}TiO_3$-$BaTiO_3$ ceramics,” Journal of the European Ceramic Society, vol. 22, no. 13, pp. 2115–2122, 2002.

[211] W. Ge, H. Cao, C. DeVreugd, J. Li, D. Viehland, Q. Zhang, and H. Luo, “Influence of $BaTiO_3$ content on the structure and properties of $Na_{0.5}Bi_{0.5}TiO_3$ crystals,” Journal of the American Ceramic Society, vol. 94, no. 9, pp. 3084–3087, 2011.

[212] W. Jo, J. E. Daniels, J. L. Jones, X. Tan, P. A. Thomas, D. Damjanovic, and J. Rödel, “Evolving morphotropic phase boundary in lead-free $(Bi_{1/2}Na_{1/2})TiO_3$–$BaTiO_3$ piezoceramics,” Journal of Applied Physics, vol. 109, no. 1, p. 014110, 2011.

[213] S.-T. Zhang, A. B. Kounga, W. Jo, C. Jamin, K. Seifert, T. Granzow, J. Rödel, and D. Damjanovic, “High-strain lead-free antiferroelectric electrostrictors,” Advanced Materials, vol. 21, no. 46, pp. 4716–4720, 2009.

[214] C. Xu, D. Lin, and K. Kwok, “Structure, electrical properties and depolarization temperature of $(Bi_{0.5}Na_{0.5})TiO_3$-$BaTiO_3$ lead-free piezoelectric ceramics,” Solid state sciences, vol. 10, no. 7, pp. 934–940, 2008.

[215] L. Schmitt, J. Kling, M. Hinterstein, M. Hoelzel, W. Jo, H.-J. Kleebe, and H. Fuess, “Structural investigations on lead-free $Bi_{1/2}Na_{1/2}TiO_3$-based piezoceramics,” Journal of Materials Science, vol. 46, no. 12, pp. 4368–4376, 2011.

[216] J. E. Daniels, W. Jo, J. Rödel, V. Honkimäki, and J. L. Jones, “Electric-field-induced phase-change behavior in $(Bi_{0.5}Na_{0.5})TiO_3$-$BaTiO_3$-$(K_{0.5}Na_{0.5})NbO_3$: A combinatorial investigations,” Acta materialia, vol. 58, no. 6, pp. 2103–2111, 2010.

[217] R. Ranjan and A. Dviwedi, “Structure and dielectric properties of $(Na_{0.50}Bi_{0.50})_{1x}Ba_xTiO_3$: $0 \leq x \leq 0.10$,” Solid State Communications, vol. 135, no. 6, pp. 394 – 399, 2005.

[218] M. Hinterstein, M. Knapp, M. Hölzel, W. Jo, A. Cervellino, H. Ehrenberg, and H. Fuess, "Field-induced phase transition in $Bi_{1/2}Na_{1/2}TiO_3$-based lead-free piezoelectric ceramics," Journal of Applied Crystallography, vol. 43, pp. 1314–1321, Dec 2010.

[219] A. J. Royles, A. J. Bell, A. P. Jephcoat, A. K. Kleppe, S. J. Milne, and T. P. Comyn, "Electric-field-induced phase switching in the lead free piezoelectric potassium sodium bismuth titanate," Applied Physics Letters, vol. 97, no. 13, p. 132909, 2010.

[220] S.-T. Zhang, A. B. Kounga, E. Aulbach, and Y. Deng, "Temperature-dependent electrical properties of $0.94Bi_{0.5}Na_{0.5}TiO_3$-$0.06BaTiO_3$ ceramics," Journal of the American Ceramic Society, vol. 91, no. 12, pp. 3950–3954, 2008.

[221] Y.-M. Chiang, G. W. Farrey, and A. N. Soukhojak, "Lead-free high-strain single-crystal piezoelectrics in the alkaline–bismuth–titanate perovskite family," Applied Physics Letters, vol. 73, no. 25, pp. 3683–3685, 1998.

[222] Y. Saito, H. Takao, T. Tani, T. Nonoyama, K. Takatori, T. Homma, T. Nagaya, and M. Nakamura, "Lead-free piezoceramics," Nature, vol. 432, no. 7013, pp. 84–87, 2004.

[223] X. Ren, "Large electric-field-induced strain in ferroelectric crystals by point-defect-mediated reversible domain switching," Nature materials, vol. 3, no. 2, pp. 91–94, 2004.

[224] L. X. Zhang, W. Chen, and X. Ren, "Large recoverable electrostrain in mn-doped $(Ba,Sr)TiO_3$ ceramics," Applied Physics Letters, vol. 85, no. 23, pp. 5658–5660, 2004.

[225] Z. Feng and X. Ren, "Striking similarity of ferroelectric aging effect in tetragonal, orthorhombic and rhombohedral crystal structures," Physial Review B, vol. 77, p. 134115, Apr 2008.

[226] H. Nagata, Y. Hiruma, and T. Takenaka, "Electric-field-induced strain for $(Bi_{1/2}Na_{1/2})TiO_3$-based lead-free multilayer actuator," Journal of the Ceramic Society of Japan, vol. 118, no. 1380, pp. 726–730, 2010.

[227] Y. Hiruma, Y. Imai, Y. Watanabe, H. Nagata, and T. Takenaka, "Large electrostrain near the phase transition temperature of $(Bi_{0.5}Na_{0.5})TiO_3$–$SrTiO_3$ ferroelectric ceramics," Applied Physics Letters, vol. 92, no. 26, p. 262904, 2008.

[228] J. Li, F. Wang, C. Leung, S. Or, Y. Tang, X. Chen, T. Wang, X. Qin, and W. Shi, "Large strain response in acceptor- and donor-doped $Bi_{0.5}Na_{0.5}TiO_3$-based lead-free ceramics," Journal of Materials Science, vol. 46, no. 17, pp. 5702–5708, 2011.

[229] C. Groh, D. J. Franzbach, W. Jo, K. G. Webber, J. Kling, L. A. Schmitt, H.-J. Kleebe, S.-J. Jeong, J.-S. Lee, and J. Rödel, "Relaxor/ferroelectric composites: A solution in the quest for practically viable lead-free incipient piezoceramics," Advanced Functional Materials, vol. 24, no. 3, pp. 356–362, 2014.

[230] T. Mihara, H. Watanabe, H. Yoshimori, C. A. P. De Araujo, B. Melnick, and L. D. McMillan, "Process dependent electrical characteristics and equivalent circuit model of sol-gel based PZT capacitors," Integrated Ferroelectrics, vol. 1, no. 2-4, pp. 269–291, 1992.

[231] D. B. A. Rep and M. W. J. Prins, "Equivalent-circuit modeling of ferroelectric switching devices," Journal of Applied Physics, vol. 85, no. 11, pp. 7923–7930, 1999.

[232] D. E. Dausch, E. Furman, F. Wang, and G. H. Haertling, "Plzt-based multilayer composite thin films, part ii: Modeling of the dielectric and hysteresis properties," Ferroelectrics, vol. 177, no. 1, pp. 237–253, 1996.

[233] O. Boser, "Statistical theory of hysteresis in ferroelectric materials," Journal of Applied Physics, vol. 62, no. 4, pp. 1344–1348, 1987.

[234] J.-H. Park, C.-S. Kim, B.-C. Choi, B. K. Moon, J. H. Jeong, and I. W. Kim, “Scaling behavior of ferroelectric hysteresis loop in pulsed-laser-deposited $SrBi_2Ta_2O_9$ thin films,” Applied Physics Letters, vol. 83, no. 3, pp. 536–538, 2003.

[235] J. Maas, T. Schulte, and H. Grotstollen, “Optimized drive control for inverter-fed ultrasonic motors,” in Industry Applications Conference, 1997. Thirty-Second IAS Annual Meeting, IAS’97., Conference Record of the 1997 IEEE, vol. 1, pp. 690–698, IEEE, 1997.

[236] P. Ge and M. Jouaneh, “Modeling hysteresis in piezoceramic actuators,” Precision engineering, vol. 17, no. 3, pp. 211–221, 1995.

[237] Y. Yu, N. Naganathan, and R. Dukkipati, “Preisach modeling of hysteresis for piezoceramic actuator system,” Mechanism and Machine Theory, vol. 37, no. 1, pp. 49–59, 2002.

[238] K. Wang, A. Hussain, W. Jo, and J. Rödel, “Temperature-dependent properties of $(Bi_{1/2}Na_{1/2})TiO_3$-$(Bi_{1/2}K_{1/2})TiO_3$-$SrTiO_3$ lead-free piezoceramics,” Journal of the American Ceramic Society, vol. 95, no. 7, pp. 2241–2247, 2012.

[239] I. Mayergoyz, Mathematical models of hysteresis and their applications. Academic Press: NY, USA, 2003.

[240] A. T. Bartic, D. J. Wouters, H. E. Maes, J. T. Rickes, and R. M. Waser, “Preisach model for the simulation of ferroelectric capacitors,” Journal of Applied Physics, vol. 89, no. 6, pp. 3420–3425, 2001.

[241] P. Chen and M. Madsen, “One dimensional polar responses of the electrooptic ceramic PLZT 7/65/35 due to domain switching,” Acta Mechanica, vol. 41, no. 3-4, pp. 255–264, 1981.

[242] Y. Huo and Q. Jiang, “Modeling of domain switching in ferroelectric ceramics: An example,” International Journal of Solids and Structures, vol. 35, no. 13, pp. 1339 – 1353, 1998.

[243] G. Arlt, “A physical model for hysteresis curves of ferroelectric ceramics,” Ferroelectrics, vol. 189, no. 1, pp. 103–119, 1996.

[244] J. Fan, W. Stoll, and C. Lynch, “Nonlinear constitutive behavior of soft and hard pzt: experiments and modeling,” Acta Materialia, vol. 47, no. 17, pp. 4415 – 4425, 1999.

[245] J. Huber, N. Fleck, C. Landis, and R. McMeeking, “A constitutive model for ferroelectric polycrystals,” Journal of the Mechanics and Physics of Solids, vol. 47, no. 8, pp. 1663 – 1697, 1999.

[246] S. C. Hwang and R. M. McMeeking, “A finite element model of ferroelastic polycrystals,” International Journal of Solids and Structures, vol. 36, no. 10, pp. 1541 – 1556, 1999.

[247] C. M. Landis, “On the fracture toughness of ferroelastic materials,” Journal of the Mechanics and Physics of Solids, vol. 51, no. 8, pp. 1347 – 1369, 2003.

[248] S. C. Hwang and R. M. McMeeking, “A finite element model of ferroelectric polycrystals,” Ferroelectrics, vol. 211, no. 1, pp. 177–194, 1998.

[249] J. A. Warren, “How does a metal freeze? a phase-field model of alloy solidification,” Computing in Science and Engineering, vol. 2, no. 2, pp. 38–49, 1995.

[250] R. Ahluwalia and W. Cao, “Size dependence of domain patterns in a constrained ferroelectric system,” Journal of Applied Physics, vol. 89, no. 12, pp. 8105–8109, 2001.

[251] W. Cao and L. E. Cross, “Theory of tetragonal twin structures in ferroelectric perovskites with a first-order phase transition,” Physial Review B, vol. 44, pp. 5–12, Jul 1991.

[252] W. Zhang and K. Bhattacharya, "A computational model of ferroelectric domains. part i: model formulation and domain switching," Acta Materialia, vol. 53, no. 1, pp. 185 – 198, 2005.

[253] W. Zhang and K. Bhattacharya, "A computational model of ferroelectric domains. part ii: grain boundaries and defect pinning," Acta Materialia, vol. 53, no. 1, pp. 199 – 209, 2005.

[254] H. L. Stadler, "Forward velocity of 180° ferroelectric domain walls in $BaTiO_3$," Journal of Applied Physics, vol. 37, no. 5, pp. 1947–1948, 1966.

[255] M. Kamlah, "Ferroelectric and ferroelastic piezoceramics - modeling of electromechanical hysteresis phenomena," Continuum Mechanics and Thermodynamics, vol. 13, pp. 219–268, 2001.

[256] D. Schrade, R. Mueller, and D. Gross, "Parameter identification in phase field models for ferroelectrics," Proceedings in Applied Mathematics and Mechanics, vol. 9, no. 1, pp. 369–370, 2009.

[257] R. Mueller, S. Kolling, and D. Gross, "On configurational forces in the context of the finite element method," International Journal for Numerical Methods in Engineering, vol. 53, no. 7, pp. 1557–1574, 2002.

[258] A. Bokov and Z.-G. Ye, "Recent progress in relaxor ferroelectrics with perovskite structure," Journal of Materials Science, vol. 41, no. 1, pp. 31–52, 2006.

[259] M. D. Glinchuk and R. Farhi, "A random field theory based model for ferroelectric relaxors," Journal of Physics: Condensed Matter, vol. 8, no. 37, p. 6985, 1996.

[260] Y. Imry and S.-k. Ma, "Random-field instability of the ordered state of continuous symmetry," Physial Review Letters, vol. 35, pp. 1399–1401, Nov 1975.

[261] L. E. Cross, "Relaxorferroelectrics: An overview," Ferroelectrics, vol. 151, no. 1, pp. 305–320, 1994.

[262] I. P. Batra, P. Wurfel, and B. D. Silverman, "Phase transition, stability, and depolarization field in ferroelectric thin films," Physial Review B, vol. 8, pp. 3257–3265, Oct 1973.

[263] X. Meng, X. Wen, and G. Qin, "DFT study on elastic and piezoelectric properties of tetragonal $BaTiO_3$," Computational Materials Science, vol. 49, no. 4, Supplement, pp. S372 – S377, 2010.

[264] M. Cernea, E. Andronescu, R. Radu, F. Fochi, and C. Galassi, "Sol-gel synthesis and characterization of $BaTiO_3$-doped $(Bi_{0.5}Na_{0.5})TiO_3$ piezoelectric ceramics," Journal of Alloys and Compounds, vol. 490, no. 1-2, pp. 690 – 694, 2010.

[265] M. Cernea, G. Poli, G. V. Aldica, C. Berbecaru, B. S. Vasile, and C. Galassi, "Preparation and properties of nanocrystalline BNT-BTx piezoelectric ceramics by sol-gel and spark plasma sintering," Current Applied Physics, vol. 12, no. 4, pp. 1100 – 1105, 2012.

[266] J. Wang, M. Kamlah, T.-Y. Zhang, Y. Li, and L.-Q. Chen, "Size-dependent polarization distribution in ferroelectric nanostructures: Phase field simulations," Applied Physics Letters, vol. 92, no. 16, p. 162905, 2008.

[267] X. Tan, E. Aulbach, W. Jo, T. Granzow, J. Kling, M. Marsilius, H.-J. Kleebe, and J. Rödel, "Effect of uniaxial stress on ferroelectric behavior of $(Bi_{1/2}Na_{1/2})TiO_3$-based lead-free piezoelectric ceramics," Journal of Applied Physics, vol. 106, no. 4, p. 044107, 2009.

[268] R. Yimnirun, Y. Laosiritaworn, and S. Wongsaenmai, "Effect of uniaxial compressive pre-stress on ferroelectric properties of soft PZT ceramics," Journal of Physics D: Applied Physics, vol. 39, no. 4, p. 759, 2006.

[269] O. Auciello, “Science and technology of thin films and interfacial layers in ferroelectric and high-dielectric constant heterostructures and application to devices,” Journal of Applied Physics, vol. 100, no. 5, p. 051614, 2006.

[270] D. H. Lowndes, D. Geohegan, A. Puretzky, D. Norton, and C. Rouleau, “Synthesis of novel thin-film materials by pulsed laser,” Science, vol. 273, p. 16, 1996.

[271] C. Ma, H. Guo, S. P. Beckman, and X. Tan, “Creation and destruction of morphotropic phase boundaries through electrical poling: A case study of lead-free $Bi_{1/2}Na_{1/2}TiO_3$-$BaTiO_3$ piezoelectrics,” Physical Review Letters, vol. 109, p. 107602, Sep 2012.

Acknowledgments

An dieser Stelle möchte ich mich bei allen bedanken, die mich während der Anfertigung meiner Arbeit unterstützt haben.

Als erstes danke ich Kyle Grant Webber für die Betreuung und Unterstützung wärend meiner Arbeit. Er war mir eine große Hilfe bei der Strukturierung und Verschriftlichung meiner wissenschaflichen Projekte.

Ich danke Ralf Müller für die Begutachtung meiner Arbeit. Ein weiterer Dank geht an Baixiang Xu für die vielen hilfreichen Erklärungen zu Phasenfeld-Implementierungen mit FEAP.

Herrn Rödel danke ich für meine Aufnahme als Doktorand, die Hilfe bei meiner wissenschaftlichen Neuorientierung und der finanziellen Unterstützung meines Auslandsaufenthaltes.

Meinen Kollegen von NAW danke ich für die kollegiale Zusammenarbeit in den letzten Jahren.

Ein großer Dank gebührt meiner Frau, die mich in schwierigen Momenten immer wieder aufbauen konnte.

Vielen Dank an Prof. Long-Qing Chen und seine Forschungsgruppe, die mich für drei Monate sehr gastfreundlich bei sich aufgenommen haben.

Schließlich danke ich der Graduate School of Excellence Computational Engineering der TU Darmstadt, die über große Strecken meine Arbeit finanziell unterstützt hat.

CURRICULUM VITAE

Daniel Jason Franzbach

Address	Pankratiusstr. 30 64289 Darmstadt
Birth	06.04.1983, in Kassel, Germany
Nationality	German

University Education

12/2008 – 09/2013	PhD Thesis: "Field Induced Phase Transitions in Ferroelectric Materials" Department of Materials Science, Graduate School of Excellence Computational Engineering, TU Darmstadt (Group NAW, Prof. Rödel)
01/2012 – 03/2012	Visiting Scholar: Department of Materials Science and Engineering Prof. Long-Qing Chen, The Pennsylvania State University, State College, USA
10/2003 – 10/2008	Studies: Physics at the Philipps-Universität Marburg Degree: Physik-Diplom Topic: Optical Amplification, Lasing und Emission Characteristic of III-V-semiconductor heterostructures on Si-Substrate

Scholarships

11/2009 – 10/2012	Scholar of the Graduate School of Excellence Computational Engineering (CE), TU Darmstadt
12/2008 – 10/2009	Scholar of the Graduiertenkolleg "TICMO", TU Darmstadt

School Education

08/1993 – 05/2002	Albert-Schweitzer-Gymnasium, Kassel (Abitur)
08/1989 – 07/1993	Mergellschule Kassel-Kirchditmold

Darmstadt, September 15th, 2013

Publications

[1] B. Kunert, I. Nemeth, S. Zinnkann, G. Lukin, T. B. Adams, R. Fritz, K. Volz, W. Stolz, C. Lange, N. S. Koester, D. J. Franzbach, S. Chatterjee, W. W. Ruhle, N. C. Gerhardt, N. Koukourakis, and M. Hofmann, "Optical gain in Ga(NAsP)/(BGa)(AsP) multi-quantum-well heterostructures grown lattice-matched on (001) silicon substrate", *2008 66th Annual Device Research Conference (DRC),* pp. 301-302302, 2008.

[2] B. Kunert, S. Liebich, S. Zinnkann, I. Nemeth, R. Fritz, K. Volz, W. Stolz, C. Lange, N. S. Koester, D. J. Franzbach, S. Chatterjee, W. W. Ruhle, N. C. Gerhardt, N. Koukourakis, and M. Hofmann, "Laser operation of the III/V compound material Ga(NAsP) grown lattice matched on (001) Si substrate", *2009 67th Annual Device Research Conference (DRC),* pp. 213-214214, 2009.

[3] C. Lange, N. S. Koster, D. J. Franzbach, S. Chatterjee, W. W. Ruhle, S. Zinnkann, S. Liebich, I. Nemeth, R. Fritz, K. Volz, W. Stolz, B. Kunert, N. C. Gerhardt, N. Koukourakis, and M. Hofmann, "Lasing in optically pumped Ga(NAsP)/(BGa)(AsP) heterostructures on silicon", *2009 Conference on Lasers and Electro-Optics (CLEO),* pp. 2 pp.-2 pp.2 pp., 2009.

[4] S. Liebich, M. Zimprich, A. Beyer, C. Lange, D. J. Franzbach, S. Chatterjee, N. Hossain, S. J. Sweeney, K. Volz, B. Kunert, and W. Stolz, "Laser operation of Ga(NAsP) lattice-matched to (001) silicon substrate", *Applied Physics Letters,* vol. 99, Aug 15 2011.

[5] D. J. Franzbach, B. X. Xu, R. Mueller, and K. G. Webber, "The effects of polarization dynamics and domain switching energies on field induced phase transformations of perovskite ferroelectrics", *Applied Physics Letters,* vol. 99, Oct 17 2011.

[6] D. J. Franzbach, Y. J. Gu, L. Q. Chen, and K. G. Webber, "Electric field-induced tetragonal to orthorhombic phase transitions in $[110]_c$-oriented $BaTiO_3$ single crystals", *Applied Physics Letters,* vol. 101, Dez 05 2012.

[7] Y.-H. Seo, D. J. Franzbach, J. Koruza, A. Benčan, B. Malič, M. Kosec, J. L. Jones, and K. G. Webber, "Nonlinear stress-strain behavior and stress-induced phase transitions in soft $Pb(Zr_{1-x}Ti_x)O_3$ at the morphotropic phase boundary", *Physical Review B,* vol. 87, Mar 28 2013.

[8] Claudia Groh, Daniel J. Franzbach, Wook Jo, Kyle G. Webber, Jens Kling, Ljubomira A. Schmitt, Hans-Joachim Kleebe, Soon-Jong Jeong, Jae-Shin Lee, and Jürgen Rödel, "Relaxor/Ferroelectric Composites: A Solution in the Quest for Practically Viable Lead-Free Incipient Piezoceramics?", *Advanced Functional Materials,* vol. 24(3), Jan 22 2014.

Conference Presentations:

[1] D. J. Franzbach, C. Lange, M. Schwalm, S. Chatterjee, B. Kunert, K. Volz, W. Stolz, and W. Ruhle, Poster: "Optical gain in Ga(NAsP) quantum wells using the variable stripe-length method", *2008 72. Annual Meeting of the DPG and DPG Spring Meeting of the Condensed Matter Division.*

[2] D. J. Franzbach, K. G. Webber, J. Rödel, Talk: "FEM Simulations of Switching Phenomena in Ferroelectric Microstructures", *2010 6th International Workshop on Direct and Inverse Problems in Piezoelectricity.*

[3] D. J. Franzbach, K. G. Webber, Talk: "The effects of polarization dynamics and domain switching energies on field induced phase transformations", *2011 The 20th IEEE International Symposium on Applications of Ferroelectrics International Symposium on Piezoresponse Force Microscopy & Nanoscale Phenomena in Polar Materials.*

[4] D. J. Franzbach, K. G. Webber, Talk: "Phasefield simulation of field induced phase transformations in ferroelectric single crystals", *2011 7th International Workshop on Direct and Inverse Problems in Piezoelectricity.*

[5] D. J. Franzbach, K. G. Webber, Talk: "Field induced phase transformations in $BaTiO_3$ single crystals", *2012 The 21th IEEE International Symposium on Applications of Ferroelectrics International Symposium on Piezoresponse Force Microscopy & Nanoscale Phenomena in Polar Materials.*

[6] D. J. Franzbach, B. Xu, W. Jo, K. G. Webber, Talk: "Modeling of relaxor-ferroelectric composite materials", *2012 8th International Workshop on Direct and Inverse Problems in Piezoelectricity.*